The role of LRP2 in sonic hedgehog dependent adult neurogenesis

Inaugural-Dissertation

to obtain the academic degree
Doctor rerum naturalium (Dr. rer. nat.)

submitted to the Department of Biology, Chemistry and Pharmacy
of Freie Universität Berlin

by

Lena Bunatyan

2019

The work was carried out from 11/2014 to 08/2019 under the supervision of Prof. Dr. Thomas E. Willnow at the Max Delbrück Center for Molecular Medicine in Berlin.

1st Reviewer:	Prof. Dr. Thomas E. Willnow Max Delbrück Center for Molecular Medicine
2nd Reviewer:	Prof. Dr. Petra Knaus Institute of Chemistry and Biochemistry, Freie Universität Berlin

Date of defense: 29.01.2020

Summary

LRP2 is an endocytic receptor of the LDL receptor gene family expressed on the apical surface of absorptive epithelia in the embryonic and the adult mammalian organisms. Binding a functionally diverse array of ligands, including morphogens, this receptor plays a crucial role not only in endocytosis but also in regulation of signal transduction in various cell types during embryonic development and in adulthood. LRP2 is best known for its ability to mediate cellular uptake of the morphogens sonic hedgehog (SHH) and bone morphogenetic protein (BMP) 4, an activity required to establish SHH and BMP signaling centers in the embryonic neural tube. Loss of receptor expression in gene targeted mice or in patients with inheritable *LRP2* gene defect (Donnai Barrow syndrome) results in disturbances in neural tube neurogenesis and in malformation of the embryonic forebrain.

Intriguingly, expression of LRP2 persists in ependyma cells of adult mammalian brain. Ependymal cells are part of the neurogenic niche of the subventricular zone (SVZ), one of two regions of the adult mammalian brain capable of sustained neurogenesis. A possible role for LRP2 in adult neurogenesis was supported by earlier work documenting a decreased proliferative capacity in the SVZ of adult receptor mutant mice. Still, the molecular details of receptor function in adult neurogenesis remained obscure. I addressed this important question by performing detailed investigations of the adult neurogenesis and relevant ependymal cell functions in wild-type and LRP2-deficient mouse models as well as in brain explants and primary ependymal cell lines derived thereof.

In my studies, I uncovered defects in SHH signaling in LRP2-deficient mice in the rostral but not the caudal regions of the SVZ. A region-specific impact of receptor deficiency in the SVZ was also observed for other morphogen pathways, including BMP and WNT, as well as for mTOR activtity in this niche. The region-specific alterations in morphogen signaling in the SVZ coincided with a loss of the neural stem cell population and with impaired neurogenesis in the rostral but not the caudal region of the LRP2-deficient SVZ. Finally, the regional specificity in LRP2 action in the adult brain was substantiated by documenting aberrant accumulation of SHH in the caudal SVZ.

Jointly, the above findings argued for a global effect of LRP2 activity on spatial control of adult neurogenesis in the mouse brain. This hypothesis received experimental support by documenting a defect in coordination of motile cilia beating in ependymal cells of LRP2 deficient mice. Because coordination of cilia beating is essential to control the flow of the cerebrospinal fluid (CSF) in a caudal to rostral direction, these findings suggested disturbed CSF flow and, hence, faulty distribution of morphogens to underlie the region-specific impact of receptor deficiency on morphogen signaling and adult neurogenesis in the SVZ. The molecular mechanism of LRP2 action in motile cilia function still remains to be fully established. However, my observations of the localization of LRP2 to the endocytically active ciliary pocket and of an altered distribution of endocytic markers in motile cilia from receptor mutant cells supports a role for LRP2 in controlling endocytic processes that safeguard coordinated cilia beating and thereby proper morphogen distribution in the neurogenic niche of the SVZ.

Zusammenfassung

LRP2 ist ein Endozytoserezeptor der LDL Rezeptor Genfamilie und wird auf der apikalen Zelloberfläche absorbierender Epithelien in embryonalen und adulten Organismen exprimiert. Durch die Bindung funktionell unterschiedlicher Liganden, einschließlich der Bindung von Morphogenen, übernimmt dieser Rezeptor nicht nur eine essentielle Rolle in der Endozytose aber auch in der Regulierung von Signaltransduktionskaskaden in verschiedenen Zelltypen während der Embryonalentwicklung sowie im adulten Organismus. Am besten wurde die Aufnahme der Morphogene Sonic Hedgehog (SHH) und knochenmorphogenetisches Protein (BMP) 4 durch LRP2 charakterisiert. Diese wird benötigt um die Signalzentren innerhalb des embryonalen Neuralrohres zu etablieren. Der genetisch bedingte Verlust der Rezeptorexpression in LRP2-defizienten Mäusen oder der vererbte *LRP2* Gendefekt in Patienten (Donnai-Barrow-Syndrom) führt zu Beeinträchtigungen der Neurogenese im Neuralrohr und zu Fehlbildungen des embryonalen Vorderhirns.

Interessanterweise bleibt die LRP2 Expression in adulten Ependymzellen des Gehirns erhalten. Ependymzellen sind Teil der neurogenen Nische der subventrikulären Zone (SVZ), eine von zwei Regionen im adulten Gehirn, die für eine anhaltende Neurogenese verantwortlich sind. Eine mögliche Rolle für LRP2 in der adulten Neurogenese wurde durch frühere Studienbereits postuliert. In diesen wurde gezeigt, dass adulte Rezeptor-defiziente Mäuse unter einer geringeren Proliferationsrate in der SVZ leiden. Dennoch blieb die molekulare Funktionsweise des Rezeptors während der adulten Neurogenese unklar. Mit Hilfe detaillierte Untersuchungen der adulten Neurogenese sowie Untersuchungen zu relevanten Aufgaben der Ependymzellen in Wildtyp Mäusen und LRP2-defizienten Maus Modellen, als auch in Gehirnexplantaten und primären Ependym Zellkulturen bearbeitete ich diese Fragestellung.

In meinen Studien konnte ich Defekte im SHH Signalweg in LRP2-defizienten Mäusen in rostralen aber nicht caudalen Regionen der SVZ feststellen. Dieser regionsspezifische Rezeptor

Defekt in der SVZ konnte auch in anderen Morphogen-Signalwegen wie dem BMP und dem WNT Signalweg aber auch in der mTOR Signalaktivität in dieser Nische nachgewiesen werden. Die regionsspezifischen Veränderungen in den Morphogen-Signalwegen in der SVZ gingen einher mit einem Verlust der neuronalen Stammzell Population sowie einer beeinträchtigten Neurogenese in der rostralen aber nicht caudalen Region der LRP2-defizienten SVZ. Schließlich konnte die regionsspezifische Aktivität von LRP2 im adulten Gehirn auch durch eine Anreicherung von SHH in der caudalen SVZ bestätigt werden.

Insgesamt zeigen die genannten Ergebnisse eine globale Wirkung der LRP2 Aktivität auf die Kontrolle der adulten Neurogenese im Mausgehirn. Diese Hypothese wird durch die Dokumentation von Defekten im koordinierten Schlagen beweglicher Zilien von Ependymzellen in LRP2-defizienten Mäusen bestätigt. Das koordinierte Schlagen der Zilien reguliert den Fluss der Zerebrospinalflüssigkeit (CSF) in einer caudal nach rostral verlaufenden Richtung. Meine Ergebnisse legen eine gestörte Richtung des CSF Flusses sowie eine fehlerhafte Verteilung der Morphogene nahe, die durch die regionalspezifischen Auswirkungen durch den Verlust der Rezeptoraktivität auf Morphogen-Signalwege und Neurogenese in der adulten SVZ ausgelöst werden. Der molekulare Mechanismus der LRP2 Aktivität auf die beweglichen Zilien muss noch genauer aufgeklärt werden. Dennoch unterstützen meine Beobachtungen zur Lokalisation von LRP2 in der endozytotisch aktiven ziliären Tasche, und eine veränderte Verteilung von endozytotischen Markern im beweglichen Zilium in Rezeptor-defizienten Zellen eine Rolle von LRP2 in der Regulierung endozytotischer Prozesse, die koordiniertes Schlagen der Zilien und somit eine richtige Verteilung von Morphogenen in der neurogenen Nische der SVZ sicherstellen.

Table of contents

Summary II

Zusammenfassung IV

Table of contents VI

List of abbreviations IX

List of figures XIII

List of tables XVII

1 Introduction 1

1.1 LRP2, a member of LDLR gene family 1

1.1.1 LDL receptor-related protein 2 (LRP2) 3

1.1.2 Role of LRP2 in formation of the embryonic forebrain 4

1.1.3 LRP2 acts as a clearance receptor during eye development 6

1.1.4 Donnai-Barrow/ Facio-oculo-acoustico-renal (FOAR)-syndrome 7

1.2 Cell biology of SHH signaling 7

1.2.1 The SHH receptorsome 12

1.2.2 LRP2 as a novel member of the SHH receptorsome 15

1.3 LRP2 expression in the adult brain 17

1.3.1 Architecture of the neurogenic niche in ventricular- subventricular zone 18

1.4 Role of LRP2 in adult neurogenesis in the SVZ 21

2 Aim of my work 23

3 Material and methods 24

3.1 Animals 24

3.1.1 Transgenic mice strains 24

3.1.2 BrdU injections 24

3.2 Molecular biology 25

3.2.1 Genomic DNA preparation 25

3.2.2 PCR genotyping 25

3.3 Protein biochemistry 26

3.3.1 Dissection of the ventricular forebrain region for western blot analyses 26

3.3.2 Preparation of tissue lysates 28

3.3.3 Protein concentration determination 28

3.3.4 SDS polyacrylamide gel electrophoresis 28

3.3.5 Western blotting 29

3.4 Dissection and culturing of lateral ventricles from the mouse brain 30

3.4.1 Dissection of mouse brain lateral ventricular walls for the en face visualization 30

3.5 Primary cultures of mouse brain ependymal cells 31

3.6 Ligand uptake assays 32

3.7 Histology 33

3.7.1 Preparation of mice for histology 33

3.7.2 Paraffin tissue sectioning 34
3.7.3 Free floating sections 34
3.7.4 Cryosections 35
3.7.5 Immunohistochemistry 35
3.7.6 Detection of β-galactosidase (lacZ) activity 35
3.7.7 Immunofluorescence stainings of adult brain tissue sections 36
3.7.8 Immunofluorescence staining of cell cultures 37
3.7.9 Immunostaining of SVZ whole mounts for en face visualization 37
3.7.10 Thyramide signal amplification 38
3.7.11 Immunostaining using peroxidase reaction 39
3.7.12 Summary of antibodies used in IHC methods and WB analysis 40
3.7.13 In Situ hybridization technique 45
3.7.14 RNA probes generation procedure 46

3.8 Quantification 47

3.8.1 Nuclear signal quantification 47
3.8.2 Cytoplasmic signal quantification 48
3.8.3 Western blot signal quantification 49
3.8.4 Co-localization analysis 50
3.8.5 Quantification of ciliary patch organization in ependymal cells of lateral ventricular walls 51
3.8.6 Statistical Analyses 53
3.8.7 Bright field 54
3.8.8 Laser scanning confocal microscopy 54

4 Results 55

4.1 Role of LRP2 in establishment of the signaling milieu in the adult mouse subventricular zone 55

4.1.1 Region-specific analysis of SHH signaling in the SVZ of adult wildtype and LRP2 mutant mice 56
4.1.2 Detection of components of the SHH receptorsome in the SVZ 60
4.1.3 Activity of the BMP signaling pathway in the SVZ 69
4.1.4 Analysis of mTOR activity in the SVZ of LRP2 mutant and control mice 72
4.1.5 Analysis of WNT signaling pathway in the SVZ of LRP2 mutant and control mice 81

4.2 Neurogenesis 83

4.2.1 Loss of LRP2 decreases the population of fast dividing cell in the rostral but not in caudal SVZ 83
4.2.2 Depletion of the neural stem cell pool in the SVZ niche of LRP2-deficient mice 87
4.2.3 The oligodendrocyte lineage is unaffected in the SVZ of *Lrp2*$^{-/-}$ mice 92

4.3 Motile cilia on ependymal cells 93

4.3.1 Ciliary patches display non-coordinated displacement in ependymal cells of LRP2-deficient mice 94
4.3.2 Absence of LRP2 affects the coordinated beating of motile ciliary patches on ependymal cells 97

4.3.3 Ependymal cells in LRP2 deficient mice show misalignment in motile ciliary patch localization and beating orientation 99
4.3.4 Individual cilium beating directions are not synchronized within a ciliary patch in LRP2

mutant mice ... 101
4.3.5 The numbers of motile cilia but not the size of the ciliary patch is altered in LRP2 mutant ependymal cells ... 103
4.3.6 Ciliary axonemal structures are unchanged in ependymal cells of *Lrp2*$^{-/-}$ compared with control brains ... 105
4.4 LRP2 mediates endocytic uptake of SHH by ependymal cells ... 106
4.4.1 Analysis of SHH uptake using primary ependymal cultures ... 106
4.4.2 Analysis of SHH uptake using ventricular lateral wall whole mounts (LWWM) ... 110
4.4.3 Localization of internalized SHH ligand in various cellular compartments ... 112
4.5 LRP2 determines localization of Rab GTPases in motile cilia ... 113
4.5.1 Early endosomal compartment markers are reduced in cell body and motile cilia of ependymal cells lacking LRP2 ... 113
4.5.2 Recycling endosomal compartment markers are unchanged in ependymal cells and in motile cilia lacking LRP2 ... 116
4.5.3 LRP2 deficiency impacts distribution of Rab GTPases involved in transcytosis and cell signaling in ependymal cell body and motile cilia ... 119
4.5.4 Late endosomal compartment markers in ependymal cells and motile ciliary structures are not affected by absence of LRP2 ... 122
5 Discussion ... 124
5.1 LRP2 controls SHH activity in a region-specific manner in the SVZ ... 125
5.1.1 Expression of members of the SHH receptorsome along the dorso-ventral and rostro-caudal axis of the SVZ ... 127
5.1.2 Production and spatial distribution of SHH in SVZ ... 128
5.1.3 LRP2 impacts adult neurogenesis in the rostral but not caudal regions of the SVZ ... 129
5.2 Activity alterations in BMP, WNT/β catenin and mTOR signaling pathways predominate in the rostral SVZ region of LRP2 mutants ... 131
5.3 CSF flow and morphogen distribution in the SVZ ... 134
5.3.1 Motile cilia on ependymal cells ... 135
5.3.2 Role of LRP2 in functional integrity of motile cilia on ependymal cells ... 136
5.3.3 LRP2 acts as endocytic receptor in ependymal cells ... 138
5.4 Summary and outlook ... 141
6 References ... 144
7 Appendices ... 179
7.1 Publications ... 179
7.2 Acknowledgement ... 180
7.3 Selbstständigkeitserklärung ... 181
7.4 Curriculum vitae ... 182

List of abbreviations

4EBP1	4E (eIF4E)-binding protein 1
ADP	Adenosine diphosphate
APOER	Apolipoprotein E receptor-2
ARH	Autosomal recessive hypercholesterolemia
ARL13B	ADP-ribosylation factor-like protein 13B
ATP	Adenosintriphosphat
BB	Basal body
BCA	Bicinchoninic acid
BCIP	5-bromo-4-chloro-3-indolyl-phosphate, 4-toluidine salt
BHLH	Basic helix-loop-helix
BLBP	Brain lipid-binding protein
BMP	Bone morphogenetic protein
BNST	Bed nuclei of the stria terminalis
BOC	Brother of CDO
CD	Caudal dorsal
CD	Cluster of differentiation
CDO	Cell-adhesion molecule-related, down-regulated by oncogenes
CK	Casein kinase 1a
CMZ	Ciliary marginal zone
CP	Cryoprotectant
CR	Complement-type repeats
CSD	The circular standard deviation
CSF	Cerebrospinal fluid
CTP	Cytidine triphosphate
CV	Caudal ventral
DAB	3’-diaminobenzidine
DAB2	Disabled homolog 2 adaptor protein
DAPI	4′,6-diamidino-2-phenylindole,
DBS	Donnai-Barrow syndrome
DBX	Developing brain homeobox 2
DIG	Digoxigenin
DIV	Differentiation day
DMEM	Dulbecco's modified eagle medium
DNA	Deoxyribonucleic acid
DPBS	Dulbecco's phosphate-buffered saline
EAA1	Early endosome antigen 1

ECD	Extracellular domain
EDTA	Ethylenediaminetetraacetic acid
EGF	Epidermal growth factor
EGFP	Enhanced green fluorescent protein
EGTA	Ethylene glycol-bis (β-aminoethyl ether)-N,N,N′,N′-tetraacetic acid
EM	Electron microscopy
ENU	N-ethyl-N-nitrosourea
ER	Endoplasmic reticulum
EVC	Ellis-van Crefeld
FBS	Fetal bovine serum
FCS	Fetal calf serum
FGFR	Fibroblast growth factor receptor
FL	Full lenght
FNII	fibronectin-type III repeat
FOAR	Facio-oculo-acoustico-renal
FOP	FGFR1 oncogene partner
GAS	Growth arrest-specific 1
GC	granular cells
GFAP	Glial fibrillary acidic protein
GFRα	Glial cell-derived neurotrophic factor receptors α
GLAST	Glutamate aspartate transporter
GLI	Glioma-associated oncogene homolog
GPCR	G protein-coupled receptor
GPI	Glycosyl-phosphatidylinositol
GPRK	G protein-coupled receptor (GPCR) kinase 2
GSK3β	Glycogen synthase kinase 3β
GST	Glutathione -transferase
GTP	Guanosine-5'-triphosphate
HBSS	Hank's balanced salt solution
HHIP	Hedgehog interacting protein
HPE	Holoprosencephaly
HRP	Horseradish peroxidase
ID3	Inhibitor of DNA binding 3
IF	Immunofluorescence
IFT	Intraflagellar transport
IHC	Immunohistochemistry
ISH	In situ hybridization
KIF3A	Kinesin-like protein 3A
LAMP1	Lysosomal-associated membrane protein 1
LDLR	Low-density lipoprotein receptor

LEF	Lymphoid enhancer-binding factor
LRP	Low-density lipoprotein receptor-related protein
LWWM	Lateral ventricular wall whole mounts
MABT	Maleic acid buffer
MGV	Mean gray values
MIV	Myosin IV
mTOR	mammalian Target of rapamycin
mTORC	mTOR Complex
NBT	Nitro blue tetrazolium
NFAT	Nuclear factor of activated T-cells
NKX	NK1 homeobox
NMII	Non-muscle myosin II
NSC	Neural stem cells
NTMT	NaCl, Tris-cl, MgCl2, Tween-20
NVP	Nodal vesicular particles
OB	Olfactory bulb
OLIG	Oligodendrocyte transcription factor
ON	Over night
ON	Optic nerve
PAX	Paired box protein
PCP	Planar cell polarity
PCR	Polymerase chain reaction
PFA	Paraformaldehyde
PGC	Periglomerular cells
PI3K	Phosphoinositide 3-kinase
PKA	Protein kinase A
PTCH	Patched
PVA	Polyvinyl alcohol
R26YFP	Roza 26 Yellow fluorescent protein
RD	Rostral dorsal
RDVM	Rostral diencephalon ventral midline
RGC	Radial glial cells
RMS	Rostral migratory stream
RNA	Ribonucleic acid
ROI	Region of interest
RT	Room temperature
RV	Rostral ventral
SC	Saline-sodium citrate
SDS	Sodium dodecyl sulfate
SEM	Standard error of mean

SGZ	Subgranular zone
SHH	Sonic hedgehog
SMO	Smoothened
SORL	Sorting protein related receptor containing LDLR class A repeats
SOX	Sex determining region Y-box
SSC	Sodium citrate buffer
SUFU	Suppressor of fused
SVZ	Subventricular zone
TBS	Tris-buffered saline
TBST	Tris-buffered saline tween-20/tritone
TCF	Transcription factor
TM	Thresholded Mander's
TNB	Tris-NaCl-blocking buffer
TNT	Tris-NaCl-Tween buffer
TSA	Thyramide signal amplification
TUB	Tubulin
UTP	Uridintriphosphat
VLDL	Very-low-density lipoprotein receptor
VPS	Vacuolar protein sorting 10 protein
VZ	Ventricular zone
WB	Western blot
WEC	Whole embryo cultures
WNT	Wingless-related integration site
WT	Wild type
ZO1	Zonula occludens-1

List of figures

Figure 1.1: Members of the low-density lipoprotein receptor (LDLR) gene family in vertebrates (modified from (Carlo et al., 2013)). 2
Figure 1.2: Sonic hedgehog signaling cascade in the primary cilium (modified from (Briscoe & Thérond, 2013)). 10
Figure 1.3: Structural organization of SHH binding proteins, SHH receptorsome (modified from (Christ et al., 2016)). 13
Figure 1.4: Maturation steps of ependymal cells (modified from (Ohata & Alvarez-Buylla, 2016)) 17
Figure 1.5: Composition of ventricular and subventricular zones in the wall of the lateral ventricles (modified from (Daniel A. Lim & Alvarez-Buylla, 2016)). 19
Figure 1.6 LRP2 is expressed at the apical cell surface and at the base of motile cilia of ependymal cells (modified from (Gajera et al., 2010)) 21
Figure 3.1: Dissection of the lateral ventricles of the adult mouse brain in a regional specific manner (modified from (Xiong et al., 2017)("The Mouse Brain in Stereotaxic Coordinates, Compact—3rd Edition," n.d.)). 27
Figure 3.2: Dissection steps for lateral ventricular wall whole mounts (LWWMs) (modified from (Labedan et al., 2016)). 30
Figure 3.3: Quantification of the nuclear immunosignals 48
Figure 3.4: Mean gray value (MGV) quantification in the region of interest (ROI) using ImageJ. 49
Figure 3.5: Quantification of signal intensity levels for protein bands in western blot analyses. 50
Figure 3.6: Co-localization analysis performed in Fiji software 51
Figure 3.7: Quantitative analyses of ciliary patch organization and activity by the Biotool software 52
Figure 4.1: Decreased SHH signaling in the SVZ of LRP2-deficient mice 57
Figure 4.2: SHH signaling is retained in the caudal SVZ of LRP2-deficient mice 58

Figure 4.3: Reduced level of ventral Gli1 expression in the rostral SVZ of LRP2-deficient mice as shown by in situ hybridization. 58
Figure 4.4: In situ hybridization analysis of Gli1 expression in the caudal SVZ........ 59
Figure 4.5: Levels of Smo expression are unchanged in the rostral SVZ of LRP2-deficient mice. 60
Figure 4.6: Levels of Smo expression are unchanged in the caudal SVZ of LRP2-deficient mice. 61
Figure 4.7: Ptch1 expression in the rostral SVZ 61
Figure 4.8: Ptch1 transcript levels are increased in the caudal SVZ of *Lrp2*$^{-/-}$ animals 62
Figure 4.9: Cdon expression in the rostral SVZ region. 63
Figure 4.10: Cdon expression in the caudal SVZ region. 63
Figure 4.11: Levels of Boc transcripts are moderately decreased in the LRP2-deficient SVZ. 64
Figure 4.12: Boc transcript levels are unaltered in the caudal SVZ of LRP2-deficient mice ... 65
Figure 4.13: Levels of full length and active forms of SHH in the rostral SVZ region. 67
Figure 4.14: Increased levels of SHH-Np in the caudal SVZ of LRP2-deficient mice........ 68
Figure 4.15: ID3 levels are increased in the rostral SVZ of LRP2-deficient mice........ 70
Figure 4.16: ID3 levels are unchanged in the caudal SVZ of LRP2-deficient mice 71
Figure 4.17: Levels of pS6RP are elevated in the rostral SVZ of LRP2-deficient mice........ 73
Figure 4.18: Levels of pS6RP are comparable in the caudal SVZ regions of LRP2-deficient mice and controls 74
Figure 4.19: The neuronal stem cell population responsive to mTOR signaling is expanded in the rostral SVZ of LRP2-deficient mice........ 75
Figure 4.20: The numbers of pS6RP and SOX2 doubly positive cells are unchanged in the caudal SVZ of LRP2-deficient mice........ 76
Figure 4.21: Mice lacking LRP2 have reduced levels of S6RP in the rostral ventral SVZ 77
Figure 4.22: Levels of p4EBP1 are increased in the rostral SVZ region in LRP2 deficient mice. 78
Figure 4.23: The level of phosphorylated 4EBP1 is increased in the caudal dorsal SVZ of *Lrp2*$^{-/-}$ mice........ 80
Figure 4.24: Total levels of 4EBP1 positive cells decline in the rostral SVZ of LRP2-deficient mice. 81

Figure 4.25: WNT signaling is decreased in the rostral SVZ of LRP2 deficient-mice. 82

Figure 4.26: WNT signaling is slightly decreased in the caudal SVZ of LRP2 deficient-mice. 83

Figure 4.27: The number of fast proliferating neuronal progenitors is reduced in ventral and dorsal areas of the rostral *Lrp2*$^{-/-}$ SVZ. 85

Figure 4.28: The numbers of fast proliferating cells are similar in caudal SVZ regions of LRP2-deficient mice and their littermate controls 86

Figure 4.29: The number of fast proliferating cells in the subgranular zone of the hippocampus is unchanged in LRP2 mutant mice 87

Figure 4.30: The neuronal stem cell pool is depleted in the rostral SVZ of mice lacking LRP2. 88

Figure 4.31: The neuronal stem cell pool is unchanged in the caudal SVZ of LRP2-deficient mice. 89

Figure 4.32: The neuronal stem cell pool is depleted in the rostral SVZ of mice lacking LRP2. 90

Figure 4.33: LRP2 deficient mice show an increase in SOX2 positive neuronal stem cell levels in the ventral medial wall of caudal SVZ 91

Figure 4.34: The population of OLIG2 positive oligodendrocytes is unchanged in the rostral SVZ of LRP2 mutant mice 92

Figure 4.35: The number of OLIG2 positive oligodendrocytes in the caudal SVZ is similar in LRP2-deficient and controls mice 93

Figure 4.36: Ciliary patch displacement in ependymal cells of LRP2-deficient mice 95

Figure 4.37: The beating orientation of the ciliary patch is not coordinated in *Lrp2*$^{-/-}$ ependymal cells. 98

Figure 4.38: Ciliary patch localization and beating orientation are not coordinated in ependymal cells of *Lrp2*$^{-/-}$ mice. 100

Figure 4.39: The beating direction of individual cilia within a ciliary patch is not coordinated in ependymal cells of *Lrp2*$^{-/-}$ mice. 101

Figure 4.40: The number of motile cilia in a ciliary patch are increased in *Lrp2*$^{-/-}$ ependymal cells. 103

Figure 4.41: The extent of ciliary patches and of ependymal cell surface are unchanged in mice lacking LRP2. 104
Figure 4.42: The structure of the ciliary axoneme is comparable in ependymal cells of *Lrp2*$^{-/-}$ and control mice 105
Figure 4.43: Ependymal cells from LRP2-deficient mice fail to take up GST-SHH-N during 2 hours of ligand incubation. 107
Figure 4.44: Ependymal cells of LRP2-deficient mice fail to take up GST-SHH-N during 24 hours of ligand treatment 108
Figure 4.45: Ependymal cells of LRP2 deficient mice fail to take up GST-SHH-N ligand during 2 hours of ligand treatment 109
Figure 4.46: En face preparations of the lateral ventricles from adult LRP2-deficient mice fail to take up exogenous GST-SHH-N. 111
Figure 4.47: Internalized SHH-N is mainly found in early endosomal and recycling compartments of ependymal cells 112
Figure 4.48: Localization of early endosomal marker Rab4 in motile cilia and in cell soma of ependymal cells 114
Figure 4.49: EEA1 levels in ependymal cells and motile cilia of *Lrp2*$^{-/-}$ and control mice 115
Figure 4.50: Levels of Rab35 in cell body and motile cilia of ependymal cultures 117
Figure 4.51: Levels of Rab11 in cell body and motile cilia of primary ependymal cells 118
Figure 4.52: Rab8a expression in cell body and motile cilia of primary ependymal cells 119
Figure 4.53: Rab17 levels in cell body and motile cilia of ependymal cells 120
Figure 4.54: Rab23 expression in cell body and motile cilia of ependymal cells 121
Figure 4.55: Rab9 expression in cell body and motile cilia of ependymal cells 122
Figure 5.1: Schematic representation of ventricular-subventricular zone (V-SVZ) from control and *Lrp2*$^{-/-}$ mice (en face view). 142

List of tables

Table 1: List of primers used for PCR genotyping. 26
Table 2: List of the primary antibodies 40
Table 3: Immunohistological conditions for staining protocol 41
Table 4: Mouse in situ hybridization probes 47

1 Introduction

1.1 LRP2, a member of LDLR gene family

The low-density lipoprotein receptor-related protein 2 (LRP2) is one of seven core members of the low-density lipoprotein receptor (LDLR) gene family (Joachim Herz, 2001), a group of endocytic receptors found in vertebrate and non-vertebrate species (Figure 1.1). All members of this gene family are type 1 transmembrane proteins consisting of an amino terminal extracellular domain (ECD), a single transmembrane segment, and a short carboxyl terminal cytoplasmic tail (Joachim Herz, 2001). In their ECD, these receptors mainly possess motifs for extracellular binding and subsequent intracellular release of ligands (M. S. Brown, Herz, & Goldstein, 1997). The diversity of ligands bound by various family members is tremendous and defined by the specificity of recognition motifs formed by clusters of complement-type repeats (CR) in the ECD. The spatial conformation of individual CR is defined by four internal disulfide bridges that form a Ca^{2+} binding element (Bieri, Djordjevic, Daly, Smith, & Kroon, 1995; Fass, Blacklow, Kim, & Berger, 1997). Another structural feature of the ECD are epidermal growth factor precursor homology domains formed by epidermal growth factor-type repeats and ß-propellers. These domains are responsible for pH-dependent release of ligands internalized by these receptors into endosomes (Rudenko et al., 2002). The cytoplasmic tail domains of the different receptor species vary greatly. They contain motifs that direct internalization of the receptors from the cell surface by binding to components of the clathrin lattice present in plasma membrane invaginations called clathrin-coated pits (Bansal & Gierasch, 1991; W. J. Chen, Goldstein, & Brown, 1990). In addition, the tail domains entail recognition sites for a multitude of adaptor proteins that link these receptors to intracellular sorting and transduction machineries (Gotthardt et al., 2000). The structural organization described above characterizes the core members of LDLR gene family, called LDLR (Yamamoto et al., 1984), LRP1 (J. Herz et al., 1988), LRP1B (C. X. Liu et al., 2000), LRP2 (Saito, Pietromonaco, Loo, & Farquhar, 1994), the very low-density lipoprotein receptor (VLDLR) (Takahashi, Kawarabayasi, Nakai, Sakai,

& Yamamoto, 1992), the apolipoprotein E receptor-2 (APOER2) (Schmechel et al., 1993), and LRP4 (Nakayama et al., 1998) (Figure 1.1).

In addition to the core members, three additional receptors are included in the LDLR gene family, namely LRP5 (Dong et al., 1998; Hey et al., 1998) and LRP6 (S. D. Brown et al., 1998) as well as the sorting protein related receptor containing LDLR class A repeats (SORLA) (Jacobsen et al., 1996; Mörwald et al., 1997) (Figure 1.1). They are classified as distant family members because of their slightly different structural organization. LRP5 and LRP6 have an inverted organization of CR clusters and EGF precursor homology domains (S. D. Brown et al., 1998; Dong et al., 1998; Hey et al., 1998). SORLA has an additional so-called vacuolar protein sorting 10 protein (VPS10P) domain not seen in the other receptors (Jacobsen et al., 1996).

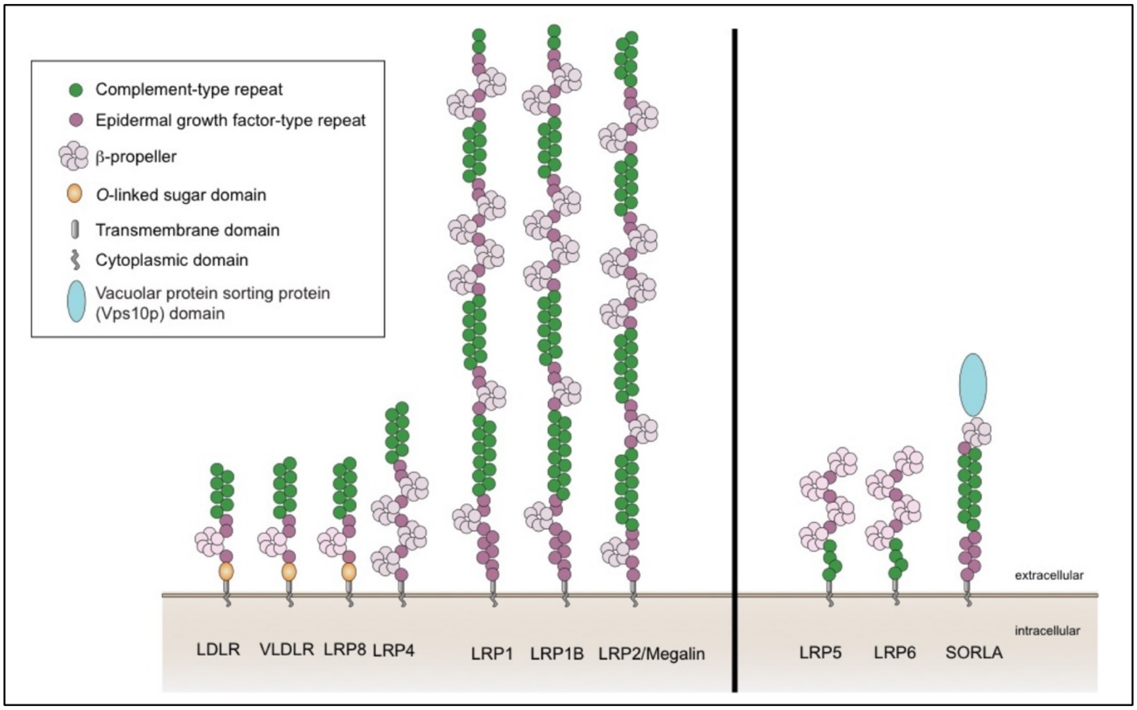

Figure 1.1: Members of the low-density lipoprotein receptor (LDLR) gene family in vertebrates (modified from (Carlo et al., 2013)).

To the left of the figure, the core members of the gene family, the LDLR, the very low-density lipoprotein receptor (VLDLR), as well as the LDLR-related protein (LRP) 8, LRP4, LRP1, LRP1B, and LRP2 are shown. To the right side of the figure, the structurally more distant related members like LRP5, LRP6, and sorting-related receptor with A-type repeats (SORLA) are displayed.

1.1.1 LDL receptor-related protein 2 (LRP2)

LRP2 was initially identified as an autoantigen in Heymann nephritis, an experimental rat model for active and passive immune-induced glomerular nephritis. (Kerjaschki & Farquhar, 1982).

Subsequent cloning efforts revealed the primary polypeptide sequence of a huge 600 kDa protein termed megalin or LRP2. The corresponding gene is located on human chromosome 2, 2q31.1 (Hjälm et al., 1996; Saito et al., 1994; Xia et al., 1993a) and on mouse chromosome 2, 2 C2|2 40.74 cM (Xia et al., 1993b). Based on more detailed analyses, LRP2 was characterized as a type-1 transmembrane glycoprotein containing 4660 amino acids. Its ECD is composed of four repetitive arrangements that include a total of 16 EGF-type repeats, 8 ß-propellers, and 36 CR (Saito et al., 1994) (Figure 1.1). The intracellular domain of LRP2 contains two classical NPxY motifs and one NPxY-like element, all of which determine sorting of this receptor to and from the apical cell surface (Gotthardt et al., 2000; Takeda, Yamazaki, & Farquhar, 2003). Yeast two hybrid screen as well as targeted analyses identified several proteins interacting with the intracellular domain of LRP2. One well characterized binding protein is Disabled2 (Dab2), which binds to the NPxY motifs in LRP2. Absence of Dab2 binding disrupts the ability of LRP2 to perform endocytosis and phenocopies defects seen in cells lacking the receptor (Oleinikov, Zhao, & Makker, 2000, p. 2; Tao, Moore, Smith, & Xu, 2016).

In mammals, expression of LRP2 is restricted to specialized absorptive epithelia in the embryonic and adult organism. In the adult, LRP2 is mainly found in the proximal tubules of the kidney, the endometrium of the uterus, in pneumocytes and Clara cells in the lung, in principal cells of the epididymis, as well as in ependyma and choroid plexus of the brain (Hermo, Lustig, Lefrancois, Argraves, & Morales, 1999; Kounnas, Haudenschild, Strickland, &

Argraves, 1994; G. Zheng et al., 1994). Although the function of LRP2 in various epithelial tissues of the adult organism is incompletely understood, it is generally perceived as a high capacity clearance receptor that scavenge a multitude of ligands from the extracellular space. Mainly, this concept is derived from studies on the role of this receptor in the kidney and reproductive organs. In the kidney, LRP2 is expressed on the apical cell surface of epithelial cells of the renal proximal tubule, a segment of the nephron specialized in reabsorption of metabolites filtered through the glomeruli, such as glucose, amino acids, and phosphate. LRP2 contributes to proximal tubular resorption processes by internalizing low-molecular weight plasma proteins from the glomerular filtrate. Absence of receptor activity in mouse models with obligate (Nykjaer et al., 1999) or kidney-specific (J. R. Leheste et al., 1999) *Lrp2* gene defects results in failure to reabsorb filtered plasma proteins, such as carriers for vitamin D (J. R. Leheste et al., 1999), vitamin A (W. Liu et al., 1998) , and vitamin B12 (Moestrup et al., 1996) and their bound ligands. This condition is called low-molecular weight proteinuria and is also seen in patients with inheritable *LRP2* deficiency (Kantarci et al., 2007). A similar function in resorption of plasma carrier proteins and their bound cargo was documented in reproductive organs of mice, where LRP2 mediates uptake of androgens and estrogens bound to the sex hormone binding protein (Hammes et al., 2005). In mice lacking LRP2, absence of this clearance pathway for sex steroids results in phenotypes reminiscent of deficiency for estrogen and androgens. These pathologies encompass defects in maturation of the reproductive organs during puberty such as maldescent of the testes into the scrotum in males (cryptorchidism) as well as the impaired opening of the vaginal cavity in females (Hammes et al., 2005).

1.1.2 Role of LRP2 in formation of the embryonic forebrain

Apart from its function as clearance receptor in absorptive epithelia of adult organism, LRP2 also plays an essential role during embryonic development, specifically in the formation of forebrain and facial structures. This notion was recognized early on by the severe forebrain malformations observed in mice with targeted *Lrp2* gene disruption, a phenotype known as holoprosencephaly (HPE) (Kruszka & Muenke, 2018). Characteristic features of HPE in animal models and in patients are distinct malformations of the face and forebrain structures, including an open fontanelle, craniofacial dysmorphology and, in severe cases, a centrally placed single eye (cyclopia). Underlying cause of these defects is the lack of separation of the brain into two hemispheres and the resultant fusion of the forebrain (prosencephalon) into a single structure, the holoprosencephalon.

HPE is the most common forebrain anomaly in humans affecting 1 in 250 pregnancies (Kruszka & Muenke, 2018). It can be caused by numerous genetic as well as environmental impacts (e.g., fetal alcohol syndrome). Studies in genetically engineered mouse models of HPE documented impairment in several morphogen pathways involved in formation of the dorso-ventral axis of the neural tube as the molecular cause of this malformation. Specifically, an increase in BMP and WNT signaling activities in dorsal neural tube were shown to cause HPE (Golden et al., 1999; Shimogori, Banuchi, Ng, Strauss, & Grove, 2004). Similarly, disturbances in ventral neural tube patterning were also identified as reason for HPE. In this respect, signaling by the morphogen sonic hedgehog (SHH) emerged as crucial for ventral cell fate specification in neural tube, and as cause of HPE (Inoue, Nakamura, & Osumi, 2000; Rubenstein & Beachy, 1998; Sur & Rubenstein, 2005). Consequently, loss of SHH activity in the ventral neural tube due to *SHH* gene disruption leads to HPE in humans and mice (Chiang et al., 1996; Roessler et al., 1996).

Findings implicating LRP2 in neural tube specification and forebrain formation stemmed from early work documenting HPE-like phenotypes in mice with targeted *Lrp2* gene disruption (T. E. Willnow et al., 1996). Further investigations documented a severe decrease in the thickness of the neuroepithelium in the rostral forebrain of mutant mice, a defect accompanied by decreased SHH signaling activity in the ventral and increased BMP4 activity in the dorsal neural tube (Spoelgen et al., 2005). *In vitro* studies demonstrated the ability of LRP2 to bind SHH (McCarthy, Barth, Chintalapudi, Knaak, & Argraves, 2002) and BMP4 (Spoelgen et al., 2005), arguing for a role of this protein as a morphogen receptor during embryonic development (Thomas E. Willnow, Christ, & Hammes, 2012). A primary role for LRP2 in SHH signaling was substantiated by further investigations by Annabel Christ and Annette Hammes in the Willnow lab who identified LRP2 as central player in establishment of the SHH signaling domain in the rostral diencephalon ventral midline (RDVM), the major forebrain organizer region. During neurulation, the RDVM receives inductive signals by SHH secreted from the prechordal plate (PrCP), a rostral extension of the notochord. From the PrCP, SHH moves by unknown mechanisms to the overlaying RDVM to induce midline formation and ventral fate identity of the developing forebrain. According to current hypotheses, LRP2 plays an essential role in this process by forming a complex with the SHH receptor Patched 1 (PTCH1) on the surface of the neuroepithelial cells in the RDVM. Formation of this co-receptor complex increases the sensitivity of the ventral neuroepithelium for the limited amounts of SHH reaching the RDVM (Christ et al., 2012; Christ, Herzog, & Willnow, 2016). Experiments in cell lines and neural tube explants suggested that LRP2 facilitates surface binding and internalization of SHH/PTCH1 complexes, a prerequisite for pathway activation (Christ et al., 2012). In addition, LRP2 may also facilitate recycling and re-secretion of SHH, a mechanism to increase local morphogen concentrations in the RDVM (Christ et al., 2012).

1.1.3 LRP2 acts as a clearance receptor during eye development

In addition to its function in SHH signaling the developing forebrain, LRP2 adopts a similar role as SHH receptor in the developing mammalian eye (Christ et al., 2015). In the eye, SHH is produced by retinal ganglion cells, forming a morphogen gradient in central to peripheral direction that provides mitogenic signals to retinal progenitors (Y. P. Wang et al., 2002). However, SHH activity is absent from the distal margin of the developing retina, the ciliary marginal zone (CMZ), where progenitor cells remain quiescent (S.-H. Cho & Cepko, 2006; S. Zhao, Chen, Hung, & Overbeek, 2002). This phenomenon restricts growth of the mammalian eye, whereas in amphibians and fish progenitor cells in the retinal margin proliferate, resulting in continuous eye growth throughout adult life (Lamba, Karl, & Reh, 2008). Recently, the role of LRP2 as a clearance receptor for SHH in the murine CMZ was discovered by the Willnow lab. In detail, LRP2 mediates the uptake and lysosomal catabolism of SHH in the CMZ, preventing its activity spread from the central retina into the retinal margin. This clearance mechanism eliminates mitogenic stimuli for progenitors in the CMZ, keeping this niche in a quiescent state. In LRP2-deficient mice, the concentration of the morphogen in the CMZ increases, resulting in the expansion of the retinal progenitor cell pool and in hyperproliferation in the tip of the retina. This hyperproliferative phenotype of retinal margin was also seen with insufficiency of inhibitors of SHH signaling as with heterozygosity of *Ptch1* mutations or absence of SUFU (Y. P. Wang et al., 2002).

1.1.4 Donnai-Barrow/ Facio-oculo-acoustico-renal (FOAR)-syndrome

The consequences of *Lrp2* mutations described initially in mouse models are recapitulated by phenotypes documented in patients with Donnai-Barrow (DBS) /Facio-oculo-acoustico-renal (FOAR)-syndrome, an autosomal-recessive disorder (DBS/FOAR, OMIM: 222448) caused by inheritable mutations on human *LRP2*. Thus, patients with DBS have low-molecular weight proteinuria as well as facial and forebrain abnormalities, including agenesis of the corpus callosum and an enlarged anterior fontanelle. They also suffer from visual and hearing impairment, frequently from diaphragmatic hernia and mental retardation (Avunduk, Aslan, Kapicioğlu, & Elmas, 2000; Chassaing et al., 2003; Donnai & Barrow, 1993; Gripp et al., 1997; Khalifa et al., 2015; Pober, Longoni, & Noonan, 2009). *LRP2* mutations identified in DBS/FOAR mainly represent frameshift or nonsense mutations in the ECD of the receptor, resulting in the expression of truncated soluble receptor fragments. No apparent genotype-phenotype correlation is observed in these individuals (Kantarci et al., 2007; Pober et al., 2009).

1.2 Cell biology of SHH signaling

Recent years witnessed the elucidation of the complex cell biology of SHH production and signaling in cells *in vitro* and *in vivo*. Initially, SHH is produced as a precursor protein called full length SHH (SHH-FL). Due to autocatalytic activity of the carboxyl terminal domain of the precursor, SHH-FL is subsequently cleaved into an 19 kDa amino terminal (SHH-N) and a 25 kDa carboxyl terminal fragment (SHH-C) (Bumcrot, Takada, & McMahon, 1995; Lee et al., 1994; Porter et al., 1995). SHH-N becomes post-translationally modified by attachment of a cholesterol moiety at its carboxyl terminal end and a palmitoyl moiety at its amino terminus. In this dual lipid modified form, SHH-Np constitutes the fully active form of the morphogen released by cells (Chamoun et al., 2001; Pepinsky et al., 1998) .

Transport and secretion of SHH-Np is a complex multistep process. According to current hypotheses, SHH-Np is released from cells by three possible mechanisms; (i) by forming high molecular weight aggregates, (ii) in a complex with lipoprotein particles, or (iii) by attaching to exovesicular carriers (Choudhry et al., 2014). In detail, in the supernatant of cultured cell lines, SHH is mainly found as multimers formed by interaction of SHH monomers through their lipid moieties. The twelve-pass transmembrane receptor Dispatched (Dsp), that interacts with the cholesterol moiety in SHH-Np, facilitates release of such multimers from the plasma membrane for long range signaling (Choudhry et al., 2014). On target cells, specific types of heparan sulfate proteoglycans, such as Dally and Dally-like help to transfer multimeric SHH-Np to PTCH1.

In the fruit fly, hedgehog tends to attach to the surface of lipoprotein particles, i.e., macromolecular structures that serve to transport lipids and lipid-soluble vitamins in the circulatory system. Attachment to lipoproteins enables long-range trafficking of lipid-modified hedgehog molecules and may foster interaction of the morphogen with lipoprotein receptors of the LDLR gene family (Eaton, 2006). A third proposed mode for SHH transport suggests that the morphogen can be attached to extracellular vesicular structures, called nodal vesicular particles (NVPs) and be transported by cilia- generated fluid flow by the node during mouse embryonic development. NVPs consist of lipophilic granules, surrounded by an outer membrane derived from microvillar structures (Eaton, 2006). One final model for SHH-Np transfer between neighboring cells is through formation of cell protrusions. These protrusions may enable direct transfer of plasma-membrane-linked SHH-Np to adjacent cells as shown in tissue cultures (Incardona et al., 2000). The transport via cell protrusions has been confirmed in another study using single-cell real-time imaging in chick embryos. In this study, it has been shown that SHH remains associated with a specialized class of actin-based filopodia. Furthermore, it has been demonstrated that in the responding cell SHH co-receptors are distributed in filopodial extensions and form a stabilized interaction with filopodia containing SHH ligand and therefore establish long range transport (Sanders, Llagostera, & Barna, 2013).

In target cells, SHH signaling starts by binding of SHH-Np to the 12-pass transmembrane receptor PTCH1 present on the cell surface. Central to SHH signal reception is a cellular organelle called the primary cilium (Figure 1.2). Upon SHH binding, PTCH1 localizes from the ciliary shaft to the base of the ciliary axoneme. This leads to the release of the inhibitory action of PTCH1 on Smoothened (SMO), a 7-pass transmembrane receptor that acts as primary mediator of SHH signal transduction into cells. Specifically, release of inhibition by PTCH1 allows SMO entry into the axoneme of primary cilia (Rohatgi, Milenkovic, & Scott, 2007). So far, no clear evidence exists concerning the mechanism of SMO inhibition by PTCH1 as no stoichiometric interaction has been documented between these two proteins (J. Taipale, Cooper, Maiti, & Beachy, 2002). Some hypotheses suggest that this interaction proceeds indirectly through messenger lipid molecules that are transported by PTCH1 and regulate SMO activity (J. K. Chen, Taipale, Young, Maiti, & Beachy, 2002; Jussi Taipale et al., 2000). The discovery of various synthetic (J. K. Chen, Taipale, Young, et al., 2002; Frank-Kamenetsky et al., 2002) and natural compounds, such as the steroidal alkaloid cyclopamine (J. K. Chen, Taipale, Cooper, & Beachy, 2002; Jussi Taipale et al., 2000) which trigger SMO activity independently of SHH, substantiated this hypothesis. In vertebrates, a homologue of PTCH1, called PTCH2 also plays a regulatory role in SHH signaling. It was demonstrated in cell culture that PTCH2 can mediate the SHH response in *Ptch1*$^{-/-}$ cells (Alfaro, Roberts, Kwong, Bijlsma, & Roelink, 2014). In addition, it was shown that PTCH2 similar to PTCH1 acts as SHH antagonist during vertebrate neural tube patterning through feedback inhibition(Holtz et al., 2013).

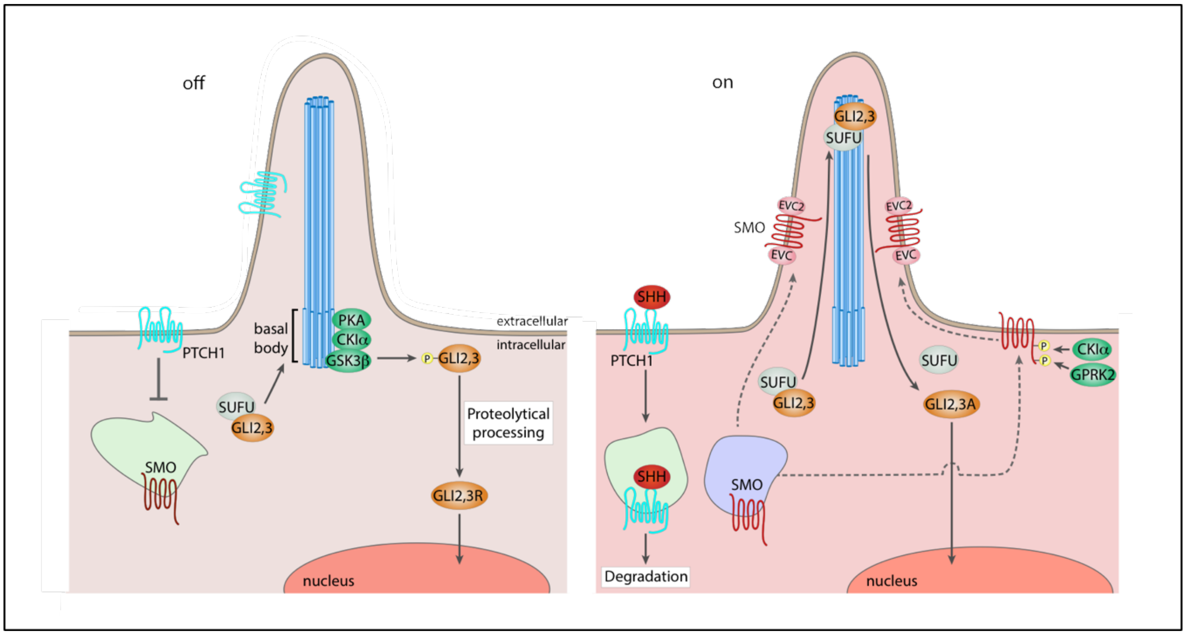

Figure 1.2: Sonic hedgehog signaling cascade in the primary cilium (modified from (Briscoe & Thérond, 2013)).

The scheme on the left side represents the processes at the primary cilium in the absence of the morphogen sonic hedgehog (SHH) (panel off). In this case, patched homolog 1 (PTCH1) is placed in the primary cilium, suppressing smoothened (SMO) activity. Suppression of SMO results in phosphorylation of transcription factors (Glioma-associated oncogene homolog 2) GLI2 and (Glioma-associated oncogene homolog 3) GLI3 by protein kinase A (PKA), glycogen synthase kinase 3 beta (GSK3β) and casein kinase 1a (CK1α) located at the base of the primary cilium. Phosphorylated variants of GLI2 and GLI3 are subjected to proteolytic cleavage to their repressor forms (GLI2R and GLI3R). The scheme on the right side depicts activation and down-stream signaling of the pathway in the presence of SHH (panel on). Upon binding of SHH, PTCH1 exits the primary cilium relieving suppression of SMO. PTCH1/SHH are internalized, where PTCH1 undergoes lysosomal degradation and SHH recycles back to the plasma membrane, recovering morphogen concentrations on the cell surface. Following phosphorylation by G protein-coupled receptor (GPCR) kinase 2 (GPRK2) and CK1α, activated SMO localizes to the cilium in close proximity to the activator proteins, (Ellis-van Creveld syndrome protein) EVC and EVC2. SMO activation enables complex formation of suppressor of fused (SUFU) with GLI2 and GLI3, facilitating entry of the transcription factors into the cilium. In the cilium, they are protected from the proteolytic cleavage and remain in their full-length activator forms that can enter the nucleus to activate SHH target gene transcription.

After SHH binding at the cell surface, PTCH1 is internalized and undergoes lysosomal degradation (Figure 1.2). Relief of inhibition by PTCH1 causes conformational changes in SMO that trigger phosphorylation at multiple sites in the carboxyl terminal domain of the protein by G-protein coupled receptor kinase 2 (GPRK2) (W. Chen et al., 2004). Subsequently, SMO moves into the axoneme of the primary cilium, either by lateral plasma membrane transport or by intracellular vesicle trafficking (Milenkovic, Scott, & Rohatgi, 2009; Yu Wang, Zhou, Walsh, & McMahon, 2009). The translocation is mediated by ß-arrestin and the kinesin-like protein 3A (KIF3A) (W. Chen et al., 2004; Kovacs et al., 2008). The pivotal point in the SHH signal transduction process is SMO binding to Ellis-van Crefeld (EVC/EVC2) proteins at a distinct ciliary location (Dorn, Hughes, & Rohatgi, 2012). This interaction results in activation of GLI transcription factors that transmit SHH signals into the nucleus for induction of targeted gene transcription. In vertebrates, three GLI proteins are found, named GLI1, GLI2, and GLI3. GLI1 is the main activator of SHH signaling and is induced in expression upon SHH pathway activation (Ding et al., 1998; Hynes et al., 1995; B. Wang, Fallon, & Beachy, 2000). By contrast, GLI2 and GLI3 are always expressed but exist in an activator or repressor form, dependent on the presence or absence of SHH (Dai et al., 1999; Sasaki, Nishizaki, Hui, Nakafuku, & Kondoh, 1999). In detail, in the absence of SHH, the suppressor of fused (SUFU) sequesters GLI2 and GLI3 at the base of the cilium and initiates their phosphorylation by protein kinase A (PKA) and glycogen synthase kinase 3β (GSK3β) (Figure 1.2). Phosphorylation results in proteolytic cleavage of the transcription factors into their repressor forms (Dai et al., 1999; Kise, Morinaka, Teglund, & Miki, 2009; Tuson, He, & Anderson, 2011). Following SHH signaling, SMO translocation into the ciliary axoneme triggers the accumulation of SUFU/full-length GLI2/3 complexes in the tip of the primary cilium (Cheung et al., 2009; Endoh-Yamagami et al., 2009). There, SUFU/GLI2/GLI3 complexes dissociate and GLI2 and GLI3 proteins move to the nucleus to induce the expression of target genes (Humke, Dorn, Milenkovic, Scott, & Rohatgi, 2010; Tukachinsky, Lopez, & Salic, 2010) (Figure 1.2). Due to the similarity in DNA binding motifs, GLI activator and GLI repressor proteins compete with each other for access to the GLI binding sites in target genes. Accordingly, the output of the SHH pathway is determined by a fine balance between levels of GLI activator and repressor forms.

1.2.1 The SHH receptorsome

As an essential signaling pathway during embryonic development and in the adult organism, several mechanisms have evolved to control SHH signal reception spatially and temporarily. One well studied mechanism is the control of signal reception through local morphogen gradients as elucidated in molecular detail in explants of the chick neural tube. In response to SHH concentration gradients, subtypes of ventral interneurons and motor neurons are produced along the ventral to dorsal axis of the neural tube (Dessaud, McMahon, & Briscoe, 2008). Conjunctional expression of homeodomain transcription factors in progenitor cells, instruct their differentiation towards distinct cells fates in neural tube. These factors are divided into two classes, based on their response to SHH signaling simulation. Class I transcription factor encompasses PAX7, DBX1, DBX2, IRX3, and PAX6 that repress gene expression upon SHH pathway activation. Expression of class 2 proteins, for instance NKX6-1, NKX2-2, NKX2-9 is induced, when SHH signaling is on. In response to different SHH concentrations, various cross-repressive interactions of class I and class II transcription actors occur, eventually leading to the formation of distinct neuronal subtypes in the neural tube (Jessell, 2000).

However how exactly progenitors transform dynamic changes in SHH levels into special gene expression programs was shown by James Briscoe and coworkers who identified the regulatory logic of Pax6, OLIG2 and Nkx2.2 transcriptional circuits to interpret graded SHH signals. Based on *in silico* modeling, they suggest a model of morphogen interpretation when at earliest time points of ventral neural tube patterning, low SHH signals translate into low levels of intracellular GLI activity. These levels are not sufficient to induce *OLIG2* and *Nkx2.2,* or to repress existing *Pax6* expression. As development progresses and SHH levels increase, a gradient of GLI activity induces *OLIG2* transcription and represses *Pax6* (Balaskas et al., 2012). Still further increasing GLI1 activity levels ultimately induce *Nkx2.2* and repress *Pax5* and *OLIG2*.

A novel concept of control of SHH signal reception evolved in recent years with the identification of several SHH binding proteins. These surface proteins act as auxiliary SHH receptors that cooperate with PTCH1 to positively or negatively regulate SHH signaling in target cells. They are jointly referred to as the SHH receptorsome (Figure 1.3).

The first identified SHH co-receptor was the hedgehog interacting protein (HHIP). It is a glycoprotein tethered in plasma membrane via its hydrophobic carboxyl terminus. Its amino terminal domain consists of frizzled-fold domain, a ß-propeller and two EGF-type repeats (Ohata & Alvarez-Buylla, 2016). The ß-propeller domain binds all three vertebrate hedgehog proteins, including SHH, with high affinity. HHIP is part of a negative regulatory loop of SHH signaling as it is transcriptionally induced upon SHH signal activation and suppresses SHH signal initiation (P. T. Chuang & McMahon, 1999; P.-T. Chuang, Kawcak, & McMahon, 2003). Mice deficient for HHIP show increased hedgehog signaling, resulting in developmental defects in lung and bone (Chuang et al., 2003).

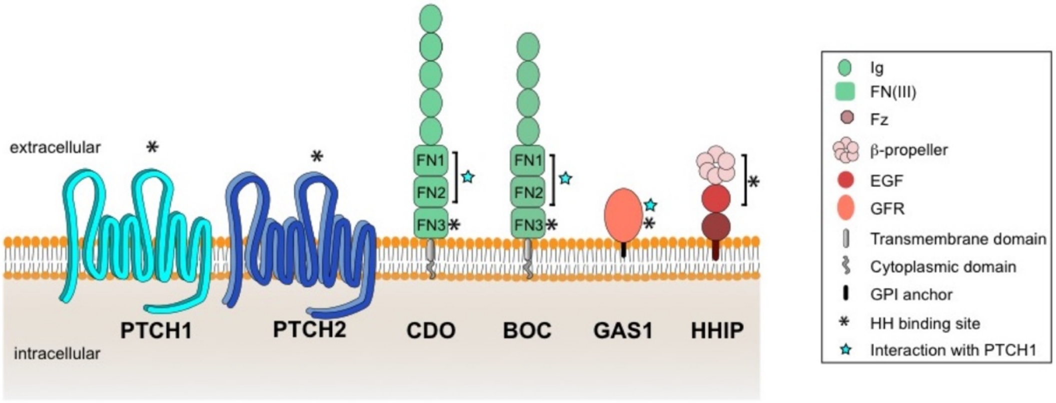

Figure 1.3: Structural organization of SHH binding proteins, SHH receptorsome (modified from (Christ et al., 2016)).

Protein Patched Homolog 1 (PTCH1), Protein Patched Homolog 2 (PTCH2), Cell-adhesion molecule-related, down-regulated by oncogenes (CDO), Brother of CDO (BOC), Growth arrest-specific 1 (GAS1) and hedgehog interacting protein (HHIP) are depicted in schematic illustration.

Asterisks highlight the binding site for SHH in the various proteins. Blue star marks the regions involved in interaction with PTCH1.

As mentioned above, PTCH2 is another regulator of signaling in the SHH receptorsome. It shares almost 56% homology with PTCH1 (Motoyama, Takabatake, Takeshima, & Hui, 1998). Despite its ability to interact with SMO and SHH, PTCH2 has a reduced SHH signaling suppressing ability as compared with PTCH1 (Rahnama, Toftgård, & Zaphiropoulos, 2004). Mice deficient for PTCH2 are viable and show no obvious defects, suggesting that PTCH1 can compensate for the loss of PTCH2 deficiency. However, combined loss of mutations in *Ptch1* and *Ptch2* aggravate phenotypes seen for PTCH1-deficient mice (Holtz et al., 2013; Jeong & McMahon, 2005).

Three other members of the SHH receptorsome have been identified due to their involvement in SHH signaling during forebrain development. These receptors encompass the cell-adhesion molecule-related, down-regulated by oncogenes (CDO), brother of CDO (BOC), and growth arrest-specific 1 (GAS1) (Figure 1.3). CDO and BOC share structural and functional similarities and positively regulate SHH signaling. They are orthologues of interference hedgehog (Ihog) and brother of ihog (Boi) in Drosophila (Tenzen et al., 2006; Yao, Lum, & Beachy, 2006). They are cell surface glycoproteins, belonging to a subgroup of the immunoglobulin (Ig) superfamily of cell adhesion molecules. In their ECD, they carry four or five Ig-like domains and three fibronectin-type III repeat (FNIII) repeats (Fn1-3). CDO and BOC are anchored to the plasma membrane through a single trans-membrane domain, followed by an intracellular domain that differs by length between the receptor species and that may explain their functional distinctions (Kang, Mulieri, Hu, Taliana, & Krauss, 2002; Mulieri, Okada, Sassoon, McConnell, & Krauss, 2000). The third FNIII domain in both receptors binds SHH (Kavran, Ward, Oladosu, Mulepati, & Leahy, 2010; McLellan et al., 2008). GAS1 is tethered to the plasma membrane through a glycosyl-phosphatidylinositol (GPI) anchor. GAS1 shares structural similarity with glial cell-derived neurotrophic factor receptors α (GFRα) (Cabrera et al., 2006; Stebel et al., 2000) and binds SHH in its extracellular domain.

The physiological relevance of CDO, BOC, and GAS1 for SHH signaling during forebrain development is documented by loss of function phenotypes seen in patients and mouse models lacking these receptors. Thus, inheritable *GAS1* mutations in humans, that decrease its affinity for SHH, result in phenotypic features reminiscent of HPE (Pineda-Alvarez et al., 2012). Also missense mutations in *Cdon,* that disrupt interaction of human CDO with other members of receptorsome, cause HPE (Bae et al., 2011). In mouse models, deficiency for GAS1 (Allen, Tenzen, & McMahon, 2007; Seppala et al., 2007) or CDO also causes HPE-related defects (Cole & Krauss, 2003; W. Zhang, Kang, Cole, Yi, & Krauss, 2006). As for BOC, loss-of-function mutations do not show apparent forebrain development defects. However, murine *Boc* mutations exacerbate forebrain malformations when introduced into the *Cdon* or *Gas1* mutant mouse lines (Allen et al., 2007; W. Zhang, Hong, Bae, Kang, & Krauss, 2011). Mice harboring loss-of-function mutations in all three receptor genes simultaneously die at earlier stages of embryogenesis (E9.5). They do so as a consequence of total ablation of SHH signaling transduction as they exhibit defects in heart development and neural tube patterning also seen in *Smo*$^{-/-}$ or *Shh*$^{-/-}$ embryos (Allen et al., 2011; X. M. Zhang, Ramalho-Santos, & McMahon, 2001).

1.2.2 LRP2 as a novel member of the SHH receptorsome

Recent research in the Willnow lab established LRP2 as yet another member of the SHH receptorsome (Christ et al., 2012). This conclusion was based on the ability of the receptor to interact with SHH and PTCH1, and on the alterations in SHH signaling observed in mice lacking this receptor (as described above).

While the importance of LRP2 for SHH signaling has unambiguously been documented in mouse models, the molecular mechanism how this receptor controls SHH signal transduction remains a matter of investigations. By now, three different modes of receptor action have been proposed. In the RDVM, LRP2 promotes SHH signaling in neuroepithelial cells by acting as a co-receptor to PTCH1. Receptor interaction promotes binding of SHH and triggers internalization of PTCH1/SHH complexes, a prerequisite for relieving inhibition of SMO. In addition, LRP2 may promote recycling of SHH in this cell type to increase the limiting concentration of the morphogen in the ventral neural tube (Christ et al., 2012). Studies in whole embryo cultures (WECs) have shed some light on endocytic compartments involved in sorting of SHH with PTCH1 or with LRP2. Thus, all three proteins initially localize to early endosomes, marked by Rab4, representing the first step in receptor/ligand internalization from the cell surface. In addition, immunoreactivity for PTCH1 is seen in lysosomes characterized by the presence of the lysosomal marker protein Lysosomal-associated membrane protein 1 (LAMP1). This observation argues for lysosomal catabolism of the SMO inhibitor subsequent to SHH binding. By contrast, LRP2 and SHH immunostainings are absent from lysosomes but accumulate in Rab11-positive recycling endosomes, suggesting recycling and re-secretion of the morphogen from the apical cell surface (Christ et al., 2012).

In the CMZ of the retina, LRP2 antagonizes SHH signaling by acting as a clearance receptor for the morphogen, depleting the ligand required to engage PTCH1 (Christ et al., 2015). To do so, LRP2 is ideally situated on the apical surface of epithelial cells in the CMZ. In this cell type, binding of SHH to LRP2 results in delivery of the morphogen to lysosomes, whereas the unliganded receptor returns to the cell surface via the recycling endosomal route (Christ et al., 2015). A third mechanism of LRP2 action in SHH signaling involves transcytosis of the morphogen as shown in the optic nerve (ON) (Ortega et al., 2012). In this tissue, LRP2 is expressed in oligodendrocytes where it mediates uptake of the morphogen from the apical and re-secretion via the basolateral cell surface. LRP2-mediated transcytosis of SHH creates a morphogen gradient in the developing ON that directs migration and proliferation of oligodendrocyte progenitor cells.

In conclusion, depending on the cellular context, LRP2 may act as an agonist, an antagonist or transcytosis factor, modulating the trafficking and activity of this morphogen. However, the molecular mechanisms governing the switch in activity in SHH signaling, SHH clearance, or SHH transcytosis are still unclear.

1.3 LRP2 expression in the adult brain

As well as during embryonic development, LRP2 expression also persists in the central nervous system of the adult organism (G. Zheng et al., 1994). Specifically, immunohistological analyses by Chandresh Gajera from the Willnow lab (Gajera et al., 2010) documented the presence of the receptor in the ependyma, a layer of polarized epithelial cells that covers the entire luminal surface of the brain ventricles. The ependymal layer forms a barrier between brain parenchyma and ventricular cavity and it participates in propulsion of the cerebrospinal fluid (CSF) through the ventricular system (Cathcart & Worthington, 1964; Worthington & Cathcart, 1963). To do so, ependymal cells exhibit a specialized apicobasal polarity characterized by a bundle of around 40 motile cilia placed on their apical cell surface facing the ventricular lumen. These motile cilia beat in a coordinated manner, both within individual bundles and across all bundles of the tissue. This coordinated beating directs proper circulation of the CSF in the ventricular system in a rostral to caudal direction (Lehtinen et al., 2011).

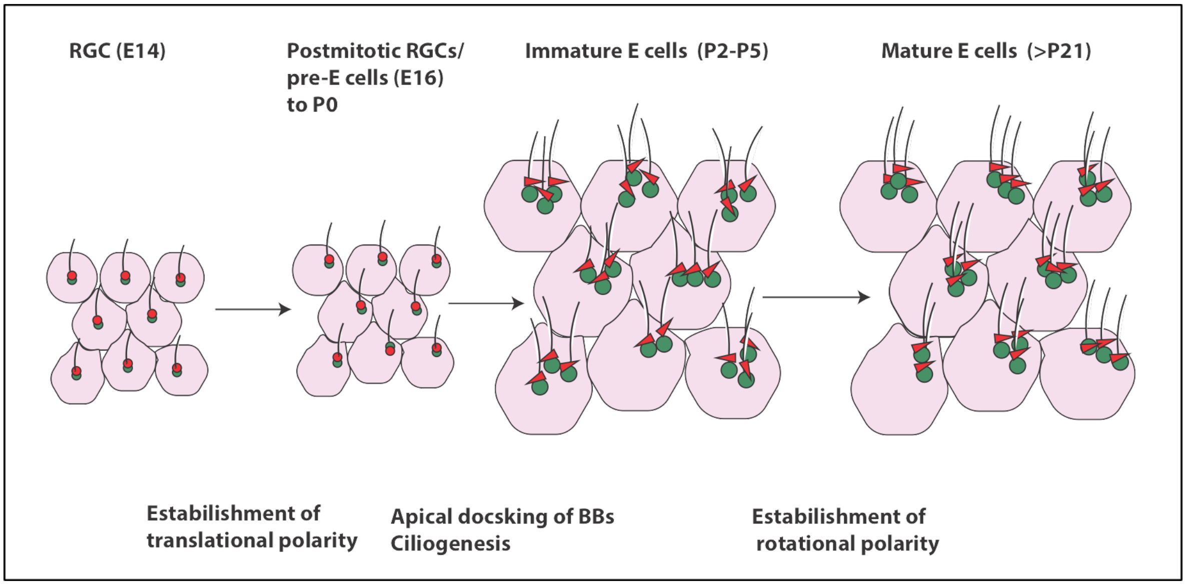

Figure 1.4: Maturation steps of ependymal cells (modified from (Ohata & Alvarez-Buylla, 2016)).

Ependymal cells are derived from radial glial cells (RGCs) around embryonic day (E) 14 of mouse development. RGCs contain primary cilia that are localized at the center of the apical cell surface. From E16 onwards, the flow of the cerebrospinal fluid (CSF) displaces the cilia from the center of the cell, resulting in acquisition of translational cell polarity. Between postnatal day (P) 2 and 5, active ciliogenesis takes place, resulting in formation of motile cilia bundles on the immature E cells. At this time of development, the CSF flow is too weak to define the direction of motile cilia beating. Thus, motile cilia show a random, non-coordinated beating orientation (visualized by randomly oriented red arrowheads in the figure). Upon maturation of the ventricular system and an increase in CSF force in the first 3 weeks of postnatal life, motile cilia on mature E cells adopt a synchronized direction of beating determined by the direction of CSF flow. The E cells have acquired so-called rotational polarity.

Ependymal cells originate from a specific subset of radial glial cells (RGCs) that complete their proliferative phase between embryonic day (E) 14 and 16 in the mouse (Spassky et al., 2005a; H. Zhao et al., 2019) (Figure 1.4). At postnatal day 1, mainly radial glial cells but no ependymal cells are seen in the ventricles. However, until P7, ependymal cells gradually appear in the ventricular epithelium as the number of radial glial cells decrease. By P15-30, formation of the ependymal cell layer has been completed and radial glial cells are completely absent from this tissue (Tramontin, García-Verdugo, Lim, & Alvarez-Buylla, 2003). In the murine brain, the differentiation process whereby multiciliated ependymal cells form from radial glial cells containing a single primary cilium encompasses not only growth of the ciliary axoneme but also acquisition of polarity. This step is followed by ciliary bundle displacement, so-called translational polarity, and finally by ciliary beating coordination, so-called rotational polarity (Figure 1.4) (Boutin et al., 2014). The significance of LRP2 for development and functional integrity of the ependyma is unclear as yet.

1.3.1 Architecture of the neurogenic niche in ventricular- subventricular zone

Initial studies reported the self-renewal capacity of ependymal cells (Bruni, 1998; Johansson et al., 1999). However, no experimental support for this hypothesis was obtained in later studies (Spassky et al., 2005a), in line with findings that multiciliated epithelial cells bearing numerous basal bodies are postmitotic (Lange, Faragher, March, & Gull, 2000) and that the ependymal layer in the mammalian brain does not regenerate after injury (Sarnat, 1992). Still, the ependyma bears considerable significance for proliferative processes in the adult brain, specifically in the generation of new neurons in a process called adult neurogenesis.

Initially, the concept of adult neurogenesis in the mammalian brain was met with considerable skepticism. According to established dogmas, cells in the brain proliferate during development but cease to do so before puberty. Today, we know that two main regions of continuing neurogenesis exist in the adult mammalian brain, namely the subventricular zone (SVZ) of the lateral ventricles and the subgranular zone (SGZ) of the dentate gyrus in the hippocampus. The SVZ resides below the ependymal cell layer in close proximity to lateral ventricular lumen.

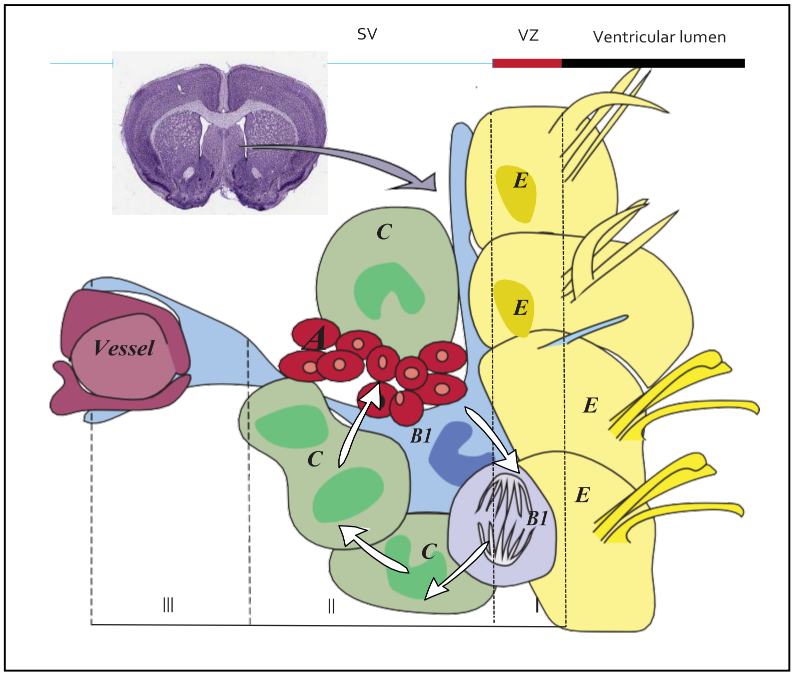

Figure 1.5: Composition of ventricular and subventricular zones in the wall of the lateral ventricles (modified from (Daniel A. Lim & Alvarez-Buylla, 2016)).

The neurogenic unit of the subventricular zone (SVZ) is composed of neural stem cells (B1 cells, in blue), activated B1 cells (in purple), fast dividing progenitors (C cells, in green) as well as neuroblasts (A cells, in red). White arrows indicate the direction of neurogenic differentiation from B cells to C cells to A cells. Ependymal cells (E cells, in yellow) are multi-ciliated postmitotic epithelial cells that form the ventricular zone (VZ). The VZ separates the neurogenic niche of the SVZ from the lumen of the ventricle. Anatomically, the V-SVZ is divided in three domains. The apically located domain I contains E cells and the apical processes of B1 cells that carry the primary cilium and protrude through the ependymal cell layer. The intermediate domain II consists of the cells bodies of B cells and most other cells of the neurogenic unit. Basally located domain III contains the basal processes of B1 cells that interact with blood vessels. The extent of the SVZ, the VZ and the ventricular lumen are highlighted by colored lines above the schematic. For comparison, a histological hematoxylin and eosin stained coronal section of the adult mouse brain depicting the lateral ventricular system is shown in the upper left corner.

It contains neural precursor cells, that constantly divide and differentiate into newborn neurons. Jointly with the ventricular zone formed by the ependyma, this niche of the brain is referred to as the ventricular- subventricular zone (V-SVZ). Four main cell types are found in the V-SVZ, the ependymal cells (E cells), the neural stem cells (B1 cells), fast dividing progenitors (C cells), and neuroblasts (A cells) (Doetsch, García-Verdugo, & Alvarez-Buylla, 1997).

As illustrated in Figure 1.5, the V-SVZ is organized into three anatomical domains, based on spatial localization of the B1 cells. In domain 1 (apical), ependymal cells and apical processes of B1 cells are found. The intermediate domain 2 consists of the cell bodies of B1 cells that are in close proximity with A and C cells. Finally, domain 3 contains basal processes of B1 cells, which interact with blood vessels (Daniel A. Lim & Alvarez-Buylla, 2016).

Type B1 cells can be in a quiescent or an activated state in the niche. Glial fibrillary acidic protein (GFAP), glutamate aspartate transporter (GLAST), and brain lipid-binding protein (BLBP) are markers commonly used to characterize B1 cells. Nestin was shown to be expressed mainly in activated B1 cells (Doetsch, Caillé, Lim, García-Verdugo, & Alvarez-Buylla, 1999; Doetsch et al., 1997; García-Verdugo, Doetsch, Wichterle, Lim, & Alvarez-Buylla, 1998). Time lapse imaging showed that activated B1 cells undergo asymmetric division, constantly renewing the B1 cell population and also giving rise to C cells (Codega et al., 2014; Mich et al., 2014). Markers for C cells are the transcription factors achaete-scute family BHLH transcription factor 1 (Ascl1) and distal-less homeobox 2 (Dlx2) (Doetsch et al., 1997). C cells are able to divide three more times symmetrically to expand their own population before differentiating to A cells (Ponti, Obernier, & Alvarez-Buylla, 2013). Type A cells usually undergo one to two more symmetric divisions in SVZ and on their migratory path to the olfactory bulb (OB) (Ponti et al., 2013). This coordinated migratory path from the SVZ to the OB is called the rostral migratory stream (RMS) (Lois & Alvarez-Buylla, 1994; Lois, García-Verdugo, & Alvarez-Buylla, 1996; Ponti et al., 2013; Wichterle, Garcia-Verdugo, & Alvarez-Buylla, 1997). Once A cells have reached the OB, these differentiated neuroblasts undergo radial migration to integrate into the interneuron layers of the OB. Various morphogen pathways control adult neurogenesis in the SVZ, including signaling by SHH. SHH determines fate acquisition by neural stem cells in the niche and the proper distribution of newborn neurons in OB cell layers (Ihrie et al., 2011).

1.4 Role of LRP2 in adult neurogenesis in the SVZ

Although ependymal cells do not actively participate in the formation of newborn neurons, they are essential to sustain ongoing adult neurogenesis by providing the proper milieu in the V-SVZ for B cells to proliferate and to differentiate. In this respect, several mechanisms have been proposed whereby ependymal cells may support adult neurogenesis in the SVZ. Ependymal cells produce the BMP inhibitor noggin which provides an inductive signal for neurogenesis and inhibits gliogenesis (Chmielnicki, Benraiss, Economides, & Goldman, 2004; D. A. Lim et al., 2000). Ependymal cells also expresses a pigment epithelium-derived factor, which initiates self-renewal of neural stem cells (Ramírez-Castillejo et al., 2006).

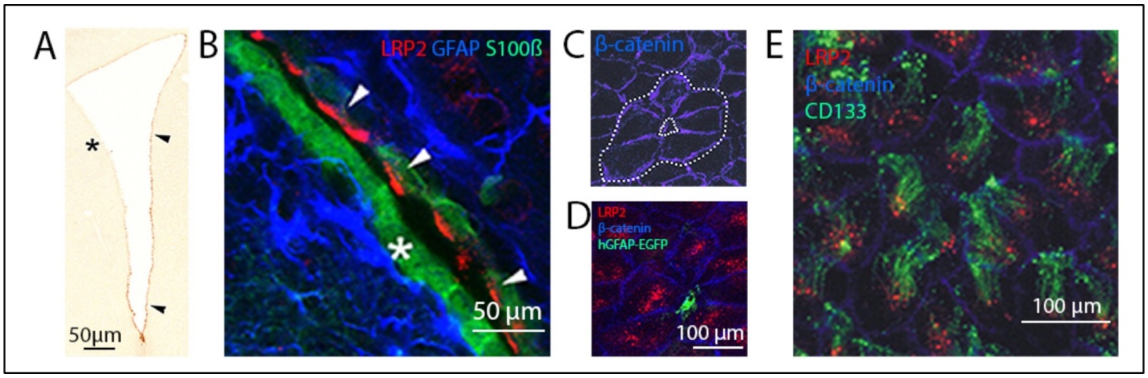

Figure 1.6 LRP2 is expressed at the apical cell surface and at the base of motile cilia of ependymal cells (modified from (Gajera et al., 2010)).

(A) Immunohistological detection of LRP2 on the apical surface of the ventricular zone of the lateral ventricles of the adult mouse brain. LRP2 expression predominantly is seen on the lateral and ventral medial side of the ventricular epithelium facing the neurogenic niche (arrowheads). Little receptor expression is seen at the medial side of the lateral ventricles (indicated by an asterisk). (**B**) Higher magnification images of immunostainings of LRP2 (red) on the apical cell surface of ependymal cells in the lateral (white arrowheads) but not the medial wall (white asterisk) of the VZ. Ependymal cells and B cells are marked by immunodetection of S100β (green) or glial fibrillary acidic protein (GFAP; blue), respectively. **(C)** En face view of the lateral ventricular wall in whole mount preparations of the adult mouse brain. Staining for β-catenin (blue) marks the surface of the ependymal cells that adopt a pinwheel arrangement around a centrally located B cell. For clarity, one pinwheel is highlighted by white dotted lines. **(D)** Immunodetection of EGFP reporter, expressed under control of the human glial fibrillary acidic protein promoter (hGFAP-EGFP; green), LRP2 (red), and β-catenin (blue) revealed LRP2 expression on the apical surface of ependymal cells. No *Lrp2* expression is seen on the apical extensions of hGFAP-EGFP+ B cells. **(E)** Speckled localization pattern of LRP2 (red) is visualized on the base of motile cilia (labeled for CD 133 in green), both located on the apical surface of ependymal cells (stained for β-catenin in blue).

LRP2 expression in the ependyma is restricted to ependymal cells located in the lateral and the most ventral part of the medial ventricular wall (Figure 1.6 A). By contrast, no receptor expression is seen in the remainder of the medial ventricular wall. Intriguingly, this expression pattern mirrors the localization of the active neurogenic niche in SVZ underlying the lateral but not the medial walls of the ventricular zone. Further detailed investigations on enface preparations of the lateral ventricular walls visualized LRP2 on the apical surface of the ependymal cells. In this enface view, ependymal cells are seen in their natural configuration in a pinwheel-like arrangement around the apical cell protrusions of B cells that extend to the ventricular lumen (Figure 1.6 B). On the apical cell surface, LRP2 localizes mainly to the base of the motile cilia but only sparsely to the ciliary axoneme (Figure 1.6 B).

An important contribution of LRP2 activity to adult neurogenesis was shown earlier by testing the number of proliferating C cells generated in receptor mutant mice (Gajera et al., 2010). Using BrdU incorporation to mark proliferating cells in the SVZ, the number of BrdU-positive cells (C cells) was markedly decreased in LRP2-deficient animals as compared with littermate controls. This proliferative defect was seen exclusively in adults but not in newborn mice, suggesting a specific role for LRP2 in adult neurogenesis. This assumption was further corroborated by documenting a significantly reduced number of B1 cells in the SVZ in brains lacking LRP2. Based on the unique localization of LRP2 on the ependyma facing the SVZ and on the impaired neurogenesis in this niche, an important role for this receptor in adult neurogenesis was proposed (Gajera et al., 2010). Yet, the cellular function of LRP2 in ependymal cells and how this activity contributes to adult neurogenesis remained unclear. Answering this question was the main goal of my thesis project.

2 Aim of my work

LRP2 is an endocytic receptor for a broad array of functionally diverse ligands including morphogens. The receptor is best known for its role in uptake and signaling of SHH, required to control neurogenesis in the developing forebrain. Expression of the receptor persists in ependymal cells of the adult brain, a cell type that neighbors the neurogenic niche in the SVZ of the adult mammalian brain. Yet, the relevance of this receptor for adult neurogenesis in mammals remains poorly explored.

My studies aimed at substantiating a proposed role for ependymal LRP2 in control of adult neurogenesis and at elucidating the underlying molecular mechanism of receptor function in this niche.

Towards these overall aims, I explored the architecture and neurogenic potential of the SVZ in control mice and in animals genetically deficient for this receptor using quantitative immunohistology and *in vivo* proliferation assays. These studies were complemented by investigations of ependymal cell functions, including endocytosis, morphogen signaling, and motile cilia activity in brain tissue explants, as well as in primary ependymal cell lines derived from wild-type and receptor-deficient mice.

3 Material and methods

3.1 Animals

3.1.1 Transgenic mice strains

All animal experimentation was carried out according to MDC guidelines following approval by local authorities (X9017/17, G 0256/13, G002/14). Adult mice were group housed with food and water available ad libitum under a fixed 12-hrs light/dark cycle. Adult (10-12- week old) and newborn (0-2 days old) mice were used in the experiments as stated.

Animals compound heterozygous for two different *Lrp2* null alleles were used as LRP2-deficient mouse model (*Lrp2*$^{-/-}$). One allele (*Lrp2*$^{+/-}$) was generated by targeted gene disruption as described by Willnow et al, 1996. This line was crossed with the *Tcf/Lef_LacZ* reporter strain (Mohamed, Clarke, & Dufort, 2004). The second mutant allele (*Lrp2*$^{267/+}$) was derived in an ENU mutagenesis screen for novel gene mutations causing forebrain malformations. In line 267, replacement of the nucleotide T by A created a stop codon at amino acid position 2721 of the LRP2 polypeptide, eliminating receptor expression (Zarbalis et al., 2004). LRP2-deficient mice (*Lrp2*$^{-/-}$) used in this study were derived from F1 crosses of (*Tcf/Lef_LacZ; Lrp2*$^{+/-}$) and *Lrp2*$^{267/+}$ animals. Mice having only one of the targeted *Lrp2* alleles (heterozygous) were phenotypically identical to wild-type animals (*Lrp2*$^{+/+}$). Therefore, both genotypes were combined and referred to as control (Ctr) animals in this thesis. To explore WNT signaling in *Lrp2* mutant and control mice, the activity of the *lacZ* transgene under control of the *Tcf/Lef* promotor was scored. To test SHH signaling, the *Gli1_LacZ* transgene (JAX; Stock 008211) was introduced in the mice carrying the *Lrp2* mutant alleles.

3.1.2 BrdU injections

5-bromo-2'-deoxyuridine (BrdU) is a synthetic nucleoside analogue that is incorporated into replicating DNA instead of thymidine. This fact can be used to trace proliferating cells *in vitro* and *in vivo*. In my experimental setup, the BrdU incorporation assay was applied to quantify the number of replicating cells during 24-hour period in the SVZ region of adult mice. In detail, an injection solution was prepared by dissolving BrdU (Sigma Aldrich, Cat. no. B5002) at a concentration of 10gm/ml in sterile saline buffer (0.9% NaCl). To facilitate the dissolving process, the solution was sonicated for 10 minutes, followed by further shaking at 300 rpm for 45 minutes at room temperature in the dark. For BrdU labeling *in vivo*, adult mice were injected intraperitoneally with one single dose of BrdU at 50 mg/kg body weight.

3.2 Molecular biology

3.2.1 Genomic DNA preparation

Tissue for genotyping was obtained from ear clips of mice and placed in a tube.75 µl alkaline lysis reagent (25 mM NaOH, 0.2 mM EDTA) was added directly. Samples were heated to 95ºC for 10 minutes to an hour (30 minutes is optimal). Next, tubes were left to cool to 4ºC (optional). Subsequently 75 µl neutralization buffer (40 mM Tris-HCl) was added. DNA can be used immediately for PCR genotyping.

3.2.2 PCR genotyping

Genotypes of mice were determined by polymerase chain reaction (PCR) using pairs of primers specific for wild-type or the targeted *Lrp2* gene alleles as described in the following.

Primer pair BPA/G21 was used to amplify a 300 bp fragment that was specific for the gene-targeted allele of *Lrp2*. The primer pair G20/G21 amplified a 200 bp fragment specific for the wild-type allele of *Lrp2*.

The primer pair 2-ENU-MseI-For and 2-ENU-MseI-Rev was used to amplify the *Lrp2* gene region carrying the point mutation in line 267. Restriction digest of the generated PCR fragment was used to detect the presence of a MseI restriction site generated by the mutation, In this analysis, the wild-type allele gave a single PCR band of 294 bp size. The mutant allele was identified by the presence of two fragments of 239 bp, and 55 bp sizes.

To detect the Tcf/Lef_LacZ reporter, primers LacZ forward and LacZ reverse were used, resulting in a specific PCR product of 600 bp.

The Gli1-LacZ reporter was identified using the primers oIMR7888, oIMR9034 and oIMR8770. While primer pair oIMR7888 and oIMR9034 amplified the wild-type PCR product (261bp), primer pair oIMR9034 and oIMR8770 amplified the mutant PCR product (480 bp) generated by insertion of the LacZ reporter into the *Gli1* gene locus.

The nucleotide sequence of the primers is shown in Table 1.

Table 1: List of primers used for PCR genotyping.

G21 J (common)	5’CATATCTTGGAAATAAAGCGAC3’
G20 J	5’GACCATTTGGCCAGCCAAGG3’
BPA J	5’GATTGGGAAGACAATAGCAGGCATGC3’
2-ENU-MseI-For	5’GTA ACT GGA AGG CAT CTT CTC 3’
2-ENU-MseI-Rev	5’CTC ATC TGA GGT GTC ATT GTC 3’
oIMR7888 (common)	5’GGGATCTGTGCCTGAAACTG 3’
oIMR8770 (Mu_rev)	5’ TCTGCCAGTTTGAGGGGACGAC3’
oIMR9034 (Wt_rev)	5’ AGGTGAGACGACTGCCAAGT3’
LacZ forward	5’ CAG TGG CGT CTG GCG GAA AAC CTC3’
LacZ reverse	5’GGC GGC AGT AAG GCG GTC GG3’

3.3 Protein biochemistry

3.3.1 Dissection of the ventricular forebrain region for western blot analyses

For western blot analyses of the murine ventricular system, rostral ventral, rostral dorsal, caudal ventral and caudal dorsal regions of lateral ventricles were dissected from the brains of adult mice as shown in Figure 3.1.

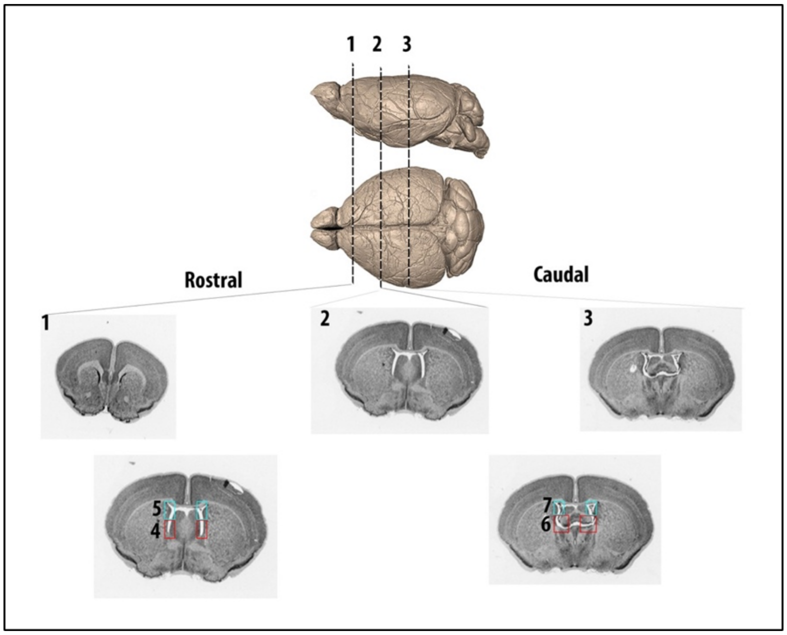

Figure 3.1: Dissection of the lateral ventricles of the adult mouse brain in a regional specific manner (modified from (Xiong et al., 2017)("The Mouse Brain in Stereotaxic Coordinates, Compact—3rd Edition," n.d.)).

The picture illustrates the three coronal cuts (1, 2, 3) placed to separate the ventricular region of the brain into rostral (1-2) and caudal (2-3) regions. Blue and red squares highlight the dissected ventral and dorsal regions of SVZ used for western blot analysis.

To do so, mice were sacrificed by cervical dislocation and the dissected fresh brains were transferred into ice cold 0.1 M Phosphate-buffered saline (1X DPBS) in a Petri dish. All further dissection steps were performed under a stereomicroscope. Specifically, the brain was trimmed from the anterior region by consecutive coronal cuts using a sharp disposable scalpel (cat. no. 5518075) until the lateral ventricles emerged (step 1, Figure 3.1). Subsequently. coronal trimming was performed from the caudal region (step 3, Figure 3.1) to the area where the two lateral ventricles merged. Finally, one more coronal cut was placed right through the middle of the trimmed tissue block (to separate it into rostral and caudal regions (step 2, Figure 3.1).

As a next step, all brain parenchymal tissues were removed by a scalpel and only the subventricular regions were left in the rostral and caudal tissue pieces. Afterwards, each ventricle was dissected by a horizontal cut with a scalpel into ventral (highlighted by a red square, Figure 3.1) and dorsal (highlighted by a blue square, Figure 3.1) halves. The ventricular regions from each brain hemispheres were collected in separate Eppendorf tubes (cat. no. 0030120086) and snap-frozen instantly in liquid nitrogen. Tissue samples were stored at -80° C until further use.

3.3.2 Preparation of tissue lysates

For lysis of lateral ventricular wall tissue samples, 400 µl of lysis buffer (20mM Tris pH 8, 10mM EDTA, 1% NP40. 1% Triton) containing complete protease inhibitor cocktail (1 tablet, (Sigma Aldrich cat. no. 11836145001) dissolved in 50 ml lysis buffer) were added directly to each tissue sample, in 2 ml Eppendorf tubes. Subsequently, tissues were homogenized by ultraturrexing for 30 seconds. The homogenized tissues were incubated at least 1 hour on ice and centrifuged afterwards for 10 min. and 1400 rpm at 4°C.

3.3.3 Protein concentration determination

Protein concentrations in lysed tissue samples were determined using the bicinchoninic acid (BCA) assay. This method is based on the principle that, in alkaline medium, protein reduces Cu^{2+} to Cu^{1+} ions. Upon this reaction, two molecules of BCA bind one cuprous ion, resulting in a purple-colored reaction product that shows absorbance at 562 nm linear in range with protein concentration in the sample.

3.3.4 SDS polyacrylamide gel electrophoresis

Proteins were separated according to their molecular mass on gels containing 12% polyacrylamide. To do so, protein samples were mixed with sample buffer (containing 4X concentrated Laemmli buffer, 8 % Sodium dodecyl sulfate (SDS), 40% glycerol, 1µl bromephenol blue mixed with 10% ß-mercaptoethanol), incubated for 5 min at 95°C, loaded on gels, and resolved at 50 V in SDS-PAGE running buffer (50 mM Tris-HCl pH 8.4, 196 mM glycine, 0.1% SDS). After electrophoresis, the gels were either subjected to western blotting.

3.3.5 Western blotting

Western blotting was performed by transferring proteins electrophoretically from polyacrylamide gels onto Hybond-C nitrocellulose membrane, with 0.2µm pore size (GE Healthcare, USA, cat. no. 10600001). Protein transfer was performed in transfer buffer (25 mM Tris-HCl, 192 mM glycine; pH 8.4) at 100 V for 2 hours or at 20 V overnight using a standard tank transfer set-up. The efficiency of the transfer was evaluated by staining the protein bands on the membrane with Ponceau S solution (0.1% (w/v) Ponceau S in 5% (v/v) acetic acid). Afterwards, the membrane was incubated with blocking solution (133 mM NaCl, 1.7 mM KCl, 4.3 mM Na2HPO4, 1.4 mM KH2PO4, 0.08% Tween 20, 5% FCS, 5% dry milk powder; pH 7.4) for 1 hour at room temperature (RT).

The primary antibody was applied in binding buffer (133 mM NaCl, 1.7 mM KCl, 4.3 mM Na_2HPO_4, 1.4 mM KH_2PO_4, 0.08% Tween 20, 5%dry milk powder; pH 7.4) at dilutions of 1:500 to 1:1000, depending on the antibody used. Incubation with the primary antibody was carried out at 4°C overnight on a rocking platform. Non-specifically bound antibodies were removed the next day by washing the membrane twice for 15 min in washing-buffer I (133 mM NaCl, 1.7 mM KCl, 4.3 mM Na_2HPO_4, 1.4 mM KH_2PO_4, 0.08% Tween 20, 0.1% SDS, 1% NP-40; pH 7.4), followed by twice incubations in washing-buffer II (133 mM NaCl, 1.7 mM KCl, 4.3 mM Na_2HPO_4, 1.4 mM KH_2PO_4, 0.08%Tween 20; pH 7.4). Finally, the membrane was incubated with peroxidase-conjugated secondary antibody (1:1000 in binding buffer) for 1 hr at RT. After washing twice for 15 min with washing-buffer I and twice for 15 min with washing-buffer II, the membrane was incubated with detection solution (Super Signal West PicoStable Peroxide/luminol enhancer solution, Pierce, USA). Immunoreactive bands were detected using a CCD-camera (Fujifilm LAS-1000/ Intelligent Dark Box, Fujifilm,Japan)

3.4 Dissection and culturing of lateral ventricles from the mouse brain

3.4.1 Dissection of mouse brain lateral ventricular walls for the en face visualization

Mice at 10-12 weeks of age were subjected to cervical dislocation. Brains were dissected quickly and transferred into a Petri dish filled with ice cold 1X Dulbecco's phosphate-buffered saline (1X DPBS), obtained from commercially available 10X concentrated DPBS (cat. no. 14200075). Further dissection procedures were performed under a stereomicroscope.

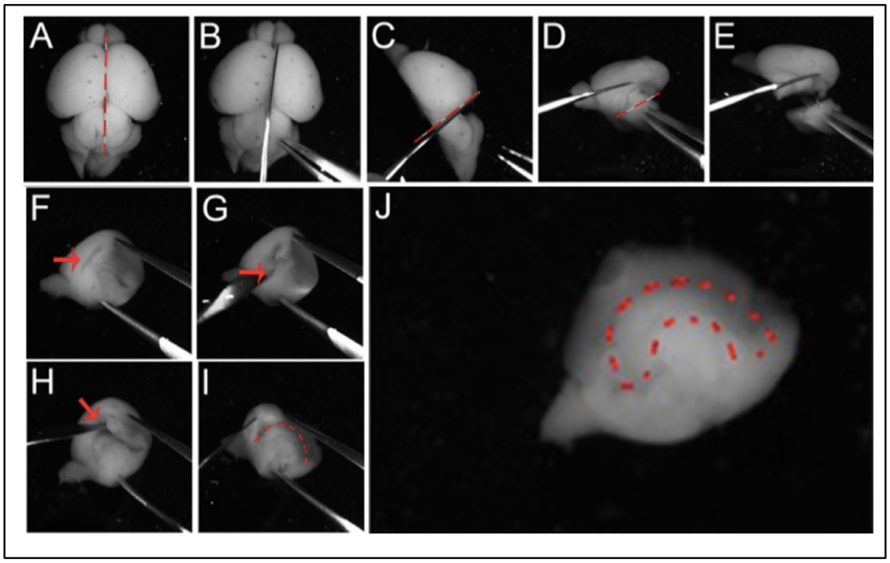

Figure 3.2: Dissection steps for lateral ventricular wall whole mounts (LWWMs) (modified from (Labedan et al., 2016)). The procedure for preparation of LWWM for the en face visualization of ependymal cells is presented. **(A)** Adult mouse brain removed from the scull. Dashed red line indicates the cut to separate the brain into two hemispheres (as shown in **B**). (**C**) The dashed red line indicates the cut for removal of the cerebellum. (**D-F**) Subsequent cuts to dissect the hippocampus are indicated. (**G-H**) Hippocampus and medial ventricular wall are removed by cuts on the area indicated by the red arrow. (**I**) Removal of the cortical wall along the dashed red line. (**J**) Lateral wall is highlighted by the dashed red line.

A detailed visualization of the lateral ventricular wall whole mounts (LWWM) dissection procedure is depicted in Figure 3.2. As a first step, the brain was divided in two hemispheres (Figure 3.2 A). Subsequently, a coronal cut was placed a few mm anterior from cerebellum, to reveal the hippocampus in the cross-section (Figure 3.2 B-E). Via a small incision on the dorsal end, connecting the hippocampus and cortex (pointed by an arrow in Figure 3.2 F-H), forceps were inserted into the ventricular space. By applying gentle force to the forceps, the hippocampus with attached medial ventricular wall was removed and opening up the surface of lateral side of ventricular wall (Figure 3.2 H-J). The excessive cortical area around lateral ventricles were removed using watchmaker scissors. After this preparation, LWWMs were either incubated with ligands for uptake studies or immediately fixed for 15 minutes in fixation solution (4% PFA, 0.1% Triton-X100) for further immunostaining procedures.

3.5 Primary cultures of mouse brain ependymal cells

To prepare culturing of the cells, 25^2 mm surface culture flasks (CellStar, cat. no. 690 170) were coated with poly-L-lysine (Sigma cat. no. P6282) to create an adhesive surface for cells. For coating, flasks were incubated with 2 ml of sterile 10% poly-L-lysine/MilliQ water solution in a cell culture incubator for 24 hours. Afterwards, the flasks were washed with sterile MilliQ water and kept for up to 2 weeks in a cell culture incubator until further use.

For the experimental procedure, mice at 0 to 2 days of age (P0-P2) were used. The neonates were quickly decapitated using a scissor. The brains were dissected carefully and transferred to ice cold 1x DPBS solution in a Petri dish. Under a stereomicroscope, the meninges were removed from the brains by pulling from the anterior to posterior brain region with fine forceps (cat. no. 11251-20 Dumont #5 Forceps). Subsequently, the olfactory bulbs, the cerebellum and the hippocampal structures were removed. The remaining brain tissue was transferred into 2 ml Eppendorf tubes filled with 500 µl 1x DPBS. Eppendorf tubes were stored on ice until all brains were dissected. Afterwards, the DPBS solution was removed and brain samples were washed twice with Hanks' Balanced Salt solution without calcium and magnesium (HBSS (-/-), Thermo Fisher, cat. no. 14170112). Afterwards, each brain sample was incubated for 8 minutes with 100 µl of 10 mg/ml Papain (Worthington, cat. no. 3126), diluted in 900 µl of activation buffer (5 mM L-cystein, 1 mM EDTA, 0.05 mM ß-mercaptoethanol in HBSS (-/-)) to perform the enzymatic digestion of the tissue. To stop the digestion reaction, 1 ml of stop solution (10% fetal bovine serum (FBS) (GIBCO, cat. no.10270), 0.05 mg/ml DNAase (Worthington, Cat. no.

2139) in Liebovitz's-L15 medium (GIBCO, cat. no.11415) was added directly to each brain sample. The brain sample was recovered from the reagent mixture by centrifugation at 1000g for 4 minutes at 4ºC. The supernatant was discarded and the brain pellet diluted in 1 ml of proliferation medium (10% FBS, 1% Penicillin/ Streptavidin (GIBCO, cat. no.15140) in DMEM (GIBCO, cat. no. 31966)). The cells were suspended by gentle pipetting up and down for 20 times by micropipettes (Gilson pipette pipetman classic (200µl-100µl), cat. no. F123602). Then, 1 ml of the cell suspension was transferred to poly-L-lysine-coated flasks and 4 ml of proliferation medium was added immediately. The flasks were transferred to cell culture incubator and kept at 37°C in 5% CO for 24hrs$_2$. On the following day, the proliferation medium was refreshed and the cells incubated for 5-6 days until reaching confluency. Then, cell cultures were washed three-times in 3 ml HBSS by vigorous shaking to detach and remove the glial cells from the surface of the culture dish. Thereafter, 1 ml of 0.05% trypsin/EDTA solution (GIBCO, cat. no 25300) was added to recover all cells from the flask surface. The cells were suspended in 11 ml of proliferation medium and cultured on poly-lysine coated sterile coverslips placed in 12-well plates. As soon as the cell cultures reached confluence on coverslips (after 2-3 days), the proliferation medium was replaced by differentiation medium (1% Penicillin/Streptavidin (GIBCO, cat. no.15140) in DMEM (GIBCO, cat. no.31966) and incubated under the same conditions as before until day10 (10 DIV). At this time point, a maximum number of cells was differentiated to vital poly-ciliated ependymal cells as evident by observing motile cilia beating of ependymal cells under a microscope using a 20x objective. Cells can stay in culture for up to 21 days.

3.6 Ligand uptake assays

For investigating the uptake of SHH ligand by ependymal cells, uptake studies were performed in primary ependymal cell cultures and in lateral ventricular wall whole mounts (LWWM). In detail, a recombinant fusion protein composed of the active amino terminal fragment of SHH (SHH-N), attached to glutathione -transferase (GST) was used for these experiments. GST-SHH-N was produced recombinantly in bacteria and purified by glutathione affinity chromatography as described previously (GST-SHH-N used in my studies was kindly provided by Kristin Kampf (technician).

For uptake studies in ependymal cells, differentiated cultures grown on coverslips, were incubated at DIV10 in differentiation media containing 10 µg/ml GST-SHH-N. After 2 hours of incubation, cell cultures were washed 3 times with ice cold 1x DPBS for 5 minutes each step. Afterwards, the cell cultures were fixed for 6 minutes in 4% PFA/DPBS, washed again 3 times with 1x DPBS and then kept in 1x DPBS solution at 4°C until performing immunostainings.

To test ligand uptake by ependymal cells in LWWM, freshly dissected brain tissue samples were incubated for 1.5 hours with 10 µg/ml GST-SHH-N in DMEM medium. After a quick wash in ice cold 1x DPBS, the tissues were fixed in 4% PFA/DPBS solution for 15 minutes at room temperature. Further staining procedures were performed as described for en face preparations below.

3.7 Histology

3.7.1 Preparation of mice for histology

To anaesthetize mice, 50 mg pentobarbital per 1 kg body weight was injected intraperitoneally (IP). Anesthesia of mice was tested by applying a gentle pressure to the animal’s toes using forceps. When no pedal reflex was noticed, the animals were considered fully anaesthetized and were subjected to intracardiac perfusion. Foremost, perfusion pump was set up and perfusion needle was attached to the pump. To clean up tubes, 100 ml of normal tap water was pumped through the tubes. Thereafter the open end of perfusion tube was placed in a beaker filled with ice cold 1X concentrated DPBS solution. Slow steady flow of the liquid was adjusted by controlling rotation speed of the pump (around 120 rotation/minutes). In the beginning the thoracic cavity of anaesthetized mice was opened in a way that the heart was easily accessible. While holding the beating heart steady with forceps a needle attached to the perfusion pump, was directly inserted into the protrusion of the left ventricle. After the needle was fixed in the heart and the heart was connected to the perfusion pump, the pump was switched on and ice cold 1x DPBS was pumped into the blood circulation of the mouse. Immediately, a cut in the right atrium was made with a sharp scissor, to provide an exit for the inserted solution. After 3-4 minute, when the blood was cleared from body and liver turned pale, perfusion was continued with 4%PFA in 1x DPBS solution for 15 minutes. Afterwards, brains were dissected and further fixed overnight in 4% PFA in 1x DPBS at 4°C.

3.7.2 Paraffin tissue sectioning

Following overnight fixation, brain tissue samples were washed in 1x DPBS and subjected to paraffin infiltration. In the first step brains were dehydrated by incubating the samples in graded ethanol solutions of 70%, 80%, 90%, 96% and 99% ethanol (2 hrs. each step). Following dehydration, the samples were incubated twice for 2 hrs. in Roti-Histol (Roth, Karlsruhe, Germany, cat. no. 6640.1). The samples were pre-infiltrated with paraffin wax for 2 hrs. at 67°C and finally infiltrated with fresh paraffin wax overnight at 67°C. The entire process from the dehydration with ethanol to the final infiltration with paraffin wax was performed using an automated Leica TP 1020 Automatic Tissue Processor setup. Finally, the infiltrated tissues were embedded in wax blocks and sectioned in 10-12 µm coronal sections using a motorized rotary microtome (Microm HM355S). Tissue sections were collected on superfrost plus glass slides (Meltzer-Fischer Scientific) and stored at RT until further processing for immunohistochemistry.

3.7.3 Free floating sections

Brain samples fixed overnight were washed twice in 1X DPBS for 5 minutes and transferred into 30% sucrose in 1x DPBS solution for equilibration at 4°C. After approximately 2 days of incubation, the samples were fully infiltrated and sank to the bottom of the storage tube. Thereafter, the brains were kept in cryoprotectant (CP) (25% glycerol, 25% ethylene glycol, 0.1M phosphate buffer) until further use. For histology, the brain samples were attached on a metallic platform of a Leica SM2000R Sliding Microtome. Dry ice placed around the metallic platform froze the brains quickly. Frozen samples were sectioned into 40 µm coronal sections. The free-floating sections were stored in CP in 96-well plates at -20ºC until further staining. For immunostaining, the floating sections were transferred to trans-well chambers (Costar, Corning) using a small paintbrush (size 2) always kept in free floating conditions during the entire staining procedure.

3.7.4 Cryosections

After overnight incubation in 4% PFA/DPBS solution, the brains were equilibrated in 30% sucrose/DPBS until fully infiltrated. The brains were embedded in Tissue-Tek OCT (Sakura, Japan) on dry ice, and stored at -20ºC. The tissues were cut into 10-15 µm coronal sections on a rotary cryotome (Leica, Germany), placed on glass slides, and stored at -20 ºC.

3.7.5 Immunohistochemistry

Various immunohistochemical techniques were applied for detection of the targeted antigen on sections, based on antigen epitope accessibility, antibody quality and tissue sectioning technique. All performed staining procedure can be categorized in 3 main types of immunohistological techniques: direct, indirect and enzymatic ‘sandwich’ methods.

3.7.6 Detection of β-galactosidase (lacZ) activity

Expression of the β-galactosidase (*lacZ)* transgene inserted into the mouse genome in various reporter strains was detected by enzyme-based histochemical staining using a chromogenic substrate for β-galactosidase, such as 5-bromo-4-chloro-3-indolyl-β-D -galactoside (X-gal). To do so, freshly dissected mouse brains were gently fixed for three hours in 4%PFA/DPBS and subjected to cryosection using a cryotome. Before immunostaining, glass slides containing the tissue sections were taken from the freezer and thawed at RT for 5 minutes. Then, the sections were fixed for 5 minutes in ice cold fixation solution (1x DPBS pH7.4, 2 mM $MgCl_2$, 5 mM EGTA, 0,2% glutaraldehyde). The sections were washed in 2mM $MgCl_2$ in DPBS and permeabilized with detergent solution (2 mM $MgCl_2$, 0.01% sodium deoxycholate, 0.02% NP-40 in DPBS) for 5 to 10 minutes. Detection of enzyme activity was performed by applying detergent solution, containing 1x DPBS (pH7.3), 2mM MgCl2, 0,01% Sodium Deoxycholate, 0,02% NP-40, 5mM Potassium Ferrocyanide, 5mM Potassium Ferricyanide, 20mM Tris (pH 7.3) and freshly added X-gal (20 mg/ml). After overnight incubation at 37°C in a humid chamber, the sections were rinsed several times in 2 mM $MgCl_2$ in 1x DPBS and then in water. After drying, the sections were mounted using the Roti-Histo-Kit II and visualized, under a bright field microscope.

3.7.7 Immunofluorescence stainings of adult brain tissue sections

For immunohistology, free floating tissue sections were first washed with TBS (83.9 mM Tris-HCl, 16 mM Tris base, 154 mM NaCl) and then with TBST (TBS with 0.1% Triton X-100) for 5 to 10 minutes before incubating them for 1 hour in blocking solution (TBS with 0.3% TritonX and 10% donkey serum). Afterwards, sections were incubated with primary antibodies in blocking solution overnight at room temperature or at 4°C, depending on the antibody used. The next day, the sections were washed 3 times with TBS and incubated with secondary fluorophore-conjugated antibodies in TBS for 2-3 hours. Thereafter, the sections were washed thoroughly with TBS and TBST before mounting them on glass slides in fluorescent mounting medium (Dako). The class slides were left to dry overnight at RT in the dark. Images were taken under a confocal SPE microscope (Leica).

3.7.8 Immunofluorescence staining of cell cultures

Primary ependymal cell cultures adhered to 20 mm glass coverslips were washed 3 times in 1x DPBS while placed in 12-well plate. Thereafter, the cells were fixed for 6 minutes by incubation in 4% PFA/DPBS solution. After three more washing steps in 1x DPBS solution, a 1 hr. incubation step in blocking solution (10% donkey serum and 0,1% Triton in 1%BSA/DPBS) followed. Cells were incubated with primary antibodies in blocking solution at 4°C overnight. The next day, the cultures were washed 3 times with 1x DPBS and incubated in secondary antibody solution in 1x DPBST (1x DPBS containing 0.1% Triton X-100) at RT for 2 hours. After several washing steps with 1x DPBS and 1x DPBST, the coverslips were mounted on glass slides using Dako fluorescent mounting medium.

3.7.9 Immunostaining of SVZ whole mounts for en face visualization

Dissected lateral ventricular wall whole mounts (LWWM) were fixed in a freshly prepared solution of 4% PFA with 0.1% Triton X-100 for 12 min at RT. Next, brains were washed 3 times for 10 minutes in 1ml of 0.1% Triton X-100 in 1x DPBS on a rocking platform. Following fixation, further sub-dissection of the LWWM tissue was carried out to remove the underlying striatum from lateral wall preparation. This step significantly improved the staining quality as it facilitated the penetration of antibody solution into the tissue block. Subsequently, the tissue samples were incubated in blocking solution (3% BSA in 1x DPBS,) for 1 hr. at RT, followed by treatment with primary antibodies diluted in blocking solution overnight at 4ºC. The next day, the tissue samples were washed 3 times with 0.1M DPBS for 10 minutes at RT, before incubation with secondary antibodies diluted in 0.1M DPBS for 1 hour. Afterwards, the samples were washed 3 times in 1 ml of 0.1% Triton X-100 in 1x DPBS (10 min at RT). After a final dissection of excessive striatal and cortical tissue attached to lateral ventricular walls, the tissue samples were placed on glass slides with ependymal surface facing up. Mounting medium (Dako, cat. no. S302380) was applied directly on the samples and coverslips placed slowly on top to avoid trapping of air bubbles. The slides were air dried at RT for a day and then stored at 4ºC until imaging under a confocal microscope (preferably within one week after mounting).

3.7.10 Thyramide signal amplification

For detection of ID3 on free floating brain sections, thyramide signal amplification (TSA) was applied to improve signal detection of this low-abundance targets in fluorescence immunohistochemistry (thyramide amplification kit, Perkin Elmer #NEL702). This amplification procedure is based on the fact that, in the presence of low concentrations of H_2O_2, horseradish peroxidase (HRP) converts a fluorescent-labeled thyramide substrate into a highly reactive product which binds covalently to tyrosine residues in proteins in close proximity to the enzyme.

As a first step in the staining procedure, free floating brain sections were collected and washed in washing buffer TNT (0.1M Tris-HCl pH 7.5, 0.15 M NaCl, 0.005% Tween-20). Afterwards, the sections were treated with 1% H_2O_2 in TNT for 1 hour and then permeabilized in TNT containing 0.2% Triton X-100 and 0.2% Tween-20 for 30 minutes. The tissue sections were placed on glass slides and left to dry for several minutes. Once the glass surface was free from water drops, circles were drawn around each section using a PAP pen (Abcam, cat. no. ab2601). This creates a hydrophobic boundary around the tissue section enabling the application of small volumes of reagents directly onto the tissue. Next, the slides were incubated with primary anti-ID3 antibody solution (1:500) in TNB buffer (0.1M Tris-HCl pH 7.5, 0.15 M NaCl) overnight at 4°C in a humid chamber. The following day, the slides were washed several times with TNT buffer and incubated with secondary donkey-anti-biotin-SP antibody solution (diluted 1:200 in TNB) for 2 hours at RT. Biotin-SP is a trade name for biotin with a 6-atom spacer positioned between biotin and the protein to which it is conjugated. The spacer makes Biotin-SP antibodies more accessible to streptavidin. After several washing steps with TNT buffer, the sections were treated with streptavidin-conjugated HRP (1:200 dilution in TNB) for one hour. Finally, the thyramide-fluorophore solution (diluted 1:100 in amplification buffer) was applied on the sections for 8 minutes, before the slides were washed thoroughly in TBN, air dried shortly and mounted under cover slips using the PVA-DABCO mounting medium.

3.7.11 Immunostaining using peroxidase reaction

As an alternative to the use of fluorophore-conjugated secondary antibodies, bound primary antibodies were detected using a biotin-labeled secondary antibody followed by signal detection using avidin-coupled peroxidase and diaminobenzidine. In this procedure, the antibody against antigen of our interest, is conjugated with a peroxidase enzyme. Upon hydrogen peroxide availability, peroxidase enzyme catalyzes the DAB, to its oxidized form, forming a brown precipate. As a first step in the procedure, paraffin sections of the adult SVZ were deparaffinized by two incubations in Roti-Histol R (Roth, Germany), rehydrated by subsequent washes in 99%, 80%, 50%, 30% ethanol solutions and H_2O (3 minutes for each solution). Next, the sections were incubated in 2.4% H_2O_2 in 1xTBS for 30 min at RT to quench endogenous peroxidases activity. Afterwards, the sections were washed in 2 N HCl for 1.5 hrs at 45°C by gentle agitation to denature the double-stranded genomic DNA and make the inserted BrdU molecules accessible for primary antibody detection. Subsequently, 0.1 M borate buffer (pH 8.5) was applied for 15 min at RT to stop the HCl reaction. Finally, the sections were washed for 5 minutes in TBS and TBST before blocking unspecific epitopes with 3% donkey serum in blocking buffer (10% BSA, 0.1% Triton X-100 in TBS) for 2 hrs at RT. Thereafter, the sections were incubated with primary anti-BrdU antibody (diluted 1:100 in blocking solution) overnight at RT. The following day, several washing steps in TBS and TBST followed before incubation of the sections with biotin-conjugated donkey-anti-rat antiserum (1:100) for 1 hour at 37°C. Afterwards, the ABC-HRP-kit (VECTASTAIN Elite, cat. no. PK-6100) was used to perform binding of biotinylated peroxidase complex to the secondary antibodies. The colorization was performed by incubation of the sections in 3’-diaminobenzidine (DAB) solution (one drop of DAB in 1 ml of TBS buffer) for 3 minutes. Finally, the sections were washed, briefly air dried, and then mounted in poly mount organic mounting medium (Roth, Germany). Imaging was performed under a bright field microscope.

3.7.12 Summary of antibodies used in IHC methods and WB analysis

Table 2: List of the primary antibodies.

Antigen	Host	Source	Catalogue Number	Dilution
Arl13b	rabbit	Proteintech	17711-1-AP	1:500
BrdU	rat	Abd serotec, Oxford, UK	OBT 0030	1:500
EEA1	rabbit	Cell Signaling	3288	1:100
FOP	mouse	Abnova	H00011116-M01	1:1500
GFAP	mouse	Merck	Mab360	1:500
GST	mouse	Sigma Aldrich	G1160	1:50
γ-tubulin	mouse	Abcam	Ab11316	1:400
ID3	rabbit	Abcam	Ab41834	1:100
LRP2	guinea pig	Eurogen tech.	DE14027	1:1500
OLIG2	goat	R&D systems	AF2418	1:20
P4EBP1	rabbit	Cell Signaling	2855	1:50
4EBP1	rabbit	Cell Signaling	9644	1:100
pS6RP	rabbit	Cell Signaling	2211S	1:50
Rab4	rabbit	Abcam	Ab13252	1:100
Rab9	rabbit	Cell Signaling	5118	1:50
Rab8	rabbit	Abcam	Ab188574	1:100
Rab11	rabbit	Abcam	5589	1:100

Rab17	rabbit	Abcam	Ab155135	1:100
Rab23	rabbit	Abcam	Ab230200	1:100
Rab35	rabbit	Abcam	Ab230838	1:100
S6RP	rabbit	Cell Signaling	2317	1:200
SHH	rabbit	Sigma	SC9024	1:500
SHH	rat	Eurogentech	DE18151	1:100
SOX2	goat	Santa Cruz	SC17320	1:200
Tubulin	mouse	Sigma Aldrich	T6793	1:400 (IF) 1:500 (WB)
ZO1	rabbit	Invitrogen	61-7300	1:500

Table 2 provides an overview of antibodies used in this thesis. It lists the host species, the commercial source, as well as the working dilution.

Table 3: Immunohistological conditions for staining protocol.

Antigen	**Sample Type**	**Blocking Solution**	**Detection method**	**Washing Buffer**	**Incubation**
Arl13b	LWWM	3% BSA in DPBS	indirect IF	DPBS	4°C, ON
BrdU	paraffin section	10% BSA, 3% donkey Serum, 0.1% Tritonin in TBS	immuno peroxidase staining	TBS	RT, ON

EEA1	cell culture	1%BSA, 10% donkey serum, 0,1% Triton in DPBS	indirect IF	DPBS	4°C, ON
FOP	LWWM	3% BSA in DPBS	indirect IF	DPBS	4°C, ON
GFAP	free floating	1% BSA, 10% donkey serum, 0.3% Triton in TBS	indirect IF	TBS	RT, ON
Ms GST	cell culture	1%BSA, 10% donkey serum, 0,1% Triton in DPBS	indirect IF	DPBS	4°C, ON
Rab GST	LWWM	3% BSA in DPBS	indirect IF	DPBS	4°C, ON
γ-tubulin	LWWM	3% BSA in DPBS	indirect IF	DPBS	4°C, ON
ID3	free floating	TNB (from the kit)	thyramide signal amplification	TNT	4°C, ON
LRP2	cell culture	1%BSA, 10% donkey serum, 0,1% Triton in DPBS	indirect IF	DPBS	4°C, ON
OLIG2	free floating	1% BSA, 10% donkey serum, 0.3% Triton in TBS	indirect IF	TBS	RT, ON
P4EBP1	free floating	1% BSA, 10% donkey serum, 0.3% Triton in TBS	indirect IF	TBS	4°C, ON

4EBP1	free floating	1% BSA, 10% donkey serum, 0.3% Triton in TBS	indirect IF	TBS	4°C, ON
pS6RP	free floating	1% BSA, 10% donkey serum, 0.3% Triton in TBS	indirect IF	TBS	4°C, ON
Rab4	cell culture	1%BSA, 10% donkey serum, 0,1% Triton in DPBS	indirect IF	DPBS	4°C, ON
Rab9	cell culture	1%BSA, 10% donkey serum, 0,1% Triton in DPBS	indirect IF	DPBS	4°C, ON
Rab8	cell culture	1%BSA, 10% donkey serum, 0,1% Triton in DPBS	indirect IF	DPBS	4°C, ON
Rab11	cell culture	1%BSA, 10% donkey serum, 0,1% Triton in DPBS	indirect IF	DPBS	4°C, ON
Rab17	cell culture	1%BSA, 10% donkey serum, 0,1% Triton in DPBS	indirect IF	DPBS	4°C, ON
Rab23	cell culture	1%BSA, 10% donkey serum, 0,1% Triton in DPBS	indirect IF	DPBS	4°C, ON

Rab35	cell culture	1%BSA, 10% donkey serum, 0,1% Triton in DPBS	indirect IF	DPBS	4°C, ON
S6RP	free floating	1% BSA, 10% donkey serum, 0.3% Triton in TBS	indirect IF	TBS	4°C, ON
Rb. SHH	wb	0.08% Tween 20, 5% dry milk powder in binding buffer	WB	Washing Buffer I &II	4°C, ON agitation
Rat SHH	cell culture	1%BSA, 10% donkey serum, 0,1% Triton in DPBS	indirect IF	DPBS	4°C, ON
SOX2	free floating	1% BSA, 10% donkey serum, 0.3% Triton in TBS	indirect IF	TBS	RT, ON
Tubulin	LWWM	3% BSA in DPBS	indirect IF	DPBS	4°C, ON
Tubulin	WB	0.08% Tween 20, 5% dry milk powder in binding buffer	WB	Washing Buffer, I &II	4°C, ON agitation
ZO1	LWWM	3% BSA in DPBS	indirect IF	DPBS	4°C, ON

Table 3 describes the specific experimental procedures applied to visualize the listed antigens.

3.7.13 In Situ hybridization technique

For *in situ* hybridization, I used 10 µm cryosections of adult mouse SVZ, which left to air dry for 30 minutes at RT before starting the hybridization procedure. To do so, the slides with the brain sections were placed in sterile incubation chambers pretreated with RNAse inhibitor from Sigma-Aldrich (cat. no. R2020). After washing with DPBST for 5 min at RT, the sections were fixed in 4% PFA in DPBS for 10 min at RT. Subsequently, the sections were washed 3 times in DPBST for 5 min and then incubated in 10 µg/ml of Proteinase K in 1x DPBS for 8 min. Subsequently sections were fixed again in 4% PFA in DPBS for 10 minutes. After several washing steps in 1x DPBS, the sections were placed in an incubation chamber humidified with 50% formamide in H_2O, and incubated for 3 hrs at 60°C in hybridization buffer , consisting of 50% formamide, 10% dextran sulfate, 1x salt solution (stock 10x: 1.96 M NaCl, 0.11M TrisHCl (pH 7.5), 0,01M Tris base, 0.056M NaH2PO4xH2O, 0.059M NaH2PO4, 0.05M EDTA in MilliQ water), 1 mg/ml tRNA, 1x Denhardt's solution (stock 50x: 1% Ficoll, 1% Polyvinylpyrrolidone, 1% BSA from Thermo Fischer, cat. no. 750018) in MilliQ water. Subsequently, the tissue sections were incubated overnight at 60°C with 1ng/µl RNA probes (See details in Table 4) in hybridization buffer, preheated to 95°C for 5 minutes. The next day, the sections were washed twice for 30 minutes in solution 1 (mixture of 10 ml formamide, 4 ml saline-sodium citrate buffer (20x SSC) pH 7.0, 5 ml MilliQ H_2O, 1 ml 20% SDS) and solution 2 (mixture of 10 ml formamide, 2 ml 20x SSC pH 7.0, 8 ml MilliQ H_2O). Afterwards, washing was performed in maleic acid buffer (MABT) (0.49M maleic acid, 0.73M NaCl, 0.1% Tween-20 in MilliQ water) twice for 5-10 min at RT, before the sections were incubated in blocking solution (MABT, 2% Roche blocking reagent's buffer (cat. no. 11096176001), 20% sheep serum) at RT for 2-4 hrs. Next, the sections were treated overnight at 4°C with sheep anti-digoxigenin antibody conjugated with alkaline phosphatase (anti-DIG-AP, Sigma Aldrich, cat. no. 11093274910) dissolved 1:1500 in blocking solution. The following day, the sections were washed 5 times in MABT solution for 20 minutes each, and then twice in NTMT solution (5M NaCl, 1M TrisHCl pH9.5, 1M MgCl2, 0.1% Tween-20 in MilliQ water) for 10 minutes each. The staining solution was prepared by gradually dissolving 10% Polyvinyl alcohol (PVA) in NTMT solution. To facilitate dissolving, the mixtures was heated gradually to 85°C and then slowly cooled down to RT. Then, 4.5 µl of nitro blue tetrazolium (NBT) and 3.5 µl of 5-bromo-

4-chloro-3-indolyl-phosphate, 4-toluidine salt (BCIP) solution (Sigma Aldrich, 11681451001) were added to 1 ml of staining solution. The sections were incubated in staining solution until signals were clearly visible (1 to 18 hrs). Then, the slides were washed in 1x DPBS, air dried at RT, and mounted in Roti-Histo-Kit II mounting medium. Image acquisition was performed under a bright field microscope.

3.7.14 RNA probes generation procedure

3.7.14.1 Enzymatic digest of DNA

Corresponding restriction enzymes described in Table 4, were incubated with certain amount of DNA and buffer at a ratio of 0.5 U enzyme/µg DNA. The digest was incubated at 37°C for 2 hrs to overnight. All restriction enzymes were obtained from New England Biolabs, USA.

3.7.14.2 In-vitro transcription of digoxigenin-labelled RNA

To generate digoxigenin (DIG)-labelled probes for *in situ* hybridization (ISH) a DIG labeling Kit was used (Roche, Switzerland, cat.no. 11175025910). Linearized template plasmid- DNA (1 µg) was incubated with transcription buffer (40 mM Tris-HCl, 6 mM MgCl2, 10 mM dithiothreitol, 2 mM spermidine; pH 8.0), 1 mM ATP, 1 mM GTP, 1 mM CTP, 0.65 mM UTP, 0.65 mM DIG-11-UTP, 40 U RNA polymerase and 20 U RNase inhibitor. After adjusting the volume of the reaction to 20 µl samples were incubated for 2 hrs at 37°C. Template DNA was removed by incubating the reaction setup with 20 U DNase I at 37°C for 15 min. The RNA was purified using the RNeasy Mini Cleanup Kit (Qiagen, Germany).

Table 4: Mouse in situ hybridization probes.

Gene name	Probe	Restr.-site	Promotor
Brother of Cdon	*Boc antisense*	*SalI*	T7
	Boc sense	*HindIII*	Sp6
Cell adhesion molecule-related/down-regulated by oncogenes	*Cdon antisense*	*XhoI*	T7
	Cdon sense	*NotI*	T3
Glioma-associated oncogene homolog1	*Gli1 antisense*	*NotI*	T3
	Gli1 sense	*XhoI*	T7
Protein patched homolog 1	*Ptch1 antisense*	*SalI*	T3
	Ptch1 sense	*NotI*	T7
Smoothened	*Smo antisense*	*SacI*	T7
	Smo sense	*SacII*	Sp6

Table 4 describes the specific restriction sites and promotors on DNA, used for generating the listed RNA probes.

3.8 Quantification

3.8.1 Nuclear signal quantification

Based on the signal characteristics and the aims of the experiment, the quantification method and parameters used varied for each experiment. Typically, protein expression levels that have a nuclear loclasiation, were determined by counting individual cells nuclei.

To calculate the number of BrdU positive cells, 12 histological sections were taken from rostral and caudal forebrain regions of each animal (Figure 3A). The entire SVZ region on each coronal section was imaged under a bright field microscope (Leica DMI6000B inverted microscope) equipped with a 20X objective. The lower half of SVZ region was considered the ventral, the upper half the dorsal domain. For nuclear proteins visualized by immunofluorescence staining, the confocal Leica SPE microscope was used (20X objective). In this instance, one single image was taken from the very ventral and one from very dorsal part of SVZ. The nuclear signal was quantified in each picture using the ImageJ software (Figure 3.3 B). For most proteins (e.g., SOX2, ID3, pS6RP), the expression levels were quantified separately for the lateral and medial sides of ventricular walls.

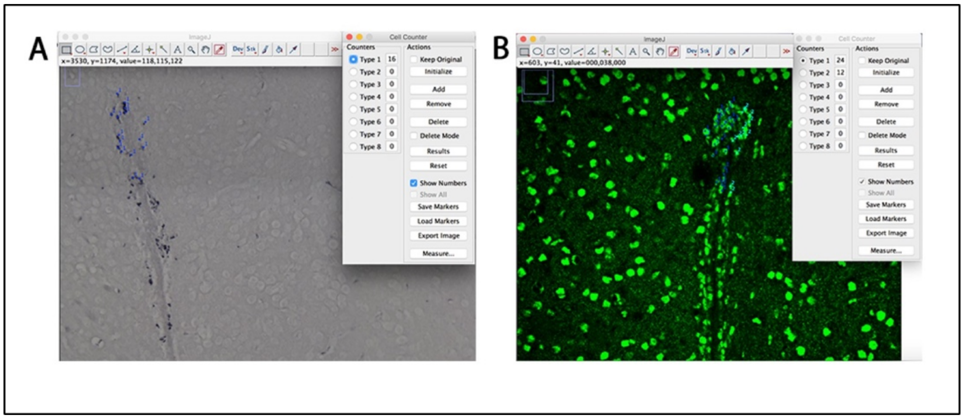

A: x=3530, y=1174, value=118,115,122

Counters	
Type 1	16
Type 2	0
Type 3	0
Type 4	0
Type 5	0
Type 6	0
Type 7	0
Type 8	0

B: x=603, y=41, value=000,038,000

Counters	
Type 1	24
Type 2	12
Type 3	0
Type 4	0
Type 5	0
Type 6	0
Type 7	0
Type 8	0

Figure 3.3: Quantification of the nuclear immunosignals.

For counting of BrdU- (A) and ID3- **(B)** positive cell nuclei, the indicated parameters of the ImageJ software were used. BrdU-positive nuclei were counted in the entire ventral SVZ area. For ID3-positive cells, medial and lateral ventricular walls were counted separately.

3.8.2 Cytoplasmic signal quantification

For the proteins with cytoplasmic localization, such as GFAP, mean gray values (MGV) from the region of interest (ROI) were used as a basis for calculation of signal, intensities. In the imageJ software, the ROI was first defined by the free select tool and then the respective MGV determined using the inserted macro (Figure 3.4). Using the move tool, the selected shape of the ROI was transferred to a neighboring region devoid of specific GFAP signals to determine the

MGV of the background to be subtracted from the MGV of the specific expression domain. The resultant value was taken for further quantification. Signal intensities of medial and lateral ventricular walls were quantified separately using the average of MGVs from three consecutive sections from each animal.

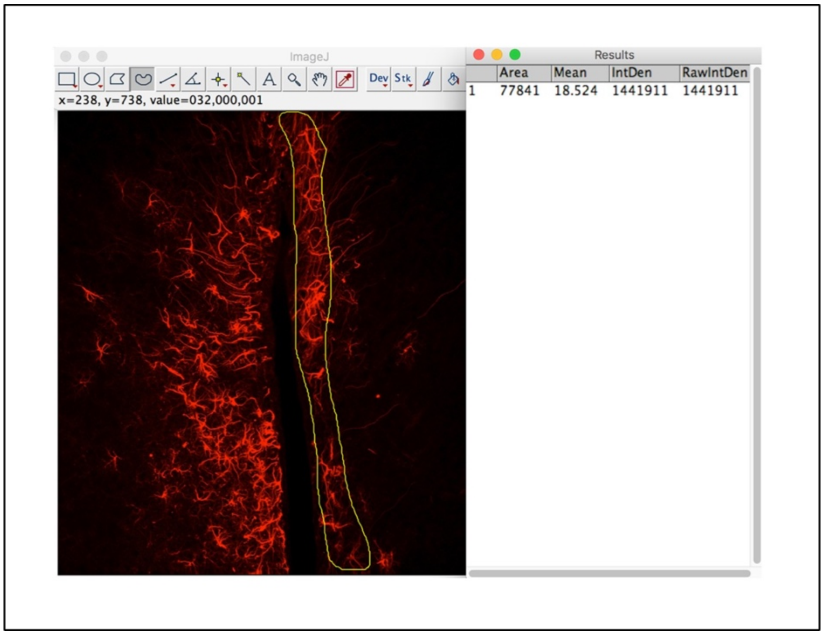

```
x=238, y=738, value=032,000,001
```

	Area	Mean	IntDen	RawIntDen
1	77841	18.524	1441911	1441911

Figure 3.4: Mean gray value (MGV) quantification in the region of interest (ROI) using ImageJ.

As shown for GFAP immunostaining in this figure, signal intensities for proteins with cytoplasmic localization were quantified in the selected ROI using the shown settings in ImageJ.

3.8.3 Western blot signal quantification

The Image Studio software was used to quantify signal intensities on densitometrical scanned images of replicate western blots. Rectangle shapes drawn around each protein band of interest were used to calculate the signal intensities following subtraction of background values from blot regions close by (Figure 3.5). On each western blot, the tubulin bands were also quantified using the same principle. The ratio of each specific signal to tubulin signal intensities was used to calculate relative protein amounts of proteins of interest. The mean value derived from individual signal intensities of four WT samples on each blot was set to 100% and used as reference for normalization for each sample value on the same blot.

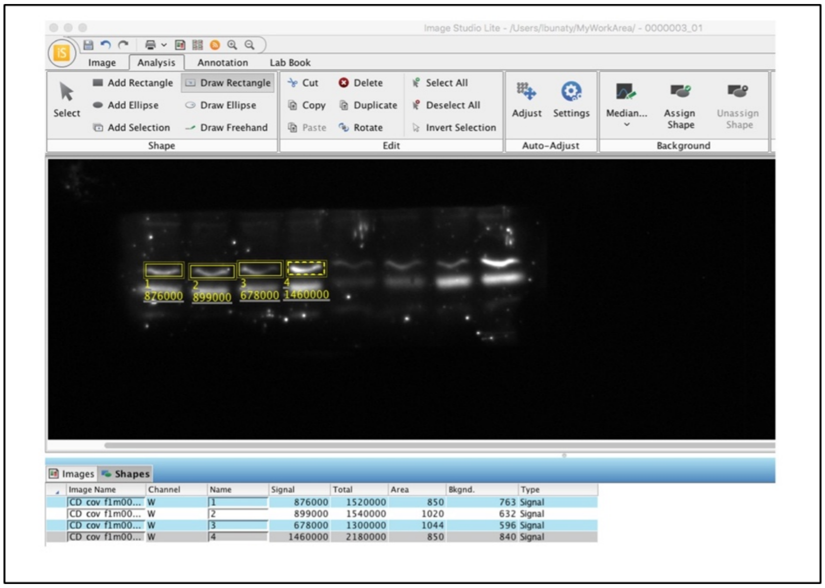

	Image Name	Channel	Name	Signal	Total	Area	Bkgnd.	Type
	CD cov f1m00...	W	1	876000	1520000	850	763	Signal
	CD cov f1m00...	W	2	899000	1540000	1020	632	Signal
	CD cov f1m00...	W	3	678000	1300000	1044	596	Signal
	CD cov f1m00...	W	4	1460000	2180000	850	840	Signal

Figure 3.5: Quantification of signal intensity levels for protein bands in western blot analyses.

Intensities of protein bands on western blots were quantified using the Image Studio Lite software. Signal intensities were quantified in the region of interest (selected by a yellow square). Around each manually selected area, the background intensities were quantified by the software using the shown settings.

3.8.4 Co-localization analysis

To determine co-localization of immunosignals from two proteins on the same image, the overlap of signals from two respective color channels was calculated using Fiji software. In detail, images from both channels were opened and set to 8-bit format (Figure 3.6 B). The cell surface perimeter of the cells was marked as ROI on images where the protein of interest was visualized by green fluorescence signal (Figure 3.6A). Then, the co-localization plugin of the software calculated the overlap of the signal in the first channel with that of the signal in the second channel in the ROI. The Manders´ co-localization coefficient TM1 values, describing the extent of co-localization, were taken for further quantification. From each image, three individual regions were used for quantification of TM1 values.

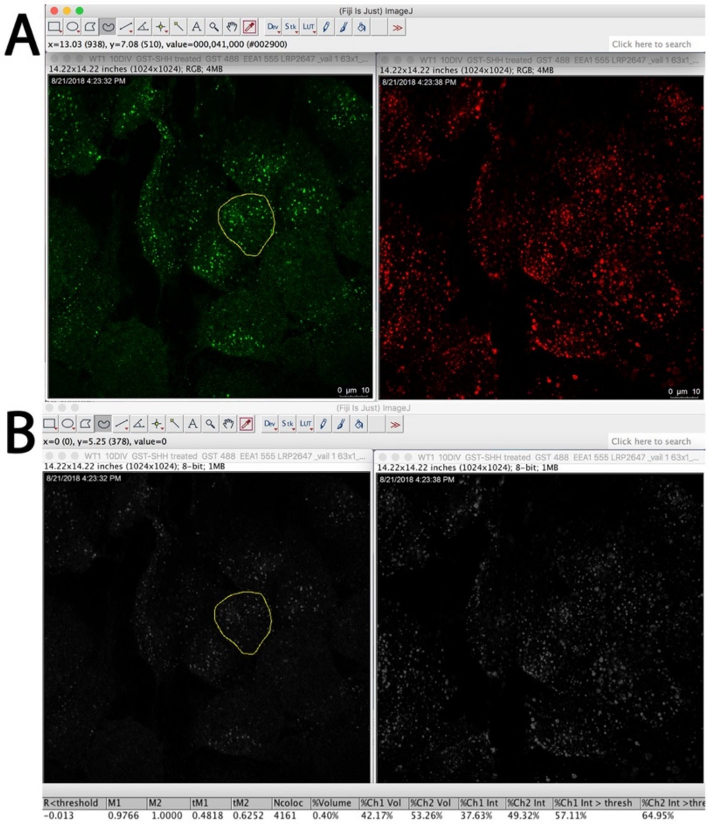

R<threshold	M1	M2	tM1	tM2	Ncoloc	%Volume	%Ch1 Vol	%Ch2 Vol	%Ch1 Int	%Ch2 Int	%Ch1 Int > thresh	%Ch2 Int >thre
-0.013	0.9766	1.0000	0.4818	0.6252	4161	0.40%	42.17%	53.26%	37.63%	49.32%	57.11%	64.95%

Figure 3.6: Co-localization analysis performed in Fiji software.

(A) Representative pictures of individual green and red channels from the same double colored image are presented. The area of interest is selected on the green channel image. (**B**)Both images were set to 8-bit format. The co-localization macro in Fiji software was used to calculate the overlap coefficient of green signals with red in the selected area. For further analysis, the overlap coefficient described by the Mander's threshold (TM1) was considered.

3.8.5 Quantification of ciliary patch organization in ependymal cells of lateral ventricular walls

To visualize and quantify cilia beating parameters in post-fixed ependymal cells of the mouse ventricular region, en face preparations of this tissue were immunostained for γ-tubulin, FOP and ZO1 as described above. The Biotool software developed by Paul Labedan and Camille Boutin (Labedan et al., 2016) was used for further analyses (Figure 3.7A-D). As a first parameter, the coordination of patch displacement was analyzed. To do so, the select tool in the software was applied to trace the contours of individual ependymal cells (blue) and their respective ciliary patches (red) (Figure 3.7A). The software calculated the geometric centers of the marked areas and defined two vectors for each cell, one that described the basal body (BB) patch displacement relative to the

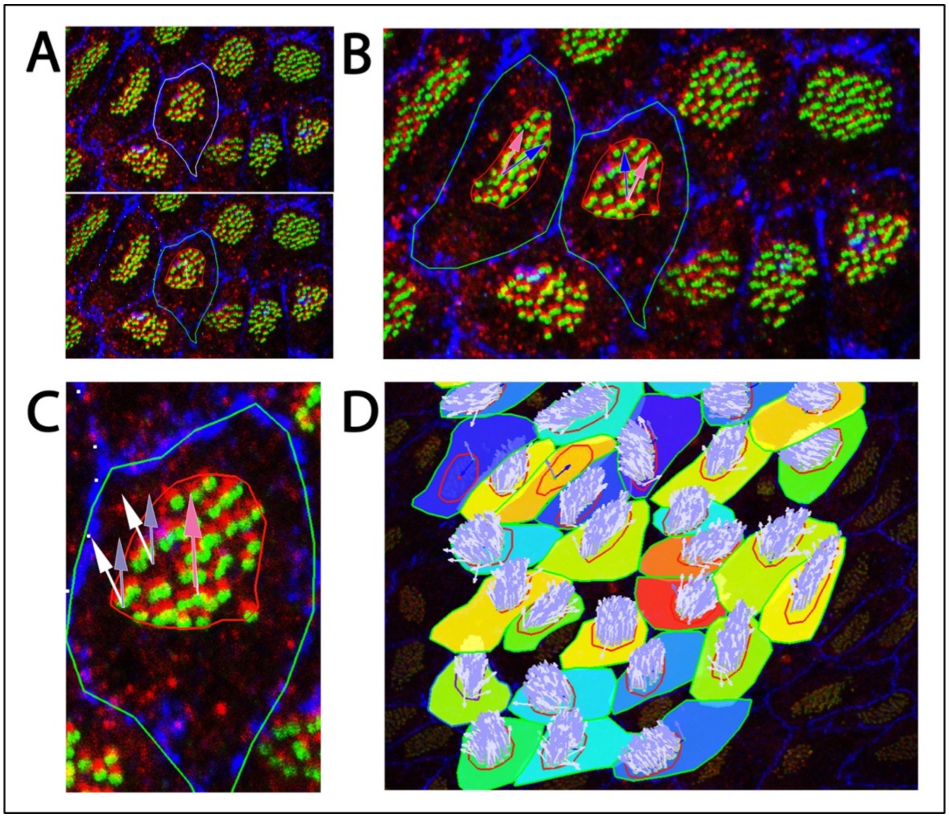

Figure 3.7: Quantitative analyses of ciliary patch organization and activity by the Biotool software.

Exemplary images of en face preparations of the lateral ventricular wall in LRP2-deficient mouse brains immunostained for ciliary basal body markers FOP; green, γ-Tub, red as well as for the apical cell surface marker ZO1; blue, opened on biotool software are depicted. (**A**) Using the select tool, perimeters of ciliary patch (red line) and ependymal cells (white line) are defined. (**B**) Next, the software generates two vectors, indicating the direction of ciliary patch displacement relative to center (blue) and one indicating the patch displacement mean vector (pink). An algorithm in Biotool calculates the angle made by these 2 vectors for each cell. (**C**) Afterwards, unit vectors (vCil) in one ciliary patch connecting immunosignals for FOP and γ-tubulin (green to red) in each individual cilium are drawn in Biotool (white). For each patch, mean resultant vector based on vCils is generated by the software (purple). (**D**) Color code representation, indicating the divergence of patch displacements in a field of ependymal cells. Colors towards more blue color spectrum indicate high variability in patch displacement values and directions within a field.

center of each cell (blue), and one (pink), describing the mean vector of displacement in the entire microscopic field (Figure 3.7 B). The angle made by those two vectors for each cell was defined as vPatchD. This parameter reflected the direction of patch displacement in a tissue.

When the patch displacement value of individual ependymal cells diverged from that of the microscopy field, the software assigned a color in the green to blue color spectrum to this cell (Figure 3.7D).

To describe the beating orientation of a motile cilia patch, the angle vPatchO parameter was introduced. This parameter is the angle between two vectors, namely the vector (white) connecting immunosignals for FOP and γ-tubulin (green to red) in individual cilia of a patch and the mean vector of all vectors (purple) in the analyzed field (Figure 3.7 C). The angle vPatchO parameter was used to evaluate the coordination of cilia orientation between all cells in a field. The angle between vPatchD and vPatchO vectors (vPatchD&vPatchO) were also quantified by the software to query the coordination of patch beating orientation with patch displacement from the cell center. Each individual cilium beating coordination within a cell was characterized by vCil vectors and used to calculate the circular standard deviation (CSD) value for each cell. A higher CSD value indicates a more non-coordinated beating of individual cilia within a cell. To describe the percentage of the apical cell surface occupied by a BB patch, the area percentile value was quantified by dividing the patch area by the cell surface area for each cell. The extent of patch displacement relative to center of the cell (strength) was determined by an algorithm in Biotool software. Counts of cilia numbers in individual patches were also generated by Biotool.

3.8.6 Statistical Analyses

For statistics, two-tailed Student's *t* test was applied using Graph Pad Prism 10. All data were presented as standard error of mean (SEM).

For circular variables (such as angles) circular statistical analysis were applied. In the course of our experimental setup, controls and LRP2-deficient genotypes were compared using the Watson's U2 test in the circular statistics software program Oriana. Difference in data were considered significant with $p<0.05$.

3.8.7 Bright field

For acquisition of the non-fluorescent images, the bright field Leica DMI6000B inverted microscope were used. To image entire SVZ or SGZ areas in BrdU-stained sections, the stitching tool was applied to combine individual images of the ROI.

3.8.8 Laser scanning confocal microscopy

The Leica SPE confocal microscope at the MDC imaging core facility (head: Anje Sporbert) was used to acquire high-resolution multicolor optical images from immunofluorescent images. All multicolor pictures were taken in sequential scanning mode to avoid bleed through of signals. For some markers, serial stack images covering the entire depth of the specimen were taken. Using the maximum projection tool in the Leica software, optical series were merged in one picture. For each staining protocol, parameters for image acquisition, such as speed, resolution, pinhole, line average, detector gain, offset and other parameters were set to optimal values and kept unchanged when acquiring comparative images from different genotype groups.

4 Results

4.1 Role of LRP2 in establishment of the signaling milieu in the adult mouse subventricular zone

As a core member of the LDL receptor gene family, LRP2 shares several functional and structural similarities with other receptors of this gene family, such as LRP1, the very-low-density lipoprotein receptor (VLDLR), the ApoE receptor 2 (LRP8), as well as LRP4 , and LRP1b (Joachim Herz, 2001)(Howell & Herz, 2001). These evolutionary conserved receptors engage in uptake of multiple ligands, not restricted to cholesterol homeostasis, but encompassing numerous other cellular processes. With relevance to my studies, members of this gene family are implicated in signaling by various morphogens, including SHH (Christ et al., 2012), WNTs (He, Semenov, Tamai, & Zeng, 2004; Pinson, Brennan, Monkley, Avery, & Skarnes, 2000), or BMPs (Derwall et al., 2012; Spoelgen et al., 2005, p. 2). Consequently, loss of receptor activities cause defects in morphogen activities during embryonic development and results in severe congenital malformations in animal models and patients (Thomas E. Willnow, Hammes, & Eaton, 2007). Specifically, earlier studies in LRP2-deficient mice identified malformations of the developing forebrain resulting in a phenotype reminiscent of holoprosencephaly (T. E. Willnow et al., 1996). These earlier observations lead the ground work for later identifying the role of LRP2 as SHH receptor in signaling of this morphogen during forebrain patterning (Christ et al., 2012).

In the adult brain, LRP2 expression persists in ependymal cells, the epithelia lining the walls of lateral ventricles. This so-called ventricular zone (VZ) is in close proximity to the subventricular zone (SVZ), the brain region with a unique capacity to act as a stem cell niche for generating new neurons in the adult mammalian brain (adult neurogenesis). The relevance of LRP2 activity for adult neurogenesis in the SVZ niche was substantiated by recent work demonstrating reduced neurogenic activity in the SVZ of receptor mutant mice (Gajera et al., 2010, p. 2). Loss of neurogenesis in LRP2 mutant mice had been correlated with increased BMP signaling in the SVZ (Gajera et al., 2010). However, it remained unclear whether hyperactivity of BMP was the primary cause or rather a secondary consequence of altered SHH signaling in this niche. Also, previous studies had focused on a global role of the receptor LRP2 in adult neurogenesis in the SVZ ignoring the obvious heterogeneity in structural and functional organization of this niche in the brain (Gajera et al., 2010). To address these questions, my thesis work now focused on elucidation of receptor functions in SHH signaling in a region-specific manner in this stem cell compartment of the adult mammalian brain.

4.1.1 Region-specific analysis of SHH signaling in the SVZ of adult wildtype and LRP2 mutant mice

4.1.1.1 Examination of expression of *Gli1*, a downstream target of SHH signaling in the SVZ

Adult LRP2-deficient mouse models manifest features of HPE, including craniofacial dysmorphology associated with a shortened snout and an open fontanelle. Also, histological analyses revealed an enlarged lumen of the lateral ventricular system, albeit with no discernible structural alterations in VZ and SVZ composition comparing mutant animals with littermate controls(Gajera et al., 2010). Also, histoanatomical investigations demonstrated an unchanged layering of the brain cortex and the olfactory bulbs, as well as no differences in hippocampal organization comparing mutant to control mice (Gajera et al., 2010). Based on these observations, LRP2 mutant mice were considered an adequate model to study the role ofLRP2 in the adult brain, specifically in SHH signaling in VZ and SVZ.

To explore the consequences of LRP2 deficiency for SHH signaling in the SVZ, mice heterozygous for the mutant *Lrp2* allele were crossed with the *Gli1_lacZ* reporter strain (see method sections for details). Expression of *lacZ* driven by the endogenous *Gli1* promoter enables testing the activity of the SHH signaling pathway by investigating activity of the *lacZ* gene product β-galactosidase. Breeding of mice positive for the *Gli1_lacZ* transgene and heterozygous for the *Lrp2* null allele generated *Gli1_lacZ* transgenic offspring either *Lrp2*$^{+/+}$, *Lrp2*$^{+/-}$, *or Lrp2*$^{-/-}$. As for this and all subsequent studies in this thesis, *Lrp2*$^{+/+}$ and *Lrp2*$^{+/-}$ animals were considered as control animals and were jointly compared to *Lrp2*$^{-/-}$ receptor mutant mice.

To evaluate the regionality of SHH activity in control and receptor mutant mice, analysis of *lacZ* activity in the SVZ was performed separately in rostral and caudal regions of the mouse brains. In addition, *lacZ* activity was always scored in the dorsal versus the ventral SVZ domain. As shown in Figure 4.1, in the rostral region of the control brain, *Gli1* expression was strongest in the ventral but gradually decreased towards the dorsal domain of the SVZ. Compared with controls, the SVZ of *Lrp2*$^{-/-}$ mice displayed a prominent decrease in *lacZ* activity, both in ventral and dorsal domains, suggesting loss of SHH activity in this region of the mutant SVZ niche.

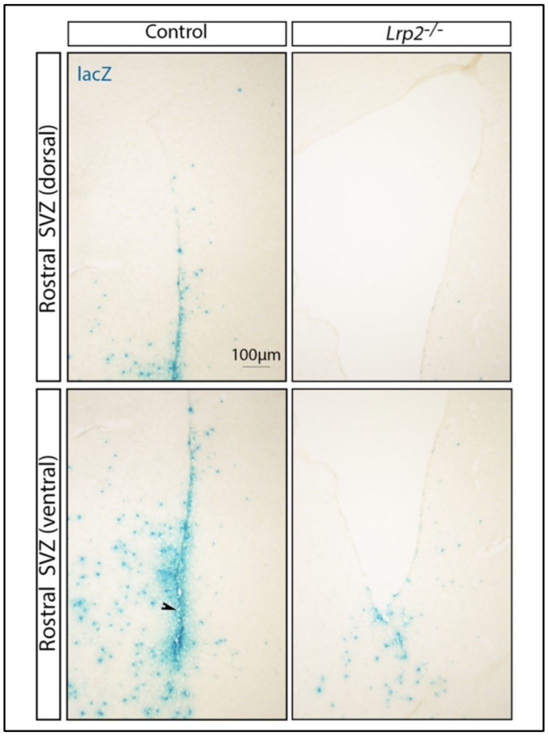

Figure 4.1: Decreased SHH signaling in the SVZ of LRP2-deficient mice.

Overview of *Gli1* expression pattern along the subventricular zone (SVZ) in adult LRP2-deficient mice and littermate controls crossed with the *Gli1_lacZ* reporter strain. X-gal staining was performed on 10 µm thick coronal brain sections to visualize the *Gli1* expression pattern. Exemplary images of a total of three sections from the rostral region of each mouse brain are shown. For each section, the dorsal and the ventral SVZ regions are depicted separately. A total of five animals per genotype were analyzed. In controls (*Lrp2*$^{+/+}$ and *Lrp2*$^{+/-}$), *Gli1* shows the strongest expression in the ventral domain of the SVZ (highlighted by an arrowhead), while the signal gradually decreases towards the dorsal SVZ region. In LRP2-deficient tissue, *Gli1* expression as deduced from the X-gal signal is decreased in both SVZ regions.

As for the caudal brain region, *lacZ* activity was decreased in the SVZ of control mice, both in the dorsal and the ventral domain (Figure 4.2).

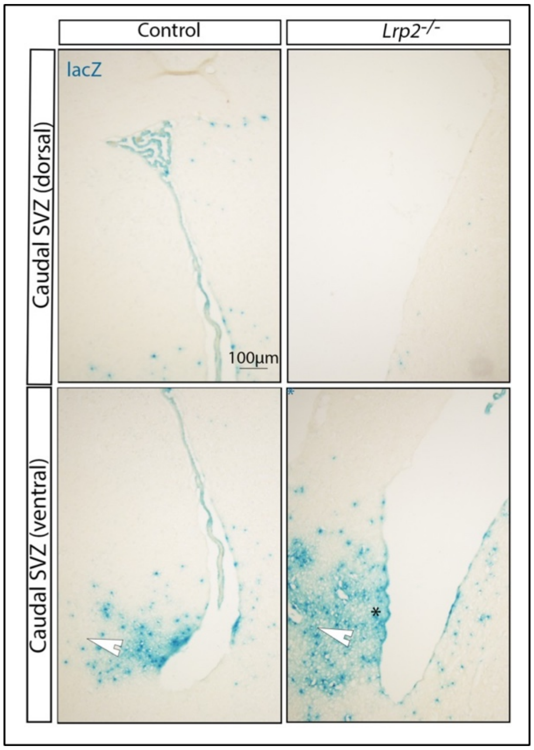

Figure 4.2: SHH signaling is retained in the caudal SVZ of LRP2-deficient mice.

Gli1 expression levels were examined in the caudal region of the SVZ in LRP2-deficient mice and littermate controls crossed with the *Gli1_lacZ* reporter strain. X-gal staining was performed on 10 µm thick coronal brain sections to visualize the *Gli1* expression pattern. Exemplary images of a total of three sections from the caudal region of individual mouse brains were analyzed (five animals per genotype). For each section, dorsal and ventral SVZ regions are depicted separately. In ventral and dorsal SVZ regions, *Gli1* expression levels are similar comparing both genotypes. In the ventral medial wall of the LRP2-deficient SVZ (indicated by an asterisk), the *Gli1* expression domain is more intense and spreads towards the medial septum area (highlighted by white arrowheads).

Levels of *Gli1* expression were also examined more directly by *in situ* hybridization (ISH) in rostral and caudal regions of the SVZ.

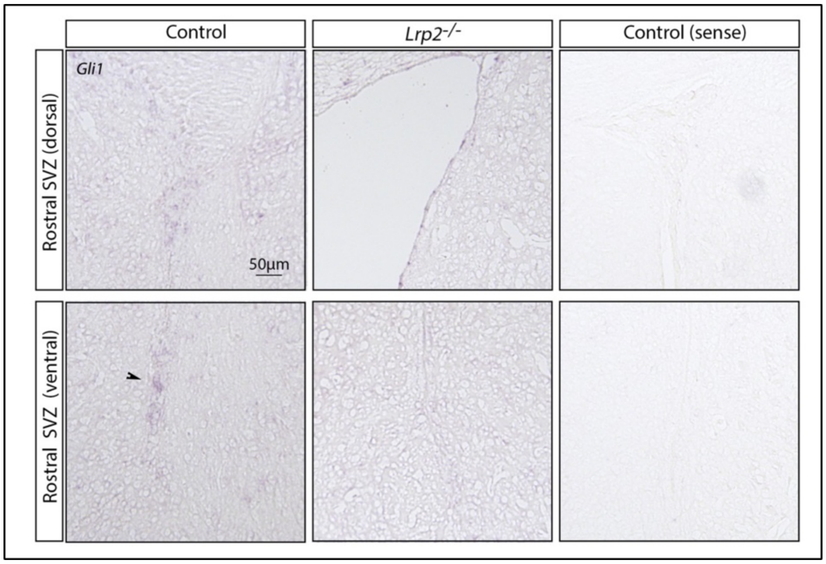

Figure 4.3: Reduced level of ventral *Gli1* expression in the rostral SVZ of LRP2-deficient mice as shown by *in situ* hybridization.

In situ hybridization (ISH) analysis on 10 µm thick coronal brain sections demonstrates distribution of *Gli1* transcripts along the rostral SVZ in adult *Lrp2*$^{-/-}$ and control mice (*Lrp2*$^{+/+}$ and *Lrp2*$^{+/-}$). Dorsal and ventral regions of each brain section are shown separately. To control for unspecific ISH signals, histological sections from control mice were alternatively incubated with the *Gli1* sense probe. In antisense treated samples, *Gli1* expression levels are pronounced in the ventral SVZ region from control mice (highlighted by arrowhead). In mice lacking LRP2, *Gli1* mRNA levels are notably decreased in the ventral but unchanged in the dorsal SVZ region. Exemplary images of three sections from each brain (four animals per genotype) are shown.

In line with findings using *lacZ*, *Gli1* RNA levels were reduced in the rostral SVZ area of LRP2 deficient mice compared with littermate controls (Figure 4.3).

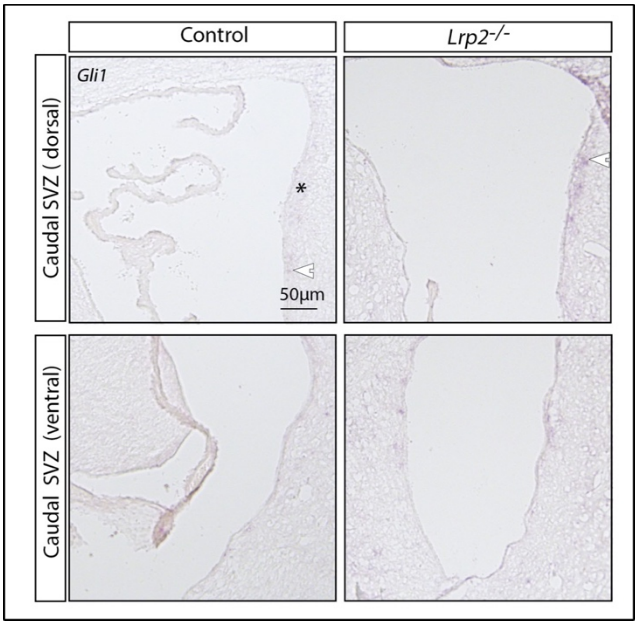

Figure 4.4: *In situ* hybridization analysis of *Gli1* expression in the caudal SVZ.

ISH on coronal brain sections documents similar levels of *Gli1* transcripts in the ventral caudal regions of the SVZ in control (*Lrp2*$^{+/+}$ and *Lrp2*$^{+/-}$) and *Lrp2*$^{-/-}$ mice (ISH signals marked by arrowheads). By contrast, *Gli1* signals in the lateral wall of the dorsal caudal SVZ (marked by asterisk) are increased in *Lrp2*$^{-/-}$ as compared to control brains. Exemplary images of a total of three sections from each brain (four animals per genotype) are shown.

Of note, no changes in *Gli1* ISH signals were observed in the caudal SVZ of mutant mice, contrasting the data from the *Gli1_lacZ* reporter experiments, where activity in the mutant caudal domain was up (Figure 4.4).

4.1.2 Detection of components of the SHH receptorsome in the SVZ

My observations were in line with the previous findings, documenting the strongest *Gli1* expression in the ventral SVZ region in of adult mice (Ihrie et al., 2011). However, the detailed examination of *Gli1* expression and activity on coronal brain sections of mutant mice uncovered a differential impact of LRP2 deficiency on this signaling domain in rostral versus caudal brain regions. To get a better understanding of the regional specification of SHH signaling along the rostro-caudal axis of the SVZ, I have investigated the regional distribution of various members of the so-called SHH receptorsome in the SVZ of adult mice.

Using ISH analyses, I documented that the distribution of *Smo* transcripts in ventral and dorsal regions of the rostral SVZ were unchanged between genotypes (Figure 4.5).

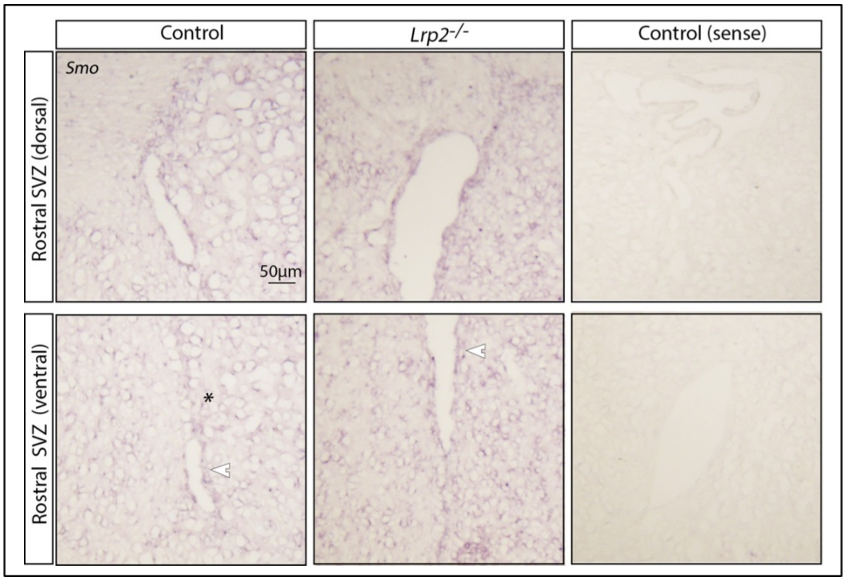

Figure 4.5: Levels of *Smo* expression are unchanged in the rostral SVZ of LRP2-deficient mice.

ISH analysis on 10 µm thick coronal brain sections was performed to show *Smoothened* (*Smo)* mRNA distribution along the rostral SVZ in adult *Lrp2*$^{-/-}$ and control mice (*Lrp2*$^{+/+}$ and *Lrp2*$^{+/-}$). Dorsal and ventral regions for each section are shown separately. To monitor for unspecific ISH signals, histological sections from control mice were alternatively incubated with the sense RNA probe (sense). Along the rostral SVZ (lateral wall marked by an asterisk), *Smo* transcripts are detected (highlighted by white arrowheads) with no apparent differences in intensities comparing *Lrp2* genotypes. Exemplary images of three sections from each brain (four animals per genotype) are shown.

Also, examinations of the caudal SVZ failed to reveal any apparent changes in *Smo* ISH in the SVZ of *Lrp2*$^{-/-}$ as compared with control mice (Figure 4.6).

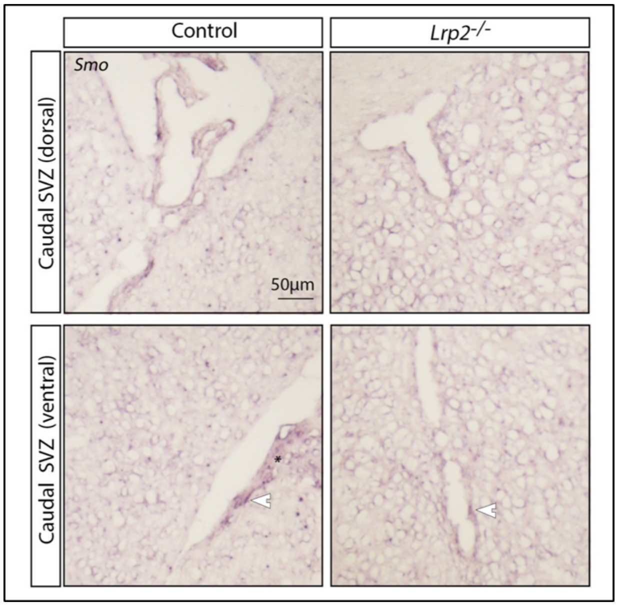

Figure 4.6: Levels of *Smo* expression are unchanged in the caudal SVZ of LRP2-deficient mice.

ISH for *Smo* on coronal sections of the caudal SVZ in adult *Lrp2*$^{-/-}$ and control mice (*Lrp2*$^{+/+}$ and *Lrp2*$^{+/-}$). Dorsal and ventral regions of each section are depicted separately. *Smo* mRNA levels (white arrowheads) show an equal spread in all regions of the SVZ comparing both genotypes. Exemplary images of three sections from each brain (four mice per genotype group) are shown.

Concerning expression of *Ptch1*, ISH signal intensity levels were also similar in medial and lateral walls of the rostral SVZ in both genotypes (Figure 4.7).

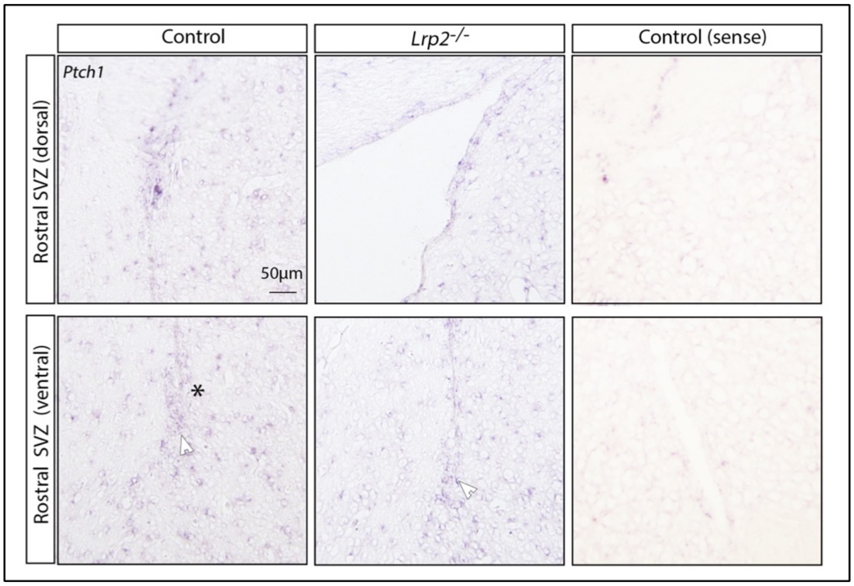

Figure 4.7: *Ptch1* expression in the rostral SVZ.

ISH analysis of *Protein patched homolog 1* (*Ptch1*) transcript levels on 10 µm thick coronal brain sections of the rostral SVZ in adult *Lrp2*$^{-/-}$ and control mice (*Lrp2*$^{+/+}$ and *Lrp2*$^{+/-}$). Dorsal and ventral regions for each section are shown separately. To monitor unspecific ISH signals, histological sections from control mice were alternatively incubated with the sense probe (sense). In antisense treated samples, *Ptch1* expression levels (white arrowheads) are robust in both lateral (and medial walls of SVZ regions from *Lrp2*$^{-/-}$ and control mice. Exemplary images of three sections from each brain (four animals per genotype) are shown.

By contrast, *Ptch1* transcript levels in the caudal SVZ were generally low as compared to the rostral SVZ, but distinctly increased in the mutant brain. This effect was particularly obvious in the dorsal domain (Figure 4.8).

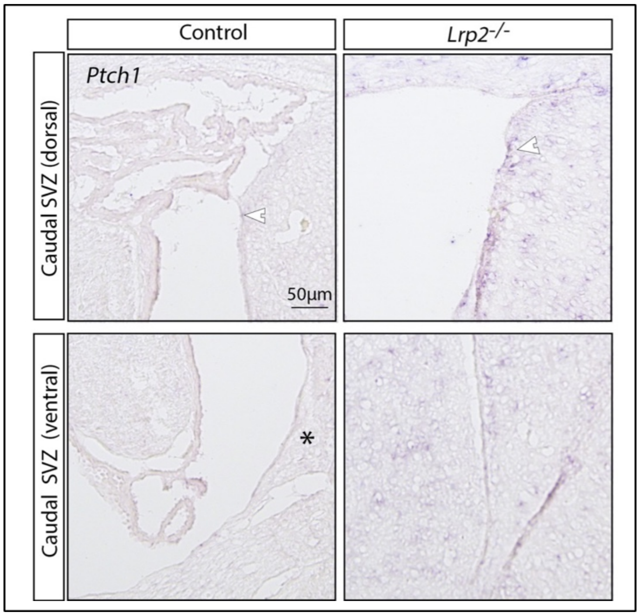

Figure 4.8: *Ptch1* transcript levels are increased in the caudal SVZ of *Lrp2*$^{-/-}$ animals.

ISH analysis of Protein *patched homolog 1* (*Ptch1*) mRNA distribution along the caudal SVZ on 10 µm thick coronal brain sections from adult *Lrp2*$^{-/-}$ and control mice (*Lrp2*$^{+/+}$ and *Lrp2*$^{+/-}$). Dorsal and ventral regions for each section are shown separately. Exemplary images of three sections from each brain (four animals per genotype) are shown. *Ptch1* mRNA signals (marked by arrowheads) are elevated in the lateral wall of SVZ (asterisk) in *Lrp2*$^{-/-}$ mice compared with littermate controls.

Cdon showed a relatively strong level of expression in both genotypes in the entire rostral SVZ with levels unchanged in LRP2 mutants compared with littermate controls (Figure 4.9).

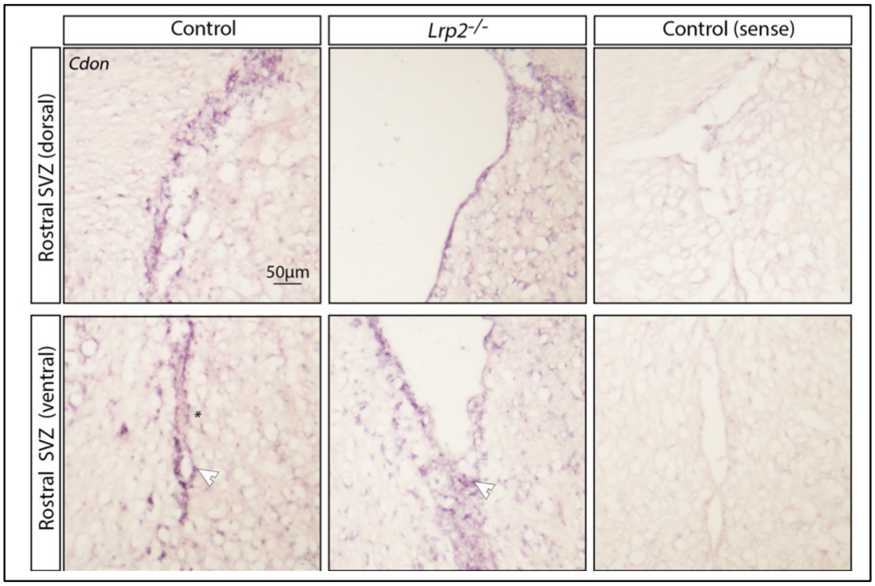

Figure 4.9: *Cdon* expression in the rostral SVZ region.

ISH analysis of *Cdon* transcript levels on 10 µm thick coronal sections of the rostral SVZ of adult *Lrp2*$^{-/-}$ and control mice. Dorsal and ventral SVZ regions for each brain are shown separately. To monitor unspecific binding of ISH probes, histological sections form control mice were alternatively incubated with the sense *Cdon* probe (sense). In antisense treated samples, *Cdon* expression levels (highlighted by arrowheads) are robust in both lateral and medial walls of SVZ region from *Lrp2*$^{-/-}$ and control mice. Exemplary images of a total of three sections from each brain (four animals per genotype) are shown.

In the caudal SVZ, *Cdon* signals were reduced as compared to the rostral SVZ, with a slight increase of *Cdon* expression in the ventral, caudal SVZ (Figure 4.10).

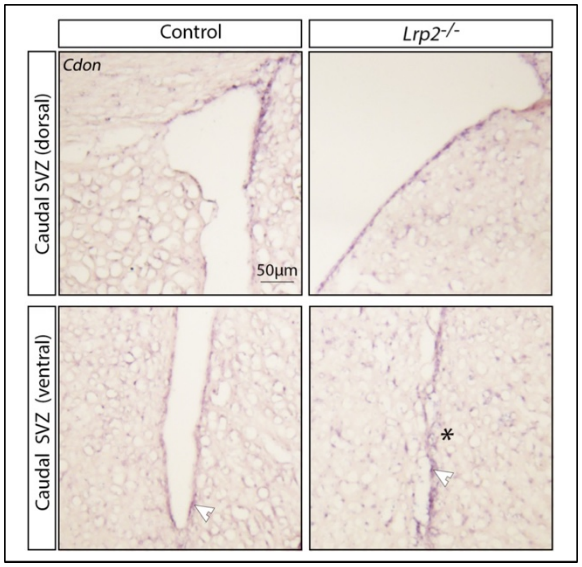

Figure 4.10: *Cdon* expression in the caudal SVZ region.

ISH analysis of *Cdon* transcript levels on 10 µm thick coronal sections of the caudal SVZ of adult *Lrp2*$^{-/-}$ and control mice. Levels of *Cdon* transcripts are similar in control and *Lrp2*$^{-/-}$ mice (ISH signals marked by arrowheads). Slightly increased *Cdon* signals are noticeable in the lateral wall (asterisk) of the ventral caudal SVZ of *Lrp2*$^{-/-}$ mice as compared to control brains. Exemplary images of a total of three sections from each brain (four animals per genotype) are shown.

Assessment of *Boc* transcript levels by ISH was technically more difficult because of the low abundance in SVZ regions.

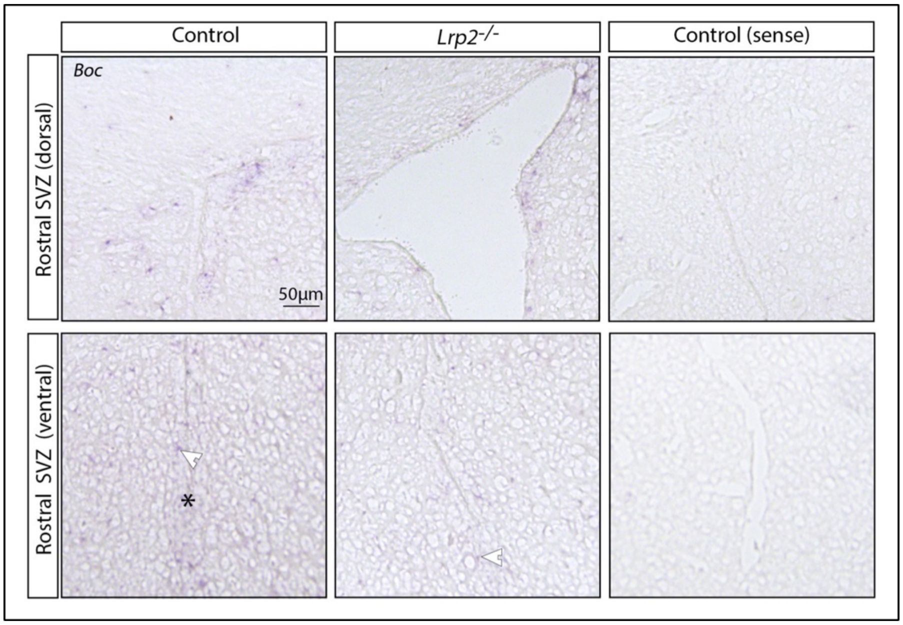

Figure 4.11: Levels of *Boc* transcripts are moderately decreased in the LRP2-deficient SVZ.

ISH analysis of *Brother of Cdon* (*Boc*) transcripts was performed on 10 µm thick coronal brain sections of the rostral SVZ in adult *Lrp2*$^{-/-}$ and control mice (*Lrp2*$^{+/+}$ and *Lrp2*$^{+/-}$). Dorsal and ventral regions for each section are shown separately. To monitor unspecific ISH signals, histological sections from control mice were alternatively incubated with the sense *Boc* probe (sense). In antisense treated samples, *Boc* expression levels (white arrowheads) are decreased in the ventral tip of the lateral (astrisk) and medial walls of *Lrp2*$^{-/-}$ mice as compared to controls. Dorsal lateral walls in both genotypes retain similar *Boc* expression levels. Exemplary images of a total of three sections from each brain (four animals per genotype) are shown.

Based on the data shown in here, *Boc* seemed to have moderately decreased transcript levels in rostral SVZ regions of LRP2-deficient animals (Figure 4.11), while signal intensities in the caudal SVZ seemed comparable in both *Lrp2* genotypes (Figure 4.12).

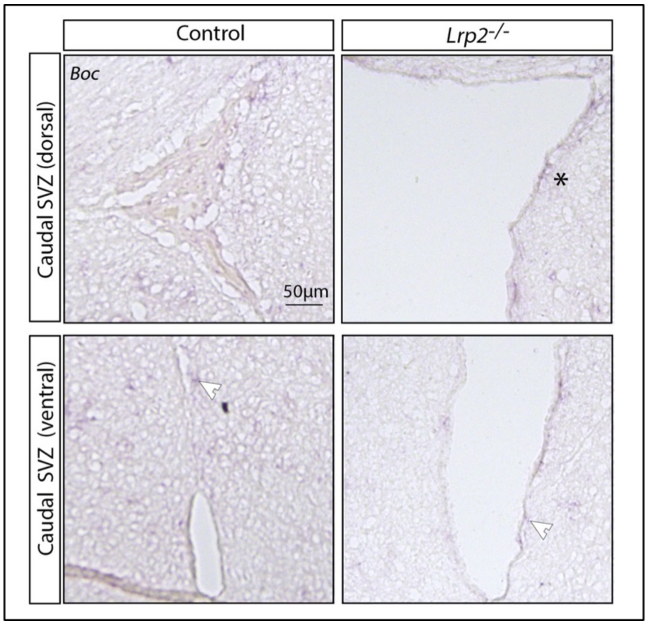

Figure 4.12: *Boc* transcript levels are unaltered in the caudal SVZ of LRP2-deficient mice.

ISH analysis of *Boc* transcripts (white arrowhead) was performed on 10 µm thick coronal sections of the caudal SVZ of *Lrp2*$^{-/-}$ mice as compared to control (*Lrp2*$^{+/+}$ and *Lrp2*$^{+/-}$) animals. The lateral wall is highlighted by an asterisk. Slightly increased signal intensity can be noticed on the lateral wall of the dorsal caudal *Lrp2*$^{-/-}$ SVZ (highlighted by an asterisk). Exemplary images of a total of three sections from each brain (four animals per genotype) are shown.

In summary, examination of rostral and caudal regions of SVZ revealed no apparent changes in expression levels of SHH signaling upstream components in LRP2 mutants compared with littermate controls. Variability in receptor expression patterns along the rostro-caudal axis of the SVZ between both genotypes, did not explain the regional specific impact of LRP2 on *Gli1* expression levels.

4.1.2.1 Distribution of SHH in rostral and caudal SVZ regions of the adult mouse brain

As a next step to explore the SHH signaling activity along the rostral to caudal axis of the adult SVZ, I assayed the distribution of this morphogen in four different areas of the control and *Lrp2*$^{-/-}$ SVZ, namely in the rostral dorsal (RD), the rostral ventral (RV), the caudal dorsal (CD), and the caudal ventral (CV) areas.

The primary translation product of mouse *Shh* is a polypeptide chain consisting of 437 amino acids and a predicted molecular mass of 47.8 kDa. Removal of the hydrophobic signaling peptide, consisting of 25 amino acid residues, results in SHH full length (SHH-FL) protein with a molecular mass of 45kDa (Bumcrot et al., 1995) (Roelink et al., 1995). Autoproteolytic activity of the carboxyl terminus cleaves SHH-FL into an amino terminal and a carboxyl terminal fragment, designated SHH-N and SHH-C, respectively. SHH-C is degraded after cleavage in the ER (X. Chen et al., 2011)~~,~~ while SHH-N is covalently modified with a cholesterol moiety at the carboxyl terminus. Thereafter, SHH-N is covalently modified with palmitate, resulting in the dual lipidated active form of the morphogen called SHH-Np. SHH-Np tends to attach to the cell membrane, resulting in formation of multimeric aggregates which are eventually released from the cell to act as paracrine signaling molecules (Bumcrot et al., 1995).

Using western blot analysis, I quantified the levels of SHH-FL and SHH-Np in the four dissected domains of the adult SVZ. As shown in figure 4.13, for micro-dissected samples from the dorsal (Figure 4.13 A) and ventral (Figure 4.13 B) regions of the rostral SVZ no obvious differences were observed in levels of SHH-FL both in the dorsal (Figure 4.13 C) and ventral (Figure 4.13D) SVZ regions comparing control with LRP2 mutant mice. Similarly, no statistically significant difference in levels of SHH-Np were detected in the rostral dorsal and rostral ventral domain of SVZ (Figure 4.13 B, E, F).

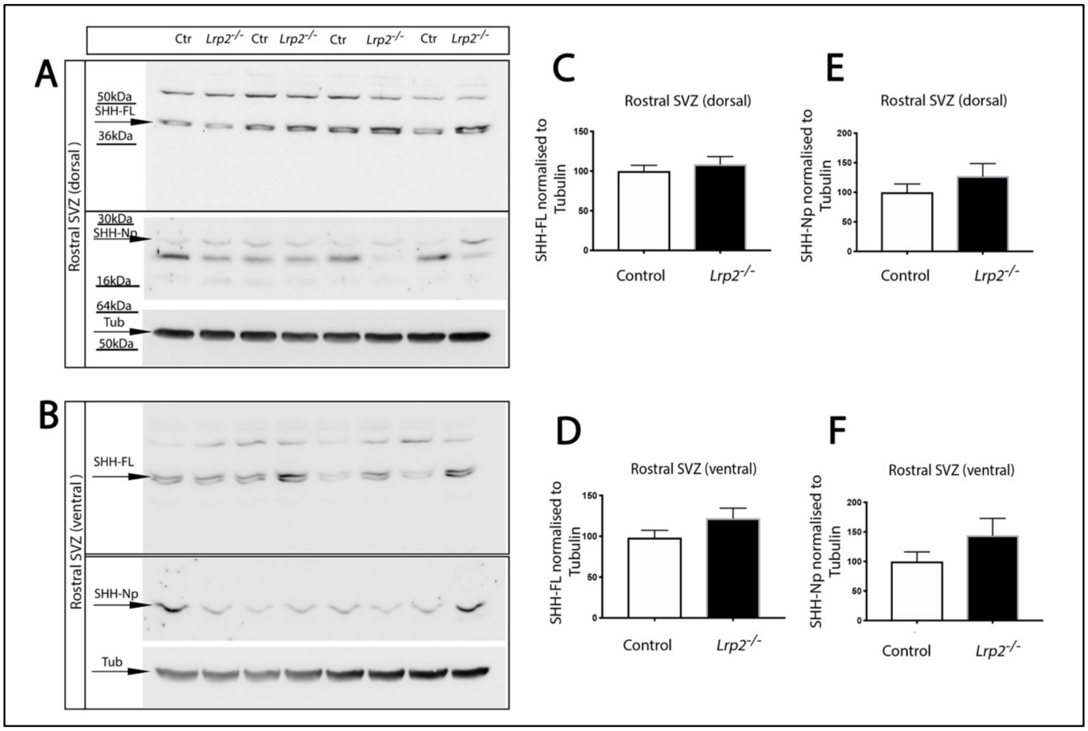

Figure 4.13: Levels of full length and active forms of SHH in the rostral SVZ region.

(**A, B**) Western blot analysis of full-length (SHH-FL) and amino terminal fragment (SHH-Np) of SHH was performed on dissected regions of the dorsal (A) and ventral (B) domains of the rostral SVZ of four LRP2-deficient mice and four littermate controls (*Lrp2*$^{+/+}$ and *Lrp2*$^{+/-}$). Immunoreactive bands representing SHH-FL or SHH-Np are indicated. Tubulin (Tub) was detected as loading control. (**C-F**) Densitometric scanning of replicate western blots (as exemplified in panels A and B) documents identical levels of SHH-FL in dorsal **(C)** and ventral (D) regions of the rostral SVZ in LRP2-deficient mice and littermate controls. Similarly, levels of SHH-Np are unchanged in the dorsal (E) and ventral (F) SVZ comparing genotypes. A total of sixteen animals from each genotype were used for quantification of SHH levels. Unpaired Student's *t*-test was applied to test for differences between controls and *Lrp2*$^{-/-}$ mice.

By contrast, examination of the caudal area of the SVZ revealed a remarkable difference with levels SHH-Np being significantly higher despite unchanged levels of SHH-FL in LRP2-deficient mice in comparison to control animals (Figure 4.14 A-B). Quantification analysis confirmed similar levels of SHH-FL in caudal dorsal and caudal ventral regions from both genotypes (Figure 4.14 C, D). By contrast, the SHH-Np levels were two-fold higher both in the dorsal and rostral SVZ of *Lrp2*$^{-/-}$ mice compared with controls (Figure 4.14 E, F). However, this difference was only statistically significant in the dorsal SVZ region (Figure 4.14 F).

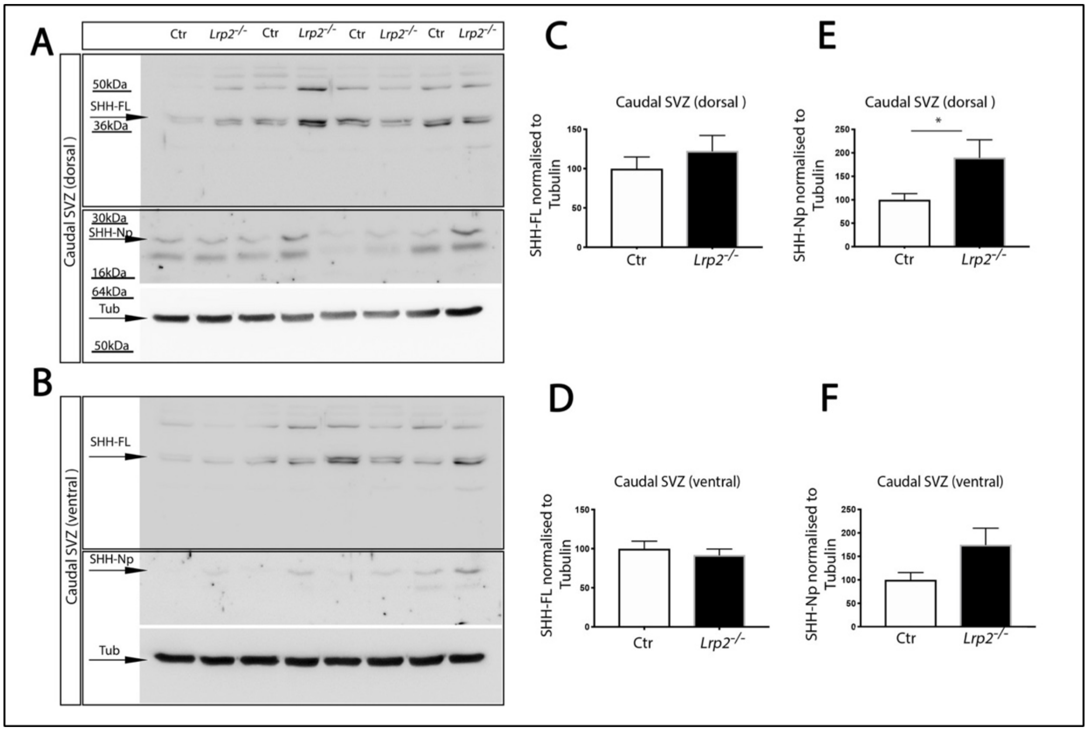

Figure 4.14: Increased levels of SHH-Np in the caudal SVZ of LRP2-deficient mice.

(**A, B**) Western blot analysis of full-length (SHH-FL) and amino terminal fragment (SHH-Np) of SHH was performed on dissected regions of the dorsal (A) and ventral (B) domains of the caudal SVZ comparing four LRP2-deficient mice and their littermate controls (*Lrp2*$^{+/+}$ and *Lrp2*$^{+/-}$). Immunoreactive bands representing SHH-FL or SHH-Np are indicated. Tubulin (Tub) was detected as loading control. (**C-F**) Densitometric scanning of replicate western blots (as exemplified in panels A and B documents unchanged levels of SHH-FL in dorsal (C) and ventral (D) regions of the caudal SVZ of LRP2-deficient mice compared with littermate controls. By contrast, levels of SHH-Np are increased in the dorsal (E) and ventral (F) SVZ domains of LRP2-deficient mice. Statistical significance of differences between controls and LRP2- deficient animals was determined by unpaired Student's *t*-test. A total of sixteen animals per genotype were used in this experiment. *, $p<0.05$

Taken together, I uncovered a significant increase in the abundance of the active form SHH-Np in the caudal SVZ region of LRP2 mutant mice. Such an increase was not seen for the intracellular precursor SHH-FL. These data argued for altered distribution of the secreted morphogen along the rostral to caudal axis in the LRP2-deficient SVZ. Accumulation of SHH-Np in the caudal SVZ coincided with a substantial increase in expression of the downstream target *Gli1* in the caudal SVZ of LRP2 mutant mice, indicating higher activity of SHH signaling in this area of the mutant brain. By contrast, a decrease in *Gli1* transcripts in the rostral region of the mutant SVZ, albeit at unchanged SHH-Np levels, argued that a SHH signaling defects in the rostral SVZ may be due to other defects than a shift in rostro-caudal SHH-Np distribution.

4.1.3 Activity of the BMP signaling pathway in the SVZ

Earlier investigations of BMP signaling during forebrain development in wildtype and LRP2-deficient embryos suggested a role for LRP2 in BMP signaling. Based on the increase in BMP activity seen in LRP2-deficient embryos, an antagonistic function, possibly as clearance receptor for BMP4, was proposed (Spoelgen et al., 2005, p. 2). A suggested function as clearance receptor for BMP4 was substantiated by subsequent investigations in adult mutant mice by documenting an increase in levels of pSMAD and ID3, downstream effectors and targets of BMP signaling in the SVZ, respectively (Gajera et al., 2010).

To investigate the region-specific consequences of LRP2 deficiency for BMP signaling in the mouse SVZ, I re-analyzed levels of ID3 in rostral and caudal SVZ regions of the mouse brain separately. Immunohistological analysis of the rostral SVZ region showed an increased density of cells immunopositive for ID3 (ID3+) in the walls of the lateral ventricles in LRP2 deficient mice (Figure 4.15 A, B). As depicted in exemplary images from the rostral SVZ region, ID3+ cells (shown by arrowheads in figure 4.15 C) were distributed in similar densities along the medial and lateral sides of the dorsal ventricular walls in control animals (Figure 4.15 A, D). However, in the ventral domain of the rostral SVZ region in LRP2 mutant mice, the number of ID3+ cells were substantially increased compared to controls (Figure 4.15 B). This difference was confirmed by statistical analysis of multiple replicate stainings, substantiating an increase in ID3+ cell counts in the entire rostral ventral SVZ region, in both sides of the walls (Figure 4.15 E, F).

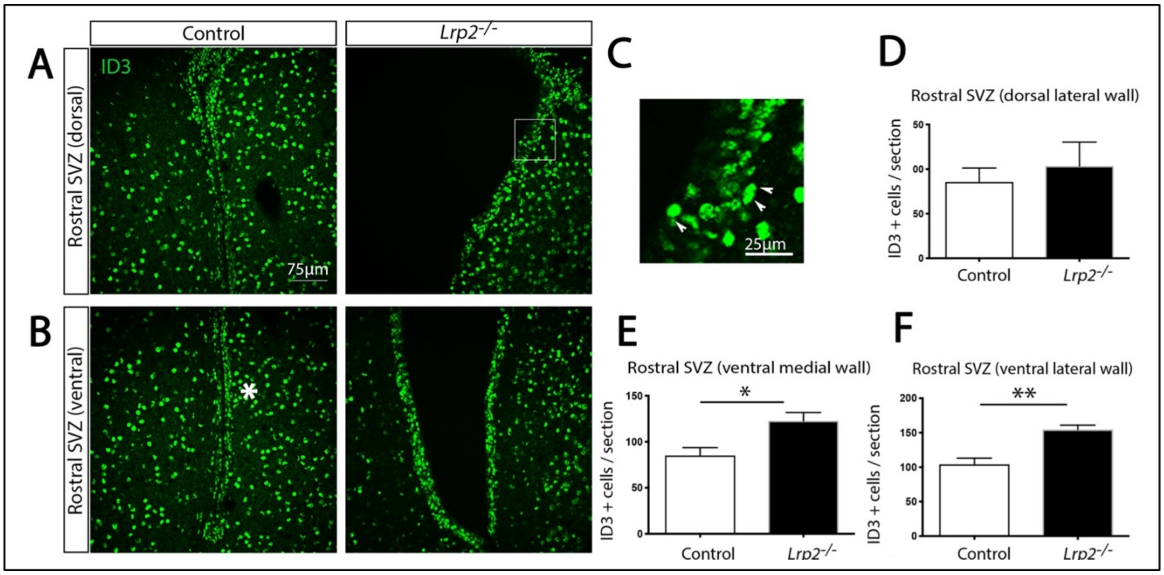

Figure 4.15: ID3 levels are increased in the rostral SVZ of LRP2-deficient mice.

(A-C) Coronal 40 µm sections of the rostral SVZ of adult mouse brains of the indicated *Lrp2* genotypes were subjected to immunohistological detection of inhibitor of DNA binding 3 (ID3). Dorsal (A) and ventral (B) domains of the rostral SVZ of each section are shown separately. In panel B, the lateral wall of the SVZ is indicated by an asterisk. A higher magnification of the boxed area in panel A is given in (C), highlighting ID3 positive cells (green signals) by arrowheads. (**D-F**) Cells positive for ID3 were quantified in the indicated regions of rostral SVZ (as exemplified in panels A and B). A total of six controls and five *Lrp2*$^{-/-}$ mice were scored. For the dorsal SVZ region (D), only cells in the lateral wall were quantified. For the ventral SVZ, cells in the medial (E) and lateral walls (F) were scored. The number of ID3 positive cells is significantly higher in medial (E) and lateral (F) walls of the rostral ventral SVZ of LRP2-deficient mice compared with controls. No significant difference in cell numbers were observed in the lateral wall of the dorsal rostral SVZ

(D) as tested by unpaired Student's *t* test. *, $p<0.05$; **, $p<0.01$

Performing the same comparative analysis in caudal regions of SVZ, I failed to detect a consistent difference in ID3+ cell numbers in the dorsal or ventral SVZ comparing *Lrp2* genotypes (Figure 4.16 A-F).

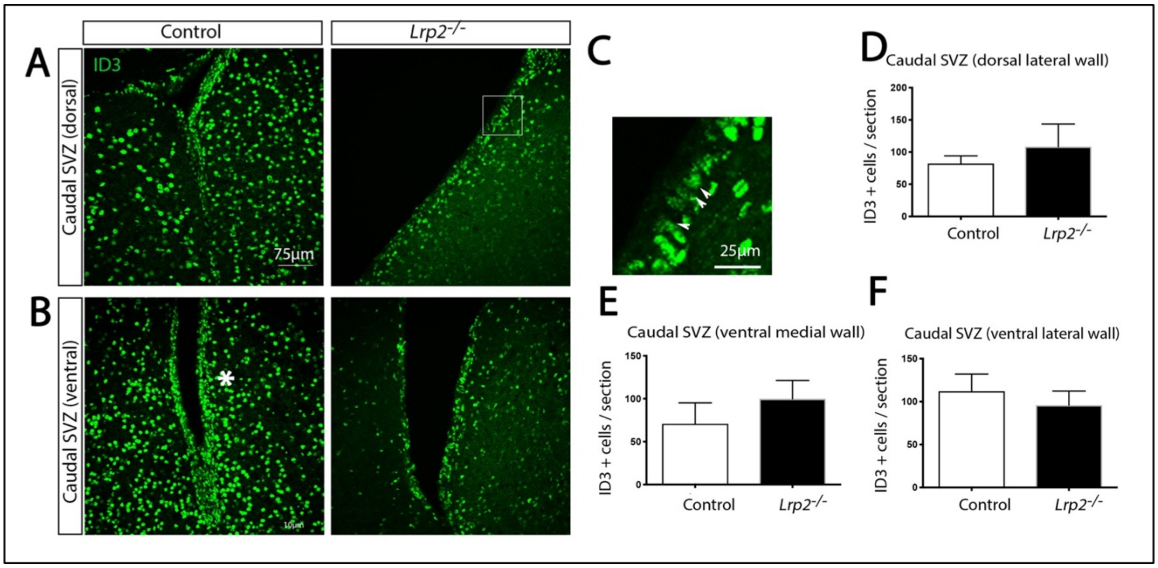

Figure 4.16: ID3 levels are unchanged in the caudal SVZ of LRP2-deficient mice.

(**A-C**) Coronal 40 µm sections of the caudal SVZ of adult mouse brains of the indicated *Lrp2* genotypes were subjected to immunohistological detection of inhibitor of DNA binding 3 (ID3). Dorsal (A) and ventral (B) domains of the caudal SVZ of each section are shown separately. The lateral wall is marked by an asterisk in panel B. A higher magnification of the boxed area in panel A is given in (C), highlighting ID3 positive cells (green signals) by arrowheads. (**D-F**) Cells positive for ID3 were quantified in the indicated regions of caudal SVZ (as exemplified in panels A and B). A total of six controls and five *Lrp2*$^{-/-}$ mice were scored. For the dorsal SVZ (D), only cells in the lateral wall were quantified. For the ventral SVZ, both cells in the medial **(E)** and the lateral walls (F) were scored. The numbers of ID3 positive cells are unchanged in the medial (E) and lateral (F) walls of the ventral and the lateral wall of the dorsal SVZ (D) of LRP2-deficient mice compared with controls. Statistical analysis was performed using unpaired Student's *t* test.

In conclusion, the region-specific alterations in SHH signaling along the rostral to caudal axis of the LRP2-deficient SVZ were paralleled by similar regional changes in BMP signaling. Specifically, BMP signaling was more active in the rostral SVZ, an area where SHH signaling was decreased in the mutant brain. These findings substantiated a region-specific impact of LRP2 on the opposing activities of BMP and SHH signaling in the adult SVZ. However, the data did not resolve which of the two morphogen pathways, BMP or SHH, may be the primary target of LRP2 deficiency.

4.1.4 Analysis of mTOR activity in the SVZ of LRP2 mutant and control mice

Activation of mTOR is pivotal in fate determination of various cells types in embryonal and adult neurogenic niches (Paliouras et al., 2012). This pathway encompasses two signaling complexes, mTORC1 and mTORC2. In both cases, signal transduction works through phosphorylation of two downstream targets, called S6-RP and 4EBP1(Sarbassov, Ali, & Sabatini, 2005). Several reports suggested that mTOR may play an important role in maintenance of neural progenitor cell pools during embryonal development, but it may also be indispensable for generation of sufficient numbers of differentiated progeny in the adult SVZ. Specifically in transient amplifying progenitors, mTORC1 seems crucial for amplification and further differentiation (Zoncu, Efeyan, & Sabatini, 2011). Of note, a growing body of evidence also highlights a crosstalk between mTOR and SHH in induction of cell proliferation, processes governing malignant tumor formation (Pócza et al., 2014; Wu et al., 2017).

Based on my above data, I hypothesized a role for LRP2 in SHH-dependent mTOR signal transduction in the SVZ. I tested this hypothesis by performing co-immunostainings for SOX2, a marker of neuronal stem cells and transient amplifying progenitors with mTOR targets pS6RP or p4EBP1 in the SVZ of control and LRP2-deficient adult mice. These analyses were performed on rostral and caudal regions of the SVZ separately to query the impact of LRP2 activity on mTOR activation in a region-specific manner.

Examination of rostral regions of the SVZ revealed no apparent differences in pS6RP positive cell numbers between *Lrp2* $^{-/-}$ and controls in the dorsal domain (Figure 4.17 A).

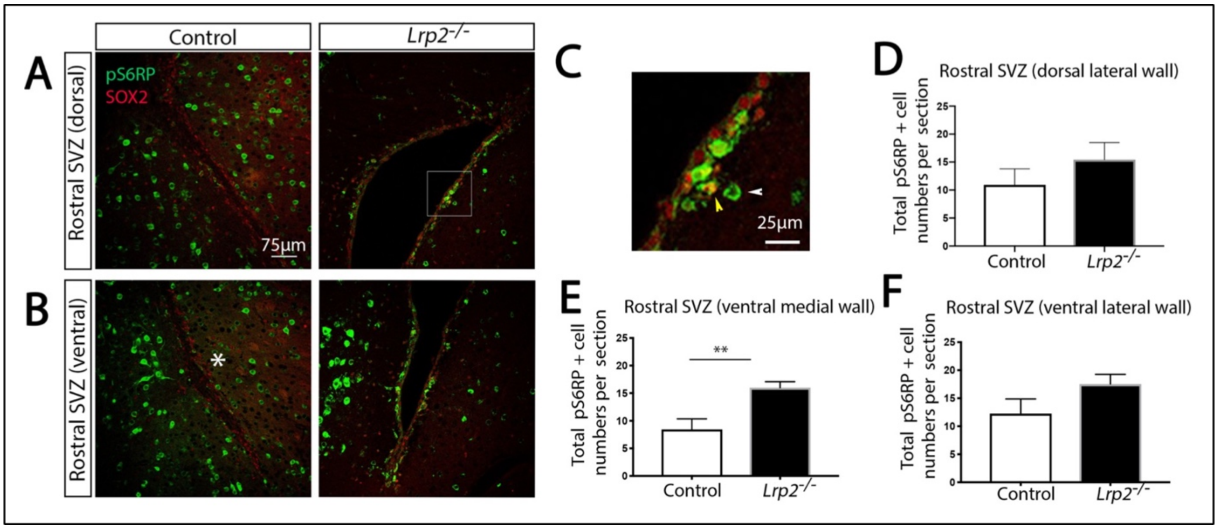

Figure 4.17: Levels of pS6RP are elevated in the rostral SVZ of LRP2-deficient mice.

(**A-C**) The activation of the mTOR pathway in adult LRP2-deficient and control mice was tested by immunohistological detection of phospho-S6 ribosomal protein (pS6RP; green) on 40 µm coronal sections from rostral regions of the brain. To test for expression of pS6RP in neuronal stem cells, co-staining for the marker sex determining region Y-box 2 (SOX2) was performed (red). Images of the dorsal (A) and ventral (B) domains of the rostral SVZ in the respective animals are shown separately. The lateral wall is indicated by an asterisk in panel B. In panel C, a higher magnification image of the boxed area in panel A is shown. Cells positive for pS6RP (green, white arrowhead) or for pS6RP and SOX2 (yellow arrowhead) are highlighted. (**D-F**) The total number of pS6RP positive cells (with or without SOX2 expression) was quantified on SVZ sections as exemplified in panels A and B. The average cell number from three consecutive sections of each mouse brain (five animals per genotype) was used for analysis. The total number of pS6RP positive cells is significantly higher in the medial wall of the ventral rostral SVZ of *Lrp2*$^{-/-}$ mice compared to littermate controls (E). No difference in pS6RP positive cell numbers are seen in the lateral wall of the dorsal (D) or the ventral (F) SVZ as tested by unpaired Student's *t* test. **, $p<0.01$

Strikingly, in the ventral domain, both on lateral and medial sides of the walls, pS6RP immunopositive cell numbers were increased almost twice (Figure 4.17 B). Statistical analysis of pS6RP positive cell counts (highlighted by arrowheads in figure 4.17 C) confirmed no changes of mTOR activity in dorsal region of SVZ (Figure 4.17 D) but a significant increase in the medial wall of the ventral SVZ in *Lrp2*$^{-/-}$ mice ´compared with littermate controls (Figure 4.17 E).

The same analysis, as in the rostral SVZ, was also performed in the caudal SVZ. The total number of pS6RP-positive cells in the caudal SVZ was not changed in LRP2 mutants compared with controls (Figure 4.18 A-F).

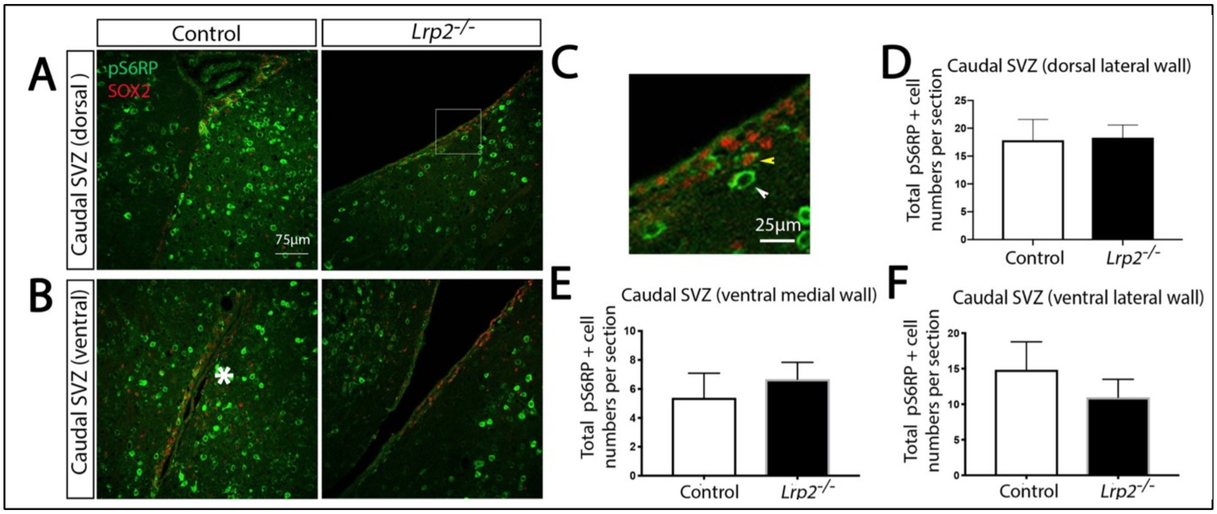

Figure 4.18: Levels of pS6RP are comparable in the caudal SVZ regions of LRP2-deficient mice and controls.

(**A-C**) Immunohistological detection of phospho-S6 ribosomal protein (pS6RP) levels (green) on 40 µm coronal sections from the caudal SVZ regions of mice of the indicated *Lrp2* genotypes. To test for expression of pS6RP in neuronal stem cells, co-staining for marker sex determining region Y-box 2 (SOX2) was performed (red). Images of the dorsal (A) and ventral (B) domains of the caudal SVZ in the animals are shown separately. The lateral wall is highlighted by an asterisk in panel B. In panel C, a higher magnification image of the boxed area in panel A is shown. Cells positive for pS6RP (green, white arrowhead) or for pS6RP and SOX2 (yellow arrowhead) are highlighted. (**D-F**) The total number of pS6RP positive cells (with or without SOX2 expression) was quantified on indicated SVZ sections exemplified in panels A and B. The average cell number from three consecutive sections of each mouse brain (three animals per genotype) was used for statistical analysis. No difference in numbers of pS6RP positive cells are seen in the caudal SVZ of both genotypes as tested by unpaired Student's *t* test.

In addition, I also counted cells that were positive for both SOX2 and pS6RP (Figure 4.19 A). Double immunopositive cells represented almost the half of the entire pS6RP positive cell population in SVZ. Cell counts and statistical analyses (Figure 4.19 B-D) confirmed a statistically significant increase in SOX2 positive cells responsive to mTOR signaling in the ventral rostral SVZ of mutant compared to control brains (Figure 4.19 C, D).

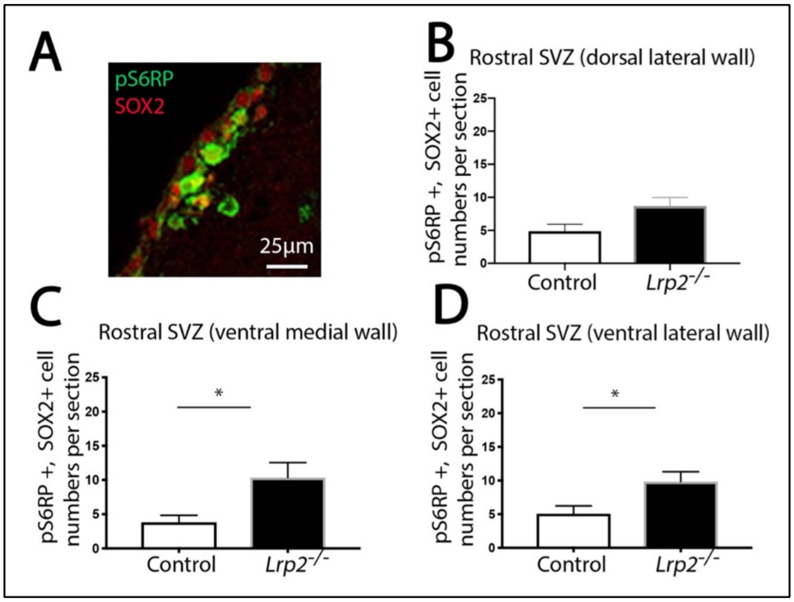

Figure 4.19: The neuronal stem cell population responsive to mTOR signaling is expanded in the rostral SVZ of LRP2-deficient mice.

(A) The activation of the mTOR pathway in neuronal stem cells of the SVZ of adult LRP2-deficient and control mice was tested by immunohistological detection of phospho-S6 ribosomal protein (pS6RP; green) and the neuronal stem cell marker sex determining region Y-box 2 (SOX2; red) on 40 µm coronal sections from the rostral brain. (**B-D**) Cells doubly positive for SOX2 and pS6RP (yellow) were quantified. The average cell number from three consecutive sections of each mouse brain (five animals per genotype) was used for statistical analysis. The number of neuronal stem cells positive for pS6RP are significantly higher in the medial (C) and lateral (D) walls of the *Lrp2*$^{-/-}$ ventral SVZ. No difference in pS6RP positive cell numbers are seen in the lateral wall of the dorsal (B) SVZ comparing both genotypes by unpaired Student's *t* test. *, $p<0.05$

Visualization of pS6RP and SOX2 double positive cells in caudal SVZ regions (Figure 4.20 A) revealed no obvious changes in the lateral wall of the dorsal (Figure 4.20 B) or in the medial wall of ventral SVZ in both genotypes (Figure 4.20 C). Interestingly, the number of SOX2 positive cells expressing pS6RP were slightly increased in the caudal ventral SVZ region of mutants, particularly in the medial ventricular wall (Figure 4.20 C). However, this trend was not statistically significant.

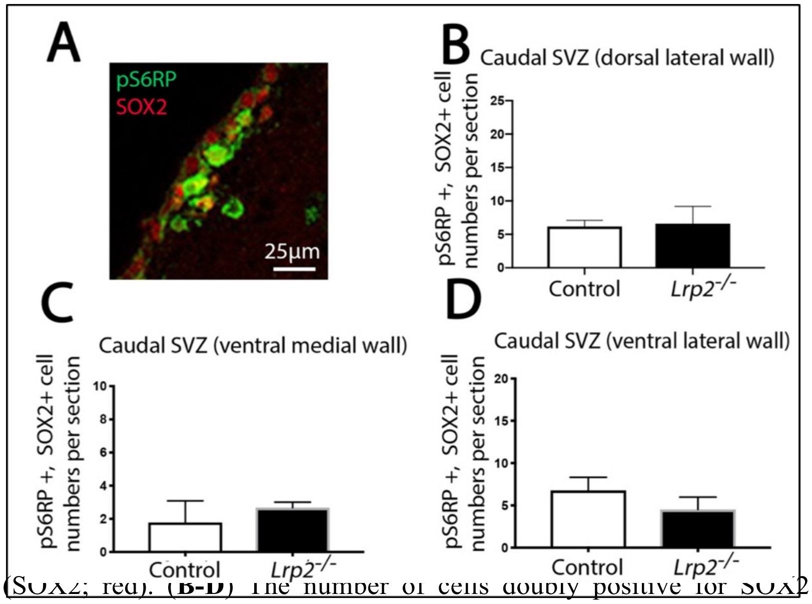

Figure 4.20: The numbers of pS6RP and SOX2 doubly positive cells are unchanged in the caudal SVZ of LRP2- deficient mice.

(A) Coronal sections (40 µm) from the caudal SVZ of mice of the indicated *Lrp2* genotypes were stained for phospho-S6 ribosomal protein (pS6RP; green) and the neuronal stem cell marker sex determining region Y-box 2 (SOX2; red). **(B-D)** The number of cells doubly positive for SOX2 and pS6RP (yellow signals) were quantified and the average cell number from two consecutive sections of each mouse brain (three animals per genotype) was used for statistical analysis. The number of pS6RP positive neuronal stem cells is unchanged in the tested SVZ regions in *Lrp2*$^{-/-}$ mice compared to control mice as shown by unpaired Student's *t*test.

In summary, I found a strong increase in the number of pS6RP positive cells in the rostral SVZ region of LRP2 mutants. To test whether this change was the result of an increase in mTOR activity or simply refleceted increased expression levels of S6RP, I assessed the levels of total and phosphorylated forms of S6RP in the SVZ by immunohistological analysis (Figure 4.21 A-F).

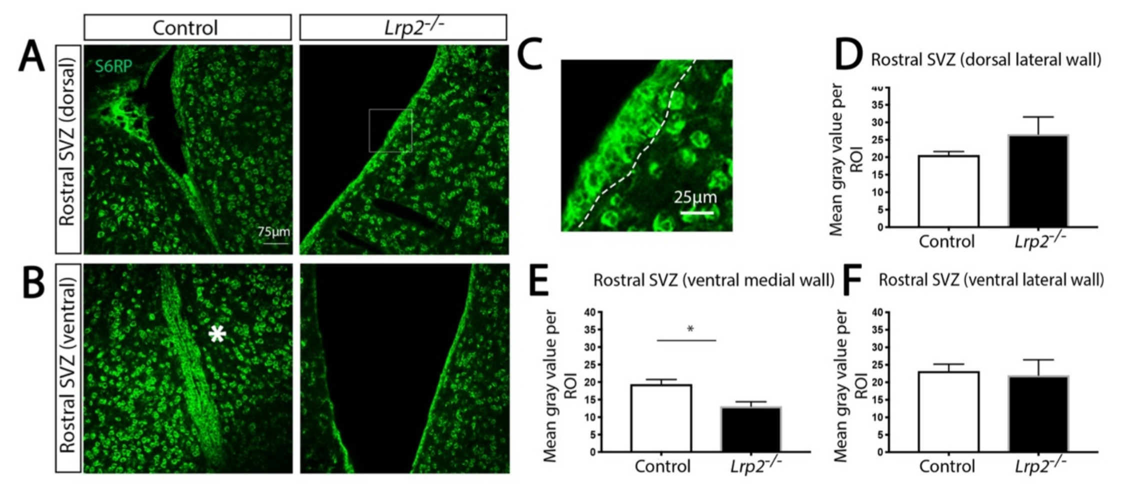

Figure 4.21: Mice lacking LRP2 have reduced levels of S6RP in the rostral ventral SVZ.

(**A, B**) Immunohistological detection of S6 Ribosomal Protein (S6RP; green) on coronal sections of the rostral SVZ of mice of the indicated *Lrp2* genotypes. Dorsal (A) and ventral (B) domains of each section are visualized separately. The lateral side of the ventricular wall is highlighted by an asterisk in panel B. In panel C, a higher magnification image of the boxed area in panel A is shown. The region of interest (ROI) used for quantification of S6RP positive cell numbers is highlighted by a dotted line. (**D-F**) Mean gray values (MGV) of the ROI were quantified on SVZ sections exemplified in panels A and B. The average MGV from three consecutive sections of each mouse brain (four animals per genotype) was used for statistical analysis by unpaired Student's *t* test. The MGV is significantly lower in the medial wall of the ventral rostral SVZ in *Lrp2*$^{-/-}$ mice compared with controls (E). No differences in MGV are seen in the lateral walls of the dorsal (D) or the ventral (F) rostral SVZ. *, $p<0.05$

Only the rostral SVZ region was taken for examination as pS6RP levels were significantly increased in the rostral region of LRP2-deficient mice compared to controls (Figure 4.17 and Figure 4.18). Examination of the dorsal region found no apparent differences between genotypes in S6RP levels (Figure 4.21 D). Surprisingly in LRP2 deficient mice, the intensity and also the area of S6RP immunosignals was prominently decreased in the rostral ventral SVZ (Figure 4.21 B) with statistically significant changes in medial (Figure 4.21 E) but not the lateral walls of the lateral ventricles (Figure 4.21 F). This result contrasted the data obtained for pS6RP expression in the same region before (Figure 4.17 B-F). Current observations indicated an even higher extent in increase of pS6RP, driven by elevated mTOR pathway activation upon LRP2 deficiency in the rostral SVZ region than initially concluded (Figure 4.17).

One of the well-established substrates of mTOR signaling is eukaryotic translation initiation factor 4E (eIF4E)-binding protein 1 (4EBP1) (Hay & Sonenberg, 2004). Phosphorylated forms of 4EBP1 play a central role in cap-dependent translation process. Upon activation of the mTORC1 complex, S6 kinase 1(S6K1) and 4EBP1 are phosphorylated. In its phosphorylated state, eIF4E dissociates from phosphorylated 4EBP1 and initiates the recruitment of eukaryotic translation initiation factor 4 G eIF4G to promote protein translation globally by binding to the 5′-cap at mRNAs, (Ma & Blenis, 2009). To examine how p4EBP1 levels were affected by LRP2 deficiency, p4EBP1 immunopositve cells were counted in the entire SVZ region in *Lrp2*$^{-/-}$ and control mice. To monitor phosphorylation of 4EBP1 in transient amplifying progenitors, co-staining was performed with the marker SOX2. Figure 4.22, shows the results of the quantification of p4EBP1 immunopositive cells in the rostral SVZ region of mutant and control mice.

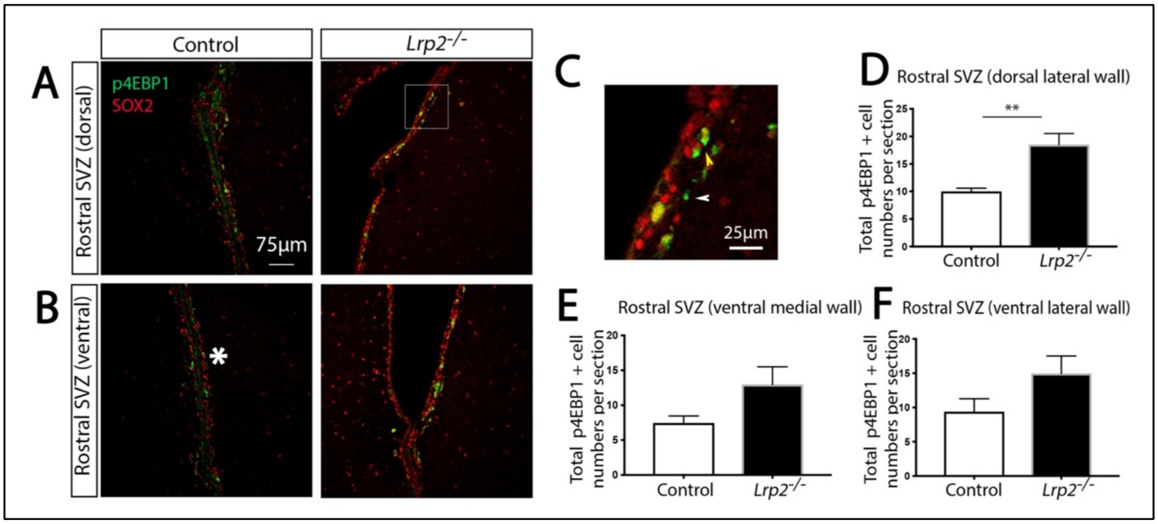

Figure 4.22: Levels of p4EBP1 are increased in the rostral SVZ region in LRP2 deficient mice.

(**A-C**) The activation of the mTOR pathway in adult LRP2-deficient and control mice was tested by immunohistological detection of phosphorylated 4E-binding protein (p4EBP1; green) on 40 µm coronal sections from the rostral SVZ. To visualize the expression of p4EBP1 in neuronal stem cells in the SVZ, co-staining for stem cell marker sex determining region Y-box 2 (SOX2; red) was performed. Images of dorsal (A) and ventral (B) domains of the rostral SVZ in each animal are shown separately. The lateral side of the wall is highlighted by an asterisk in panel B. In panel C, a higher magnification image of the boxed area in panel A is shown. Cells positive for p4EBP1 (green, white arrowhead) or for p4EBP1 and SOX2 (yellow arrowhead) are highlighted. (**D-F**) The total number of p4EBP1-positive cells (with or without SOX2 expression) was quantified on SVZ sections exemplified in panels A and B. The average cell number from three consecutive sections of each mouse brain (four animals per genotype) was used for statistical analysis by unpaired Student's *t* test. The total numbers of p4EBP1 positive cells are unchanged in the medial (E) and lateral (F) walls of the ventral rostral SVZ in *Lrp2*$^{-/-}$ mice compared with controls. By contrast, a significant increase in p4EBP1 positive cell numbers is seen in the lateral wall of the dorsal rostral SVZ (D) of mutant mice. **, $p<0.01$

In the ventral domain of the control SVZ, sparse immunosignals for p4EBP1 were seen compared with the dorsal SVZ (Figure 4.22 A, B). Cells immunopositve for p4EBP1 are indicated by an arrow in Figure 4.22 C. On average, 6 to 8 p4EBP1 positive cells were counted in the ventral domain per section and slightly more in the dorsal domain of the SVZ in controls (Figure 4.22 D-F).

In LRP2-deficient mice, p4EBP1 immunosignals were increased almost two-fold in both ventral and dorsal domains of the rostral SVZ compared with controls (Figure 4.22 D-F). This change was statistically significant in the dorsal SVZ region (Figure 4.22 D).

Alterations in levels of mTOR signaling components in LRP2 mutants in the rostral SVZ were recapitulated by comparable alterations in the dorsal but not in the ventral domain of the caudal SVZ (Figure 4.23 A-F) with an almost 30% increase in the number of p4EBP1 immunopositive cells in the dorsal SVZ of LRP2 mutants (Figure 4.23 A, C, D). By contrast, the number of p4EBP1 positive cells in the ventral domain of the caudal SVZ of LRP2 mutants were slightly decreased (Figure 4.23 B, E, F).

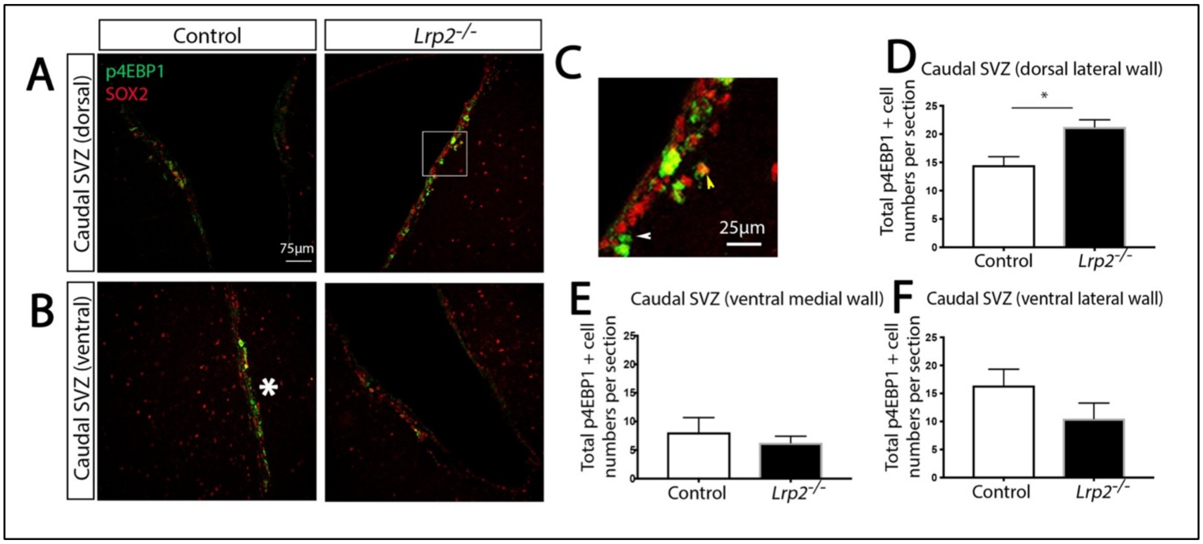

Figure 4.23: The level of phosphorylated 4EBP1 is increased in the caudal dorsal SVZ of *Lrp2*$^{-/-}$ mice.

(**A-C**) Activation of the mTOR pathway in adult LRP2-deficient and control mice was tested by immunohistological detection of 4E-binding protein (p4EBP1; green) on 40 µm coronal sections from caudal SVZ regions. To visualize p4EBP1 expression in neuronal stem cells, co-staining for stem cell marker sex determining region Y-box 2 (SOX2) was performed (red). Images of the dorsal (A) and ventral (B) domains of the caudal SVZ are shown separately. In panel B, the lateral side of the SVZ wall is marked by an asterisk. In panel C, a higher magnification image of the boxed area in panel A is shown. Cells positive for p4EBP1 (green, white arrowhead) or for p4EBP1 and SOX2 (yellow arrowhead) are highlighted. (**D-F**) Total numbers of p4EBP1-positive cells (with or without SOX2 expression) were quantified on SVZ sections exemplified in panels A and B. The average cell number from three consecutive sections of each mouse brain (two animals per genotype) was used for statistical analysis using unpaired Student’s *t* test. Total numbers of p4EBP1 positive cells are unchanged in medial (E) and lateral (F) walls of the ventral caudal SVZ in *Lrp2*$^{-/-}$ brains. By contrast, an increase in p4EBP1 positive cell numbers are seen in the lateral wall of the dorsal caudal SVZ (D). *, $p<0.05$

Next, I again examined the expression levels of total 4EBP1 in rostral SVZ to exclude the possibility that higher levels of p4EBP1 seen in Figure 4.22 were the result of elevated levels of the substrate 4EBP1 (Figure 4.24 A-F). The area of expression and the signal intensity levels for total 4EBP1 were not altered in the dorsal SVZ (Figure 4.24 A, C, D). Contrary in the ventral tip of rostral SVZ, both in medial and lateral walls, 4EBP1 levels were markedly decreased in LRP2 mutants compared with controls (Figure 4.24 B, E, F).

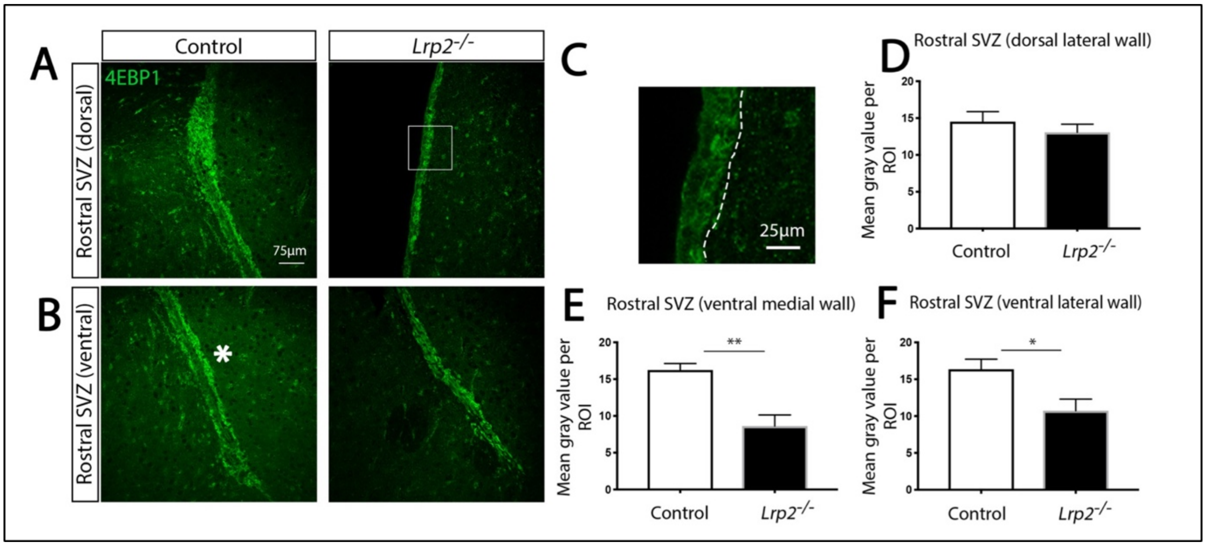

Figure 4.24: Total levels of 4EBP1 positive cells decline in the rostral SVZ of LRP2-deficient mice.

(A-C) Immunohistological detection of cells positive for 4E-binding protein (p4EBP1; green) in the rostral SVZ of mice with indicated *Lrp2* genotypes. Images of the dorsal (A) and ventral (B) SVZ regions are visualized separately. In panel B, the lateral side of the ventricular wall is highlighted by an asterisk. In panel C, a higher magnification image of the boxed area in panel A is shown. The region of interest (ROI) taken for quantification of p4EBP1 positive cell numbers is highlighted by a dotted line. (**D-F**) Mean gray values (MGV) of the ROI were quantified on SVZ sections exemplified in panels A and B. The average MGV from three consecutive sections of each mouse brain (six animals per genotype) was used for statistical analysis by unpaired Student's *t* test. The MGV is significantly lower in the medial (E) and lateral (F) walls of the ventral SVZ in *Lrp2*$^{-/-}$ compared with control mice. No difference in the MGV is detected in the lateral wall of the dorsal SVZ (D). *, $p<0.05$; **, $p<0.01$

4.1.5 Analysis of WNT signaling pathway in the SVZ of LRP2 mutant and control mice

The canonical WNT pathway is pivotal during embryogenesis, implicated in specification of body axis and morphogenesis, but also in control of stem cell proliferation and differentiation (van Amerongen & Nusse, 2009). In the adult SVZ, WNT/β catenin signaling is activated in precisely determined regions at specific time points. Given the importance of WNT signaling in the adult SVZ neurogenesis, I also aimed to explore the consequences of LRP2 deficiency for WNT signaling in this niche. To do so, I employed the *Tcf/lef_lacZ* reporter strain of mice (Mohamed et al., 2004). In this strain, expression of *lacZ* is driven by the promoter of *Tcf/Lef,* a downstream target in the canonical WNT signaling pathway. Similar to my approach with the *Gli1_lacZ* reporter (Figure 4.1 and Figure 4.2), I introduced the *Tcf/lef_lacZ* transgene into the line heterozygous for the *Lrp2* null allele by breeding of the two strains. By subsequent breeding of animal transgenic for *Tcf/lef_lacZ* and *Lrp2*$^{+/-}$*,* I generated homozygous *Lrp2* mutants and controls carrying the reporter gene for characterization of *Tcf/lef_lacZ* activity. Performing *lacZ* activity assays on histological sections of the adult SVZ, I documented reduced activity of the WNT pathway in the rostral SVZ of *Lrp2*$^{-/-}$ as compared with control mice (Figure 4.25).

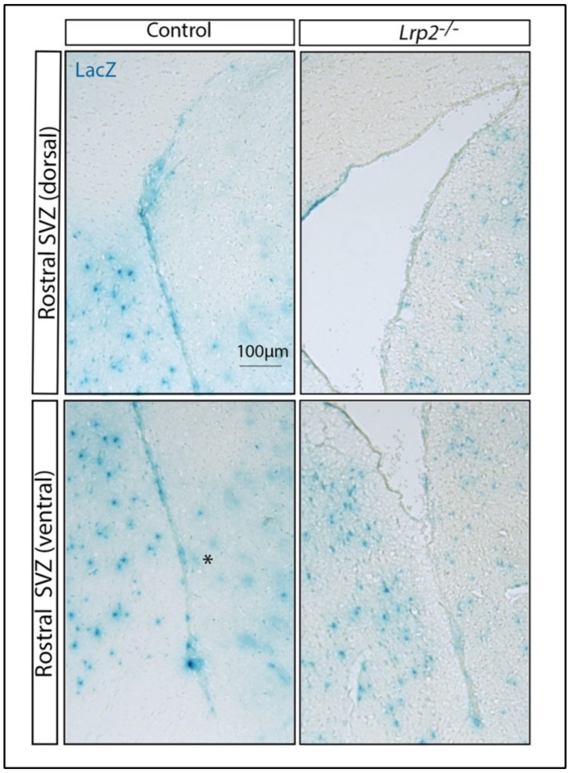

Figure 4.25: WNT signaling is decreased in the rostral SVZ of LRP2 deficient-mice.

LacZ activity was examined by X-gal staining on 10 µm coronal sections of the rostral SVZ in LRP2-deficient mice and littermate controls crossed with the *Tcf/lef_lacZ* reporter strain of mice. Exemplary images of a total of three sections of each mouse brain were analyzed (three animals per genotype). For each section, the dorsal and the ventral SVZ regions are depicted separately. The lateral side of the ventricular wall is highlighted by an asterisk. In ventral and dorsal SVZ regions, *Tcf/lef* expression levels, as deduced from the X-gal signal, are decreased in *Lrp2*$^{-/-}$ animals.

Upon examination of the caudal SVZ region, no obvious changes in the dorsal domain of the SVZ were detected comparing genotypes (Figure 4.26). However, I noticed a decreased signal for *Tcf/lef_lacZ* activity in the medial ventricular wall of the ventral SVZ in mutants compared with controls (Figure 4.26).

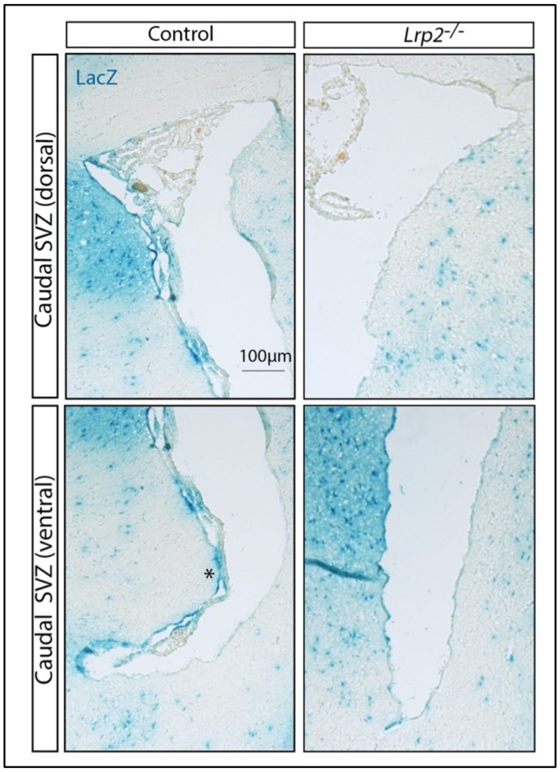

Figure 4.26: WNT signaling is slightly decreased in the caudal SVZ of LRP2 deficient-mice.

LacZ activity was examined by X-gal staining on 10 µm coronal sections of the caudal SVZ in LRP2-deficient mice and littermate controls crossed with the *Tcf/lef_lacZ* reporter strain of mice. Exemplary images of a total of three sections from the caudal region of each mouse brain are shown. For each section, the dorsal and the ventral SVZ regions are depicted separately. A total of three animals per genotype were analyzed. In control mice, *Tcf/lef_lacZ* shows the strongest expression in the medial wall (asterisk) of the ventral SVZ. In LRP2-deficient mice, *Tcf/lef_lacZ* expression, as deduced from the X-gal signal, is slightly decreased in ventral and dorsal SVZ regions.

These findings confirmed once more the regional specificity of LRP2 action in the adult SVZ, an activity that impact multiple morphogens (SHH, WNT, BMP) and regulatory pathways (mTOR) in this neurogenic niche.

4.2 Neurogenesis

4.2.1 Loss of LRP2 decreases the population of fast dividing cell in the rostral but notin caudal SVZ

So far, my studies had identified a region-specific effect of LRP2 activity on morphogen signaling in the neurogenic niche of the SVZ. Specifically, they documented distinct alterations in the rostral versus the caudal SVZ in mutant mice that hinted towards a regulatory role of this receptor in control of morphogen signaling along the rostral to caudal axis of the ventricular system. The following experiments were conducted to test whether this region-specific impact of LRP2 activity on morphogen signaling was paralleled in a similar region-specific impact on adult neurogenesis.

In the germinal niche of the SVZ, three main cell types are relevant for neurogenesis. Neural stem cells (also called B cells) exhibit self-renewing capacity. They proliferate to produce new neural stem cells but also to differentiate into fast dividing progenitors (called C cells). Although C cells have a residual capacity for self-renewal, they mainly differentiate into neuroblasts (A cells). Neuroblasts migrate from the SVZ via the rostral migratory stream (RMS) to the olfactory bulbs (OB). During this migration process, A cells undergo further differentiation and finally integrate into OB as interneurons (Adachi et al., 2007; Lois & Alvarez-Buylla, 1994).

To examine the effect of LRP2 deficiency on the proliferative capacity of the SVZ niche, I performed BrdU incorporation assays in LRP2 mutant and control mice *in vivo*. In my approach, I intraperitoneally injected BrdU, a synthetic nucleoside analogue into mice. BrdU is incorporated into replicating DNA instead of thymidine. Immunostaining for BrdU on histological sections enables detection of proliferating cells, as in the SVZ. To explore the regionality of LRP2 deficiency on cell proliferation in this niche, I again analyzed the rostral and caudal regions of the SVZ separately. Also, for the rostral region (Figure 4.27 A), I scored BrdU positive cell counts separately for the respective dorsal and ventral SVZ domains (Figure 4.27 B, C). As shown by arrowheads in figure 4.27 D, BrdU positive cells were considered for quantification in SVZ area. Statistical analysis of BrdU positive cells counts on replicate histological sections revealed a significant reduction in cell proliferation in the dorsal domain of the rostral SVZ in LRP2-deficient mice as compared with littermate controls (Figure 4.27 B, E). A similar impact of LRP2 deficiency on reducing the BrdU+ cell counts was also seen in the ventral domain of the rostral SVZ (Figure 4.27 C, F).

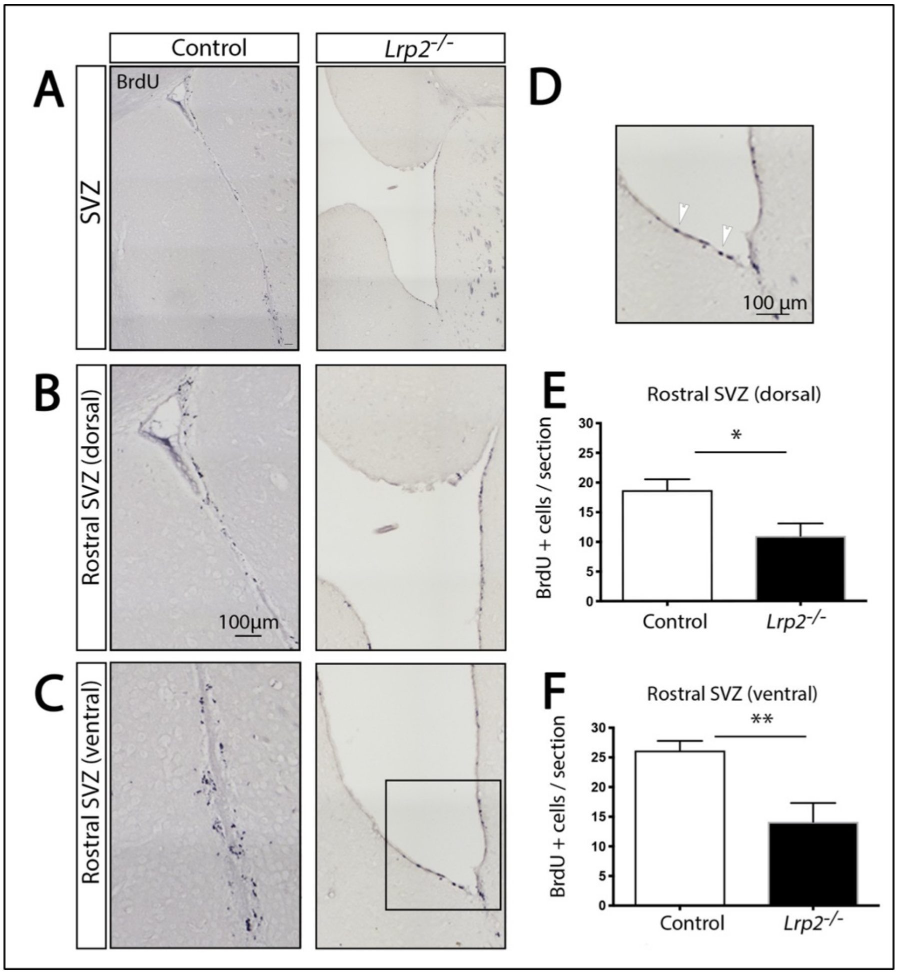

Figure 4.27: The number of fast proliferating neuronal progenitors is reduced in ventral and dorsal areas of the rostral *Lrp2*$^{-/-}$ SVZ.

(A-D) Fast dividing progenitor cells in the SVZ were labeled by 24 hours *in vivo* application of 5-bromo-2'-deoxyuridine (BrdU). Subsequently, BrdU positive cells were immunodetected on 12 µm coronal sections of the rostral SVZ in control and LRP2-deficient mice. SVZ overviews (A) as well as separate views of the dorsal (B) and ventral (C) domains of the rostral SVZ of each section are given. A higher magnification of the boxed area in panel C is given in panel D, highlighting BrdU positive cells by arrowheads. (**E, F**) Cells positive for BrdU were quantified in the indicated regions of the rostral SVZ (exemplified in panels B and C). A total of five animals per genotype were scored. The average cell number from twelve consecutive sections of each mouse brain was used for statistical analysis by unpaired Student's *t* test. Cell numbers are significantly decreased in the dorsal (E) and ventral (F) rostral SVZ in LRP2-deficient mice. *, $p<0.05$

In the caudal SVZ, no significant difference in the numbers of BrdU+ cells were observed comparing both genotypes (Figure 4.28).

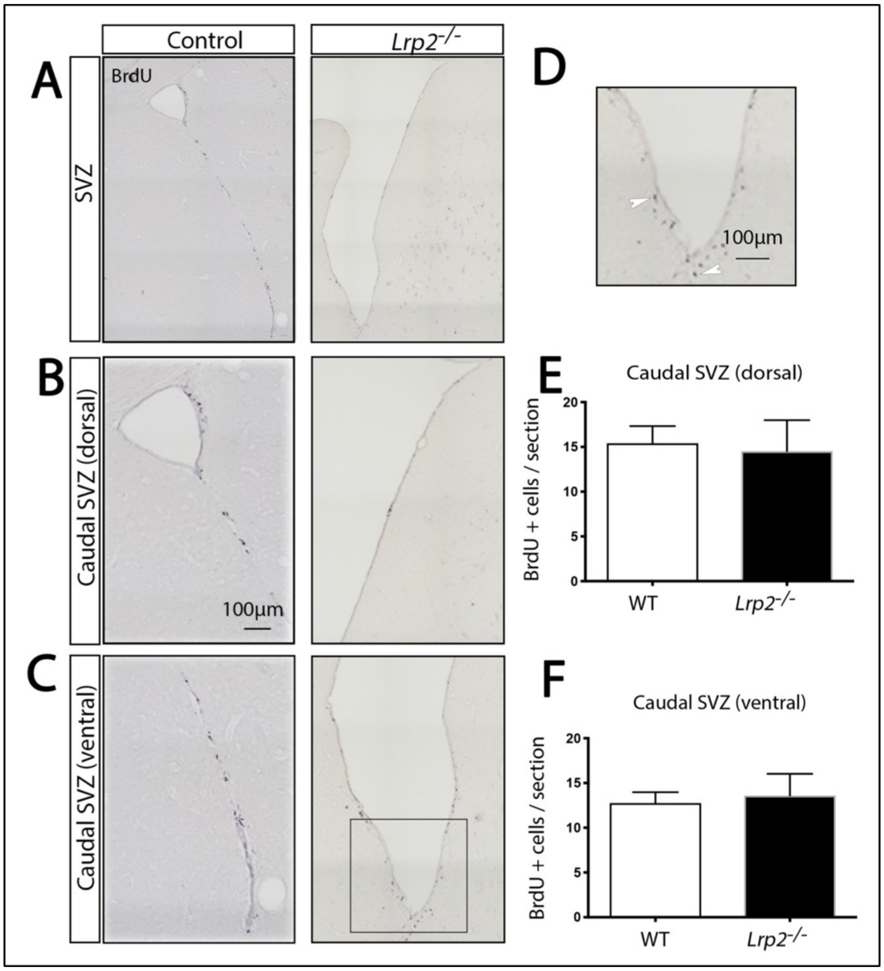

Figure 4.28: The numbers of fast proliferating cells are similar in caudal SVZ regions of LRP2-deficient mice and their littermate controls.

(**A-D**) Fast dividing progenitor cells in the SVZ were labeled by 24 hours application of BrdU *in vivo*. Subsequently, BrdU positive cells were immunodetected on 12 µm coronal sections of the caudal SVZ in control and LRP2-deficient mice. SVZ overviews (A) as well as separate views of the dorsal (B) and ventral (C) domains of the caudal SVZ of each section are given. A higher magnification of the boxed area in panel C is given in panel D, highlighting BrdU positive cells by white arrowheads. (**E, F)** Cells positive for BrdU were quantified in the indicated regions of caudal SVZ (exemplified in panels B and C). A total of five animals per genotype were scored. The average cell number from twelve consecutive sections of each mouse brain was taken for statistical analysis by unpaired Student's *t* test. No obvious differences in BrdU positive cell counts were detected in dorsal (E) or ventral (F) SVZ regions comparing LRP2-deficient mice with littermate controls (*Lrp2*$^{+/+}$ and *Lrp2*$^{+/-}$).

I also inspected the impact of LRP2 deficiency on the proliferative capacity of C cells in the subgranular zone (SGZ) of the hippocampus, the second neurogenic niche in the adult mammalian brain. In line with the absence of LRP2 expression in this niche in the wildtype brain (Gajera et al., 2010), receptor deficiency did not impact the numbers of BrdU+ cells in the SGZ in mutants as compared to control mice in a 24 hours chase experiment (Figure 4.29).

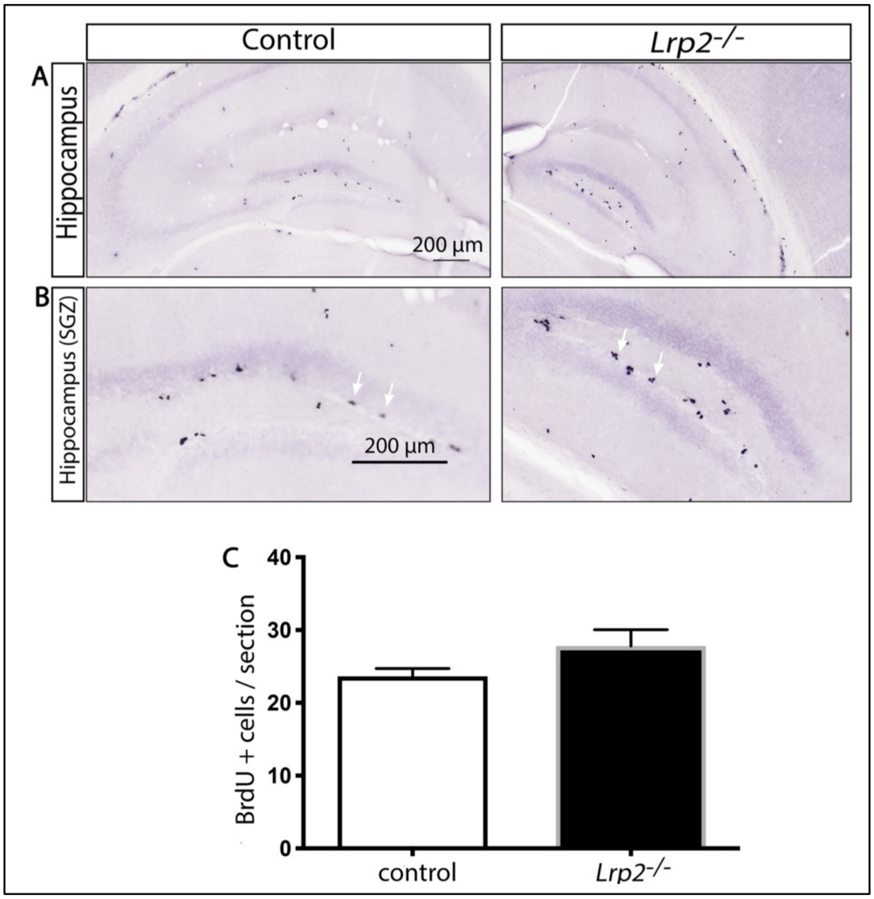

Figure 4.29: The number of fast proliferating cells in the subgranular zone of the hippocampus is unchanged in LRP2 mutant mice.

(A-B) Fast dividing progenitor cells in the subgranular zone (SGZ) of the hippocampus were labeled by 24 hours application of BrdU *in vivo*. Subsequently, BrdU positive cells were immunodetected on 20 µm sections of the hippocampi of mice with indicated *Lrp2* genotypes. In panel B, BrdU positive cells in the SGZ are highlighted by arrows. (**C**) Number of BrdU positive cells in the SGZ of LRP2-deficient and control mice. The average cell number from seven consecutive sections of each brain was taken for quantification and statistical analysis by unpaired Student's *t* test. No significant difference in cell numbers were observed comparing both genotypes.

These findings served as an important control that the reduction in proliferative capacity seen in the rostral mutant SVZ was the consequence of the local loss of LRP2 activity rather than a global effect on brain activities.

4.27.2 Depletion of the neural stem cell pool in the SVZ niche of LRP2-deficient mice

To identify the cause of the reduced proliferative capacity of C cells in the mutant SVZ, I investigated the number of neuronal stem cells (B cells) in the rostral and caudal SVZ of the respective mouse strain. To do so, I stained histological sections of the rostral and caudal SVZ of mutant and control mice for GFAP, a marker of B cells (Gajera et al., 2010). In the rostral SVZ, the immunosignal intensity for GFAP was not altered in the lateral wall of the dorsal SVZ but was markedly decreased in the ventral tip of the SVZ in LRP2 mutants as compared with controls (Figure 4.30 A-F). Quantification and statistical analysis of intensity levels of fluorescent signal (highlighted in figure 29 C) confirmed unchanged GFAP levels in dorsal SVZ (Figure 4.30 D) but a reduction in the ventral region of LRP2 deficient mice as compared to controls (Figure 4.30 E, F). This change was statistically significant in the ventral lateral wall (Figure 4.30 F).

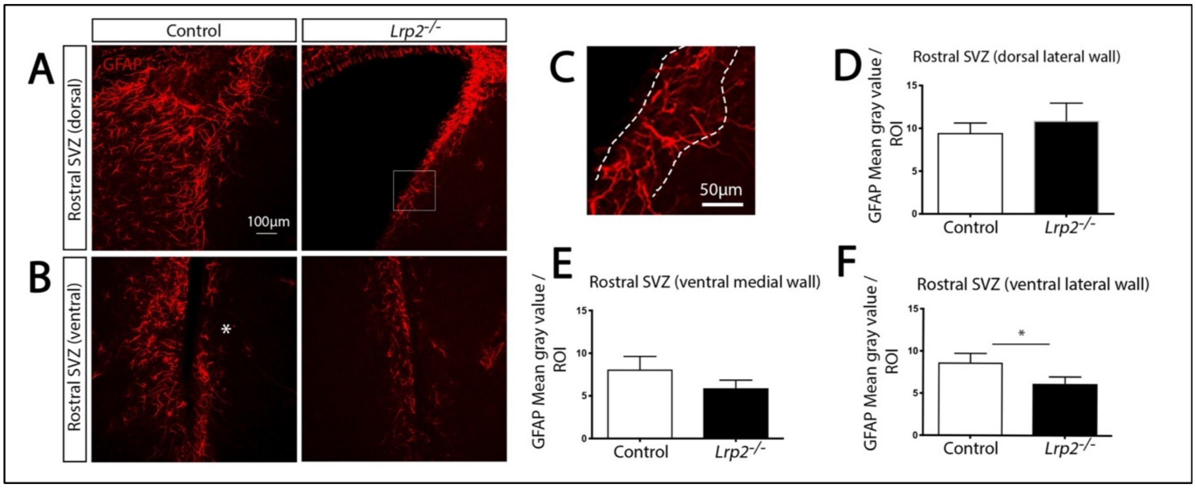

Figure 4.30: The neuronal stem cell pool is depleted in the rostral SVZ of mice lacking LRP2.

(**A-C**) Immunohistological detection of cells positive for glial fibrillary acidic protein (GFAP), a marker of neuronal stem cells. Coronal 40 µm sections of the rostral SVZ from control (*Lrp2*$^{+/+}$ and *Lrp2*$^{+/-}$) and *Lrp2*$^{-/-}$ animals are shown. Maximal projection of optical section series are presented (interval of imaging in the Z-axis is 1.52 µm). In panel C, a higher magnification image of the boxed area in panel A is shown. The region of interest (ROI) taken for quantification is highlighted by a dotted line. (**D-F**) Mean gray values (MGV) of the ROI were quantified on rostral SVZ sections exemplified in panels A and B (asterisk indicates the lateral wall of the ventricle). The average MGV from three consecutive sections of each mouse brain from six controls and five *Lrp2*$^{-/-}$ animals was used for statistics by unpaired Student's *t* test. The MGV is significantly lower in the lateral wall of ventral rostral SVZ in *Lrp2*$^{-/-}$ mice as compared with controls (F). No statistically significant differences in the MGV are observed in the medial wall of ventral SVZ (E) or in the lateral wall of the dorsal (D) SVZ. *, $p<0.05$

The GFAP positive B cell count in the caudal SVZ was not affected by LRP2 deficiency (Figure 4.31).

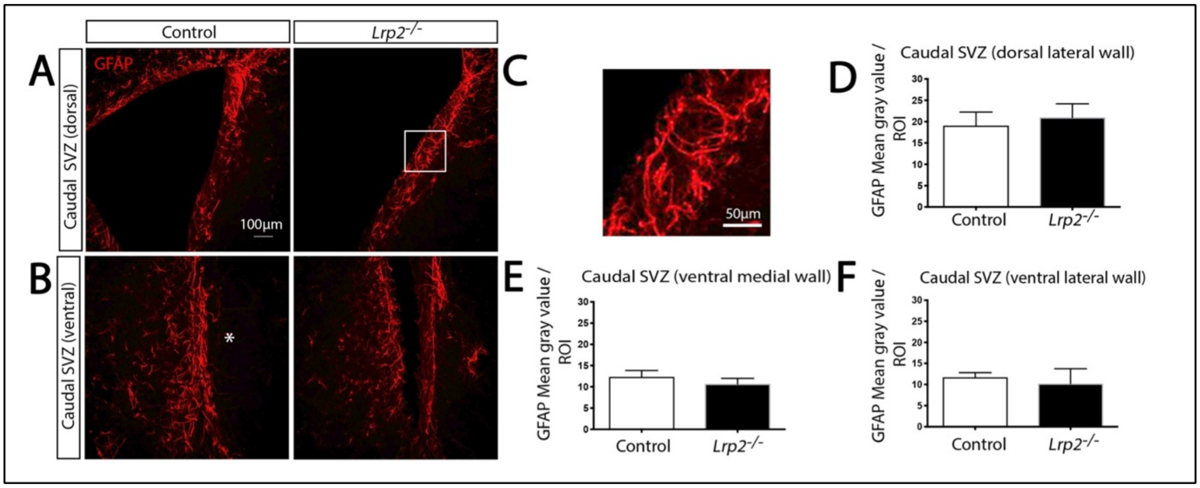

Figure 4.31: The neuronal stem cell pool is unchanged in the caudal SVZ of LRP2-deficient mice.

(A-C) Immunohistological detection of cells positive for glial fibrillary acidic protein (GFAP), a marker of neuronal stem cells. Coronal 40 µm sections of the caudal SVZ from control (*Lrp2*$^{+/+}$ and *Lrp2*$^{+/-}$) and *Lrp2*$^{-/-}$ animals are given. In panel C, a higher magnification image of the boxed area in panel A is shown. (**D-F**) Mean gray values (MGV) of the regions of interest (ROI) were quantified on the indicated regions of the caudal SVZ as exemplified in panels A and B (lateral side of the ventricular wall highlighted by an asterisk). The average MGV from three consecutive sections of each mouse brain (four animals per genotype) was used for statistical analysis by unpaired Student's *t* test. No statistically significant differences in MGVs are observed comparing both genotypes.

Another commonly used marker of the B cell population is SOX2. As compared to the diffuse cytoplasmic signal of GFAP, the nuclear immunosignal for this transcription factors greatly facilitates counting the number of B cells in the SVZ niche (Figure 4.32 A-F). Again, dorsal and ventral regions of rostral SVZ region were examined separately (Figure 4.32 A, B). Quantification of the number of SOX2 positive nuclei, as highlighed in figure 4.32 C, documented no apparent changes of immunopositive B cells in the dorsal domain of rostral SVZ in LRP2 mutants (Figure 4.32 A, D). In the ventral region of rostral SVZ, LRP2 deficiency significantly impacted the population of SOX2 immunopositive cells (Figure 4.32 B, E, F) as B cell numbers were robustly decreased in the lateral ventricular wall of ventral rostral SVZ in LRP2 deficient mice in comparison to controls (Figure 4.32 F). No consistent differences were noted in the medial ventricular wall of the same region (Figure 4.32 E).

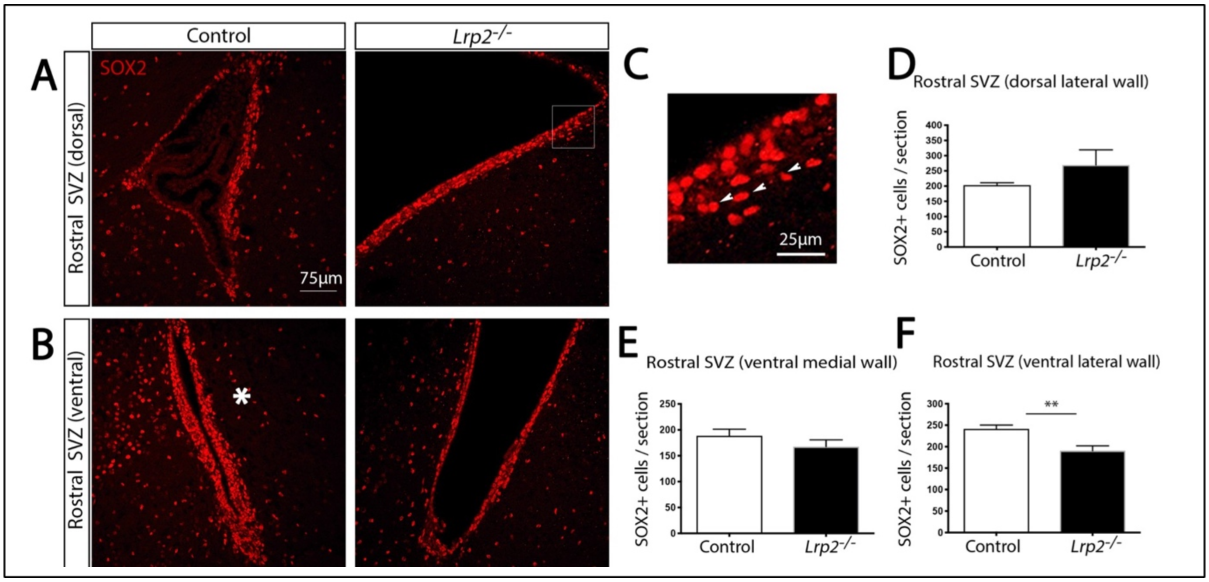

Figure 4.32: The neuronal stem cell pool is depleted in the rostral SVZ of mice lacking LRP2.

(**A-C**) Immunohistological detection of cells positive for glial fibrillary acidic protein (GFAP), a marker of neuronal stem cells. Coronal 40 µm sections of the rostral SVZ from control (*Lrp2*$^{+/+}$ and *Lrp2*$^{+/-}$) and *Lrp2*$^{-/-}$ animals are shown. Maximal projection of optical section series is presented (interval of imaging in the Z-axis is 1.52 µm). In panel C, a higher magnification image of the boxed area in panel A is shown. The region of interest (ROI) taken for quantification is highlighted by a dotted line. (**D-F**) Mean gray values (MGV) of the ROI were quantified on rostral SVZ sections exemplified in panels A and B (asterisk indicates the lateral wall of the ventricle). The average MGV from three consecutive sections of each mouse brain from six controls and five *Lrp2*$^{-/-}$ animals was used for statistics by unpaired Student's *t* test. The MGV is significantly lower in the lateral wall of ventral rostral SVZ in *Lrp2*$^{-/-}$ mice as compared with controls (F). No statistically significant differences in the MGV are observed in the medial wall of ventral SVZ (E) or in the lateral wall of the dorsal (D) SVZ. *, $p<0.05$

Examination of SOX2 immunopositive cell numbers in the caudal SVZ region found no alterations in the dorsal domain of *Lrp2*$^{-/-}$ as compared with controls (Figure 4.33 A-D). In contrast to the rostral SVZ (Figure 4.32 B-F), an elevation of SOX2 positive B cells in the ventral domain of the caudal SVZ was noted when compared with controls (Figure 4.33 B). This effect was specifically seen in the medial ventricular wall with statistically significant change between genotypes (Figure 4.33 E).

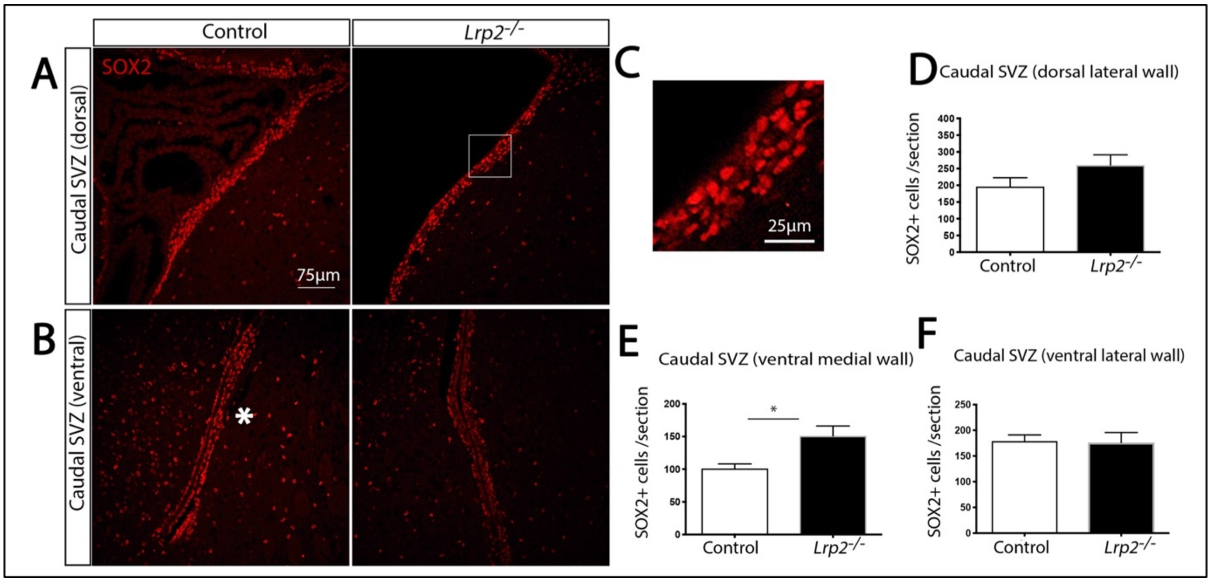

Figure 4.33: LRP2 deficient mice show an increase in SOX2 positive neuronal stem cell levels in the ventral medial wall of caudal SVZ.

(A-C) Immunohistological detection of cells expressing the neuronal stem cell marker sex determining region Y-box 2 (SOX2) on 40 µm coronal sections from the caudal SVZ of LRP2-deficient and control mice. Dorsal (A) and ventral (B) domains of the caudal SVZ of each section are shown separately. The lateral wall is highlighted by an asterisk in panel B. A higher magnification image of the boxed area in panel A is given in (C). (**D-F**) Cells positive for SOX2 were quantified in the indicated regions of caudal SVZ (exemplified in panels A and B). A total of six control (*Lrp2*$^{+/+}$ and *Lrp2*$^{+/-}$) and five *Lrp2*$^{-/-}$ mice were scored. For the dorsal SVZ (D), only the cells in the lateral wall were quantified. For the ventral SVZ, cells both in the medial (E) and lateral walls (F) were scored. The numbers of SOX2 positive cells are significantly increased in the medial wall of the ventral SVZ (E) as determined by unpaired Student's *t* test. *, $p<0.05$

4.27.3 The oligodendrocyte lineage is unaffected in the SVZ of *Lrp2*$^{-/-}$ mice

In the SVZ, a small population of cells of the oligodendroglial lineage maintain their proliferative capacity. To examine the consequences of LRP2 deficiency on this oligodendroglial cell population, I have visualized oligodendrocytes by staining for the marker OLIG2 (Gajera et al., 2010).

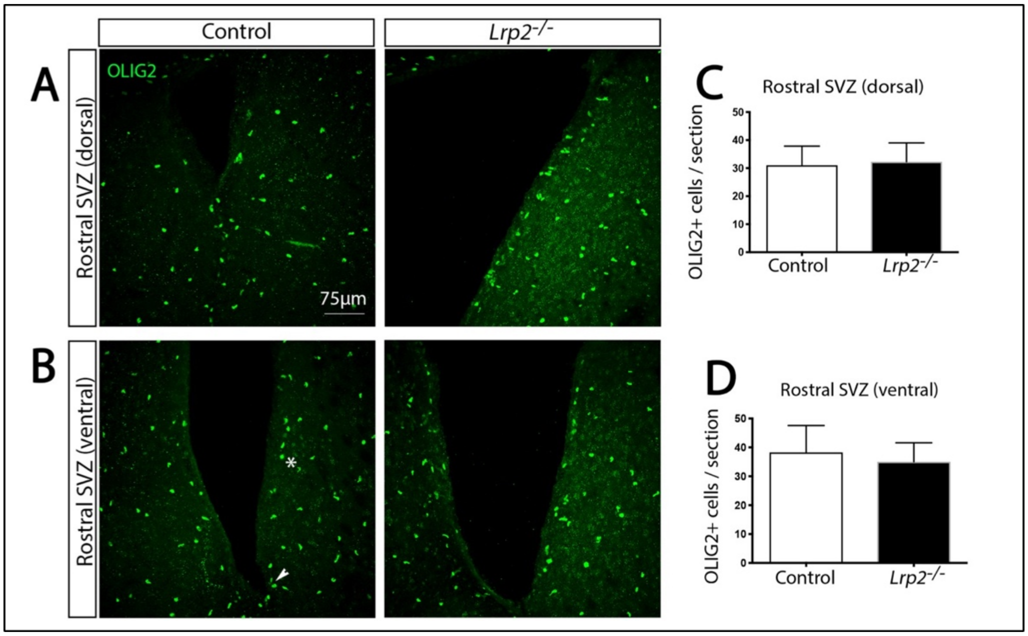

Figure 4.34: The population of OLIG2 positive oligodendrocytes is unchanged in the rostral SVZ of LRP2 mutant mice.

(A, B) Imunohistological detection of OLIG2 (green) on 40 µm coronal sections of the rostral SVZ in control and in LRP2-deficient mice. (**C, D**) The numbers of OLIG2 positive cells in dorsal (C) and ventral (D) domains of the rostral SVZ were quantified on three consecutive sections per brain of four animals per genotype. No statistically significant differences in cell numbers were detected by unpaired Student's *t* test comparing both genotypes.

Quantification of the number of OLIG2 immunopositive cells failed to show obvious alterations in LRP2 mutants compared with littermate controls, neither in rostral (Figure 4.34) nor the caudal SVZ regions (Figure 4.35).

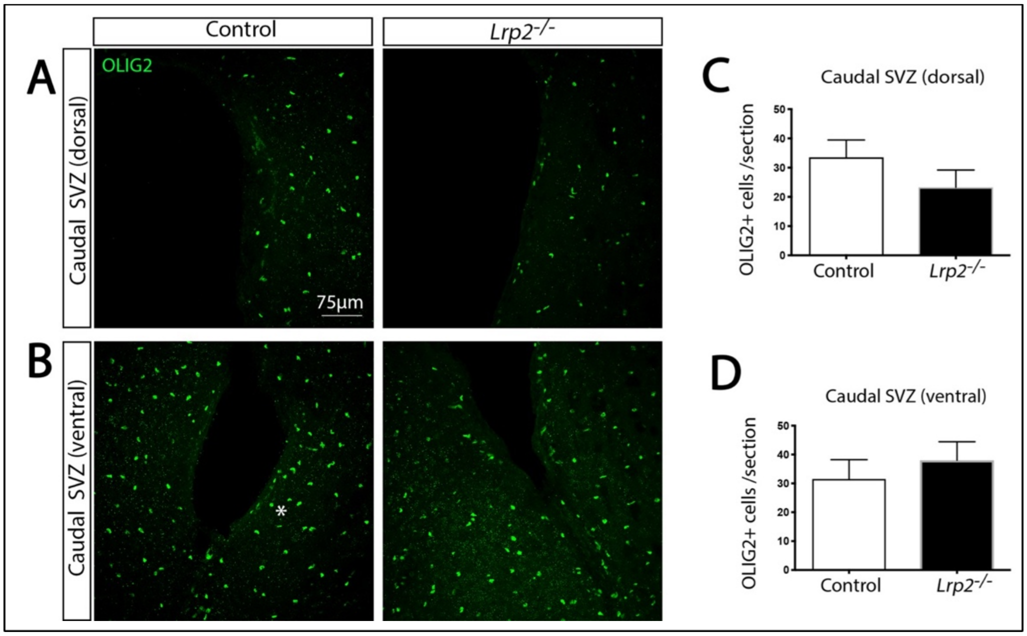

Figure 4.35: The number of OLIG2 positive oligodendrocytes in the caudal SVZ is similar in LRP2-deficient and controls mice

(A, B) Imunohistological detection of OLIG2 (green) on 40 µm coronal sections of the caudal SVZ in control and in LRP2-deficient mice. (**C, D**) The numbers of OLIG2 positive cells in dorsal (C) and ventral (D) domains of the caudal SVZ were quantified on three consecutive sections per brain of four animals per genotype. No statistically significant differences in cell numbers were detected by unpaired Student's *t* test comparing genotypes.

4.3 Motile cilia on ependymal cells

In summary, the region-specific analysis of cell populations in the SVZ of control and LRP2-mutant mouse brains substantiated distinct effects of LRP2 activity on neurogenic processes in the rostral versus the caudal area of this niche. Based on the concurrent alterations in numbers of B cells (Figure 4.30 and Figure 4.32) and proliferative C cells (Figure 4.27), LRP2 likely exerts a primary regulatory role on the size of the stem cell pool in the SVZ, secondarily impacting the number of C cell progeny derived thereof. This receptor activity specifically impacts cell fates in the neuronal but not the oligodendroglial lineages in the SVZ. This regional specificity in LRP2 activity was surprising given the fact that expression of this receptor in the wildtype brain is seen uniformly in the ependymal cell layer from rostral to caudal regions of the SVZ (Gajera et al., 2010). Conceptually, my findings argued against a cell autonomous function for LRP2 in ependymal cells. Rather, they suggested a global effect of LRP2 activity on the regionality of the SVZ niche.

A process that may affect regionality of the SVZ niche is the flow of the cerebrospinal fluid (CSF) through the ventricular system distributing nutrients but also so signaling molecules in a region specific manner (Telano & Baker, 2019; Veening & Barendregt, 2010). Flow of the CSF is driven by the activity of motile cilia present on ependymal cells (Olstad et al., 2019). By coordinated beating of the motile cilia on the apical surface, ependymal cells determine CSF flow and direction of neuroblast migration (Doetsch & Alvarez-Buylla, 1996; Jiménez, Domínguez-Pinos, Guerra, Fernández-Llebrez, & Pérez-Fígares, 2014). Based on the distinct expression of LRP2 on the apical surface of the ependymal cells, I explored a role for this receptor in control of motile cilia activity and cilia beating defects as the possible underlying cause of the region-specific alterations on SVZ activity in the LRP2 mutant SVZ.

4.3.1 Ciliary patches display non-coordinated displacement in ependymal cells of LRP2-deficient mice

To explore the functional integrity of the motile cilia in control and LRP2 mutant ependymal cells, I employed an experimental strategy developed by Camille Boutin (Boutin et al., 2014; Labedan et al., 2016). In this technique, freshly dissected lateral ventricular wall whole mounts (LWWM) from adult mouse brain (Figure 3.2) were shortly fixed and stained for ciliary basal body markers FGFR1 Oncogene Partner (FOP) and tubulin and for the cell surface marker

Zonula Occludens-1 ZO1. Tissue samples were mounted and coverslipped in fluorescent mounting medium for the further en face inspection. Serial stack images covering the entire depth of the specimen was taken on a confocal microscope Leica SPE and then merged using the maximum projection tool in the Leica software. Using the Biotool software (Labedan et al., 2016), the contours of individual ependymal cells (blue) and their respective ciliary patches were traced (Figure 3.7 A).

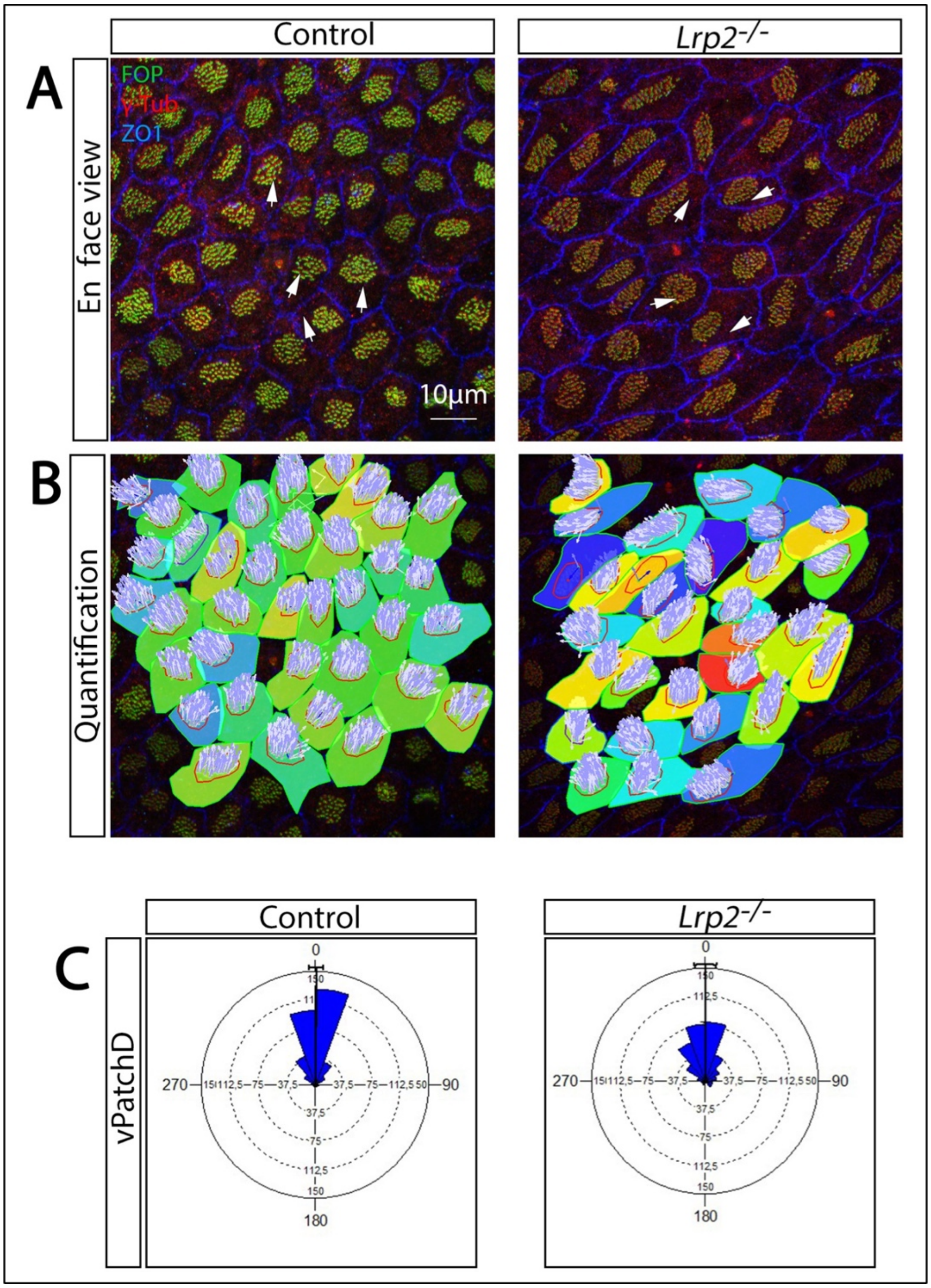

Figure 4.36: Ciliary patch displacement in ependymal cells of LRP2-deficient mice.

(A) En face preparations of the lateral ventricular wall in control and LRP2-deficient mouse brains were immunostained for ciliary basal body markers FGFR1 Oncogene Partner (FOP; green) and gamma tubulin (γ-Tub; red), as well as for the apical cell surface marker zonula occludens-1 (ZO1; blue). Arrows indicate the direction of ciliary patch displacement relative to the cell center in representative ependymal cells (**B**) Color coding of individual ependymal cells, describes the degree of patch displacement relative to the cell center in the field of interest. The stronger the displacement asymmetries of a patch is, the further the color shifts towards the red or blue color spectrum. (**C**) Angle vPatchD value for each cell represents the angle between the vector of displacement from the cell center and the mean vector of displacement in the entire field of observation. Circular dispersion of vPatchD parameter angles around the mean in control and LRP2-deficient ependymal cells are represented. Circular statistical analysis (Watson U^2 test) carried on vPatchD values of 358 cells from control and 374 cells from LRP2-deficient mice confirms a statistically significant difference in ciliary patch displacement between the two genotypes ($p<0.001$).

Subsequently, the software calculated the geometric centers of the marked areas and characterized the ciliary patch displacement relative to the center of each cell.

Initially, I tested the impact of LRP2 deficiency on displacement of the ciliary patch on the apical cell surface relative to the center of the ependymal cells (Figure 4.36). The ciliary basal bodies are initially widely scattered in immature ependymal cells, but upon further differentiation they cluster in an off-centered patch. In adjacent cells, ciliary patches acquire the same direction of the displacement from the cell center, matching the direction of CSF flow (Mirzadeh, Han, Soriano-Navarro, García-Verdugo, & Alvarez-Buylla, 2010).

As depicted in immunostained en face preparations in Figure 4.36 A, ependymal cells in the control SVZ manifested a coordinated and directed displacement of the ciliary patches relative to cell center. This was not the case for the LRP2-deficient SVZ, where patches of many ependymal cells showed a random displacement (Figure 4.36 A).

In Figure 4.36 B, the coordination of the patch displacement is illustrated by color codes assigned by Biotool software. In controls, the dominance of green color is an indicator of coordinated and directed patch displacement. By contrast, a shift to blue and red color spectra in LRP2 mutants highlights the non-coordinated displacement of the patches within the field of view. The integrated angle values vPATCHDs, characterizing the degree of patch displacement, are depicted in the circular statistics graphs in figure 4.36 C as dispersion around the mean for each genotype. The degree of displacement coordination abnormalities in mutants is reflected in a wider dispersion range around the mean in the circular statistics graph of LRP2-deficient mice compared with controls (Figure 4.36 C).

4.3.2 Absence of LRP2 affects the coordinated beating of motile ciliary patches on ependymal cells

To test how LRP2 activity impacts coordination of the cilia beating direction, I scored the FOP and γ-Tub protein expression patterns on ventricular LWWM preparations by en face visualization. Thus, immunostained images used for patch displacement characterization (Figure 4.37 A) were also analyzed for ciliary beating orientation. Motile Cilia beating is driven by longitudinally arranged 9 doublets of microtubules around a central pair of microtubule. Anchoring point of those microtubular structures are the basal bodies. A protruding appendage from basal body, the so-called basal foot invariably points in the direction of the effective cilia stroke, revealing the orientation of each cilium (Marshall & Kintner, 2008). Accordingly, in my analysis, inspection of the relative localization of the basal foot marker γ-Tub to the basal body FOP was used to determine the orientation of the ciliary beating (Figure 4.37).

The orientation of ciliary patch beating is highlighted by arrows in figure 4.37 A. Exemplary image show coordinated ciliary beating orientation in ependymal cells within the field of interest in the control mice. By contrast, in *Lrp2*$^{-/-}$ mice, many randomly beating ciliary patches were observed in the region of interest (Figure 4.37 A, B). The overview of the quantification of the ciliary beating orientation in the Biotool software is shown in figure 4.37 B as a group of vectors pointing at the γ-Tub position relative to FOP in each cilium within a patch.

As a quantitative parameter, I evaluated the vPATCHO angle value that describes the beating orientation of the motile cilia in each cell within the field of analysis. The circular dispersion analysis, describing the dispersion around the mean of vPATCHO values for each genotype, revealed statistically significant changes between controls and LRP2 deficient mice (Figure 4.37 C), substantiating misaligned orientation of ciliary patches between adjacent ependymal cells in the lateral ventricular walls of LRP2 deficient mice in comparison to controls.

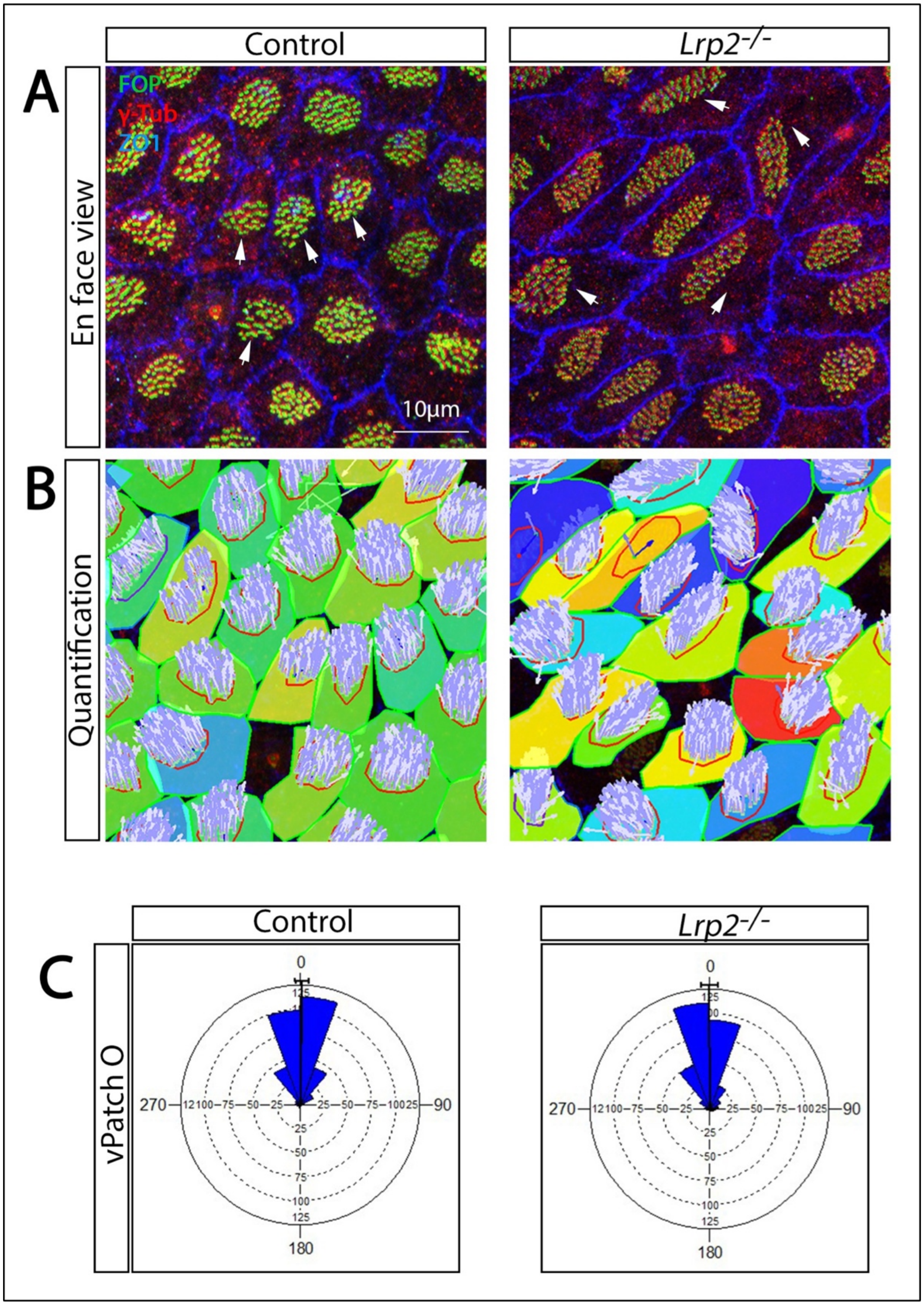

Figure 4.37: The beating orientation of the ciliary patch is not coordinated in *Lrp2*$^{-/-}$ ependymal cells.

(**A**) En face preparations of the lateral ventricular wall in control and LRP2-deficient mouse brains were immunostained for ciliary basal body markers FGFR1 Oncogene Partner (FOP; green) and gamma tubulin (γ-Tub, red), as well as for the apical cell surface marker zonula occludens-1 (ZO1; blue). Arrows indicate the ciliary patch beating orientation in representative ependymal cell as deduced from the orientation of the immunosignals for FOP and G-TUB. (**B**) Depiction of vectors from FOP (green) to γ-Tub, (red) signals indicate the orientation of individual cilia in ependymal cells of control and LRP2 mutant brains. (**C**) The angle VpatchO value represents the angle between the vector of ciliary orientation of the patch and the mean vector of orientation in the field. Circular dispersion of vPatchO parameter angles around the mean in control and LRP2 deficient mice are depicted. Circular statistical analysis (Watson U^2 test) on vPatchO values of 337 cells from controls and 342 cells from LRP2-deficient mice confirms a statistically significant decrease ($p<0.05$) in coordination of ciliary beating in LRP2 mutant cells as compared to control cells (five animals per genotype).

4.3.3 Ependymal cells in LRP2 deficient mice show misalignment in motile ciliary patch localization and beating orientation

According to earlier reports, ciliary beating orientation within a patch and patch displacement directions are aligned in ependymal cells of adult murine brain (Boutin et al., 2014).

So as a next step in my analyses, I calculated the angle created by patch displacement and ciliary beating orientation vectors, designated vPATCHD&vPATCHO. As presented in exemplary images in Figure 4.38 A, the beating orientation (highlighted by pink arrows) and the patch displacement direction (indicated by white arrows) were well aligned in control ependymal cells. By contrast, vPATCHD and vPATCHO vectors indicated random directions in LRP2 mutants (Figure 4.38 A). These observations were also reflected in the circular dispersion graphs around the mean, where parameters from LRP2 mutants displayed a wider range of angle values compared with controls (Figure 4.38 B).

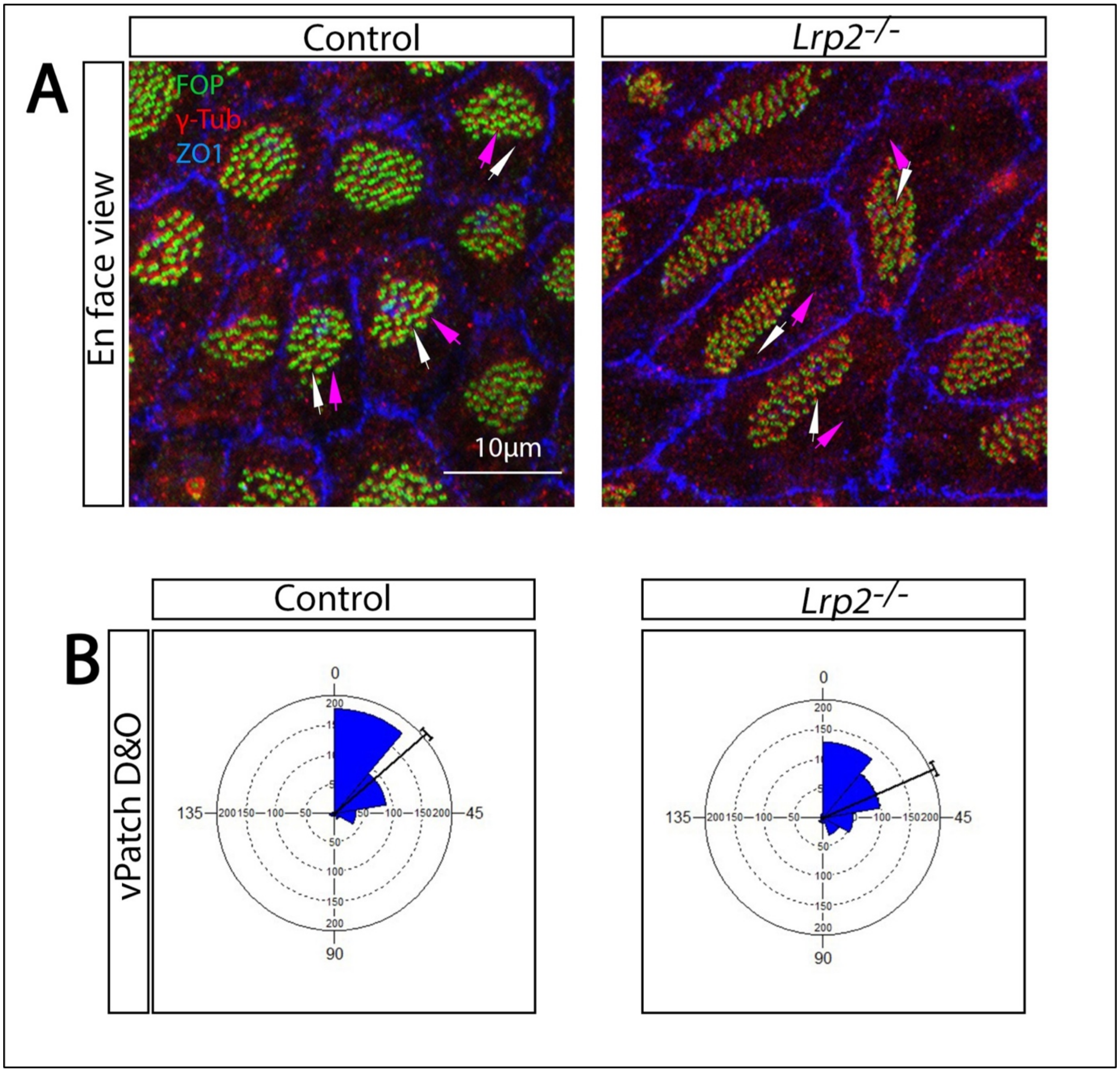

Figure 4.38: Ciliary patch localization and beating orientation are not coordinated in ependymal cells of *Lrp2*$^{-/-}$ mice.

(**A**) En face preparations of the lateral ventricular wall in control and LRP2-deficient mouse brains were immunostained for ciliary basal body markers FGFR1 Oncogene Partner (FOP; green) and gamma tubulin (γ-Tub, red), as well as for the apical cell surface marker zonula occludens-1 (ZO1; blue). White colored arrows show the direction of ciliary patch displacement. Pink arrows indicate the orientation of ciliary patch beating. In ependymal cells from control mice, ciliary beating orientation and ciliary displacement match within each cell. This match is not seen in LRP2-deficient ependymal cells. (**B**) vPatchD&vPatchO values represent the angle between the vector of displacement and the vector of orientation. Circular dispersion of vPatchD&vPatchO parameter angles around the mean in control and LRP2-deficient mice are shown. Circular statistical analysis (Watson U^2 test) comparing values of 337 cells from control and 342 cells from LRP2-deficient mice confirms statistically significant differences in ciliary patch displacement and beating orientation comparing the two genotypes ($p<0.001$).

4.3.4 Individual cilium beating directions are not synchronized within a ciliary patch in LRP2 mutant mice

Beating directions of individual motile cilia within a ciliary patch are coordinated (Boutin et al., 2014).

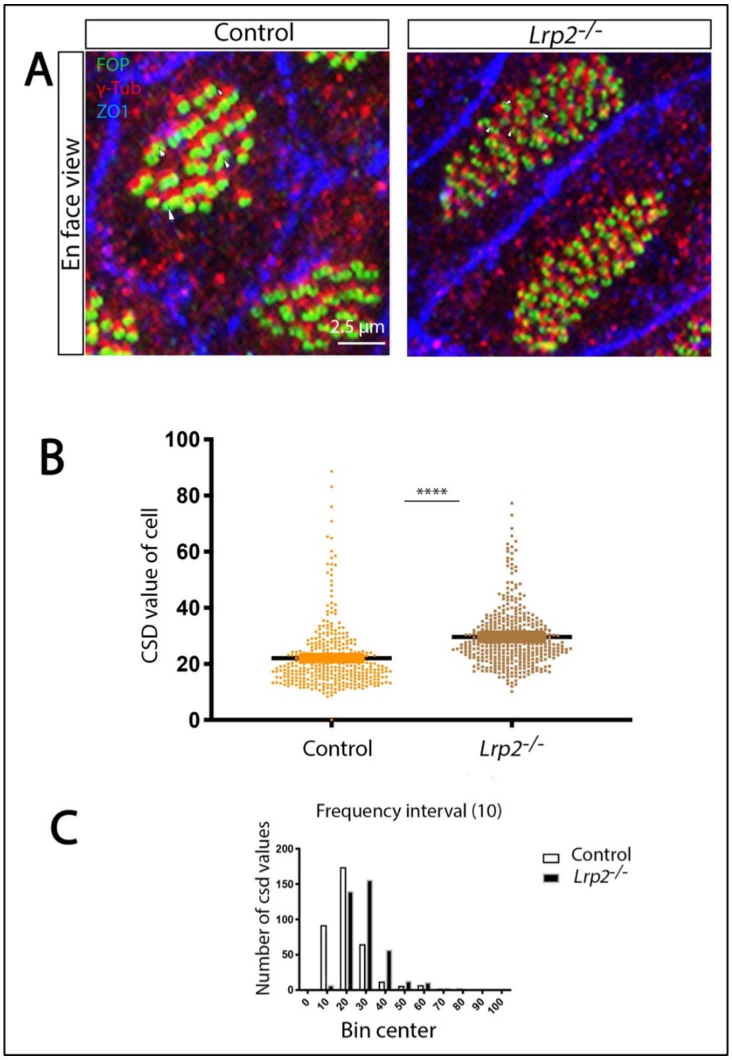

Figure 4.39: The beating direction of individual cilia within a ciliary patch is not coordinated in ependymal cells of *Lrp2*$^{-/-}$ mice.

(A) En face preparations of the lateral ventricular wall in control and LRP2-deficient mouse brains were immunostained for ciliary basal body markers FGFR1 Oncogene Partner (FOP; green) and gamma tubulin (γ-Tub, red), as well as for the apical cell surface marker P (ZO1; blue). Beating orientation of individual cilia within a patch are defined by a unit vector (vCil) connecting the two dots (green and red). (B) These vectors were used to calculate the circular standard deviation (CSD) values for each patch. In this presentation, each dot represents an individual cell, while Y-axis represents

CSD values of the cell. vCil vectors were randomly oriented in many cells of LRP2 deficient mice, resulting in high CSD values.

(C) Distribution of cells according to Vcil CSD values are represented. CSD values are depicted on X-axis from 0 to 100, by frequency interval 10. On the Y-axis, corresponding cell numbers are represented. Higher extent of control cells has lower CSD values, and oppositely more cells from LRP2 deficient mice posess higher CSD values. CSD values of 363 ependymal cells were quantified for LRP2 deficient mice and compared with CSD values of 391 cells from controls (five animals per genotype). Unpaired t test analysis revealed statistically significant difference between genotypes with $p<0.0001$.

Images used in previous investigations (Figure 4.36-4.38) were analyzed in this respect in wildtype and LRP2 mutant brains. In detail, the orientation vectors connecting basal feet marker γ-Tub and basal body marker FOP characterize beating orientation for an individual cilium within a ciliary patch.

This coordination of individual ciliary beating orientation within a patch was confirmed in control cells of the adult SVZ (Figure 4.39 A). By contrast, examination of the same number of ependymal cells in LRP2 mutants revealed many cells with non-coordinated cilia beating within a patch (Figure 4.39 A).

After manually defining vectors for orientation of each individual cilium in a given patch, circular standard deviation (CSD) values for each cell patch were generated by the Biotool software. In Figure 4.39 B, each cell is represented as a dot. Higher CSD values indicate more asynchronicity and non-coordination of individual cilium beating within a patch. In LRP2 mutants, the number of cells with high CSD values were significantly increased compared with littermate controls. Representation of the CSD values on the X-axis by distribution intervals of 10 demonstrated a higher number of control cells in the range of 0 to 20 CSD value. By contrast, in the range of 30 and higher CSD values, the numbers gradually increased in LRP2 mutant cells, indicating elevated non-coordinated beating within a patch in the mutants (Figure 4.39 C).

4.3.5 The numbers of motile cilia but not the size of the ciliary patch is altered in LRP2 mutant ependymal cells

As a next question, I have addressed whether LRP2 activity may influence the number of motile cilia per cell patch. Based on previous analysis, the numbers of individual cilia in cell patches were determined using the Biotool software (Figure 4.40 A, B). In these analyses, significantly increased numbers of cilia were observed in ependymal cell patches of LRP2 mutants compared with controls (Figure 4.40 C).

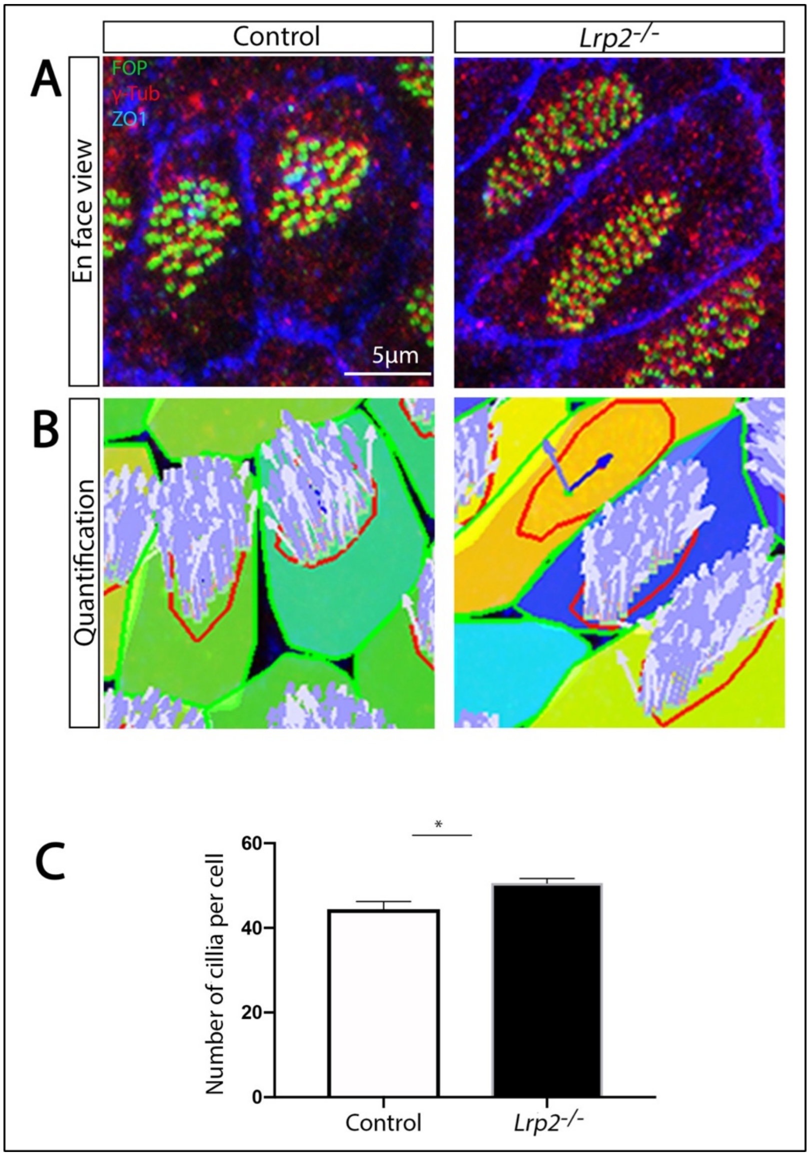

Figure 4.40: The number of motile cilia in a ciliary patch are increased in *Lrp2*$^{-/-}$ ependymal cells.

(A) En face preparations of the lateral ventricular wall in control and LRP2-deficient mouse brains were immunostained for ciliary basal body markers FGFR1 Oncogene Partner (FOP; green) and gamma tubulin (γ-Tub, red), as well as for the apical cell surface marker zonula occludens-1 (ZO1; blue). (**B**) Unit vector (vCil) connecting the two dots (green and red) was defined manually in the software. Those individual vCil vector numbers correspond to cilia numbers in the patch. (**C**) Cilia number per patch were counted in individual ependymal cells and averaged for each animal (five mice per genotype). Analysis by unpaired

Student's *t* test documents a significant increase in cilia number per patch in *Lrp2*$^{-/-}$ mice as compared with controls. *, $p<0.05$)

Despite this increase in number of motile cilia, the patch area and cell surface area covered by ciliary patches were similar in both genotypes (Figure 4.41 A-D). Also, the parameter describing the ratio of apical cell surface area to cilia patch area was unchanged in LRP2 mutants compared with controls (Figure 4.41 C). Finally, despite the direction of patch displacement from the cell center not being coordinated in LRP2 mutant cells (Figure 4.36), the extent of displacement from the center (Strength) was similar to that in the control genotype (Figure 4.41 E).

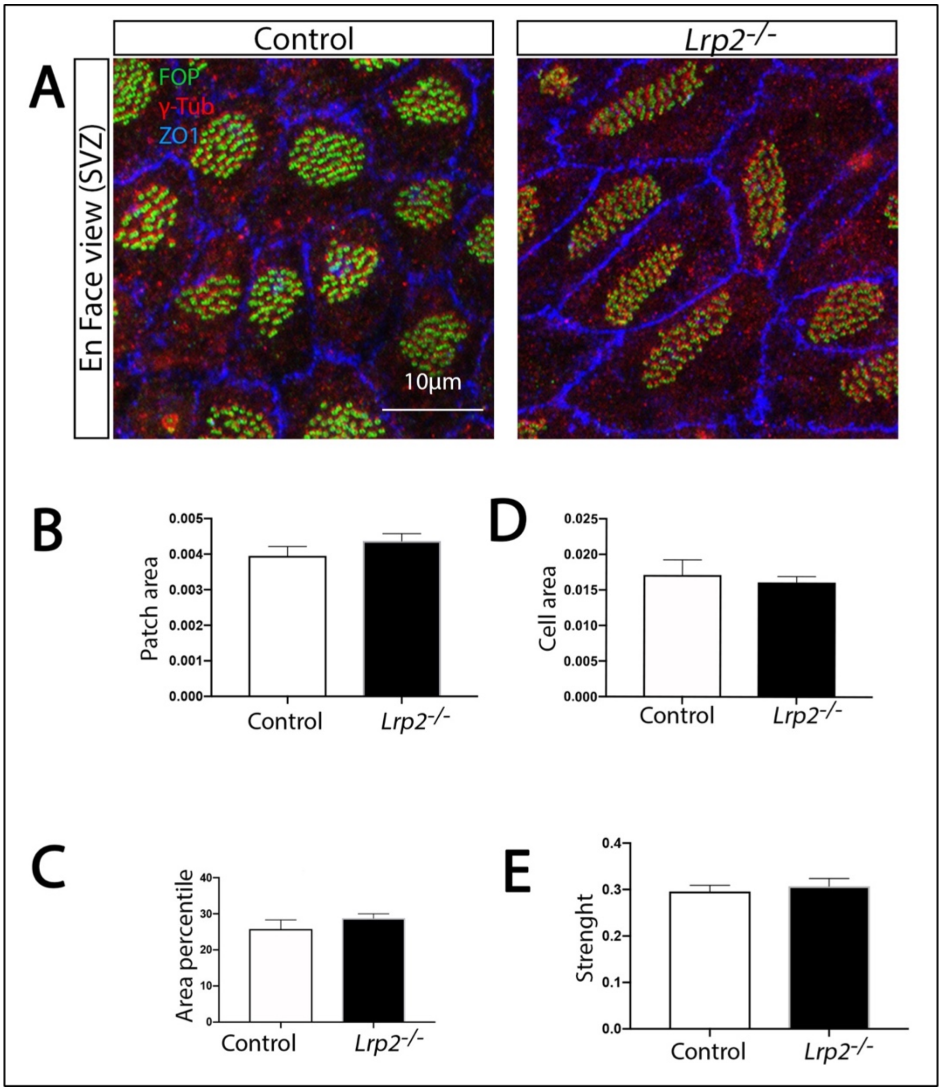

Figure 4.41: The extent of ciliary patches and of ependymal cell surface are unchanged in mice lacking LRP2.

(A) En face preparations of the lateral ventricular wall in control and LRP2-deficient mouse brains were immunostained for ciliary basal body markers FGFR1 Oncogene Partner (FOP; green) and gamma tubulin (γ-Tub, red), as well as for the apical cell surface marker zonula occludens-1 (ZO1; blue). (**B**) Patch areas of ependymal cells in control and LRP2 mutant mice are given. (**C**) The percentage of the apical cell surface occupied with ciliary patches in control and LRP2 mutant mice are given. (**D**) The surface area of individual ependymal cells in control and LRP2 mutant mice is shown. (**E**) Strength parameter estimating the amount of ciliary patch displacement relative to the center of ependymal cells is given. All parameters (B-E) were quantified in 363 ependymal cells from *Lrp2*$^{-/-}$ and 391 ependymal cells from control mice. Five mice per genotype were used. No statistically significant differences between the two genotypes were detected using unpaired Student's *t* test.

4.3.6 Ciliary axonemal structures are unchanged in ependymal cells of *Lrp2*$^{-/-}$ compared with control brains

My analyses of motile cilia beating described above were based on visualization of the position of the basal body marker FOP relative to the position of the basal foot marker γ-tubulin. To confirm that the observed alterations reflected changes in cilia beating not structural organization, I stained for additional markers of motile cilia in LRP2 mutant and control SVZs.

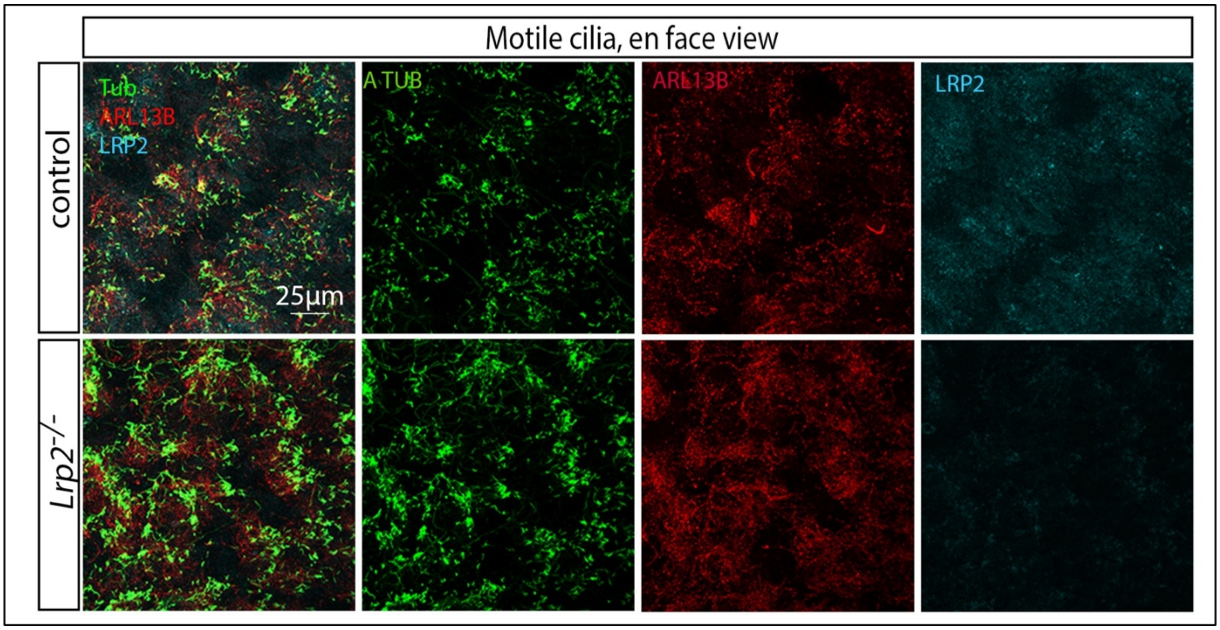

Figure 4.42: The structure of the ciliary axoneme is comparable in ependymal cells of *Lrp2*$^{-/-}$ and control mice.

En face preparations of the lateral ventricular wall of control and LRP2 mutant brains were immunostained for acetylated tubulin (Tub; green) and ADP-ribosylation factor-like protein 13B (ARL13B; red) to visualize the ciliary axoneme. Also, localization of LRP2 was documented (blue). Color channels are shown separately as well as in merged configuration. No discernable difference in the patterns of the two axoneme proteins are seen comparing LRP2-deficient and control cells.

Specifically I immunostained for acetylated tubulin (Tub) and ADP-ribosylation factor-like protein 13B (ARL13B), two markers of the ciliary axoneme (Mirvis, Stearns, & James Nelson, 2018). As shown in figure 4.42, no discernable differences in immunosignals for either protein were seen in LRP2 mutant compared with control cells. My observations supported previous findings from electron microscopy analyses indicating structural integrity of the ciliary axoneme in LRP2 mutant mice (Gajera et al., 2010).

4.4 LRP2 mediates endocytic uptake of SHH by ependymal cells

4.4.1 Analysis of SHH uptake using primary ependymal cultures

A role for LRP2 in the endocytic uptake of SHH-N was initially reported in cultured cells (McCarthy et al., 2002) and in the rat epididymis *in vivo* (Morales et al., 2006). Later studies substantiated the relevance of LRP2 as SHH receptor by documenting its ability to act as auxiliary binding site for the morphogen on neuroepithelia cells in the neural tube. LRP2-mediated binding and uptake of SHH-N in this cell type facilitates morphogen signaling through its cognate receptor PTCH1(Christ et al., 2012). LRP2-dependent uptake of SHH-N was also documented in the cells of the embryonic retina. However in this tissue, receptor-mediated clearance of SHH-N reduces rather than promotes morphogen action (Christ et al., 2015). Whether LRP2 also mediates endocytic uptake of SHH-N in multiciliated ependymal cells in the adult SVZ and whether such uptake may promote or antagonize SHH action remained unclear.

Here, I addressed this question by using a primary cell culture model of ependymal cells. For this experimental procedure, mice at 0 to 2 days of age (P0-P2) were used. Freshly dissected walls of lateral ventricles were digested with papain solution to obtain a single cell suspension which was plated on culture dishes. As soon as the cultures reached confluency (after 2-3 days), the proliferation medium was replaced by differentiation medium to trigger their differentiation to ependyla cells.(Delgehyr et al., 2015, p. 2) From differentiation day 10 (10 DIV) onwards, cells in culture expressed actively beating motile cilia, a feature reminiscent of fully mature ependymal cells in the adult murine brain.

To study endocytic uptake of SHH in primary ependymal cells, I treated cultures derived from control and LRP2 mutant embryos at 10 DIV with a fusion protein of glutathione S-transferase and SHH-N (GST-SHH-N) produced and purified from bacteria as previously described (Christ et al., 2012). Following incubation for 2 hours, the cells were fixed and immunostained for GST-SHH-N using an antibody directed against GST. As shown in Figure 4.43, multiciliated ependymal cells lacking LRP2 fail to take up GST-SHH-N as compared with control cells.

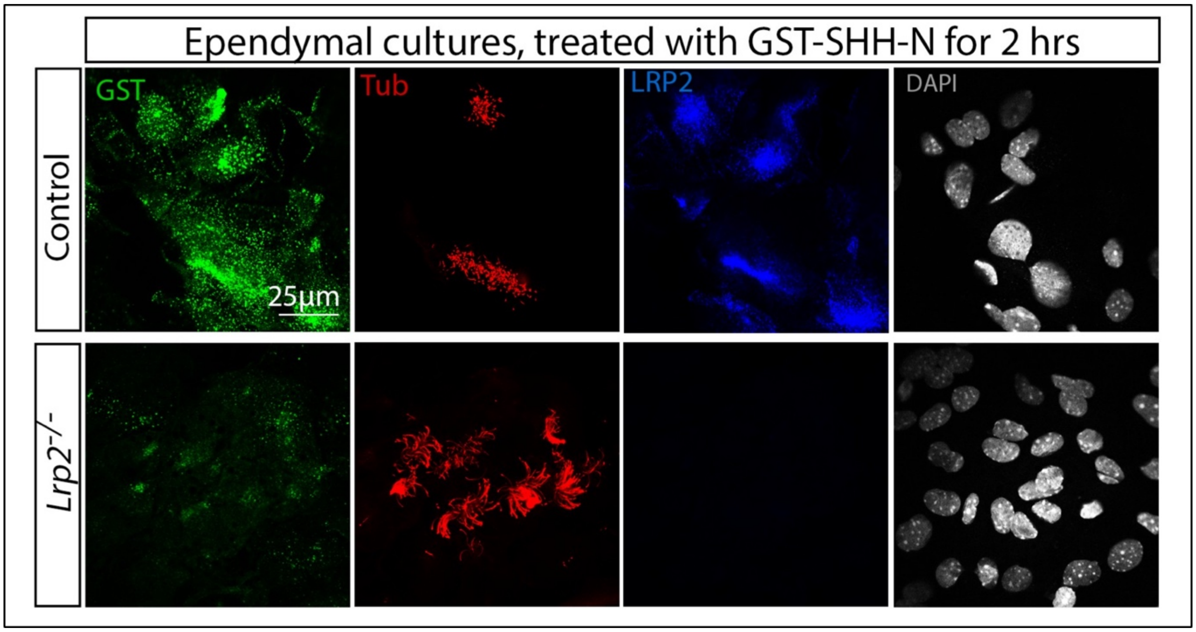

Figure 4.43: Ependymal cells from LRP2-deficient mice fail to take up GST-SHH-N during 2 hours of ligand incubation.

Ependymal cultures (differentiation day 10, DIV10) from *Lrp2*$^{-/-}$ and control mice (*Lrp2*$^{+/+}$ and *Lrp2* $^{+/-}$) were treated with 10 µg/ml GST-SHH-N for 2 hours at 37°C with 5% CO_2 and 95% humidity. Subsequently, cells were fixed and immunostained for GST-SHH-N (using anti-GST IgG; green), acetylated tubulin (a Tub; red), and LRP2 (blue). Cell nuclei were counterstained with DAPI (white). Color channels are shown individually and in merged configuration. Reduced uptake of GST-SHH-N is seen in LRP2-deficient ependymal cells as compared to control cells.

A similar defect in endocytic uptake of GST-SHH-N was also observed after 24 hours of incubation (Figure 4.44).

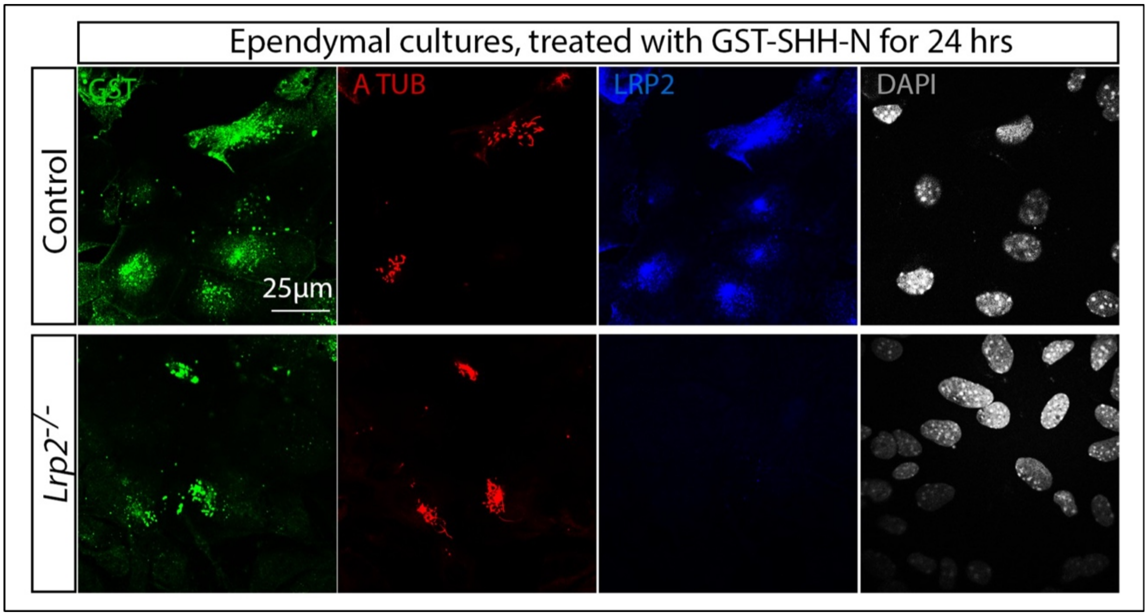

Figure 4.44: Ependymal cells of LRP2-deficient mice fail to take up GST-SHH-N during 24 hours of ligand treatment.

Ependymal cell cultures derived from *Lrp2*$^{-/-}$ and control mice were treated at DIV10 with 10 µg/ml GST-SHH-N. After 24 hours of incubation, the cells were fixed and immunostained for GST-SHH-N (using anti-GST IgG; green), acetylated tubulin (Tub; red), and LRP2 (blue). Cell nuclei were counterstained with DAPI (white). Color channels are shown individually and in merged configuration. A significant reduction in uptake of GST-SHH-N is seen in LRP2-deficient ependymal cells as compared to control cells.

To more directly monitor the cellular fate of SHH-N, I repeated the above experiments using an antibody directed against SHH. Immunocytochemical analysis of post-fixed ependymal cultures treated with GST-SHH-N for 2 hours substantiated a significant decrease in the capacity of mutant ependymal cells to internalize SHH-N (Figure 4.45).

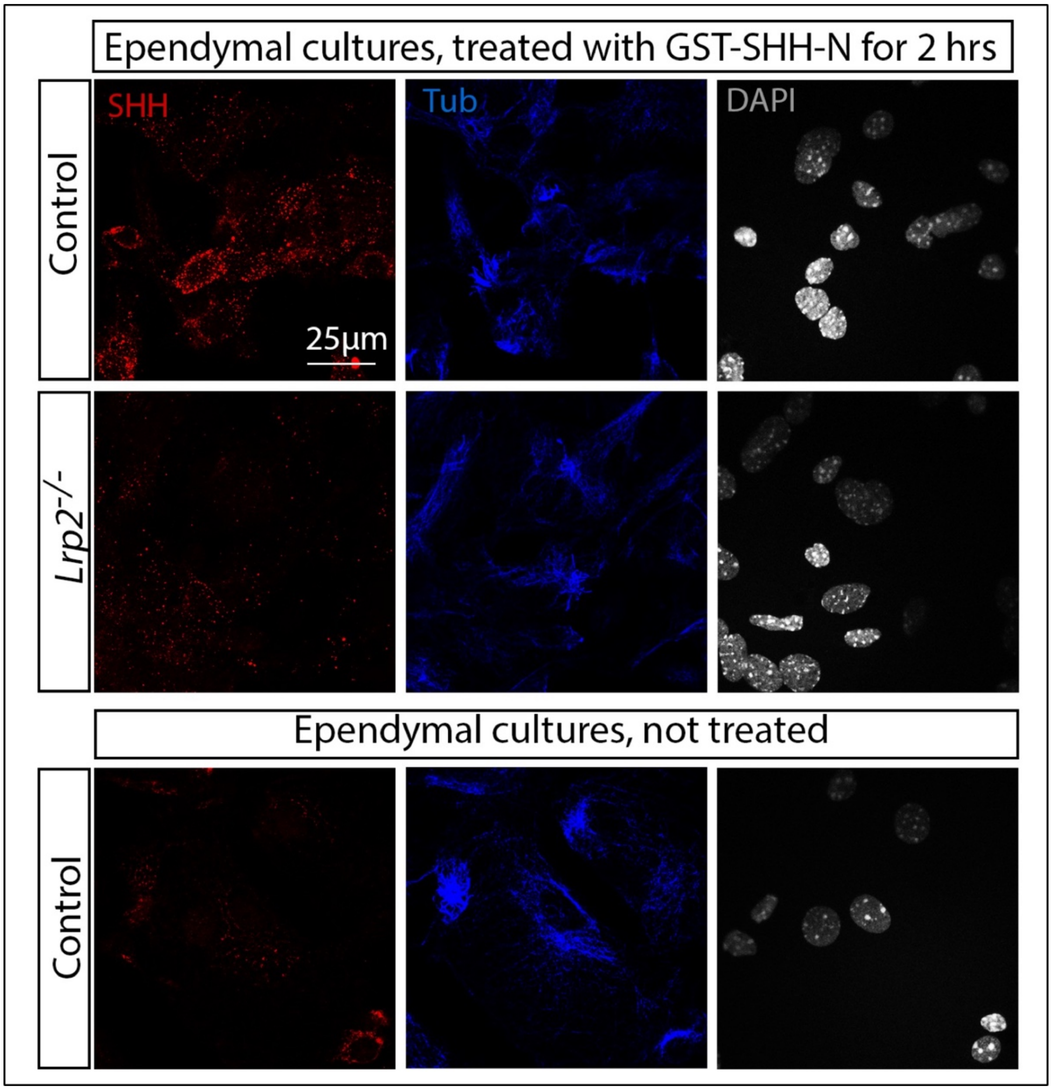

Figure 4.45: Ependymal cells of LRP2 deficient mice fail to take up GST-SHH-N ligand during 2 hours of ligand treatment.

Ependymal cell cultures derived from *Lrp2*$^{-/-}$ and control mice were treated at DIV10 with 10 µg/ml GST-SHH-N. After 2 hours of ligand incubation, cells were fixed and immunostained for SHH (using anti-SHH

IgG; red) and acetylated tubulin (a Tub; blue). Cell nuclei were counterstained with DAPI (white). Color channels are shown individually and in merged configuration. Little uptake of SHH-N is seen in LRP2-deficient ependymal cells as compared to control cells. As a control, cultures of control ependymal cells not incubated with GST-SHH-N were subjected to the same staining procedure to monitor levels of endogenous SHH present in these cells (lower panels). No immunosignal for SHH is seen under these conditions.

4.4.2 Analysis of SHH uptake using ventricular lateral wall whole mounts (LWWM)

To test the *in vivo* relevance of my previous findings with GST-SHH-N uptake in cultured cells, I treated en face preparations of the VZ from controls and *Lrp2*$^{-/-}$ mice with recombinant GST-SHH-N. For internal control, freshly dissected preparations from one brain hemisphere were treated with GST-SHH-N, while the other hemisphere was treated with GST. After ligand treatment, the tissue samples were fixed and immunostained for GST-SHH-N. Despite a slight deterioration of the ependymal layer integrity after 1.5 hours of incubation, most ependymal cells retained the characteristic pattern of FOP immunopositive ciliary bundles (Figure 4.46).

Following detection of GST-SHH-N by anti-GST antibody, uptake of GST-SHH-N was clearly seen in control but not in LRP2 mutant tissues (Figure 4.46), recapitulating my findings in primary ependymal cells. No specific immunosignal was seen in the hemispheres treated with GST, confirming that the intracellular immunosignal detected with anti-GST antisera represented GST-SHH-N.

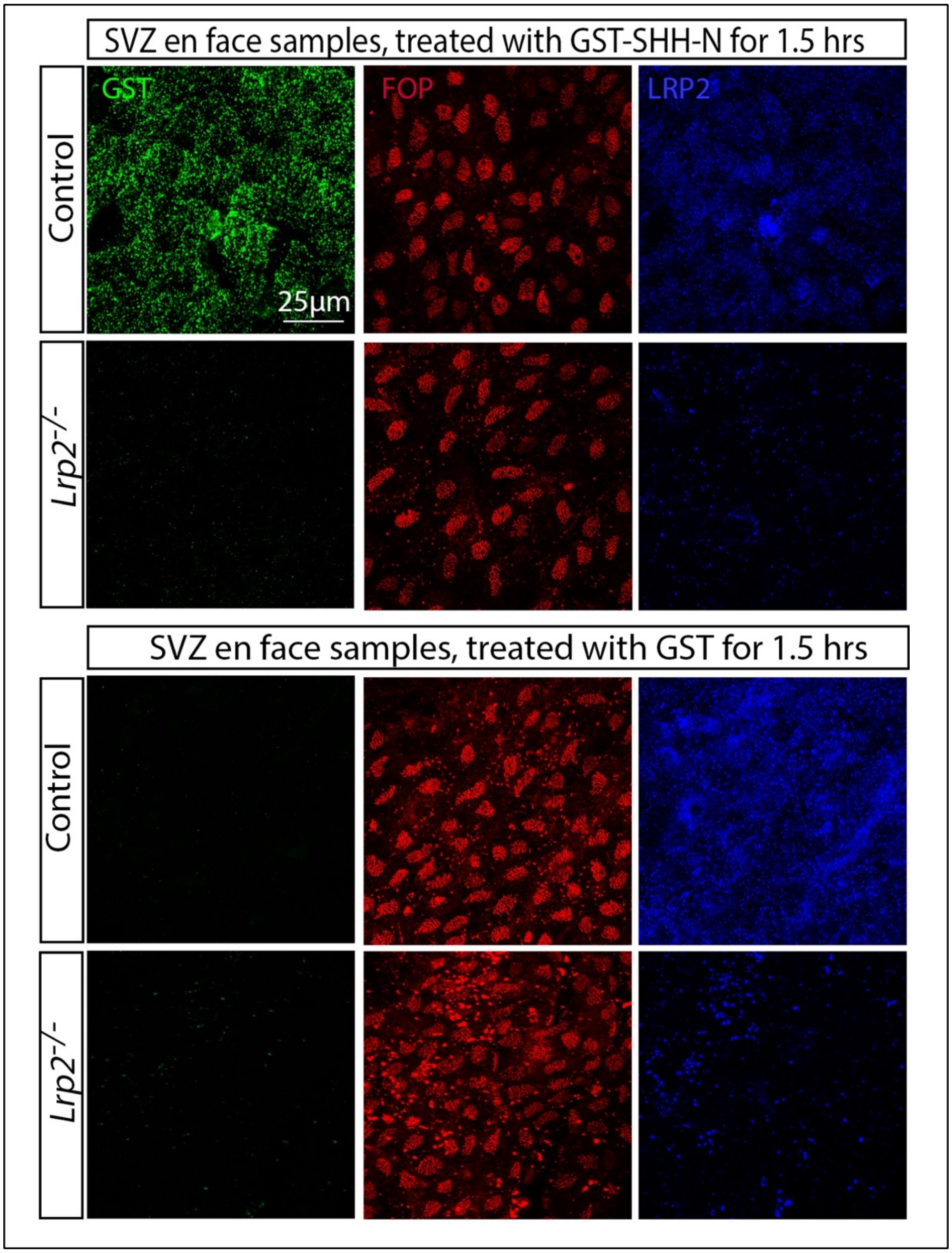

Figure 4.46: En face preparations of the lateral ventricles from adult LRP2-deficient mice fail to take up exogenous GST-SHH-N.

Freshly dissected lateral ventricles from LRP2-deficient and control mice were treated for 1.5 hours with 10µg/ml GST-SHH-N (upper panel) or 10µg/ml GST (lower panel). Subsequently, tissues were fixed and immunostained for GST (green), FOP (red), and LRP2 (blue). Whole mounts of the lateral ventricle from LRP2-deficient mice fail to take up GST-SHH-N, whereas uptake of this ligand is prominent in control cells. No uptake of GST is seen in either genotype.

4.4.3 Localization of internalized SHH ligand in various cellular compartments

Next, I traced the intracellular fate of internalized SHH in primary wildtype ependymal cells.

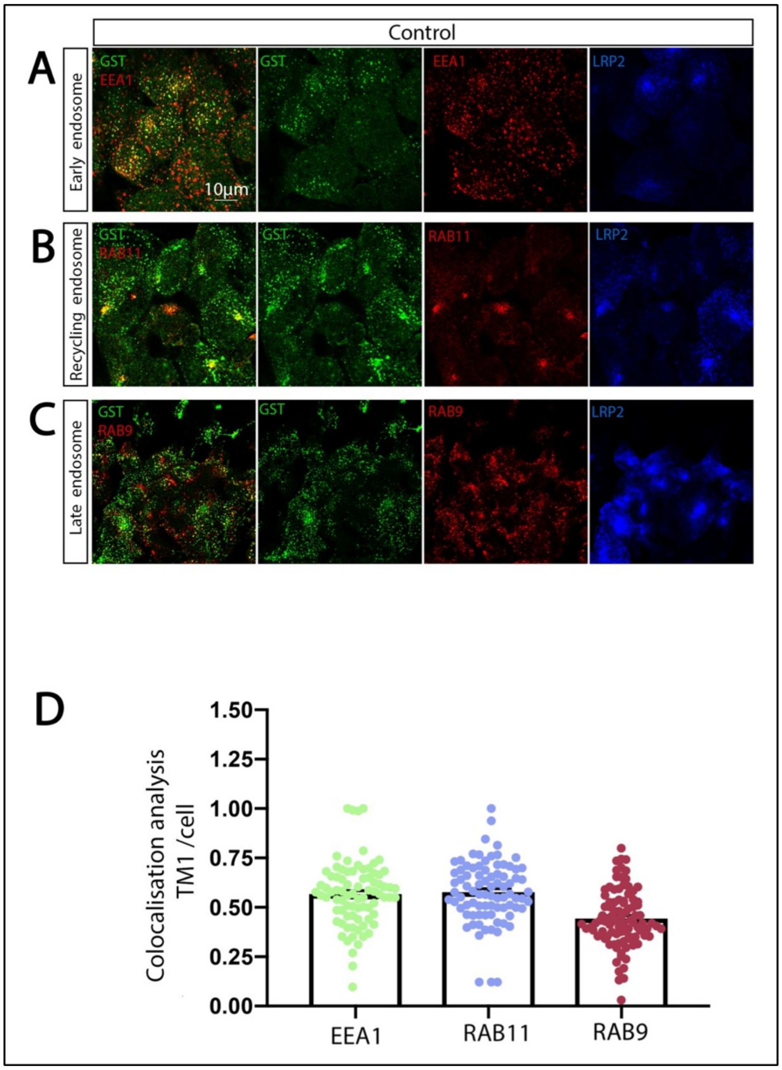

Figure 4.47: Internalized SHH-N is mainly found in early endosomal and recycling compartments of ependymal cells.

(**A-C**) Ependymal cell cultures derived from control mice were treated at DIV10 with 10 µg/ml GST-SHH-N. After 2 hours of ligand incubation, the cells were fixed and immunostained for GST-SHH-N (green), LRP2 (blue), and either early endosome antigen 1 (EEA1; panel A), Ras-related protein antigen 11 (Rab11; panel B) or Rab9 (panel C). Color channels are shown individually or in merged configuration. (**D**) Localization analysis using the thresholded Mander's value TM1 documents the extent of co-localization of GST-SHH-N with EEA1 (early endosomes), Rab11 (recycling endosome), and Rab9 (late endosomes).

For this, primary ependymal cultures were treated with GST-SHH-N (Figure 4.47 A-C), fixed, and co-immunostained for GST-SHH-N and markers of early, late, and recycling endosomal compartments. Co-localization analysis of ependymal cells stained for EEA1 and GST-SHH-N revealed a substantial localization of the ligand with this marker of early endosomal compartment (Figure 4.47 A, D). A similar extent of co-localization was seen for GST-SHH-N with the recycling endosomal compartment marker Rab11 (Figure 4.47 B, D). By contrast, the extent of co-localization was significantly lower for the late endosomal marker Rab9 (Figure 4.47 C, D).

In conclusion, SHH internalized by LRP2 in ependymal cells seemed to undergo a recycling rather than a late endosomal/lysosomal fate.

4.5 LRP2 determines localization of Rab GTPases in motile cilia

Over 70 G proteins of the so-called Rab GTPases superfamily have been discovered. Rab proteins are localized to all membrane compartments of cellular organelles, including endoplasmic reticulum, Golgi, endosomes, lysosomes, and the nucleus, just to name a few.

In epithelial cells, Rab GTPases are implicated in trafficking of junctional proteins and, consequently, in establishing cellular polarity. As well as controlling vesicular trafficking in the endosomal-lysosomal system. Rab GTPases have also been shown to interact with ciliary compartment proteins and to determine trafficking processes in primary cilia (Blacque, Scheidel, & Kuhns, 2017).

4.5.1 Early endosomal compartment markers are reduced in cell body and motile cilia of ependymal cells lacking LRP2

So far, the relevance of Rab proteins for functional integrity of motile cilia has not been investigated. However, my observation of LRP2-dependent sorting of SHH-N to Rab positive compartments of the endosomal system (Figure 4.47) prompted me to test the impact of LRP2 activity on potential sorting of Rab proteins to and from motile cilia in primary ependymal cells.

Initially, I stained primary ependymal cells treated with GST-SHH-N for early endosomal markers Rab4 and EEA1. In control cells, Rab4 displayed an obvious perinuclear pattern (Figure 4.48 A). In addition, the protein also showed extensive localization to the ciliary axoneme as documented by co-staining for tubulin (Figure 4.48 B). In LRP2-deficient ependymal cells, levels of Rab4 in the cell body (Figure 4.48 C) and in motile cilia (Figure 4.48 D) were significantly decreased, in line with the obvious endocytic defect in cells lacking LRP2.

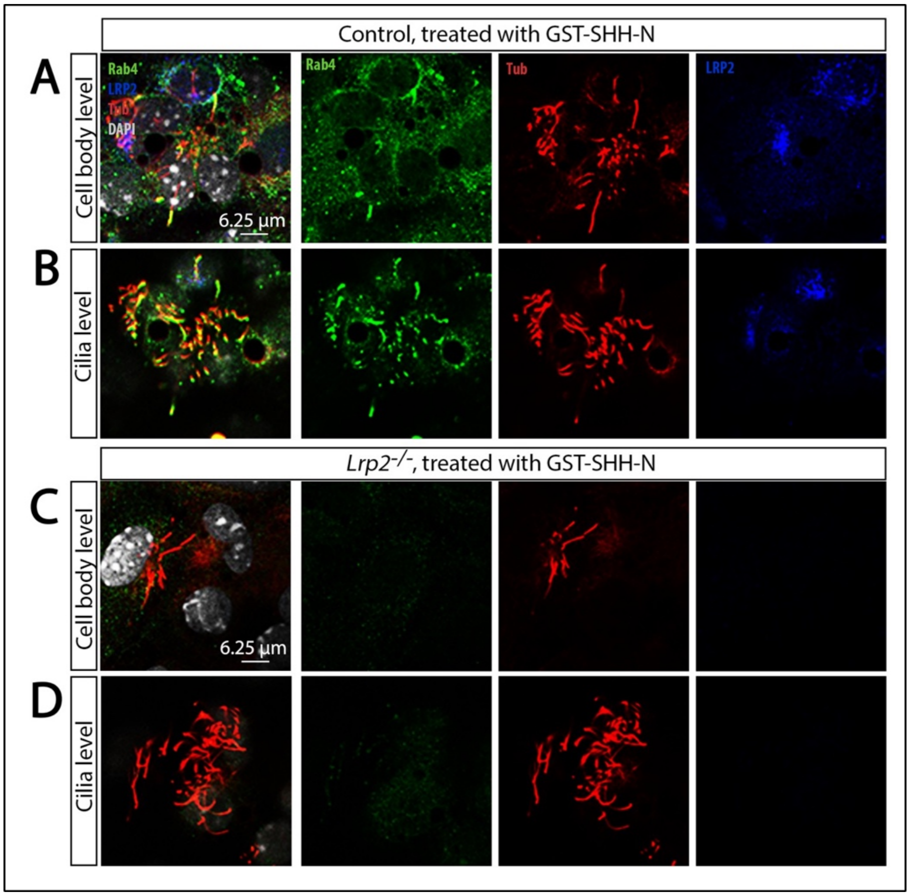

Figure 4.48: Localization of early endosomal marker Rab4 in motile cilia and in cell soma of ependymal cells.

Ependymal cell cultures derived from control (A, B) and *Lrp2*$^{-/-}$ (C, D) newborn mice were treated at DIV10 with 10 µg/ml GST-SHH-N. After 2 hours of ligand incubation, the cells were fixed and immunostained for early endosomal marker Rab4 (green), ciliary axoneme marker acetylated tubulin (a Tub; red) and LRP2 (blue). Cell nuclei were counterstained with DAPI (white). Color channels are shown individually or in merged configuration. Single plane of section images from the cell body (A, C) or the ciliary axoneme (B, D) were chosen from an optical series and displayed separately.

Prominent immunosignals for Rab4 are seen in the axoneme of the motile cilia and in the cell body in control but not in LRP2 mutant ependymal cells. Immunosignals for the axoneme marker acetylated tubulin are comparable in cells from control and *Lrp2*$^{-/-}$ mice.

Early endosome antigen 1 (EEA1) is a membrane bound protein that interacts with Rab5 and plays an important role in early endosomal trafficking(Jovic, Sharma, Rahajeng, & Caplan, 2010). EEA1 is widely used as a marker for early endosomes. In my studies, EEA1 was strongly expressed in ependymal cells where it localized to the base of the motile cilia (Figure 4.49 A, B). As seen for Rab4 before, levels for EEA1 were decreased in the soma of ependymal cells from LRP2 deficient mice (Figure 4.49 C) and no EEA1 signal was noted at the level of the cilia (Figure 4.49 D).

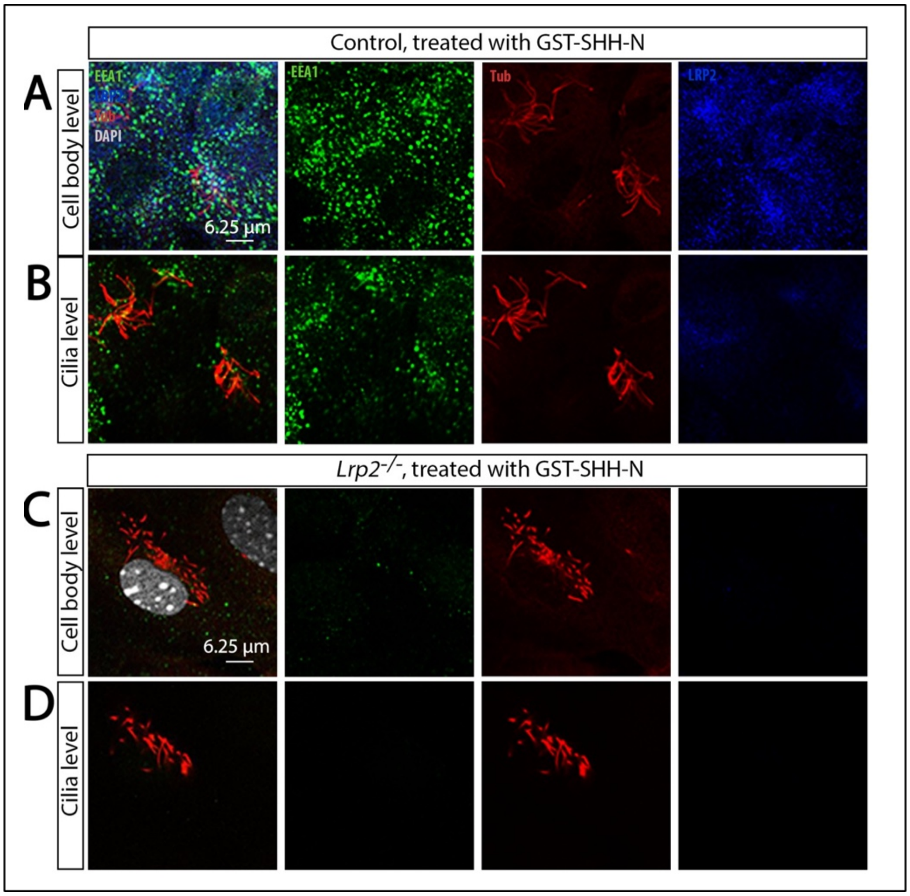

Figure 4.49: EEA1 levels in ependymal cells and motile cilia of *Lrp2*$^{-/-}$ and control mice.

Ependymal cell cultures derived from control (A, B) and *Lrp2*$^{-/-}$ (C, D) newborn mice were treated at DIV10 with 10 µg/ml GST-SHH-N for 2 hrs. Subsequently, the cells were fixed and immunostained for early endosome antigen 1 (EAA1; green), axonem marker acetylated tubulin (a Tub; red), and LRP2 (blue). Cell nuclei were counterstained with DAPI (white). Color channels are shown individually or in merged configuration. Single plane of section images from the cell body (A, C) or the ciliary axoneme (B, D) were chosen from an optical series and displayed separately. In cell bodies and at the base of the ciliary axonome, levels of EEA1 (representing early endosomes) are significantly reduced in *Lrp2*$^{-/-}$ ependymal cells compared with controls. Immunosignals for the axoneme marker acetylated tubulin are comparable in both genotypes.

Jointly, these data documented a significant decrease in the early endosomal compartment of LRP2-deficint ependymal cells, both in the cell body and in the motile cilia.

4.5.2 Recycling endosomal compartment markers are unchanged in ependymal cells and in motile cilia lacking LRP2

Next, I investigated the impact of LRP2 deficiency on the composition of the recycling compartment in primary ependymal cells. To do so, I tested for the subcellular pattern of Rab35. As a regulator of rapid recycling, Rab35 is localized mainly to the plasma membrane and to early endosomal structures (Kouranti, Sachse, Arouche, Goud, & Echard, 2006, p. 35; Sato et al., 2008).

Immunostaining for Rab35 in ependymal cells treated with GST-SHH-N indicated localization pattern of this protein to cell body and the motile ciliary axoneme of control cells (Figure 4.50 A, B). Examination of LRP2-deficient ependymal cells failed to detect any obvious differences in this pattern (Figure 4.50 C, D).

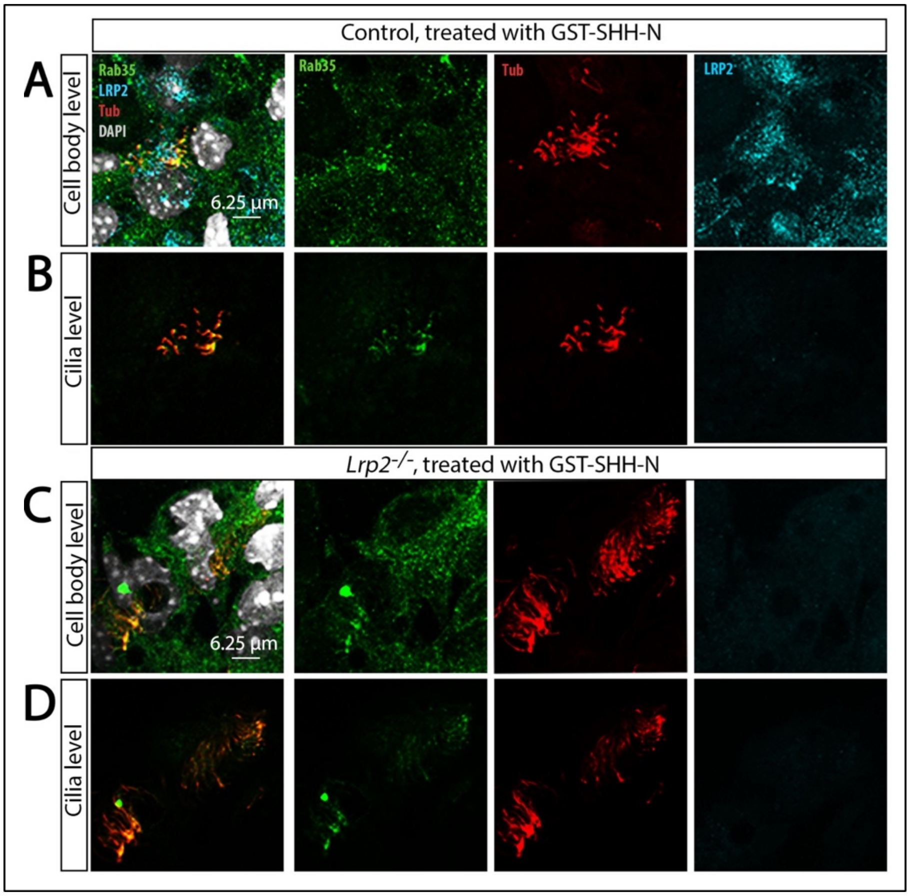

Figure 4.50: Levels of Rab35 in cell body and motile cilia of ependymal cultures.

Ependymal cell cultures derived from *Lrp2*$^{-/-}$ and control mice at DIV10 were treated with 10 µg/ml GST-SHH-N for 2 hrs. Thereafter, cell cultures were immunostained for fast recycling endosome marker Rab35, axoneme marker acetylated tubulin (a Tub; red), and for LRP2 (blue). Cell nuclei were counterstained with DAPI (white). Color channels are shown individually or in merged configuration. Single plane of section images from the cell body (A, C) or the ciliary axoneme (B, D) were chosen from an optical series and displayed separately. Immunosignals for Rab35 are seen in the cell body and ciliary axoneme of ependymal cells with no apparent differences comparing control and *Lrp2*$^{-/-}$ cultures.

Rab11 GTPase is considered a specific marker for the slow recycling compartment in the endosomal circuitry. In my immunostainings, Rab11 showed a pronounced perinuclear pattern in ependymal cells of controls (Figure 4.51 A). In addition, Rab11 localized to the base of the cilia but not to axonemal structures (Figure 4.51 B). No consistent differences in the Rab11 pattern were noted comparing *Lrp2* $^{-/-}$ and control ependymal cells (Figure 4.51 C). Also, analysis of motile cilia in *Lrp2*$^{-/-}$ ependymal cells recapitulated the same basal localization as seen for controls (Figure 4.51 B, D).

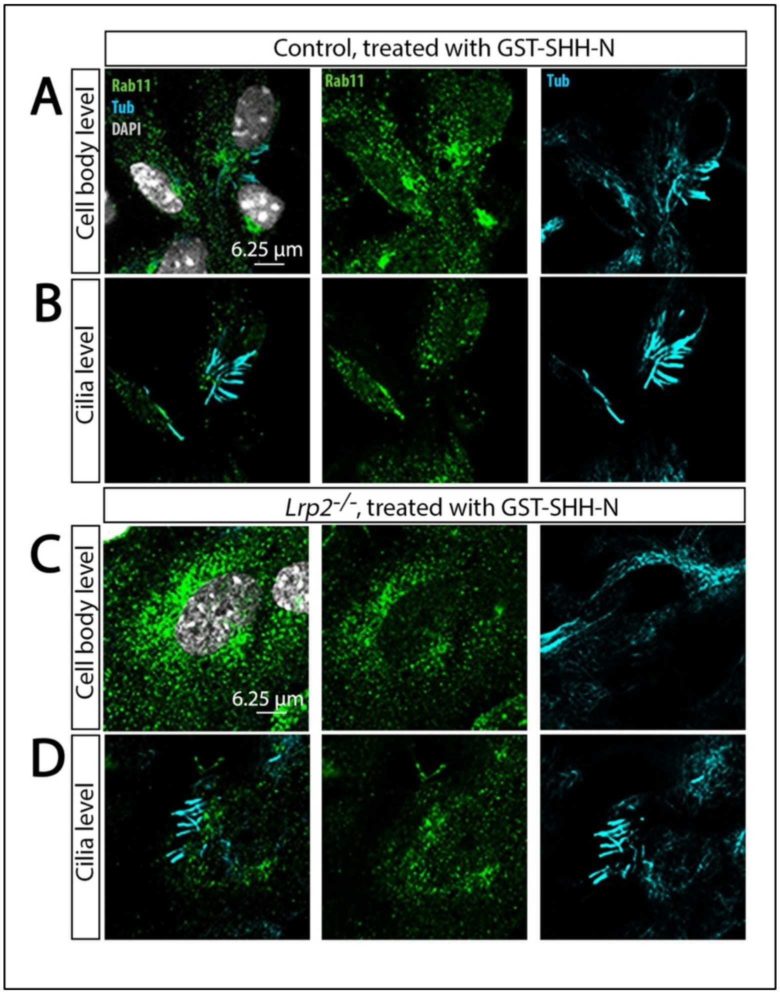

Figure 4.51: Levels of Rab11 in cell body and motile cilia of primary ependymal cells.

Ependymal cell cultures derived from *Lrp2*$^{-/-}$ and control mice at DIV10 were treated with 10 µg/ml GST-SHH-N for 2 hrs. Thereafter, cell cultures were immunostained for recycling endosome marker Rab11 (green) and axonem marker acetylated tubulin (a Tub; blue). Cell nuclei were counterstained with DAPI (white). Color channels are shown individually or in merged configuration. Single plane of section images from the cell body (A, C) or the ciliary axoneme (B, D) were chosen from an optical series and displayed separately. Rab11 can be detected in the cell body (A, C) and at the base of the ciliary axoneme (cyan signal in B and D) with no apparent difference in levels comparing the two genotypes.

In summary, my investigation of rapid and slow recycling compartment markers failed to reveal obvious differences in subcellular localization in ependymal cells and motile cilia comparing *Lrp2* genotypes.

4.5.3 LRP2 deficiency impacts distribution of Rab GTPases involved in transcytosis and cell signaling in ependymal cell body and motile cilia

Several recycling endosome markers are involved in control of transcytosis as well. For example, Rab8a can be found not only in slow recycling compartments but also in vesicular structures that traffic to the basolateral membrane of polarized cells. It is therefore considered as a apico-basal recycling marker (Henry & Sheff, 2008).

In ependymal cells from controls, Rab8a showed extensive immunostaining in the cell body (Figure 4.52 A). It also showed localization to the axoneme and the base of motile cilia (Figure 4.52 B). Ependymal cells from *Lrp2*$^{-/-}$ exhibited a similar subcellular localization of Rab8a to cell body (Figure 4.52 C) and motile cilia (Figure 4.52 D).

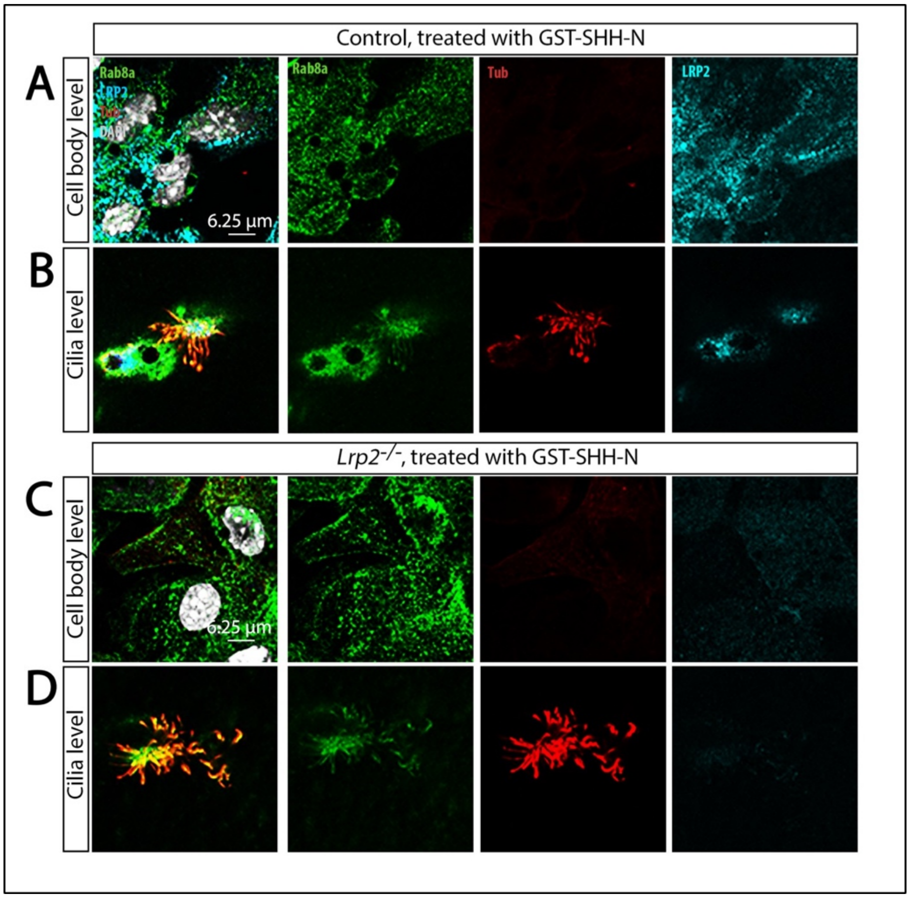

Figure 4.52: Rab8a expression in cell body and motile cilia of primary ependymal cells.

Ependymal cell cultures derived from *Lrp2*$^{-/-}$ and control mice at DIV10 were treated with 10 µg/ml GST-SHH-N for 2hrs. Thereafter, cell cultures were immunostained for the apico-basal recycling endosome marker Rab8a, for axoneme marker acetylated tubulin (aTub; red), and for LRP2 (blue). Cell nuclei were counterstained with DAPI (white). Color channels are shown individually or in merged configuration. Single plane of section images from the cell body (A, C) or the ciliary axoneme (B, D) were chosen from an optical series and displayed separately. In the cell body, Rab8a levels are comparable between *Lrp2*$^{-/-}$ and control ependymal cultures (A, C). Also, Rab8a can be detected in the axoneme of the motile cilia with no apparent difference in intensities comparing the two genotypes (B, D).

Another marker characterizing transcytosis and apico-basal recycling processes is Rab17(Hunziker & Peters, 1998; Zacchi et al., 1998, p. 17). It localized to subcellular structures in the cell body with no apparent differences in pattern and intensity comparing control and LRP2-deficient ependymal cells (Figure 4.53 A, C).

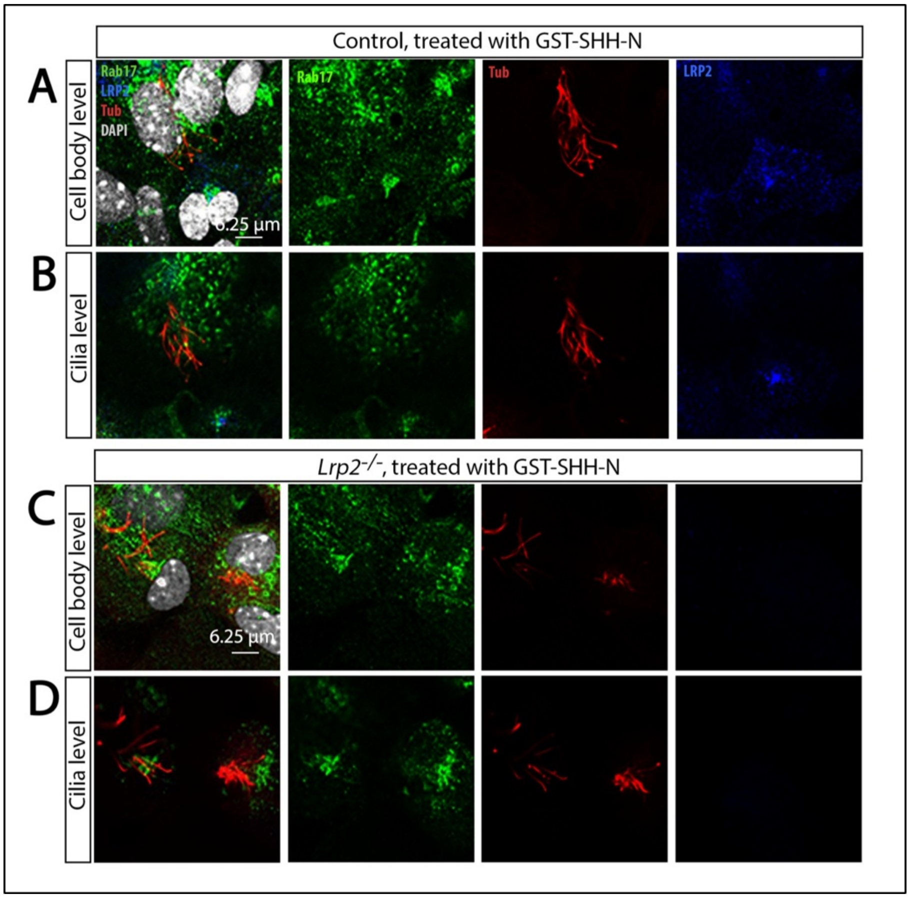

Figure 4.53: Rab17 levels in cell body and motile cilia of ependymal cells.

Ependymal cell cultures derived from *Lrp2*$^{-/-}$ and control mice at DIV10 were treated with 10 µg/ml GST-SHH-N for 2hrs. Thereafter, cell cultures were immunostained for apico-basal recycling endosome marker Rab17 (green), axoneme marker acetylated tubulin (aTub; red), and for LRP2 (blue). Cell nuclei were counterstained with DAPI (white). Color channels are shown individually or in merged configuration. Single plane of section images from the cell body (A, C) or the ciliary axoneme (B, D) were chosen from an optical series and displayed separately. Rab17 levels are unchanged in *Lrp2*$^{-/-}$ ependymal cultures compared with control cells (A, C). At the level of the cilia, Rab17 protein can be detected at the base but not in the ciliary axoneme of ependymal cells (B, D), with no apparent difference comparing genotypes.

In motile cilia of control cells, Rab17 localized to the ciliary base (Figure 4.53 B), a pattern also shared by LRP2 mutant cells (Figure 4.53 D).

Rab23 is a marker for recycling endosomes with a regulatory role in trafficking processes during SHH signaling (Evans, Ferguson, Wainwright, Parton, & Wicking, 2003, p. 23; Fuller, O'Connell, Gordon, Mauti, & Eggenschwiler, 2014, p. 23; L.-Q. Zheng, Chi, & Li, 2017, p. 23). In ependymal cells from controls, Rab23 showed sparse distribution in the cell body and an obvious absence from motile cilia structures (Figure 4.54 A, B).

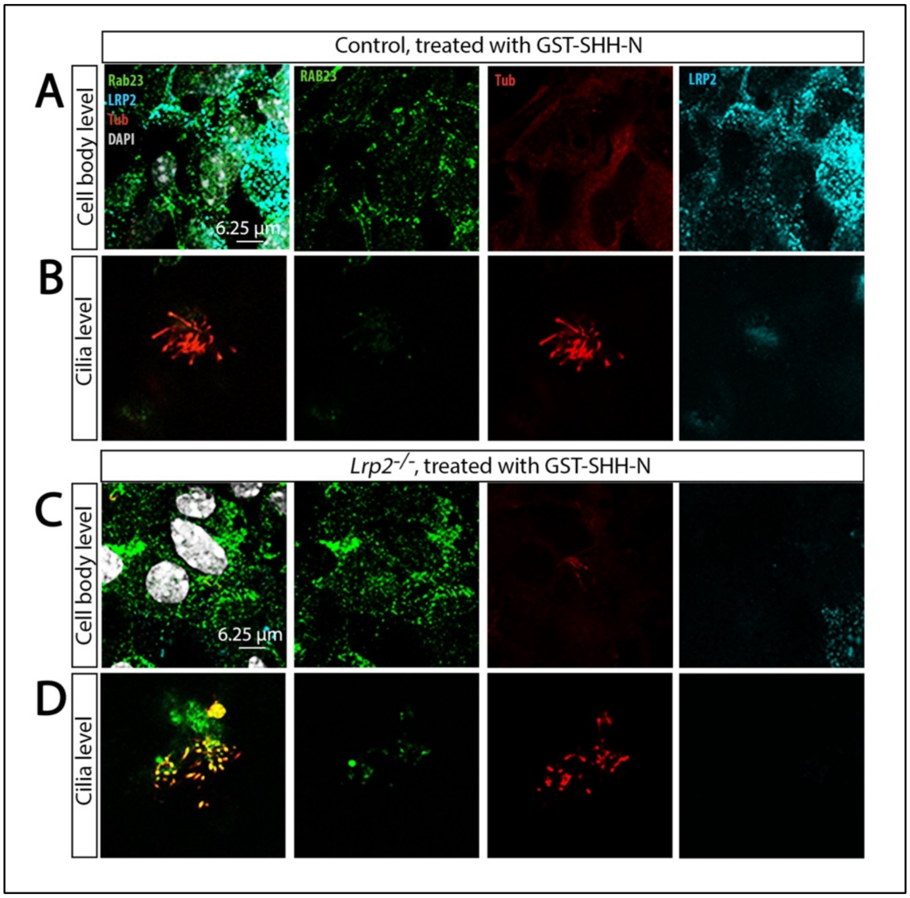

Figure 4.54: Rab23 expression in cell body and motile cilia of ependymal cells.

Ependymal cell cultures derived from *Lrp2*$^{-/-}$ and control mice at DIV10 were treated with 10 µg/ml GST-SHH-N for 2hrs. Thereafter, cell cultures were immunostained for recycling endosome marker Rab23 (green), for axoneme marker acetylated tubulin (aTub; red), and for LRP2 (blue). Cell nuclei were counterstained with DAPI (white). Color channels are shown individually or in merged configuration. Single plane of section images from the cell body (A, C) or the ciliary axoneme (B, D) were chosen from an optical series and displayed separately.

In the cell body, Rab23 levels are robust in *Lrp2*$^{-/-}$ ependymal cultures but barely detectable in controls (A, C). Similarly, Rab23 levels are significantly increased in the axoneme of motile cilia of mutant as compared with control ependymal cells (B, D).

Strikingly, in *Lrp2*$^{-/-}$ cells, the levels of Rab23 were notably elevated as compared with controls, including prominent localization to the motile ciliary axoneme (Figure 4.54 C, D).

4.5.4 Late endosomal compartment markers in ependymal cells and motile ciliary structures are not affected by absence of LRP2

As a late endosomal compartment marker, I examined Rab9 levels and distribution in ependymal cell body and motile ciliary structures.

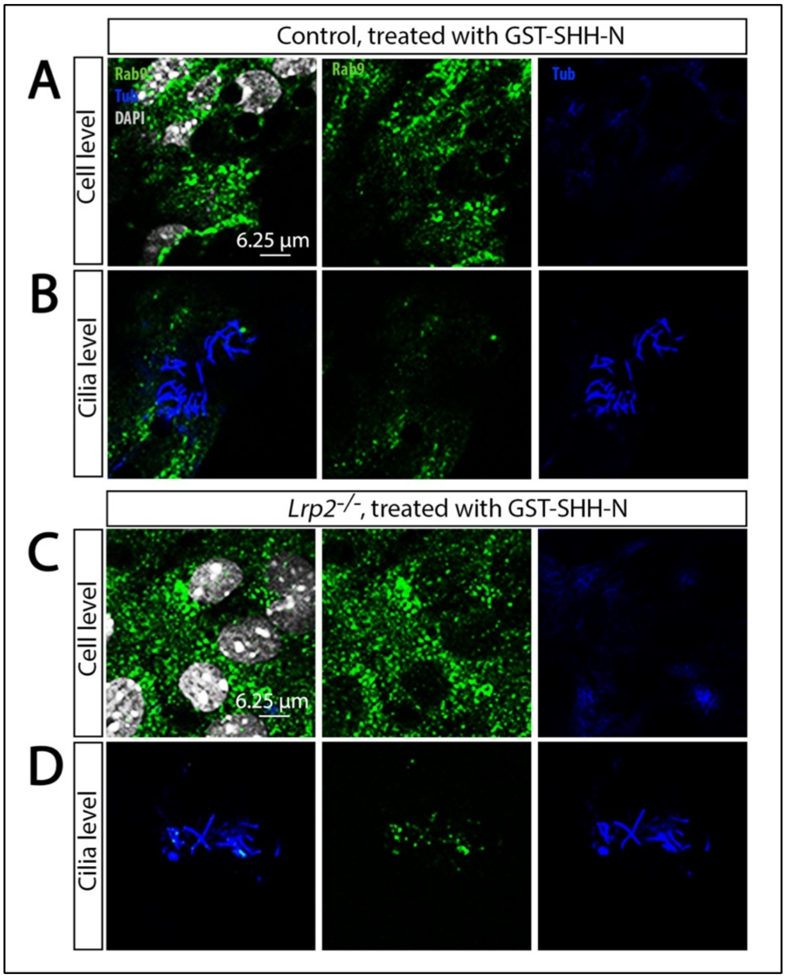

Figure 4.55: Rab9 expression in cell body and motile cilia of ependymal cells.

Ependymal cell cultures derived from *Lrp2*$^{-/-}$ and control mice at DIV10 were treated with 10 µg/ml GST-SHH-N for 2 hrs. Thereafter, cell cultures were immunostained for late endosome marker Rab9 (green) and for axoneme marker acetylated tubulin (a Tub; blue). Cell nuclei were counterstained with DAPI (white). Color channels are shown individually or in merged configuration. Single plane of section images from the cell body (A, C) or the ciliary axoneme (B, D) were chosen from an optical series and displayed separately. In the cell body, Rab9 levels are comparable between *Lrp2*$^{-/-}$ and control ependymal cultures (A, C). Rab9 cannot be detected in ciliary axoneme in both genotypes (B, D).

These studies showed comparable levels of Rab9 in the cell body in both genotypes (Figure 4.55 A, B). In motile ciliary structures, no Rab9 positive immunosignal was detected in LRP2-deficient or control cells (Figure 4.55 C, D).

5 Discussion

Previous research in the Willnow lab showed that LRP2 is expressed in ependymal cells neighboring the stem cell niche in the SVZ of the adult mouse brain. Loss of receptor expression resulted in depletion of the B cell population and in reduced proliferative capacity of their progeny, the C cells (Gajera et al., 2010). While these findings established a role for LRP2 in adult neurogenesis, the molecular mechanism of receptor action remained less clear. Based on the ability of the receptor to bind BMP4 (Spoelgen et al., 2005) and on the increased activity of the BMP pathway in the mutant SVZ (Gajera et al., 2010), a function as a clearance receptor in BMP signal suppression during neurogenesis was proposed. This hypothesis was recently challenged by findings that during embryonic neurogenesis LRP2 acts in SHH signaling (Christ et al., 2012). Further refining the mode of receptor action in adult neurogenesis, and whether it also acts as a SHH receptor in this context was the main goal of my thesis project.

Studying the cellular and molecular pathways that define the functional integrity of the V-SVZ niche in wild-type and LRP2 mutant mice *in vivo*, and in SVZ explants and primary ependymal cell cultures derived thereof, I now substantiated a role for LRP2 in SHH signaling in the adult brain. Specifically, I uncovered a decrease in progenitor cell proliferation in the rostral but not the caudal SVZ of LRP2-deficient mice. These regional specific defects in adult neurogenesis coincide with loss of SHH uptake and SHH signaling in the rostral and an aberrant accumulation of SHH in the caudal SVZ of mutant animals. Because coordinated beating of motile cilia is lost in ependymal cells lacking LRP2, I propose a model whereby the activity of this receptor may be required to direct proper cilia-driven flow of the CSF throughout the ventricular system of the brain. Directionally flow of the CSF assures proper distribution of signaling molecules, including SHH, and controls region-specific aspects of adult neurogenesis in the SVZ. Although the molecular mechanism of LRP2 action in ciliary movement could not be fully established in this work, my findings of an altered distribution of endocytic markers in the LRP2-deficient ependyma argues for a specific role of this endocytic receptor in directing endosomes to the motile ciliary compartment.

5.1 LRP2 controls SHH activity in a region-specific manner in the SVZ

My initial goal was to query a role for LRP2 in SHH signaling in the adult SVZ.

The relevance of this morphogen pathway for adult neurogenesis had been shown by several labs previously. Thus, SHH-responsive cells, characterized by *Gli1* expression were found in cells located in the ventral SVZ region (Ihrie et al., 2011). Most of these cells had neural stem cell (B1 cell) characteristics (Palma et al., 2005). These cells were quiescent as administration of antimitotic drugs into SVZ region of mice *in vivo* to acutely eliminate proliferative cells did not impact their progenies (Ahn & Joyner, 2005). Further experimental evidences showed that conditional deactivation of *Shh* in adult mice resulted in the reduction of interneurons derived from the ventral but not the dorsal SVZ (Ihrie et al., 2011). These results were in line with findings that, following induced expression of activated SMO progenitors of the dorsal SVZ region acquire the fate of ventral progenitors (Ihrie et al., 2011). One model proposed that the region-specific activity of SHH in the ventral SVZ may be explained by a morphogen expression domain located in the ventral forebrain.

Whether any of these functions in SHH signaling depends on LRP2 was unknown. To study SHH signaling in the SVZ of control and LRP2 mutant adult mouse brain, I initially assessed the expression levels of *Gli1* in the entire dorso-ventral and rostro-caudal axis of the SVZ using the *Gli1*-lacZ reporter mouse model and ISH analysis. In the rostral region of the control *Gli1*-lacZ reporter mouse brain, *Gli1* expression was strongest in the ventral but gradually decreased towards the dorsal domain of the SVZ. The SVZ of *Lrp2*$^{-/-}$ mice displayed a prominent decrease in lacZ activity, both in ventral and dorsal domains as compared to controls, suggesting loss of SHH activity in this region of the mutant SVZ niche. Similarly, using ISH, I documented highest *Gli1* transcript levels in the ventral tip of the SVZ but almost no *Gli1* signal in more dorsal regions (Figure 4.1, figure 4.3). As shown for the *Gli1*-lacZ reporter model, *Gli1* transcript levels were also prominently decreased in the SVZ of *Lrp2*$^{-/-}$ mice. These observations are in line with previous findings describing SHH signaling mainly in the ventral region of the SVZ (Ihrie et al., 2011).

As for the caudal brain area, *Gli1*-dependent lacZ activity was decreased in the SVZ of control mice, both in the dorsal and the ventral domains (Figure 4.2). By contrast, in LRP2 mutants, SHH signaling as deduced by lacZ staining was increased, particularly in the ventral SVZ region (Figure 4.2). Of note, no changes in *Gli1* ISH signals were observed in the caudal SVZ of mutant mice, contrasting the data from the *Gli1*_lacZ reporter experiments, where activity in the caudal domain was up in the mutant (Figure 4.4).

While the above findings provided strong experimental support for my hypothesis of a role for LRP2 as SHH receptor in the adult brain, I was surprised by the observation that the decrease in SHH signaling in mutant brains was specific for the rostral SVZ. Thus, no changes in *Gli1* mRNA levels were observed comparing genotypes (Figure 4.4). In the *Gli1_lacZ* reporter mouse model, SHH-induced lacZ activity in the caudal SVZ, particularly in the ventral medial wall, was even higher in mutants as compared with controls (Figure 4.2). These observations were particularly puzzling considering the uniform expression of LRP2 along the rostro-caudal axis of the SVZ (Gajera et al., 2010).

What may be the reasons for this spatial heterogeneity in LRP2 activity in the V-SVZ? Before further exploring this question, I considered several factors that may underlie the regional differences in morphogen activity in V-SVZ. Initially, I considered two factors that may contribute to regional-specific aspects of SHH signaling in the V-SVZ, namely distinct expression patterns of members of the SHH receptorsome along the dorso-ventral and rostro-caudal axis of the brain ventricle or the discrete localization of the SHH source relative to its target domain. These analyses are discussed in the following.

5.1.1 Expression of members of the SHH receptorsome along the dorso-ventral and rostro-caudal axis of the SVZ

To untangle the regional specification of SHH signaling along the rostro-caudal axis of the SVZ, I examined the regional distribution of various members of the SHH receptorsome in the SVZ of adult mice.

Previous studies identified several SHH binding proteins, including PTCH1, GAS1, CDO, and BOC that control the spread of SHH signaling through the embryonic neural tube, by either enhancing or blocking signaling in a cell-autonomous manner. PTCH1 sequesters SHH and demonstrates a cell-autonomous inhibitory role on signal transduction by endocytosis and degradation of the morphogen (Incardona et al., 2000). As a part of negative-feedback regulatory loop in SHH signaling, *Ptch1* is also a transcriptional target of SHH signaling and is consequently upregulated in the ventral neural tube. GAS1, CDO and BOC also bind SHH, but act as cell-autonomous activators of SHH signaling. In contrast to PTCH1, the latter receptors are transcriptionally repressed by SHH signal activation. (Dessaud et al., 2008).

To test the relevance of members of the SHH receptorsome for SHH signaling in adult brain, I examined the expression domains of these receptors in various SVZ regions in controls and *Lrp2*$^{-/-}$ mice. ISH analyses revealed no obvious differences in transcript levels for *Smo, Ptch1, Cdon* and *Boc* comparing rostral-ventral, rostral-dorsal, caudal-ventral and caudal-dorsal SVZ regions in both genotypes (Figure 4.5-4.12). These findings argued that the distinct impact of LRP2 activity on SHH signaling in the rostral but not the caudal SVZ is not explained by spatial differences in the expression pattern of this receptor or of other members of the SHH receptorsome.

5.1.2 Production and spatial distribution of SHH in SVZ

In the developing neural tube, SHH is produced by cells of the prechordal plate and initiates signaling in the overlaying neuroepithelium to pattern the ventral neural tube. Interaction with LRP2 sequesters SHH on the apical surface of the ventral neuroepithelial cells, increasing local concentrations of the morphogen. After birth, morphogen producing centers typically shrink in size and are confined to discrete cell clusters, decreasing diffusion of these signaling molecules throughout the brain parenchyma. As for SHH, several regional sources were found in adult brain (Ihrie et al., 2011). In detail, *Shh* transcripts were detected in the medial septum, the ventral forebrain, and in infrequent cells close to the ventral but not to the dorsal SVZ regions (Ihrie et al., 2011). Using tamoxifen-inducible ShhCre; R26YFP reporter mice, the precise expression patterns for *Shh* in postnatal development were further refined documenting *Shh* expressing cells predominantly in the medial and ventral septum, in the preoptic nuclei near the hypothalamus, and in the bed nuclei of the stria terminalis (BNST). Some SHH-positive cells were also observed in cortical brain regions. With relevance to SHH signaling in the V-SVZ, SHH positive cells in the BNST located in close proximity to the ventral tip of the lateral ventricles. Apparently, SHH produced in BNST cells is transferred via anterograde transport along the axons and is secreted distally at axon terminals close to the ventral tip of the SVZ (Traiffort, Moya, Faure, Hässig, & Ruat, 2001). While the above studies provided important information about the local source of SHH in the adult brain, i.e. SVZ, these studies described *Shh* gene transcription spatially, but did not specify the localization of full length (SHH-FL) versus the active forms (SHH-Np) of this morphogen.

To explore the consequence of LRP2 activity on the distribution of the secreted morphogen, I examined levels of SHH-FL and SHH-Np in different regions of the SVZ by western blot analysis. Specifically, I scored SHH-FL and SHH-Np intensity levels in four dissected domains of the adult SVZ. My studies documented that SHH-FL levels were not changed in micro-dissected samples from the dorsal (Figure 4.13 A, C) and ventral (Figure 4.13 B, D) regions of the rostral SVZ in LRP2 mutants compared with control mice. Similarly, no statistically significant differences in levels of SHH-Np were detected in the rostral dorsal and rostral ventral domains of the SVZ (Figure 4.13 B, E, F). Also, the examination of the micro-dissected medial septum showed no obvious differences in levels of SHH-FL and SHH-Np comparing genotypes (data is not shown). Based on these results, I concluded that LRP2 activity does not impact expression and maturation of SHH in the rostral ventral forebrain. The situation was different however for the caudal SVZ. Here, SHH-Np levels were increased two-fold, both in the dorsal and ventral regions of the caudal SVZ in LRP2 mutants as compared to littermate controls (Figure 4.14 A, B, E, F). No changes in SHH-FL levels were observed comparing both genotypes (Figure 4.14 A, B, C, D).

In summary, my analysis of the nascent and active forms of SHH identified remarkably higher levels of the secreted active SHH-Np in the caudal SVZ of LRP2 mutants. By contrast, levels of the precursor SHH-FL, reflecting protein production in the source, were not affected. Increased levels of SHH-Np in the caudal SVZ mirrored the shift of *Gli1* expression levels from the rostral to the caudal SVZ domain in LRP2 mutants described above. Thus, I hypothesize that the increased levels of the active form of the morphogen are the primary cause of higher SHH signaling activity in the caudal region of *Lrp2* deficient mice. Dose-dependent actions of SHH was shown earlier by James Briscoe and colleagues as an essential regulatory mechanism for ventral neural tube patterning (Balaskas et al., 2012).

5.1.3 LRP2 impacts adult neurogenesis in the rostral but not caudal regions of the SVZ

Having identified altered levels and activity of SHH-Np in the rostral versus the caudal regions of the LRP2-deficient SVZ, I next explore whether these region-specificity in morphogen signaling would be paralleled by similar region-specific alteration in adult neurogenesis. Defects in adult neurogenesis in the SVZ of LRP2 mutant mice had been reported before (Gajera et al., 2010). Yet, these studies did not investigate this phenotype along the dorso-ventral or rostro-caudal axis of the ventricular system.

Previous investigations of the neurogenic niche in the mouse brain revealed its heterogeneity in terms of cell density and composition along the rostro-caudal and dorso-ventral axis (Azim et al., 2012; Falcão et al., 2012; Mirzadeh, Merkle, Soriano-Navarro, Garcia-Verdugo, & Alvarez-Buylla, 2008). Also, depending on localization, B cells exhibit distinct differentiation fate. Thus, B cells having a more rostral localization in the SVZ generate granular cells (GCs) placed in more superficial layers of the OB, as compared to B1 cells residing in the caudal SVZ (Kelsch, Mosley, Lin, & Lois, 2007). Later studies documented that region specificity in NSCs differentiation is also seen along the dorso-ventral axis. These experiments used selective electroporation of cells in sub-regions of the V-SVZ to untangle the link between the location of the B cells in medial, dorsal and lateral walls of the lateral ventricles and the ultimate localization of their progeny in the various layers of the OB (de Chevigny et al., 2012; Fernández, Croce, Boutin, Cremer, & Raineteau, 2011). According to these studies, B cells residing in the medial wall of ventricles tend to generate periglomerular cells (PGCs) (>85%), whereas those in the lateral wall primarily adopt a granule cells (GC) fate (>90%).

To explore the consequences of the region-specific impact of LRP2 deficiency on the extend of adult neurogenesis, I analyzed the proliferative capacity of progenitor (C) cells in the wild-type and the LRP2-deficient SVZ. These analyses revealed an almost 50% decreased proliferation in the ventral and dorsal SVZ in LRP2-deficient as compared to control mice (Figure 4.27). Overall, these observations were in accordance with findings reported by Gajera and colleagues showing a globally decreased proliferation in the *Lrp2*$^{-/-}$ SVZ (Gajera et al., 2010). However, upon my further examination of the caudal SVZ, I failed to detect any consistent changes in proliferative capacity between both genotypes in those brain regions (Figure 4.28). Further examination of the neural stem cell population in the SVZ by staining for GFAP or SOX2 produced the same pattern of local changes in the rostral but bot not the caudal SVZ of mutants (Figure 4.30-4.33). These results tied in well with the observed region-specific changes in SHH signaling activity in the SVZ of LRP2 mutant mice.

5.2 Activity alterations in BMP, WNT/β catenin and mTOR signaling pathways predominate in the rostral SVZ region of LRP2 mutants

Multiple signaling pathways control SVZ neurogenesis. So, as a next question, I wanted to test how LRP2 deficiency may affect such neurogenic signaling pathways.

Among various morphogens, BMP4 and BMP7 provide regulatory signals for adult neurogenesis (Mikawa, Wang, & Sato, 2006; Peretto et al., 2004). Specifically, ectopic induction of BMP signaling by overexpression of BMP7 results in a decrease in proliferation in the SVZ. Suppression of BMP signaling by increasing the action of the antagonist Noggin changes the differentiation fate of B cells towards the oligodendroglial linage (Colak et al., 2008). A possible role for LRP2 in BMP-dependent regulation of adult neurogenesis was suggested in a previous study that documented elevated levels of phosphorylated forms of SMAD3/5/8 and of ID3, downstream targets of BMP signaling in the LRP2-deficient SVZ (Gajera et al., 2010). Because LRP2 is able to bind BMP4 and to deliver it to cellular catabolism, a possible role for this receptor as clearance receptor for BMP was proposed earlier. In this model, LRP2 would promote stem cell proliferation by antagonizing the anti-proliferative actions of BMPs in the niche. However, increase of BMP signaling in the LRP2 mutant niche may also be a secondary consequence of alterations of other signaling pathways in the SVZ. My current observations confirmed previous findings by showing increased ID3 levels in the SVZ of LRP2-defcient mice as compared to controls. Again, these changes were specific to the rostral SVZ region whereas no differences were observed caudally (Figure 4.15-4-16). Although my new findings substantiated earlier work by Gajera and colleagues, they did not ultimately resolve whether the BMP pathway may be a direct or indirect target of LRP2 activity. Earlier investigations on neural tube development revealed the importance of an antagonistic crosstalk between SHH and BMP signaling in dorso-ventral patterning of the floor plate (Patten & Placzek, 2002). Consequently, loss of SHH signaling in the LRP2-deficient neural tube resulted in a secondary increase in BMP signals (Spoelgen et al., 2005). The same mechanism may be operable in the SVZ and the decreased levels of SHH activity in this niche may secondarily increase BMP signaling in the LRP2 deficient SVZ. Irrespective of the exact mode of action, my finding on the BMP signaling pathways still fully substantiated the region-specific action of LRP2 in the V-SVZ.

In addition to SHH and BMP, I also characterized the consequences of LRP2 deficiency for Wnt signaling in the SVZ. Multiple lines of evidence suggest an indispensable role of Wnt signaling in cell proliferation and differentiation, not only during embryonic development but also in the adult organism. With relevance to my studies, alteration in Wnts are connected with impaired neurogenesis in the adult SVZ (Hirota et al., 2016). Mechanistically, there are several ways of Wnt signal conduction, namely canonical Wnt/β-catenin signaling, the Wnt/Ca^{2+} pathway, and the Wnt/planar cell polarity pathway (Komiya & Habas, 2008). Canonical Wnt signaling acts through transfer of β-catenin into the nucleus, initiating downstream target gene transcription through TCF/LEF transcription factor (MacDonald, Tamai, & He, 2009). In the Wnt/Ca^{2+} pathway, Wnt5a and Wnt11 activate cyclin-dependent kinase 2 and protein kinase C to increase cellular Ca^{2+} concentration. Elevated Ca^{2+} levels, in turn, stimulate serine/threonine phosphatase activity of calcineurin, which dephosphorylates nuclear factor of activated T-cells (NFAT) transcription factors. This results in NFATs' import into the nucleus and transcription complex formation to initiate or to repress the transcription of target genes (Peifer & McEwen, 2002). Wnt/planar cell polarity operates mainly through cytoskeletal rearrangements (Komiya & Habas, 2008).

As part of my thesis work, I collaborated with the group of Nikolaus Rajewski in using differential gene expression analysis of single cell transcriptomic data from *Lrp2*$^{-/-}$ and control SVZ regions. In these studies, I identified a significant decrease in β-catenin expression levels in transient amplifying progenitors (C cells) of the *Lrp2*$^{-/-}$ SVZ. To test whether those changes reflected changes in canonical Wnt signaling, I scored *Tcf/Lef* expression levels in rostral and caudal SVZ regions using a *lacZ* reporter mouse. Decreased levels of the lacZ reporter activity in the receptor-deficient SVZ confirmed my assumption of Wnt/β-catenin pathway inactivation in the absence of LRP2. Although not proven experimentally by me or others as yet, a direct role for LRP2 in canonical Wnt signaling seems plausible. This assumption is based on the reported function of several members of the LDL receptor gene family as coreceptors to Frizzled in Wnt signal transduction (He et al., 2004; Pinson et al., 2000). However, my findings cannot exclude that the changes in Wnt activity may also stem from alterations in SHH and/or BMP activities. For example, previous studies reported a role for SHH as an upstream activator for expression of the Wnt signal transducer *Tcf3/4*, which, in turn, regulates cell cycle progression in neural progenitor cells (Alvarez-Medina, Dreau, Ros, & Martí, 2009). In addition, a number of recent studies discussed the existence of feedback loops whereby Wnt initiates SHH activation but active SHH suppresses the Wnt pathway (S.-W. Cho et al., 2011; Martinez-Ferre, Navarro-Garberi, Bueno, & Martinez, 2013; Winkler, Mahoney, Sinner, Wylie, & Dahia, 2014).

Finally, I explored the consequences of LRP2 action for activity of the mTOR pathway in the SVZ. In these studies, I showed that levels of the downstream targets of mTOR activation, pS6RP and p4EBP1m were markedly higher in LRP2 mutants (Figure 4.17-4.24). Again, these changes were specific for the rostral SVZ region (Figure 4.17 and figure 4.22), while no obvious alterations were observed caudally (Figure 4.19 and figure 4.23). As an initiator of CAP-dependent protein translation, high levels of mTOR activity typically reflect an active cell metabolism and correlate with higher proliferative capacity of cells (Hay & Sonenberg, 2004; Laplante & Sabatini, 2009; Ma & Blenis, 2009).

Increased mTOR activity in the mutant SVZ seems to contradict the decrease in proliferative capacity seen in the rostral SVZ. However, this apparent contradiction may be explained by a model wherein mTOR activation in LRP2 mutant SVZ may occur in slow dividing cell populations (i.e., stem cells) not marked by BrdU incorporation during a 24 hours period (as used in my work). In line with this hypothesis, almost half of the pS6RP immunosignals were found in SOX2-positive neural stem cells in controls and LRP2 deficient mice (Figure 4.18). Accordingly, I propose that increased mTOR activity in the neural stem cell population may affect stem cell fate determination, particularly turning B cells from a quiescent into an activated state. As a consequence, a depletion of the quiescent neural stem cell pool in LRP2 mutants may occur, eventually resulting in a decreased rate of proliferation of fast dividing progenitors seen in this mouse model. Obviously, this hypothesis has to be taken with caution until further confirmed by more experimental evidence.

Also, how exactly LRP2 activity may affect mTOR needs further exploration. Increased activity of mTOR in the rostral SVZ region of LRP2 mutants may be a consequence of elevated BMP signaling. As demonstrated in lung carcinomas, BMP2 induced-activation of the PI3K/mTOR pathway is essential for regulation of stem cell differentiation (Langenfeld, Kong, & Langenfeld, 2005). Alternatively, alterations in SHH activity may be the underlying reason as a crosstalk between SHH and mTOR exists (Sharma et al., 2015; Yan Wang et al., 2012).

5.3 CSF flow and morphogen distribution in the SVZ

Obviously, changes in the proliferative capacity of the SVZ in LRP2 mutant mice may be explained by a direct role of LRP2 in signaling through BMP, Wnt, and/or SHH in this niche. Such a cell autonomous action of the receptor should occur in E cells, the only cell type in the SVZ that expresses this receptor. However, this hypothesis is challenged by my observations that LRP2 activity impacts these pathways in the rostral but not the caudal V-SVZ, although expression of this receptor is seen uniformly throughout the lateral ventricles. Therefore, I explored an alternative explanation for a more global role of this receptor in control of morphogen action, namely through regulation of CSF flow. Coordinated beating of motile cilia on ependymal cells regulate the CSF flow and thereby morphogen distribution in the ventricular system (Mirzadeh et al., 2008; Spassky et al., 2005b). In the adult neurogenic niche, CSF flow is involved in the gradient formation of chemorepellents, like Slit, that instruct neuroblast migration from SVZ to OBs (Nguyen-Ba-Charvet et al., 2004; Sawamoto et al., 2006).

5.3.1 Motile cilia on ependymal cells

Motile cilia are hair-like organelles, consisting of a basal part anchored in the cell membrane and of an axoneme, extending from the cell surface. The basal part of the cilium is composed of the basal body, associated with the basal feet, transitional fibers or alar sheets, and striated rootlets. Besides a role in cell surface anchoring, the basal apparatus determines the beating direction of motile cilia. In their axonemes, motile cilia possess a central pair of microtubules surrounded by nine outer doublet microtubules, connected by inner and outer dynein arms. Dynein arms generate ATP-dependent sliding movements of the microtubules, resulting in a whip-like beating motion. In mature ciliated cells, the basal feet are pointing in the same direction. This direction matches the effective stroke direction of the ciliary shaft, providing coordinated beating of a ciliary bundle on a cell (Satir, Heuser, & Sale, 2014). Alignment of basal body orientation in epithelial cells of the skin of *Xenopus laevis* larvae for example is a 2-step process. In the first step, PCP pathway activity in non-ciliated outer cells instructs the docking of basal bodies in intercalating ciliated epithelial cells, creating bias in cilia beating orientation along the embryonic axis. This ciliary beating orientation bias creates a weak directional fluid flow, which in turn refines the ciliary alignment via a positive feedback loop (Mitchell, Jacobs, Li, Chien, & Kintner, 2007; Mitchell et al., 2009). In ependymal cells of the mouse brain, no such bias in basal body orientation exists during development. Instead, the CSF flow itself provides the first long-range polarization bias leading to ciliary alignment at the level of the entire tissue. Before ciliogenesis, CSF is secreted by the choroid plexus and absorbed in the foramen of Monroe, defining CSF flow in a caudo-rostral direction. The hydrodynamic forces generated by this directed CSF flow align the randomly beating motile cilia on murine ependymal cells towards the flow orientation (Guirao et al., 2010). Still, also in the mouse brain, Vangl2, a core component of the PCP pathway, plays an indispensable role in coordination of cilia beating. Being localized to several ciliary structures, Vangl2 may acts as a sensor of hydrodynamic forces, initiating polarization of the cytoskeleton and reorientation of basal bodies towards the flow direction (Guirao et al., 2010). According to recent observations, Wnt5a directly controls the level of Vangl2 phosphorylation in a dose-dependent manner. Vangl2 phosphorylation plays an essential role in regulation of developmental processes in mammals.

Additionally, phosphorylation-dependent endocytosis of Vangl2 is critical for PCP obtainment (Yang et al., 2017).

5.3.2 Role of LRP2 in functional integrity of motile cilia on ependymal cells

Previous immunohistological analyses reported LRP2 localization at the base of the motile cilium in ependymal cells (Gajera et al., 2010). To uncover a so far unknown role for LRP2 in motile cilia function, I applied an experimental technique developed by Camille Boutin (Boutin et al., 2014; Labedan et al., 2016). In this procedure, lateral ventricular wall whole mount (LWWM) preparations are immunostained for the basal body marker FGFR1 Oncogene Partner (FOP), the basal foot marker gamma tubulin (γ-Tub), and the apical cell surface marker zonula occludens-1 (ZO1). This combination of markers not only allows the visualization of the ciliary bundle localization on individual ependymal cells, but also to deduce beating direction as detailed in the method and result section.

Initially, I tested the impact of LRP2 deficiency on the displacement of the ciliary patch on the apical cell surface relative to the center of the ependymal cell (Figure 4.36). In immature ependymal cells, the ciliary bundles are scattered on the apical cell surface. Upon further differentiation, they cluster in an off-centered patch towards the direction of CSF flow. Eventually adjacent cells acquire the same direction of displacement from the cell center, acquiring translational polarity (Mirzadeh et al., 2010). My studies confirmed that ciliary patches in control ependymal cells have a coordinated and directed displacement relative to cell center. By contrast, the LRP2 mutant cells showed a random displacement of ciliary patches relative to the cell center (Figure 4.36 A). Using the same approach, I also scored the relative localization of the basal foot marker γ-Tub to the basal body marker FOP. Since the basal foot invariably points in the direction of the effective cilia stroke, the relative localization of both markers to one another reveals the beating orientation of individual cilia (Marshall & Kintner, 2008). The average vectors, characterizing ciliary patch beating direction for each ependymal cell, were oriented randomly in LRP2 mutants. By contrast, in littermate controls these vectors pointed in a uniform direction. In many ependymal cells from LRP2 deficient mice, the cilia also manifested a non-coordinated orientation within the patch, a situation not seen in control ependymal cells (Boutin et al., 2014; Mirzadeh et al., 2010). Finally, the total number of cilia in individual patches was increased in LRP2 mutants compared with controls (Figure 4.40). Despite all those changes, the general geometric characteristics of cells and patches were similar between genotypes. No difference in patch area and cell surface area covered by ciliary patches were observed between LRP2 mutants and littermate controls (Figure 4.41 A-D). Also, the ratio of apical cell surface area to cilia patch area was similar in LRP2 mutants as compared to controls (Figure 4.41 C). Furthermore, the structural organization of the ciliary axoneme seemed unperturbed in mutant cells as deduced from immunostainings for markers of the axoneme including acetylated tubulin (Tub) and ADP-ribosylation factor-like protein 13B (ARL13B) (Figure 4.42). My conclusion of a normal anatomy is in line with previous observations using scanning EM to characterize structural aspects of motile cilia architecture in LRP2-deficient mice (Gajera et al., 2010).

Taken together, my studies were the first to identify a role for LRP2 in coordination of cilia beating in ependymal cells. They suggested aberrant distribution of morphogens (i.e., SHH) due to a disturbed CSF flow as the underlying cause for the region-specific defects in adult neurogenesis that I uncovered in receptor-mutant mice. Because the structural architecture of individual cilia seemed normal, I suspected a crucial role for LRP2 in coordination of ciliary beating.

What may be the molecular mechanisms behind this regulatory role of LRP2?

Previous investigations demonstrated the importance of two pools of cortical actins in the coordination of motile cilia beating in epithelial cells of *Xenopus laevis* larvae. The first pool is apical actin, forming a mesh-like network in the plane of the basal body. The ciliary axoneme extends from the apical cell surface through holes in this mesh. The second actin pool is localized slightly subapically below the cell surface. This pool of actin consists of aligned short filaments, connecting neighboring cilia. In detail, these actin filaments connect the basal body of one cilium with the distal tip of the striated rootlet of a neighboring cilium. Application of cytochalasin D to block subapical actin function impairs the coordinated beating of cilia and, consequently, reduces the CSF flow velocity. Subapical actin also impacts the uniform distribution of basal bodies within a cell and its disturbance widens the distance and randomizes the distribution of basal bodies (Werner et al., 2011). Mature ependymal cells acquire cell polarity already during embryonal development on radial glia cell stage. In further postnatal differentiation processes, translational polarity is established by the anterior migration of basal bodies in the apical membrane. Recently, non-muscle myosin II (NMII) was found to play a key regulatory role in this process (Hirota et al., 2010). Whether LRP2 impacts translational and rotational polarity of ependymal cells, affecting actin, NMII and overall cytoskeletal architecture is still elusive.

5.3.3 LRP2 acts as endocytic receptor in ependymal cells

Because LRP2 is an endocytic receptor and loss of receptor activity impairs endocytosis in cells of the adult kidney (Jörg R. Leheste et al., 2003), I considered a defect in the endocytic machinery of ependymal cells as the underlying cause of ciliary beating defects seen in receptor mutant E cells.

Although not known for motile cilia yet, recent studies suggest a link between endocytosis and activity in primary cilia. As transmission electron microscopy analysis demonstrated, the membrane of the ciliary pocket is rich in clathrin-coated pits, indicating a higher potential for endocytic cargo trafficking in this region of the primary cilium (Fonte, Searls, & Hilfer, 1971; Haycraft et al., 2005; Jensen et al., 2004). Another feature of ciliary pocket area is its interaction with the actin cytoskeleton. Several lines of evidences illustrated a connection of actin cables with ciliary basal bodies and the role of this cytoskeletal structures in the migration and docking of basal bodies to the membrane (Vladar & Axelrod, 2008). Dynamic rearrangements of actin cytoskeletal structures determine the curving and bending of the ciliary axoneme. The actin remodeling around ciliary pocket may also play a transductory role for mechanosensory stimuli.

Several lines of evidence suggest a role for actin polymerization in endocytosis processes from apical cell membrane in polarized cells (Hyman, Shmuel, & Altschuler, 2006; Sandvig, Torgersen, Raa, & van Deurs, 2008). Actin polymerization creates thicker apical cortex. How this structure contributes to endocytosis was elusive until recently when a role for NMII emerged as a primary regulator of tension in the cortical actin network (Chandrasekar et al., 2014). Actomyosin works in a manner analogous to a purse-string around the coated pit. Upon decreased cortical pressure, (e.g., due to membrane expansion) the network around the coated pit contracts and increases the tension (pulls the strings). If the tension is higher than normal (e.g., due to increased actin polymerization), the network relaxes (loosens the strings). The NMII contraction regulates membrane curving, coated pit progression as well as recruitment of other membrane curvature proteins to form the neck. Several other lines of evidence suggest a role for myosin IV (MIV) in endocytosis at the apical membrane of polarized cells (Buss, Luzio, & Kendrick-Jones, 2002). Interestingly MIV interacts with Dab2, a cytosolic adaptor that controls the endocytic activity of LRP2 (Dance et al., 2004; Morris et al., 2002). Jointly, these results suggest the existence of molecular links between endocytic ligand uptake and modulation of actin dynamics, that may also be relevant for ciliary functions.

Similar to previous observations in the developing neural tube (Christ et al., 2012) and retina (Christ et al., 2015), I documented the inability of receptor-deficient primary ependymal cells to internalize the receptor ligand SHH-N (Figures 4.43, 4.44, and 4.45). SHH-N internalized by LRP2 was directed to early as well as recycling endosomes as shown by co-staining for the respective compartment markers EEA1 and Rab11 (Figure 4.47 A-D). I confirmed a defect in internalization of the ligand in freshly dissected LWWM preparations from mutant mice (Figure 4.46). These findings substantiated the role of LRP2 as endocytic receptor in the adult ependyma, and indicated possible defects in handling of SHH by this tissue in mutants *in vivo*. LRP2 has two intracellular NPXY domains of which the distal NPXY motif interacts with

DAB2 (Oleinikov et al., 2000) to mediate endocytosis (Nagai et al., 2005; Shah, Baterina, Taupin, & Farquhar, 2013; Traub, 2009). Potentially, LRP2-mediated endocytosis may also proceed via clathrin-independent pathways involving small GTPase ADP-ribosylation factor 6 (Arf6) and caveolin 1 (Bento-Abreu et al., 2009; Oleinikov et al., 2000). Once in the early endosomal compartment, the proximal NPXY domain of LRP2 binds to a clathrin-associated sorting protein termed autosomal recessive hypercholesterolemia (ARH). This interaction tethers LRP2 to dynein motor complexes which facilitates further receptor transport from early to recycling endosomal compartment. Whether LRP2 mediates uptake and possibly recycling of SHH in ependymal cells via clathrin-dependent or -independent mechanisms was not further explored in my thesis project.

Based on prior work in embryonic tissues, loss of SHH uptake in ependymal cells from mutant mice may not be too surprising. However, my studies also detect an impact of LRP2 deficiency on trafficking of Rab proteins to motile cilia that was unexpected. In epithelial cells, Rab GTPases are involved in trafficking of junctional proteins and in cell polarity formation. Several Rab GTPases interact with ciliary proteins and determine epithelial transport processes into the axoneme of primary cilia (Blacque et al., 2017). For example, Rab8 and Rab11 are involved in early steps of ciliogenesis. Interestingly, I found higher levels of Rab8a in the cell body and in motile cilia of *Lrp2*$^{-/-}$ ependymal cells (Figure 4.52). This observation fits well with the slightly increased number of cilia in mutant cells (Figure 4.40). Another important finding was my documentation of elevated levels of Rab23 in cell body and in motile cilia of LRP2-deficient ependymal cells (Figure 4.54). Several studies reported an inhibitory role of Rab23 on SHH signaling in primary cilia, downstream of SMO and upstream of the GLIs (J. T. Eggenschwiler, Espinoza, & Anderson, 2001; Jonathan T. Eggenschwiler, Bulgakov, Qin, Li, & Anderson, 2006; Y. S. Lim & Tang, 2015).

How may LRP2 controls trafficking of Rabs to motile cilia? A clue to answer this question may stem from the distinct localization of the receptor at the ciliary pocket, as shown for primary cilia (Christ et al., 2012). As for motile cilia, ciliary pockets may fuse and several cilia emerge from one pocket. Despite this difference, motile ciliary pockets otherwise share many structural features with primary ciliary pocket and their role in endocytosis is quite plausible (Molla-Herman et al., 2010). Possibly, LRP2 due to its localization in the endocytically active membrane compartment of motile cilia, may actively sort early endosomes in or out of this organelle. Alternatively, LRP2 may act in the IFT transport machinery by regulating Rab GTPases transport into the axoneme (Deane, Cole, Seeley, Diener, & Rosenbaum, 2001).

5.4 Summary and outlook

My results have refined a role for LRP2 in neurogenesis in the adult SVZ by documenting an impact of receptor deficiency on the rostral but not the caudal domain of this niche. Changes in the rostral SVZ of the LRP2 mutant brain include alterations in signaling of SHH, BMP and WNTs, as well as in mTOR-related activities. These alterations are the likely cause of the depletion of the stem cell pool and the decrease in proliferative capacity of progenitor cells seen in this subdomain of the V-SVZ. Based on the cumulative evidence obtained in my work, I propose the loss of LRP2-dependent endocytic activity in ependymal cells as the underlying reason for these defects. In a simple model, loss of LRP2-dependent uptake and recycling of SHH in ependymal cells may alter the morphogenic milieu of the underlying SVZ niche. In this scenario, impaired SHH activity in the rostral SVZ affects the balance of various competing morphogen pathways in the stem cell niche, ultimately compromising neurogenesis. A more exciting hypothesis may be that the endocytic activity of LRP2 is required for coordination of motile cilia beating.

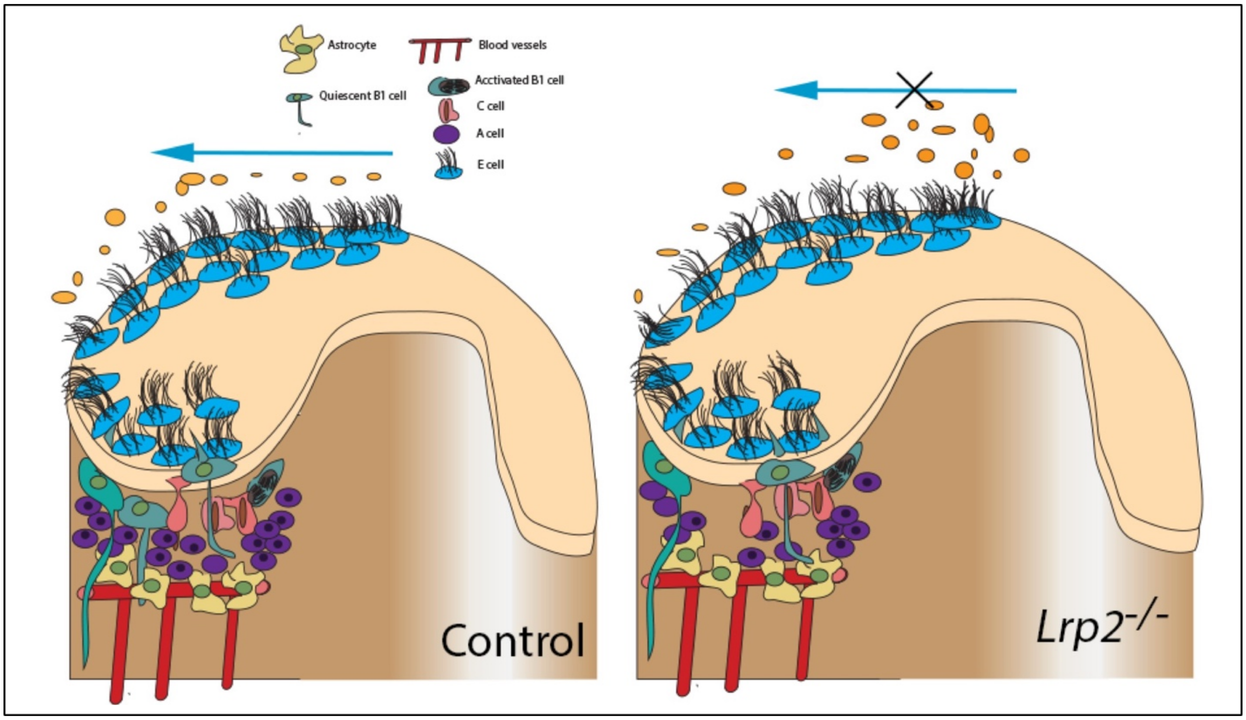

Figure 5.1: Schematic representation of ventricular-subventricular zone (V-SVZ) from control and *$Lrp2^{-/-}$* mice (en face view).

The schematic illustrates the V-SVZ from control and LRP2-deficient mice in an en face presentation. In control brains, coordinated beating of the cilia on ependymal cells directs the cerebrospinal fluid (CSF) flow in a caudal to rostral direction (blue arrow). Directional CSF flow safeguards distribution of morphogens throughout the entire ventricular lumen and establishes the proper milieu for neurogenesis in the rostral SVZ region. In LRP2-deficient mice, loss of LRP2 activity results in uncoordinated cilia beating and, consequently, in morphogen accumulation in the caudal SVZ domain. Absence of proper morphogen (i.e., SHH) signaling in the rostral SVZ, causes depletion of the neural stem cell pool and impairment of progenitor (C) cell formation in this region of the niche.

In this hypothesis, uncoordinated cilia beating seen in the mutant disturbs the directed flow of CSF, causing defects in morphogen distribution along the rostral to caudal axis of the lateral ventricles (Figure 5.1). The latter hypothesis receives support from the aberrant accumulation of active SHH-Np in the caudal domain of the LRP2-deficient SVZ and from a concomitant region-specific defect in adult neurogenesis. Although rather speculative at present, impaired endocytic activity in LRP2-deficient ependymal cells may affects apical membrane dynamics in this cell type, inducing cytoskeletal disarrangements at the ciliary base and impairing coordinated positioning of the basal body, a prerequisite for coordinated cilia beating (Figure 5.1). Obviously, both models are not mutually exclusive and several activities of this multifunctional endocytic receptor may be necessary to assure the functional integrity of ependymal cells, an essential cell type in the neurogenic niche of the adult V-SVZ.

6 References

Adachi, K., Mirzadeh, Z., Sakaguchi, M., Yamashita, T., Nikolcheva, T., Gotoh, Y., … Sawamoto, K. (2007). Beta-catenin signaling promotes proliferation of progenitor cells in the adult mouse subventricular zone. *Stem Cells (Dayton, Ohio)*, *25*(11), 2827–2836. https://doi.org/10.1634/stemcells.2007-0177

Ahn, S., & Joyner, A. L. (2005). In vivo analysis of quiescent adult neural stem cells responding to Sonic hedgehog. *Nature*, *437*(7060), 894–897. https://doi.org/10.1038/nature03994

Alfaro, A. C., Roberts, B., Kwong, L., Bijlsma, M. F., & Roelink, H. (2014). Ptch2 mediates the Shh response in Ptch1-/- cells. *Development (Cambridge, England)*, *141*(17), 3331–3339. https://doi.org/10.1242/dev.110056

Allen, B. L., Song, J. Y., Izzi, L., Althaus, I. W., Kang, J.-S., Charron, F., … McMahon, A. P. (2011). Overlapping roles and collective requirement for the coreceptors GAS1, CDO, and BOC in SHH pathway function. *Developmental Cell*, *20*(6), 775–787. https://doi.org/10.1016/j.devcel.2011.04.018

Allen, B. L., Tenzen, T., & McMahon, A. P. (2007). The Hedgehog-binding proteins Gas1 and Cdo cooperate to positively regulate Shh signaling during mouse development. *Genes & Development*, *21*(10), 1244–1257. https://doi.org/10.1101/gad.1543607

Alvarez-Medina, R., Dreau, G. L., Ros, M., & Martí, E. (2009). Hedgehog activation is required upstream of Wnt signalling to control neural progenitor proliferation. *Development*, *136*(19), 3301–3309. https://doi.org/10.1242/dev.041772

Avunduk, A. M., Aslan, Y., Kapicioğlu, Z., & Elmas, R. (2000). High myopia, hypertelorism, iris coloboma, exomphalos, absent corpus callosum, and sensorineural deafness: Report of a case and further evidence for autosomal recessive inheritance. *Acta Ophthalmologica Scandinavica*, *78*(2), 221–222.

Azim, K., Fiorelli, R., Zweifel, S., Hurtado-Chong, A., Yoshikawa, K., Slomianka, L., & Raineteau, O. (2012). 3-Dimensional Examination of the Adult Mouse Subventricular Zone Reveals Lineage-Specific Microdomains. *PLOS ONE*, *7*(11), e49087. https://doi.org/10.1371/journal.pone.0049087

Bae, G.-U., Domené, S., Roessler, E., Schachter, K., Kang, J.-S., Muenke, M., & Krauss, R. S. (2011). Mutations in CDON, encoding a hedgehog receptor, result in holoprosencephaly and defective interactions with other hedgehog receptors. *American Journal of Human Genetics*, *89*(2), 231–240. https://doi.org/10.1016/j.ajhg.2011.07.001

Balaskas, N., Ribeiro, A., Panovska, J., Dessaud, E., Sasai, N., Page, K. M., … Ribes, V. (2012). Gene Regulatory Logic for Reading the Sonic Hedgehog Signaling Gradient in the Vertebrate Neural Tube. *Cell*, *148*(1–2), 273–284. https://doi.org/10.1016/j.cell.2011.10.047

Bansal, A., & Gierasch, L. M. (1991). The NPXY internalization signal of the LDL receptor adopts a reverse-turn conformation. *Cell*, *67*(6), 1195–1201.

Bento-Abreu, A., Velasco, A., Polo-Hernández, E., Lillo, C., Kozyraki, R., Tabernero, A., & Medina, J. M. (2009). Albumin endocytosis via megalin in astrocytes is caveola- and Dab-1 dependent and is required for the synthesis of the neurotrophic factor oleic acid. *Journal of Neurochemistry*, *111*(1), 49–60. https://doi.org/10.1111/j.1471-4159.2009.06304.x

Bieri, S., Djordjevic, J. T., Daly, N. L., Smith, R., & Kroon, P. A. (1995). Disulfide bridges of a cysteine-rich repeat of the LDL receptor ligand-binding domain. *Biochemistry*, *34*(40), 13059–13065.

Blacque, O. E., Scheidel, N., & Kuhns, S. (2017). Rab GTPases in cilium formation and function. *Small GTPases*, *9*(1–2), 76–94. https://doi.org/10.1080/21541248.2017.1353847

Boutin, C., Labedan, P., Dimidschstein, J., Richard, F., Cremer, H., André, P., … Tissir, F. (2014). A dual role for planar cell polarity genes in ciliated cells. *Proceedings of the National Academy of Sciences of the United States of America*, *111*(30), E3129-3138. https://doi.org/10.1073/pnas.1404988111

Briscoe, J., & Thérond, P. P. (2013). The mechanisms of Hedgehog signalling and its roles in development and disease. *Nature Reviews Molecular Cell Biology*, *14*(7), 416–429. https://doi.org/10.1038/nrm3598

Brown, M. S., Herz, J., & Goldstein, J. L. (1997). LDL-receptor structure. Calcium cages, acid baths and recycling receptors. *Nature*, *388*(6643), 629–630. https://doi.org/10.1038/41672

Brown, S. D., Twells, R. C., Hey, P. J., Cox, R. D., Levy, E. R., Soderman, A. R., … Hess, J. F. (1998). Isolation and characterization of LRP6, a novel member of the low density lipoprotein receptor gene family. *Biochemical and Biophysical Research Communications*, *248*(3), 879–888. https://doi.org/10.1006/bbrc.1998.9061

Bruni, J. E. (1998). Ependymal development, proliferation, and functions: A review. *Microscopy Research and Technique*, *41*(1), 2–13. https://doi.org/10.1002/(SICI)1097-0029(19980401)41:1<2::AID-JEMT2>3.0.CO;2-Z

Bumcrot, D. A., Takada, R., & McMahon, A. P. (1995). Proteolytic processing yields two secreted forms of sonic hedgehog. *Molecular and Cellular Biology*, *15*(4), 2294–2303.

Buss, F., Luzio, J. P., & Kendrick-Jones, J. (2002). Myosin VI, an actin motor for membrane traffic and cell migration. *Traffic (Copenhagen, Denmark)*, *3*(12), 851–858.

Cabrera, J. R., Sanchez-Pulido, L., Rojas, A. M., Valencia, A., Mañes, S., Naranjo, J. R., & Mellström, B. (2006). Gas1 is related to the glial cell-derived neurotrophic factor family receptors alpha and regulates Ret signaling. *The Journal of Biological Chemistry*, *281*(20), 14330–14339. https://doi.org/10.1074/jbc.M509572200

Carlo, A.-S., Gustafsen, C., Mastrobuoni, G., Nielsen, M. S., Burgert, T., Hartl, D., … Willnow, T. E. (2013). The pro-neurotrophin receptor sortilin is a major neuronal apolipoprotein E receptor for catabolism of amyloid-β peptide in the brain. *The Journal of Neuroscience: The Official Journal of the Society for Neuroscience*, *33*(1), 358–370. https://doi.org/10.1523/JNEUROSCI.2425-12.2013

Cathcart, R. S., & Worthington, W. C. (1964). CILIARY MOVEMENT IN THE RAT CEREBRAL VENTRICLES: CLEARING ACTION AND DIRECTIONS OF CURRENTS. *Journal of Neuropathology and Experimental Neurology*, *23*, 609–618. https://doi.org/10.1097/00005072-196410000-00002

Chamoun, Z., Mann, R. K., Nellen, D., von Kessler, D. P., Bellotto, M., Beachy, P. A., & Basler, K. (2001). Skinny hedgehog, an acyltransferase required for palmitoylation and activity of the hedgehog signal. *Science (New York, N.Y.)*, *293*(5537), 2080–2084. https://doi.org/10.1126/science.1064437

Chandrasekar, I., Goeckeler, Z. M., Turney, S. G., Wang, P., Wysolmerski, R. B., Adelstein, R. S., & Bridgman, P. C. (2014). Nonmuscle Myosin II is a Critical Regulator of Clathrin Mediated Endocytosis. *Traffic (Copenhagen, Denmark)*, *15*(4), 418–432. https://doi.org/10.1111/tra.12152

Chassaing, N., Lacombe, D., Carles, D., Calvas, P., Saura, R., & Bieth, E. (2003). Donnai-Barrow syndrome: Four additional patients. *American Journal of Medical Genetics. Part A*, *121A*(3), 258–262. https://doi.org/10.1002/ajmg.a.20266

Chen, J. K., Taipale, J., Cooper, M. K., & Beachy, P. A. (2002). Inhibition of Hedgehog signaling by direct binding of cyclopamine to Smoothened. *Genes & Development*, *16*(21), 2743–2748. https://doi.org/10.1101/gad.1025302

Chen, J. K., Taipale, J., Young, K. E., Maiti, T., & Beachy, P. A. (2002). Small molecule modulation of Smoothened activity. *Proceedings of the National Academy of Sciences of the United States of America*, *99*(22), 14071–14076. https://doi.org/10.1073/pnas.182542899

Chen, W. J., Goldstein, J. L., & Brown, M. S. (1990). NPXY, a sequence often found in cytoplasmic tails, is required for coated pit-mediated internalization of the low density lipoprotein receptor. *The Journal of Biological Chemistry*, *265*(6), 3116–3123.

Chen, W., Ren, X.-R., Nelson, C. D., Barak, L. S., Chen, J. K., Beachy, P. A., … Lefkowitz, R. J. (2004). Activity-dependent internalization of smoothened mediated by beta-arrestin 2 and GRK2. *Science (New York, N.Y.)*, *306*(5705), 2257–2260. https://doi.org/10.1126/science.1104135

Chen, X., Tukachinsky, H., Huang, C.-H., Jao, C., Chu, Y.-R., Tang, H.-Y., … Salic, A. (2011). Processing and turnover of the Hedgehog protein in the endoplasmic reticulum. *The Journal of Cell Biology*, *192*(5), 825–838. https://doi.org/10.1083/jcb.201008090

Cheung, H. O.-L., Zhang, X., Ribeiro, A., Mo, R., Makino, S., Puviindran, V., … Hui, C.-C. (2009). The kinesin protein Kif7 is a critical regulator of Gli transcription factors in mammalian hedgehog signaling. *Science Signaling*, *2*(76), ra29. https://doi.org/10.1126/scisignal.2000405

Chiang, C., Litingtung, Y., Lee, E., Young, K. E., Corden, J. L., Westphal, H., & Beachy, P. A. (1996). Cyclopia and defective axial patterning in mice lacking Sonic hedgehog gene function. *Nature*, *383*(6599), 407–413. https://doi.org/10.1038/383407a0

Chmielnicki, E., Benraiss, A., Economides, A. N., & Goldman, S. A. (2004). Adenovirally expressed noggin and brain-derived neurotrophic factor cooperate to induce new medium spiny neurons from resident progenitor cells in the adult striatal ventricular zone. *The Journal of Neuroscience: The Official Journal of the Society for Neuroscience*, *24*(9), 2133–2142. https://doi.org/10.1523/JNEUROSCI.1554-03.2004

Cho, S.-H., & Cepko, C. L. (2006). Wnt2b/β-catenin-mediated canonical Wnt signaling determines the peripheral fates of the chick eye. *Development*, *133*(16), 3167–3177. https://doi.org/10.1242/dev.02474

Cho, S.-W., Kwak, S., Woolley, T. E., Lee, M.-J., Kim, E.-J., Baker, R. E., … Jung, H.-S. (2011). Interactions between Shh, Sostdc1 and Wnt signaling and a new feedback loop for spatial patterning of the teeth. *Development*, *138*(9), 1807–1816. https://doi.org/10.1242/dev.056051

Choudhry, Z., Rikani, A. A., Choudhry, A. M., Tariq, S., Zakaria, F., Asghar, M. W., … Mobassarah, N. J. (2014). Sonic hedgehog signalling pathway: A complex network. *Annals of Neurosciences*, *21*(1), 28–31. https://doi.org/10.5214/ans.0972.7531.210109

Christ, A., Christa, A., Klippert, J., Eule, J. C., Bachmann, S., Wallace, V. A., … Willnow, T. E. (2015). LRP2 Acts as SHH Clearance Receptor to Protect the Retinal Margin from Mitogenic Stimuli. *Developmental Cell*, *35*(1), 36–48. https://doi.org/10.1016/j.devcel.2015.09.001

Christ, A., Christa, A., Kur, E., Lioubinski, O., Bachmann, S., Willnow, T. E., & Hammes, A. (2012). LRP2 Is an Auxiliary SHH Receptor Required to Condition the Forebrain Ventral Midline for

Inductive Signals. *Developmental Cell*, *22*(2), 268–278. https://doi.org/10.1016/j.devcel.2011.11.023

Christ, A., Herzog, K., & Willnow, T. E. (2016). LRP2, an auxiliary receptor that controls sonic hedgehog signaling in development and disease. *Developmental Dynamics*, *245*(5), 569–579. https://doi.org/10.1002/dvdy.24394

Chuang, P. T., & McMahon, A. P. (1999). Vertebrate Hedgehog signalling modulated by induction of a Hedgehog-binding protein. *Nature*, *397*(6720), 617–621. https://doi.org/10.1038/17611

Chuang, P.-T., Kawcak, T., & McMahon, A. P. (2003). Feedback control of mammalian Hedgehog signaling by the Hedgehog-binding protein, Hip1, modulates Fgf signaling during branching morphogenesis of the lung. *Genes & Development*, *17*(3), 342–347. https://doi.org/10.1101/gad.1026303

Codega, P., Silva-Vargas, V., Paul, A., Maldonado-Soto, A. R., Deleo, A. M., Pastrana, E., & Doetsch, F. (2014). Prospective identification and purification of quiescent adult neural stem cells from their in vivo niche. *Neuron*, *82*(3), 545–559. https://doi.org/10.1016/j.neuron.2014.02.039

Colak, D., Mori, T., Brill, M. S., Pfeifer, A., Falk, S., Deng, C., … Götz, M. (2008). Adult Neurogenesis Requires Smad4-Mediated Bone Morphogenic Protein Signaling in Stem Cells. *Journal of Neuroscience*, *28*(2), 434–446. https://doi.org/10.1523/JNEUROSCI.4374-07.2008

Cole, F., & Krauss, R. S. (2003). Microform holoprosencephaly in mice that lack the Ig superfamily member Cdon. *Current Biology: CB*, *13*(5), 411–415.

Dai, P., Akimaru, H., Tanaka, Y., Maekawa, T., Nakafuku, M., & Ishii, S. (1999). Sonic Hedgehog-induced Activation of the Gli1Promoter Is Mediated by GLI3. *Journal of Biological Chemistry*, *274*(12), 8143–8152. https://doi.org/10.1074/jbc.274.12.8143

Dance, A. L., Miller, M., Seragaki, S., Aryal, P., White, B., Aschenbrenner, L., & Hasson, T. (2004). Regulation of myosin-VI targeting to endocytic compartments. *Traffic (Copenhagen, Denmark)*, *5*(10), 798–813. https://doi.org/10.1111/j.1600-0854.2004.00224.x

de Chevigny, A., Coré, N., Follert, P., Gaudin, M., Barbry, P., Béclin, C., & Cremer, H. (2012). MiR-7a regulation of Pax6 controls spatial origin of forebrain dopaminergic neurons. *Nature Neuroscience*, *15*(8), 1120–1126. https://doi.org/10.1038/nn.3142

Deane, J. A., Cole, D. G., Seeley, E. S., Diener, D. R., & Rosenbaum, J. L. (2001). Localization of intraflagellar transport protein IFT52 identifies basal body transitional fibers as the docking site for IFT particles. *Current Biology*, *11*(20), 1586–1590. https://doi.org/10.1016/S0960-9822(01)00484-5

Delgehyr, N., Meunier, A., Faucourt, M., Bosch Grau, M., Strehl, L., Janke, C., & Spassky, N. (2015). Chapter 2—Ependymal cell differentiation, from monociliated to multiciliated cells. In R. Basto & W. F. Marshall (Eds.), *Methods in Cell Biology* (pp. 19–35). https://doi.org/10.1016/bs.mcb.2015.01.004

Derwall, M., Malhotra, R., Lai, C. S., Beppu, Y., Aikawa, E., Seehra, J. S., … Yu, P. B. (2012). Inhibition of bone morphogenetic protein signaling reduces vascular calcification and atherosclerosis. *Arteriosclerosis, Thrombosis, and Vascular Biology*, *32*(3), 613–622. https://doi.org/10.1161/ATVBAHA.111.242594

Dessaud, E., McMahon, A. P., & Briscoe, J. (2008). Pattern formation in the vertebrate neural tube: A sonic hedgehog morphogen-regulated transcriptional network. *Development*, *135*(15), 2489–2503. https://doi.org/10.1242/dev.009324

Ding, Q., Motoyama, J., Gasca, S., Mo, R., Sasaki, H., Rossant, J., & Hui, C. C. (1998). Diminished Sonic hedgehog signaling and lack of floor plate differentiation in Gli2 mutant mice. *Development (Cambridge, England)*, *125*(14), 2533–2543.

Doetsch, F., & Alvarez-Buylla, A. (1996). Network of tangential pathways for neuronal migration in adult mammalian brain. *Proceedings of the National Academy of Sciences of the United States of America*, *93*(25), 14895–14900. https://doi.org/10.1073/pnas.93.25.14895

Doetsch, F., Caillé, I., Lim, D. A., García-Verdugo, J. M., & Alvarez-Buylla, A. (1999). Subventricular zone astrocytes are neural stem cells in the adult mammalian brain. *Cell*, *97*(6), 703–716.

Doetsch, F., García-Verdugo, J. M., & Alvarez-Buylla, A. (1997). Cellular composition and three-dimensional organization of the subventricular germinal zone in the adult mammalian brain. *The Journal of Neuroscience: The Official Journal of the Society for Neuroscience*, *17*(13), 5046–5061.

Dong, Y., Lathrop, W., Weaver, D., Qiu, Q., Cini, J., Bertolini, D., & Chen, D. (1998). Molecular cloning and characterization of LR3, a novel LDL receptor family protein with mitogenic activity. *Biochemical and Biophysical Research Communications*, *251*(3), 784–790. https://doi.org/10.1006/bbrc.1998.9545

Donnai, D., & Barrow, M. (1993). Diaphragmatic hernia, exomphalos, absent corpus callosum, hypertelorism, myopia, and sensorineural deafness: A newly recognized autosomal recessive disorder? *American Journal of Medical Genetics*, *47*(5), 679–682. https://doi.org/10.1002/ajmg.1320470518

Dorn, K. V., Hughes, C. E., & Rohatgi, R. (2012). A Smoothened-Evc2 complex transduces the Hedgehog signal at primary cilia. *Developmental Cell*, *23*(4), 823–835. https://doi.org/10.1016/j.devcel.2012.07.004

Eaton, S. (2006). Release and trafficking of lipid-linked morphogens. *Current Opinion in Genetics & Development*, *16*(1), 17–22. https://doi.org/10.1016/j.gde.2005.12.006

Eggenschwiler, J. T., Espinoza, E., & Anderson, K. V. (2001). Rab23 is an essential negative regulator of the mouse Sonic hedgehog signalling pathway. *Nature*, *412*(6843), 194–198. https://doi.org/10.1038/35084089

Eggenschwiler, Jonathan T., Bulgakov, O. V., Qin, J., Li, T., & Anderson, K. V. (2006). Mouse Rab23 regulates Hedgehog signaling from Smoothened to Gli proteins. *Developmental Biology*, *290*(1), 1–12. https://doi.org/10.1016/j.ydbio.2005.09.022

Endoh-Yamagami, S., Evangelista, M., Wilson, D., Wen, X., Theunissen, J.-W., Phamluong, K., … Peterson, A. S. (2009). The mammalian Cos2 homolog Kif7 plays an essential role in modulating Hh signal transduction during development. *Current Biology: CB*, *19*(15), 1320–1326. https://doi.org/10.1016/j.cub.2009.06.046

Evans, T. M., Ferguson, C., Wainwright, B. J., Parton, R. G., & Wicking, C. (2003). Rab23, a negative regulator of hedgehog signaling, localizes to the plasma membrane and the endocytic pathway. *Traffic (Copenhagen, Denmark)*, *4*(12), 869–884.

Falcão, A. M., Palha, J. A., Ferreira, A. C., Marques, F., Sousa, N., & Sousa, J. C. (2012). Topographical Analysis of the Subependymal Zone Neurogenic Niche. *PLOS ONE*, *7*(6), e38647. https://doi.org/10.1371/journal.pone.0038647

Fass, D., Blacklow, S., Kim, P. S., & Berger, J. M. (1997). Molecular basis of familial hypercholesterolaemia from structure of LDL receptor module. *Nature*, *388*(6643), 691–693. https://doi.org/10.1038/41798

Fernández, M. E., Croce, S., Boutin, C., Cremer, H., & Raineteau, O. (2011). Targeted electroporation of defined lateral ventricular walls: A novel and rapid method to study fate specification during postnatal forebrain neurogenesis. *Neural Development*, *6*, 13. https://doi.org/10.1186/1749-8104-6-13

Fonte, V. G., Searls, R. L., & Hilfer, S. R. (1971). The Relationship of Cilia with Cell Division and Differentiation. *The Journal of Cell Biology*, *49*(1), 226–229. https://doi.org/10.1083/jcb.49.1.226

Frank-Kamenetsky, M., Zhang, X. M., Bottega, S., Guicherit, O., Wichterle, H., Dudek, H., … Porter, J. A. (2002). Small-molecule modulators of Hedgehog signaling: Identification and characterization of Smoothened agonists and antagonists. *Journal of Biology*, *1*(2), 10.

Fuller, K., O'Connell, J. T., Gordon, J., Mauti, O., & Eggenschwiler, J. (2014). Rab23 regulates Nodal signaling in vertebrate left-right patterning independently of the Hedgehog pathway. *Developmental Biology*, *391*(2), 182–195. https://doi.org/10.1016/j.ydbio.2014.04.012

Gajera, C. R., Emich, H., Lioubinski, O., Christ, A., Beckervordersandforth-Bonk, R., Yoshikawa, K., … Hammes, A. (2010). LRP2 in ependymal cells regulates BMP signaling in the adult neurogenic niche. *Journal of Cell Science*, *123*(Pt 11), 1922–1930. https://doi.org/10.1242/jcs.065912

García-Verdugo, J. M., Doetsch, F., Wichterle, H., Lim, D. A., & Alvarez-Buylla, A. (1998). Architecture and cell types of the adult subventricular zone: In search of the stem cells. *Journal of Neurobiology*, *36*(2), 234–248.

Golden, J. A., Bracilovic, A., McFadden, K. A., Beesley, J. S., Rubenstein, J. L., & Grinspan, J. B. (1999). Ectopic bone morphogenetic proteins 5 and 4 in the chicken forebrain lead to cyclopia and holoprosencephaly. *Proceedings of the National Academy of Sciences of the United States of America*, *96*(5), 2439–2444. https://doi.org/10.1073/pnas.96.5.2439

Gotthardt, M., Trommsdorff, M., Nevitt, M. F., Shelton, J., Richardson, J. A., Stockinger, W., … Herz, J. (2000). Interactions of the low density lipoprotein receptor gene family with cytosolic adaptor and scaffold proteins suggest diverse biological functions in cellular communication and signal transduction. *The Journal of Biological Chemistry*, *275*(33), 25616–25624. https://doi.org/10.1074/jbc.M000955200

Gripp, K. W., Donnai, D., Clericuzio, C. L., McDonald-McGinn, D. M., Guttenberg, M., & Zackai, E. H. (1997). Diaphragmatic hernia-exomphalos-hypertelorism syndrome: A new case and further evidence of autosomal recessive inheritance. *American Journal of Medical Genetics*, *68*(4), 441–444.

Guirao, B., Meunier, A., Mortaud, S., Aguilar, A., Corsi, J.-M., Strehl, L., … Spassky, N. (2010). Coupling between hydrodynamic forces and planar cell polarity orients mammalian motile cilia. *Nature Cell Biology*, *12*(4), 341–350. https://doi.org/10.1038/ncb2040

Hammes, A., Andreassen, T. K., Spoelgen, R., Raila, J., Hubner, N., Schulz, H., … Willnow, T. E. (2005). Role of endocytosis in cellular uptake of sex steroids. *Cell*, *122*(5), 751–762. https://doi.org/10.1016/j.cell.2005.06.032

Hay, N., & Sonenberg, N. (2004). Upstream and downstream of mTOR. *Genes & Development*, *18*(16), 1926–1945. https://doi.org/10.1101/gad.1212704

Haycraft, C. J., Banizs, B., Aydin-Son, Y., Zhang, Q., Michaud, E. J., & Yoder, B. K. (2005). Gli2 and Gli3 localize to cilia and require the intraflagellar transport protein polaris for processing and function. *PLoS Genetics*, *1*(4), e53. https://doi.org/10.1371/journal.pgen.0010053

He, X., Semenov, M., Tamai, K., & Zeng, X. (2004). LDL receptor-related proteins 5 and 6 in Wnt/β-catenin signaling: Arrows point the way. *Development*, *131*(8), 1663–1677. https://doi.org/10.1242/dev.01117

Henry, L., & Sheff, D. R. (2008). Rab8 Regulates Basolateral Secretory, But Not Recycling, Traffic at the Recycling Endosome. *Molecular Biology of the Cell*, *19*(5), 2059–2068. https://doi.org/10.1091/mbc.E07-09-0902

Hermo, L., Lustig, M., Lefrancois, S., Argraves, W. S., & Morales, C. R. (1999). Expression and regulation of LRP-2/megalin in epithelial cells lining the efferent ducts and epididymis during postnatal development. *Molecular Reproduction and Development*, *53*(3), 282–293. https://doi.org/10.1002/(SICI)1098-2795(199907)53:3<282::AID-MRD4>3.0.CO;2-A

Herz, J., Hamann, U., Rogne, S., Myklebost, O., Gausepohl, H., & Stanley, K. K. (1988). Surface location and high affinity for calcium of a 500-kd liver membrane protein closely related to the LDL-receptor suggest a physiological role as lipoprotein receptor. *The EMBO Journal*, *7*(13), 4119–4127.

Herz, Joachim. (2001). The LDL Receptor Gene Family: (Un)Expected Signal Transducers in the Brain. *Neuron*, *29*(3), 571–581. https://doi.org/10.1016/S0896-6273(01)00234-3

Hey, P. J., Twells, R. C., Phillips, M. S., Yusuke Nakagawa, null, Brown, S. D., Kawaguchi, Y., … Hess, J. F. (1998). Cloning of a novel member of the low-density lipoprotein receptor family. *Gene*, *216*(1), 103–111.

Hirota, Y., Meunier, A., Huang, S., Shimozawa, T., Yamada, O., Kida, Y. S., … Sawamoto, K. (2010). Planar polarity of multiciliated ependymal cells involves the anterior migration of basal bodies regulated by non-muscle myosin II. *Development*, *137*(18), 3037–3046. https://doi.org/10.1242/dev.050120

Hirota, Y., Sawada, M., Huang, S.-H., Ogino, T., Ohata, S., Kubo, A., & Sawamoto, K. (2016). Roles of Wnt Signaling in the Neurogenic Niche of the Adult Mouse Ventricular-Subventricular Zone. *Neurochemical Research*, *41*(1–2), 222–230. https://doi.org/10.1007/s11064-015-1766-z

Hjälm, G., Murray, E., Crumley, G., Harazim, W., Lundgren, S., Onyango, I., … Morse, B. (1996). Cloning and sequencing of human gp330, a Ca(2+)-binding receptor with potential intracellular signaling properties. *European Journal of Biochemistry*, *239*(1), 132–137.

Holtz, A. M., Peterson, K. A., Nishi, Y., Morin, S., Song, J. Y., Charron, F., … Allen, B. L. (2013). Essential role for ligand-dependent feedback antagonism of vertebrate hedgehog signaling by PTCH1, PTCH2 and HHIP1 during neural patterning. *Development (Cambridge, England)*, *140*(16), 3423–3434. https://doi.org/10.1242/dev.095083

Howell, B. W., & Herz, J. (2001). The LDL receptor gene family: Signaling functions during development. *Current Opinion in Neurobiology*, *11*(1), 74–81.

Humke, E. W., Dorn, K. V., Milenkovic, L., Scott, M. P., & Rohatgi, R. (2010). The output of Hedgehog signaling is controlled by the dynamic association between Suppressor of Fused and the Gli proteins. *Genes & Development*, *24*(7), 670–682. https://doi.org/10.1101/gad.1902910

Hunziker, W., & Peters, P. J. (1998). Rab17 Localizes to Recycling Endosomes and Regulates Receptor-mediated Transcytosis in Epithelial Cells. *Journal of Biological Chemistry*, *273*(25), 15734–15741. https://doi.org/10.1074/jbc.273.25.15734

Hyman, T., Shmuel, M., & Altschuler, Y. (2006). Actin Is Required for Endocytosis at the Apical Surface of Madin-Darby Canine Kidney Cells where ARF6 and Clathrin Regulate the Actin Cytoskeleton. *Molecular Biology of the Cell*, *17*(1), 427–437. https://doi.org/10.1091/mbc.E05-05-0420

Hynes, M., Porter, J. A., Chiang, C., Chang, D., Tessier-Lavigne, M., Beachy, P. A., & Rosenthal, A. (1995). Induction of midbrain dopaminergic neurons by Sonic hedgehog. *Neuron*, *15*(1), 35–44.

Ihrie, R. A., Shah, J. K., Harwell, C. C., Levine, J. H., Guinto, C. D., Lezameta, M., … Alvarez-Buylla, A. (2011). Persistent sonic hedgehog signaling in adult brain determines neural stem cell positional identity. *Neuron*, *71*(2), 250–262. https://doi.org/10.1016/j.neuron.2011.05.018

Incardona, J. P., Lee, J. H., Robertson, C. P., Enga, K., Kapur, R. P., & Roelink, H. (2000). Receptor-mediated endocytosis of soluble and membrane-tethered Sonic hedgehog by Patched-1. *Proceedings of the National Academy of Sciences of the United States of America*, *97*(22), 12044–12049. https://doi.org/10.1073/pnas.220251997

Inoue, T., Nakamura, S., & Osumi, N. (2000). Fate mapping of the mouse prosencephalic neural plate. *Developmental Biology*, *219*(2), 373–383. https://doi.org/10.1006/dbio.2000.9616

Jacobsen, L., Madsen, P., Moestrup, S. K., Lund, A. H., Tommerup, N., Nykjaer, A., … Petersen, C. M. (1996). Molecular characterization of a novel human hybrid-type receptor that binds the alpha2-macroglobulin receptor-associated protein. *The Journal of Biological Chemistry*, *271*(49), 31379–31383. https://doi.org/10.1074/jbc.271.49.31379

Jensen, C. G., Poole, C. A., McGlashan, S. R., Marko, M., Issa, Z. I., Vujcich, K. V., & Bowser, S. S. (2004). Ultrastructural, tomographic and confocal imaging of the chondrocyte primary cilium in situ. *Cell Biology International*, *28*(2), 101–110. https://doi.org/10.1016/j.cellbi.2003.11.007

Jeong, J., & McMahon, A. P. (2005). Growth and pattern of the mammalian neural tube are governed by partially overlapping feedback activities of the hedgehog antagonists patched 1 and Hhip1. *Development (Cambridge, England)*, *132*(1), 143–154. https://doi.org/10.1242/dev.01566

Jessell, T. M. (2000). Neuronal specification in the spinal cord: Inductive signals and transcriptional codes. *Nature Reviews. Genetics*, *1*(1), 20–29. https://doi.org/10.1038/35049541

Jiménez, A. J., Domínguez-Pinos, M.-D., Guerra, M. M., Fernández-Llebrez, P., & Pérez-Fígares, J.-M. (2014). Structure and function of the ependymal barrier and diseases associated with ependyma disruption. *Tissue Barriers*, *2*, e28426. https://doi.org/10.4161/tisb.28426

Johansson, C. B., Momma, S., Clarke, D. L., Risling, M., Lendahl, U., & Frisén, J. (1999). Identification of a neural stem cell in the adult mammalian central nervous system. *Cell*, *96*(1), 25–34.

Jovic, M., Sharma, M., Rahajeng, J., & Caplan, S. (2010). The early endosome: A busy sorting station for proteins at the crossroads. *Histology and Histopathology*, *25*(1), 99–112.

Kang, J.-S., Mulieri, P. J., Hu, Y., Taliana, L., & Krauss, R. S. (2002). BOC, an Ig superfamily member, associates with CDO to positively regulate myogenic differentiation. *The EMBO Journal*, *21*(1–2), 114–124. https://doi.org/10.1093/emboj/21.1.114

Kantarci, S., Al-Gazali, L., Hill, R. S., Donnai, D., Black, G. C. M., Bieth, E., … Pober, B. R. (2007). Mutations in LRP2, which encodes the multiligand receptor megalin, cause Donnai-Barrow and facio-oculo-acoustico-renal syndromes. *Nature Genetics*, *39*(8), 957–959. https://doi.org/10.1038/ng2063

Kavran, J. M., Ward, M. D., Oladosu, O. O., Mulepati, S., & Leahy, D. J. (2010). All mammalian Hedgehog proteins interact with cell adhesion molecule, down-regulated by oncogenes (CDO) and brother of CDO (BOC) in a conserved manner. *The Journal of Biological Chemistry*, *285*(32), 24584–24590. https://doi.org/10.1074/jbc.M110.131680

Kelsch, W., Mosley, C. P., Lin, C.-W., & Lois, C. (2007). Distinct mammalian precursors are committed to generate neurons with defined dendritic projection patterns. *PLoS Biology*, *5*(11), e300. https://doi.org/10.1371/journal.pbio.0050300

Kerjaschki, D., & Farquhar, M. G. (1982). The pathogenic antigen of Heymann nephritis is a membrane glycoprotein of the renal proximal tubule brush border. *Proceedings of the National Academy of Sciences of the United States of America*, *79*(18), 5557–5561. https://doi.org/10.1073/pnas.79.18.5557

Khalifa, O., Al-Sahlawi, Z., Imtiaz, F., Ramzan, K., Allam, R., Al-Mostafa, A., … Al-Zaidan, H. (2015). Variable expression pattern in Donnai-Barrow syndrome: Report of two novel LRP2 mutations and review of the literature. *European Journal of Medical Genetics*, *58*(5), 293–299. https://doi.org/10.1016/j.ejmg.2014.12.008

Kise, Y., Morinaka, A., Teglund, S., & Miki, H. (2009). Sufu recruits GSK3beta for efficient processing of Gli3. *Biochemical and Biophysical Research Communications*, *387*(3), 569–574. https://doi.org/10.1016/j.bbrc.2009.07.087

Komiya, Y., & Habas, R. (2008). Wnt signal transduction pathways. *Organogenesis*, *4*(2), 68–75.

Kounnas, M. Z., Haudenschild, C. C., Strickland, D. K., & Argraves, W. S. (1994). Immunological localization of glycoprotein 330, low density lipoprotein receptor related protein and 39 kDa receptor associated protein in embryonic mouse tissues. *In Vivo (Athens, Greece)*, *8*(3), 343–351.

Kouranti, I., Sachse, M., Arouche, N., Goud, B., & Echard, A. (2006). Rab35 regulates an endocytic recycling pathway essential for the terminal steps of cytokinesis. *Current Biology: CB*, *16*(17), 1719–1725. https://doi.org/10.1016/j.cub.2006.07.020

Kovacs, J. J., Whalen, E. J., Liu, R., Xiao, K., Kim, J., Chen, M., … Lefkowitz, R. J. (2008). Beta-arrestin-mediated localization of smoothened to the primary cilium. *Science (New York, N.Y.)*, *320*(5884), 1777–1781. https://doi.org/10.1126/science.1157983

Kruszka, P., & Muenke, M. (2018). Syndromes associated with holoprosencephaly. *American Journal of Medical Genetics Part C: Seminars in Medical Genetics*, *178*(2), 229–237. https://doi.org/10.1002/ajmg.c.31620

Labedan, P., Matthews, C., Kodjabachian, L., Cremer, H., Tissir, F., & Boutin, C. (2016). Dissection and Staining of Mouse Brain Ventricular Wall for the Analysis of Ependymal Cell Cilia Organization. *BIO-PROTOCOL*, *6*(6). https://doi.org/10.21769/BioProtoc.1757

Lamba, D., Karl, M., & Reh, T. (2008). Neural regeneration and cell replacement: A view from the eye. *Cell Stem Cell*, *2*(6), 538–549. https://doi.org/10.1016/j.stem.2008.05.002

Lange, B. M., Faragher, A. J., March, P., & Gull, K. (2000). Centriole duplication and maturation in animal cells. *Current Topics in Developmental Biology*, *49*, 235–249.

Langenfeld, E. M., Kong, Y., & Langenfeld, J. (2005). Bone morphogenetic protein-2-induced transformation involves the activation of mammalian target of rapamycin. *Molecular Cancer Research: MCR*, *3*(12), 679–684. https://doi.org/10.1158/1541-7786.MCR-05-0124

Laplante, M., & Sabatini, D. M. (2009). MTOR signaling at a glance. *Journal of Cell Science*, *122*(20), 3589–3594. https://doi.org/10.1242/jcs.051011

Lee, J. J., Ekker, S. C., von Kessler, D. P., Porter, J. A., Sun, B. I., & Beachy, P. A. (1994). Autoproteolysis in hedgehog protein biogenesis. *Science (New York, N.Y.)*, *266*(5190), 1528–1537.

Leheste, J. R., Rolinski, B., Vorum, H., Hilpert, J., Nykjaer, A., Jacobsen, C., … Willnow, T. E. (1999). Megalin knockout mice as an animal model of low molecular weight proteinuria. *The American Journal of Pathology*, *155*(4), 1361–1370. https://doi.org/10.1016/S0002-9440(10)65238-8

Leheste, Jörg R., Melsen, F., Wellner, M., Jansen, P., Schlichting, U., Renner-Müller, I., … Willnow, T. E. (2003). Hypocalcemia and osteopathy in mice with kidney-specific megalin gene defect. *FASEB Journal: Official Publication of the Federation of American Societies for Experimental Biology*, *17*(2), 247–249. https://doi.org/10.1096/fj.02-0578fje

Lehtinen, M. K., Zappaterra, M. W., Chen, X., Yang, Y. J., Hill, A. D., Lun, M., … Walsh, C. A. (2011). The cerebrospinal fluid provides a proliferative niche for neural progenitor cells. *Neuron*, *69*(5), 893–905. https://doi.org/10.1016/j.neuron.2011.01.023

Lim, D. A., Tramontin, A. D., Trevejo, J. M., Herrera, D. G., García-Verdugo, J. M., & Alvarez-Buylla, A. (2000). Noggin antagonizes BMP signaling to create a niche for adult neurogenesis. *Neuron*, *28*(3), 713–726.

Lim, Daniel A., & Alvarez-Buylla, A. (2016). The Adult Ventricular–Subventricular Zone (V-SVZ) and Olfactory Bulb (OB) Neurogenesis. *Cold Spring Harbor Perspectives in Biology*, *8*(5). https://doi.org/10.1101/cshperspect.a018820

Lim, Y. S., & Tang, B. L. (2015). A role for Rab23 in the trafficking of Kif17 to the primary cilium. *Journal of Cell Science*, *128*(16), 2996–3008. https://doi.org/10.1242/jcs.163964

Liu, C. X., Musco, S., Lisitsina, N. M., Forgacs, E., Minna, J. D., & Lisitsyn, N. A. (2000). LRP-DIT, a putative endocytic receptor gene, is frequently inactivated in non-small cell lung cancer cell lines. *Cancer Research*, *60*(7), 1961–1967.

Liu, W., Yu, W. R., Carling, T., Juhlin, C., Rastad, J., Ridefelt, P., … Hellman, P. (1998). Regulation of gp330/megalin expression by vitamins A and D. *European Journal of Clinical Investigation*, *28*(2), 100–107.

Lois, C., & Alvarez-Buylla, A. (1994). Long-distance neuronal migration in the adult mammalian brain. *Science (New York, N.Y.)*, *264*(5162), 1145–1148.

Lois, C., García-Verdugo, J. M., & Alvarez-Buylla, A. (1996). Chain migration of neuronal precursors. *Science (New York, N.Y.)*, *271*(5251), 978–981.

Ma, X. M., & Blenis, J. (2009). Molecular mechanisms of mTOR-mediated translational control. *Nature Reviews. Molecular Cell Biology*, *10*(5), 307–318. https://doi.org/10.1038/nrm2672

MacDonald, B. T., Tamai, K., & He, X. (2009). Wnt/β-catenin signaling: Components, mechanisms, and diseases. *Developmental Cell*, *17*(1), 9–26. https://doi.org/10.1016/j.devcel.2009.06.016

Marshall, W. F., & Kintner, C. (2008). Cilia Orientation and the Fluid Mechanics of Development. *Current Opinion in Cell Biology*, *20*(1), 48–52. https://doi.org/10.1016/j.ceb.2007.11.009

Martinez-Ferre, A., Navarro-Garberi, M., Bueno, C., & Martinez, S. (2013). Wnt Signal Specifies the Intrathalamic Limit and Its Organizer Properties by Regulating Shh Induction in the Alar Plate. *Journal of Neuroscience*, *33*(9), 3967–3980. https://doi.org/10.1523/JNEUROSCI.0726-12.2013

McCarthy, R. A., Barth, J. L., Chintalapudi, M. R., Knaak, C., & Argraves, W. S. (2002). Megalin functions as an endocytic sonic hedgehog receptor. *The Journal of Biological Chemistry*, *277*(28), 25660–25667. https://doi.org/10.1074/jbc.M201933200

McLellan, J. S., Zheng, X., Hauk, G., Ghirlando, R., Beachy, P. A., & Leahy, D. J. (2008). The mode of Hedgehog binding to Ihog homologues is not conserved across different phyla. *Nature*, *455*(7215), 979–983. https://doi.org/10.1038/nature07358

Mich, J. K., Signer, R. A., Nakada, D., Pineda, A., Burgess, R. J., Vue, T. Y., … Morrison, S. J. (2014). Prospective identification of functionally distinct stem cells and neurosphere-initiating cells in adult mouse forebrain. *ELife*, *3*, e02669. https://doi.org/10.7554/eLife.02669

Mikawa, S., Wang, C., & Sato, K. (2006). Bone morphogenetic protein-4 expression in the adult rat brain. *The Journal of Comparative Neurology*, *499*(4), 613–625. https://doi.org/10.1002/cne.21125

Milenkovic, L., Scott, M. P., & Rohatgi, R. (2009). Lateral transport of Smoothened from the plasma membrane to the membrane of the cilium. *The Journal of Cell Biology*, *187*(3), 365–374. https://doi.org/10.1083/jcb.200907126

Mirvis, M., Stearns, T., & James Nelson, W. (2018). Cilium structure, assembly, and disassembly regulated by the cytoskeleton. *Biochemical Journal*, *475*(14), 2329–2353. https://doi.org/10.1042/BCJ20170453

Mirzadeh, Z., Han, Y.-G., Soriano-Navarro, M., García-Verdugo, J. M., & Alvarez-Buylla, A. (2010). Cilia Organize Ependymal Planar Polarity. *Journal of Neuroscience*, *30*(7), 2600–2610. https://doi.org/10.1523/JNEUROSCI.3744-09.2010

Mirzadeh, Z., Merkle, F. T., Soriano-Navarro, M., Garcia-Verdugo, J. M., & Alvarez-Buylla, A. (2008). Neural stem cells confer unique pinwheel architecture to the ventricular surface in neurogenic regions of the adult brain. *Cell Stem Cell*, *3*(3), 265–278. https://doi.org/10.1016/j.stem.2008.07.004

Mitchell, B., Jacobs, R., Li, J., Chien, S., & Kintner, C. (2007). A positive feedback mechanism governs the polarity and motion of motile cilia. *Nature*, *447*(7140), 97–101. https://doi.org/10.1038/nature05771

Mitchell, B., Stubbs, J. L., Huisman, F., Taborek, P., Yu, C., & Kintner, C. (2009). The PCP pathway instructs the planar orientation of ciliated cells in the Xenopus larval skin. *Current Biology: CB*, *19*(11), 924–929. https://doi.org/10.1016/j.cub.2009.04.018

Moestrup, S. K., Birn, H., Fischer, P. B., Petersen, C. M., Verroust, P. J., Sim, R. B., … Nexø, E. (1996). Megalin-mediated endocytosis of transcobalamin-vitamin-B12 complexes suggests a role of the receptor in vitamin-B12 homeostasis. *Proceedings of the National Academy of Sciences of the United States of America*, *93*(16), 8612–8617. https://doi.org/10.1073/pnas.93.16.8612

Mohamed, O. A., Clarke, H. J., & Dufort, D. (2004). Beta-catenin signaling marks the prospective site of primitive streak formation in the mouse embryo. *Developmental Dynamics: An Official Publication of the American Association of Anatomists*, *231*(2), 416–424. https://doi.org/10.1002/dvdy.20135

Molla-Herman, A., Ghossoub, R., Blisnick, T., Meunier, A., Serres, C., Silbermann, F., … Benmerah, A. (2010). The ciliary pocket: An endocytic membrane domain at the base of primary and motile cilia. *Journal of Cell Science*, *123*(10), 1785–1795. https://doi.org/10.1242/jcs.059519

Morales, C. R., Zeng, J., El Alfy, M., Barth, J. L., Chintalapudi, M. R., McCarthy, R. A., … Argraves, W. S. (2006). Epithelial trafficking of Sonic hedgehog by megalin. *The Journal of Histochemistry and Cytochemistry: Official Journal of the Histochemistry Society*, *54*(10), 1115–1127. https://doi.org/10.1369/jhc.5A6899.2006

Morris, S. M., Arden, S. D., Roberts, R. C., Kendrick-Jones, J., Cooper, J. A., Luzio, J. P., & Buss, F. (2002). Myosin VI binds to and localises with Dab2, potentially linking receptor-mediated endocytosis and the actin cytoskeleton. *Traffic (Copenhagen, Denmark)*, *3*(5), 331–341.

Mörwald, S., Yamazaki, H., Bujo, H., Kusunoki, J., Kanaki, T., Seimiya, K., … Saito, Y. (1997). A novel mosaic protein containing LDL receptor elements is highly conserved in humans and chickens. *Arteriosclerosis, Thrombosis, and Vascular Biology*, *17*(5), 996–1002.

Motoyama, J., Takabatake, T., Takeshima, K., & Hui, C. (1998). Ptch2, a second mouse Patched gene is co-expressed with Sonic hedgehog. *Nature Genetics*, *18*(2), 104–106. https://doi.org/10.1038/ng0298-104

Mulieri, P. J., Okada, A., Sassoon, D. A., McConnell, S. K., & Krauss, R. S. (2000). Developmental expression pattern of the cdo gene. *Developmental Dynamics: An Official Publication of the American Association of Anatomists*, *219*(1), 40–49. https://doi.org/10.1002/1097-0177(2000)9999:9999<::AID-DVDY1032>3.0.CO;2-M

Nagai, J., Christensen, E. I., Morris, S. M., Willnow, T. E., Cooper, J. A., & Nielsen, R. (2005). Mutually dependent localization of megalin and Dab2 in the renal proximal tubule. *American Journal of Physiology. Renal Physiology*, *289*(3), F569-576. https://doi.org/10.1152/ajprenal.00292.2004

Nakayama, M., Nakajima, D., Nagase, T., Nomura, N., Seki, N., & Ohara, O. (1998). Identification of high-molecular-weight proteins with multiple EGF-like motifs by motif-trap screening. *Genomics*, *51*(1), 27–34. https://doi.org/10.1006/geno.1998.5341

Nguyen-Ba-Charvet, K. T., Picard-Riera, N., Tessier-Lavigne, M., Baron-Van Evercooren, A., Sotelo, C., & Chédotal, A. (2004). Multiple roles for slits in the control of cell migration in the rostral migratory stream. *The Journal of Neuroscience: The Official Journal of the Society for Neuroscience*, *24*(6), 1497–1506. https://doi.org/10.1523/JNEUROSCI.4729-03.2004

Nykjaer, A., Dragun, D., Walther, D., Vorum, H., Jacobsen, C., Herz, J., … Willnow, T. E. (1999). An endocytic pathway essential for renal uptake and activation of the steroid 25-(OH) vitamin D3. *Cell*, *96*(4), 507–515.

Ohata, S., & Alvarez-Buylla, A. (2016). Planar Organization of Multiciliated Ependymal (E1) Cells in the Brain Ventricular Epithelium. *Trends in Neurosciences*, *39*(8), 543–551. https://doi.org/10.1016/j.tins.2016.05.004

Oleinikov, A. V., Zhao, J., & Makker, S. P. (2000). Cytosolic adaptor protein Dab2 is an intracellular ligand of endocytic receptor gp600/megalin. *The Biochemical Journal*, *347 Pt 3*, 613–621.

Olstad, E. W., Ringers, C., Hansen, J. N., Wens, A., Brandt, C., Wachten, D., … Jurisch-Yaksi, N. (2019). Ciliary Beating Compartmentalizes Cerebrospinal Fluid Flow in the Brain and Regulates Ventricular Development. *Current Biology: CB*, *29*(2), 229-241.e6. https://doi.org/10.1016/j.cub.2018.11.059

Ortega, M. C., Cases, O., Merchán, P., Kozyraki, R., Clemente, D., & de Castro, F. (2012). Megalin mediates the influence of sonic hedgehog on oligodendrocyte precursor cell migration and proliferation during development. *Glia*, *60*(6), 851–866. https://doi.org/10.1002/glia.22316

Paliouras, G. N., Hamilton, L. K., Aumont, A., Joppé, S. E., Barnabé-Heider, F., & Fernandes, K. J. L. (2012). Mammalian target of rapamycin signaling is a key regulator of the transit-amplifying progenitor pool in the adult and aging forebrain. *The Journal of Neuroscience: The Official Journal of the Society for Neuroscience*, *32*(43), 15012–15026. https://doi.org/10.1523/JNEUROSCI.2248-12.2012

Palma, V., Lim, D. A., Dahmane, N., Sánchez, P., Brionne, T. C., Herzberg, C. D., … Ruiz i Altaba, A. (2005). Sonic hedgehog controls stem cell behavior in the postnatal and adult brain. *Development (Cambridge, England)*, *132*(2), 335–344. https://doi.org/10.1242/dev.01567

Patten, I., & Placzek, M. (2002). Opponent activities of Shh and BMP signaling during floor plate induction in vivo. *Current Biology: CB*, *12*(1), 47–52.

Peifer, M., & McEwen, D. G. (2002). The Ballet of Morphogenesis: Unveiling the Hidden Choreographers. *Cell*, *109*(3), 271–274. https://doi.org/10.1016/S0092-8674(02)00739-0

Pepinsky, R. B., Zeng, C., Wen, D., Rayhorn, P., Baker, D. P., Williams, K. P., … Galdes, A. (1998). Identification of a palmitic acid-modified form of human Sonic hedgehog. *The Journal of Biological Chemistry*, *273*(22), 14037–14045. https://doi.org/10.1074/jbc.273.22.14037

Peretto, P., Dati, C., De Marchis, S., Kim, H. H., Ukhanova, M., Fasolo, A., & Margolis, F. L. (2004). Expression of the secreted factors noggin and bone morphogenetic proteins in the subependymal layer and olfactory bulb of the adult mouse brain. *Neuroscience*, *128*(4), 685–696. https://doi.org/10.1016/j.neuroscience.2004.06.053

Pineda-Alvarez, D. E., Roessler, E., Hu, P., Srivastava, K., Solomon, B. D., Siple, C. E., … Muenke, M. (2012). Missense substitutions in the GAS1 protein present in holoprosencephaly patients reduce the affinity for its ligand, SHH. *Human Genetics*, *131*(2), 301–310. https://doi.org/10.1007/s00439-011-1078-6

Pinson, K. I., Brennan, J., Monkley, S., Avery, B. J., & Skarnes, W. C. (2000). An LDL-receptor-related protein mediates Wnt signalling in mice. *Nature*, *407*(6803), 535. https://doi.org/10.1038/35035124

Pober, B. R., Longoni, M., & Noonan, K. M. (2009). A review of Donnai-Barrow and facio-oculo-acoustico-renal (DB/FOAR) syndrome: Clinical features and differential diagnosis. *Birth Defects Research. Part A, Clinical and Molecular Teratology*, *85*(1), 76–81. https://doi.org/10.1002/bdra.20534

Pócza, T., Sebestyén, A., Turányi, E., Krenács, T., Márk, A., Sticz, T. B., … Hauser, P. (2014). MTOR pathway as a potential target in a subset of human medulloblastoma. *Pathology Oncology Research: POR*, *20*(4), 893–900. https://doi.org/10.1007/s12253-014-9771-0

Ponti, G., Obernier, K., & Alvarez-Buylla, A. (2013). Lineage progression from stem cells to new neurons in the adult brain ventricular-subventricular zone. *Cell Cycle*, *12*(11), 1649–1650. https://doi.org/10.4161/cc.24984

Porter, J. A., von Kessler, D. P., Ekker, S. C., Young, K. E., Lee, J. J., Moses, K., & Beachy, P. A. (1995). The product of hedgehog autoproteolytic cleavage active in local and long-range signalling. *Nature*, *374*(6520), 363–366. https://doi.org/10.1038/374363a0

Rahnama, F., Toftgård, R., & Zaphiropoulos, P. G. (2004). Distinct roles of PTCH2 splice variants in Hedgehog signalling. *The Biochemical Journal*, *378*(Pt 2), 325–334. https://doi.org/10.1042/BJ20031200

Ramírez-Castillejo, C., Sánchez-Sánchez, F., Andreu-Agulló, C., Ferrón, S. R., Aroca-Aguilar, J. D., Sánchez, P., … Fariñas, I. (2006). Pigment epithelium-derived factor is a niche signal for neural stem cell renewal. *Nature Neuroscience*, *9*(3), 331–339. https://doi.org/10.1038/nn1657

Roelink, H., Porter, J. A., Chiang, C., Tanabe, Y., Chang, D. T., Beachy, P. A., & Jessell, T. M. (1995). Floor plate and motor neuron induction by different concentrations of the amino-terminal cleavage product of sonic hedgehog autoproteolysis. *Cell*, *81*(3), 445–455.

Roessler, E., Belloni, E., Gaudenz, K., Jay, P., Berta, P., Scherer, S. W., … Muenke, M. (1996). Mutations in the human Sonic Hedgehog gene cause holoprosencephaly. *Nature Genetics*, *14*(3), 357–360. https://doi.org/10.1038/ng1196-357

Rohatgi, R., Milenkovic, L., & Scott, M. P. (2007). Patched1 regulates hedgehog signaling at the primary cilium. *Science (New York, N.Y.)*, *317*(5836), 372–376. https://doi.org/10.1126/science.1139740

Rubenstein, J. L., & Beachy, P. A. (1998). Patterning of the embryonic forebrain. *Current Opinion in Neurobiology*, *8*(1), 18–26.

Rudenko, G., Henry, L., Henderson, K., Ichtchenko, K., Brown, M. S., Goldstein, J. L., & Deisenhofer, J. (2002). Structure of the LDL receptor extracellular domain at endosomal pH. *Science (New York, N.Y.)*, *298*(5602), 2353–2358. https://doi.org/10.1126/science.1078124

Saito, A., Pietromonaco, S., Loo, A. K., & Farquhar, M. G. (1994). Complete cloning and sequencing of rat gp330/"megalin," a distinctive member of the low density lipoprotein receptor gene family. *Proceedings of the National Academy of Sciences of the United States of America*, *91*(21), 9725–9729. https://doi.org/10.1073/pnas.91.21.9725

Sanders, T. A., Llagostera, E., & Barna, M. (2013). Specialized filopodia direct long-range transport of SHH during vertebrate tissue patterning. *Nature*, *497*(7451), 628–632. https://doi.org/10.1038/nature12157

Sandvig, K., Torgersen, M. L., Raa, H. A., & van Deurs, B. (2008). Clathrin-independent endocytosis: From nonexisting to an extreme degree of complexity. *Histochemistry and Cell Biology*, *129*(3), 267–276. https://doi.org/10.1007/s00418-007-0376-5

Sarbassov, D. D., Ali, S. M., & Sabatini, D. M. (2005). Growing roles for the mTOR pathway. *Current Opinion in Cell Biology*, *17*(6), 596–603. https://doi.org/10.1016/j.ceb.2005.09.009

Sarnat, H. B. (1992). Role of human fetal ependyma. *Pediatric Neurology*, *8*(3), 163–178.

Sasaki, H., Nishizaki, Y., Hui, C., Nakafuku, M., & Kondoh, H. (1999). Regulation of Gli2 and Gli3 activities by an amino-terminal repression domain: Implication of Gli2 and Gli3 as primary mediators of Shh signaling. *Development (Cambridge, England)*, *126*(17), 3915–3924.

Satir, P., Heuser, T., & Sale, W. S. (2014). A Structural Basis for How Motile Cilia Beat. *Bioscience*, *64*(12), 1073–1083. https://doi.org/10.1093/biosci/biu180

Sato, M., Sato, K., Liou, W., Pant, S., Harada, A., & Grant, B. D. (2008). Regulation of endocytic recycling by C. elegans Rab35 and its regulator RME-4, a coated-pit protein. *The EMBO Journal*, *27*(8), 1183–1196. https://doi.org/10.1038/emboj.2008.54

Sawamoto, K., Wichterle, H., Gonzalez-Perez, O., Cholfin, J. A., Yamada, M., Spassky, N., … Alvarez-Buylla, A. (2006). New neurons follow the flow of cerebrospinal fluid in the adult brain. *Science (New York, N.Y.)*, *311*(5761), 629–632. https://doi.org/10.1126/science.1119133

Schmechel, D. E., Saunders, A. M., Strittmatter, W. J., Crain, B. J., Hulette, C. M., Joo, S. H., … Roses, A. D. (1993). Increased amyloid beta-peptide deposition in cerebral cortex as a consequence of apolipoprotein E genotype in late-onset Alzheimer disease. *Proceedings of the National Academy of Sciences of the United States of America*, *90*(20), 9649–9653.

Seppala, M., Depew, M. J., Martinelli, D. C., Fan, C.-M., Sharpe, P. T., & Cobourne, M. T. (2007). Gas1 is a modifier for holoprosencephaly and genetically interacts with sonic hedgehog. *The Journal of Clinical Investigation*, *117*(6), 1575–1584. https://doi.org/10.1172/JCI32032

Shah, M., Baterina, O. Y., Taupin, V., & Farquhar, M. G. (2013). ARH directs megalin to the endocytic recycling compartment to regulate its proteolysis and gene expression. *The Journal of Cell Biology*, *202*(1), 113–127. https://doi.org/10.1083/jcb.201211110

Sharma, N., Nanta, R., Sharma, J., Gunewardena, S., Singh, K. P., Shankar, S., & Srivastava, R. K. (2015). PI3K/AKT/mTOR and sonic hedgehog pathways cooperate together to inhibit human pancreatic cancer stem cell characteristics and tumor growth. *Oncotarget*, *6*(31), 32039–32060.

Shimogori, T., Banuchi, V., Ng, H. Y., Strauss, J. B., & Grove, E. A. (2004). Embryonic signaling centers expressing BMP, WNT and FGF proteins interact to pattern the cerebral cortex. *Development*, *131*(22), 5639–5647. https://doi.org/10.1242/dev.01428

Spassky, N., Merkle, F. T., Flames, N., Tramontin, A. D., García-Verdugo, J. M., & Alvarez-Buylla, A. (2005a). Adult Ependymal Cells Are Postmitotic and Are Derived from Radial Glial Cells during Embryogenesis. *Journal of Neuroscience*, *25*(1), 10–18. https://doi.org/10.1523/JNEUROSCI.1108-04.2005

Spassky, N., Merkle, F. T., Flames, N., Tramontin, A. D., García-Verdugo, J. M., & Alvarez-Buylla, A. (2005b). Adult Ependymal Cells Are Postmitotic and Are Derived from Radial Glial Cells during Embryogenesis. *Journal of Neuroscience*, *25*(1), 10–18. https://doi.org/10.1523/JNEUROSCI.1108-04.2005

Spoelgen, R., Hammes, A., Anzenberger, U., Zechner, D., Andersen, O. M., Jerchow, B., & Willnow, T. E. (2005). LRP2/megalin is required for patterning of the ventral telencephalon. *Development (Cambridge, England)*, *132*(2), 405–414. https://doi.org/10.1242/dev.01580

Stebel, M., Vatta, P., Ruaro, M. E., Del Sal, G., Parton, R. G., & Schneider, C. (2000). The growth suppressing gas1 product is a GPI-linked protein. *FEBS Letters*, *481*(2), 152–158.

Sur, M., & Rubenstein, J. L. R. (2005). Patterning and plasticity of the cerebral cortex. *Science (New York, N.Y.)*, *310*(5749), 805–810. https://doi.org/10.1126/science.1112070

Taipale, J., Cooper, M. K., Maiti, T., & Beachy, P. A. (2002). Patched acts catalytically to suppress the activity of Smoothened. *Nature*, *418*(6900), 892–897. https://doi.org/10.1038/nature00989

Taipale, Jussi, Chen, J. K., Cooper, M. K., Wang, B., Mann, R. K., Milenkovic, L., … Beachy, P. A. (2000). Effects of oncogenic mutations in Smoothened and Patched can be reversed by cyclopamine. *Nature*, *406*(6799), 1005. https://doi.org/10.1038/35023008

Takahashi, S., Kawarabayasi, Y., Nakai, T., Sakai, J., & Yamamoto, T. (1992). Rabbit very low density lipoprotein receptor: A low density lipoprotein receptor-like protein with distinct ligand specificity. *Proceedings of the National Academy of Sciences of the United States of America*, *89*(19), 9252–9256. https://doi.org/10.1073/pnas.89.19.9252

Takeda, T., Yamazaki, H., & Farquhar, M. G. (2003). Identification of an apical sorting determinant in the cytoplasmic tail of megalin. *American Journal of Physiology. Cell Physiology*, *284*(5), C1105-1113. https://doi.org/10.1152/ajpcell.00514.2002

Tao, W., Moore, R., Smith, E. R., & Xu, X.-X. (2016). Endocytosis and Physiology: Insights from Disabled-2 Deficient Mice. *Frontiers in Cell and Developmental Biology*, *4*. https://doi.org/10.3389/fcell.2016.00129

Telano, L. N., & Baker, S. (2019). Physiology, Cerebral Spinal Fluid (CSF). In *StatPearls*. Retrieved from http://www.ncbi.nlm.nih.gov/books/NBK519007/

Tenzen, T., Allen, B. L., Cole, F., Kang, J.-S., Krauss, R. S., & McMahon, A. P. (2006). The cell surface membrane proteins Cdo and Boc are components and targets of the Hedgehog signaling pathway and feedback network in mice. *Developmental Cell*, *10*(5), 647–656. https://doi.org/10.1016/j.devcel.2006.04.004

The Mouse Brain in Stereotaxic Coordinates, Compact—3rd Edition. (n.d.). Retrieved August 11, 2019, from https://www.elsevier.com/books/the-mouse-brain-in-stereotaxic-coordinates-compact/franklin/978-0-12-374244-5

Traiffort, E., Moya, K. L., Faure, H., Hässig, R., & Ruat, M. (2001). High expression and anterograde axonal transport of aminoterminal sonic hedgehog in the adult hamster brain. *The European Journal of Neuroscience*, *14*(5), 839–850.

Tramontin, A. D., García-Verdugo, J. M., Lim, D. A., & Alvarez-Buylla, A. (2003). Postnatal Development of Radial Glia and the Ventricular Zone (VZ): A Continuum of the Neural Stem Cell Compartment. *Cerebral Cortex*, *13*(6), 580–587. https://doi.org/10.1093/cercor/13.6.580

Traub, L. M. (2009). Tickets to ride: Selecting cargo for clathrin-regulated internalization. *Nature Reviews. Molecular Cell Biology*, *10*(9), 583–596. https://doi.org/10.1038/nrm2751

Tukachinsky, H., Lopez, L. V., & Salic, A. (2010). A mechanism for vertebrate Hedgehog signaling: Recruitment to cilia and dissociation of SuFu-Gli protein complexes. *The Journal of Cell Biology*, *191*(2), 415–428. https://doi.org/10.1083/jcb.201004108

Tuson, M., He, M., & Anderson, K. V. (2011). Protein kinase A acts at the basal body of the primary cilium to prevent Gli2 activation and ventralization of the mouse neural tube. *Development (Cambridge, England)*, *138*(22), 4921–4930. https://doi.org/10.1242/dev.070805

van Amerongen, R., & Nusse, R. (2009). Towards an integrated view of Wnt signaling in development. *Development (Cambridge, England)*, *136*(19), 3205–3214. https://doi.org/10.1242/dev.033910

Veening, J. G., & Barendregt, H. P. (2010). The regulation of brain states by neuroactive substances distributed via the cerebrospinal fluid; a review. *Cerebrospinal Fluid Research*, *7*, 1. https://doi.org/10.1186/1743-8454-7-1

Vladar, E. K., & Axelrod, J. D. (2008). Dishevelled links basal body docking and orientation in ciliated epithelial cells. *Trends in Cell Biology*, *18*(11), 517–520. https://doi.org/10.1016/j.tcb.2008.08.004

Wang, B., Fallon, J. F., & Beachy, P. A. (2000). Hedgehog-regulated processing of Gli3 produces an anterior/posterior repressor gradient in the developing vertebrate limb. *Cell*, *100*(4), 423–434.

Wang, Y. P., Dakubo, G., Howley, P., Campsall, K. D., Mazarolle, C. J., Shiga, S. A., … Wallace, V. A. (2002). Development of normal retinal organization depends on Sonic hedgehog signaling from ganglion cells. *Nature Neuroscience*, *5*(9), 831–832. https://doi.org/10.1038/nn911

Wang, Yan, Ding, Q., Yen, C.-J., Xia, W., Izzo, J. G., Lang, J.-Y., … Hung, M.-C. (2012). The Crosstalk of mTOR/S6K1 and Hedgehog pathways. *Cancer Cell*, *21*(3), 374–387. https://doi.org/10.1016/j.ccr.2011.12.028

Wang, Yu, Zhou, Z., Walsh, C. T., & McMahon, A. P. (2009). Selective translocation of intracellular Smoothened to the primary cilium in response to Hedgehog pathway modulation. *Proceedings of the National Academy of Sciences of the United States of America*, *106*(8), 2623–2628. https://doi.org/10.1073/pnas.0812110106

Werner, M. E., Hwang, P., Huisman, F., Taborek, P., Yu, C. C., & Mitchell, B. J. (2011). Actin and microtubules drive differential aspects of planar cell polarity in multiciliated cells. *The Journal of Cell Biology*, *195*(1), 19–26. https://doi.org/10.1083/jcb.201106110

Wichterle, H., Garcia-Verdugo, J. M., & Alvarez-Buylla, A. (1997). Direct evidence for homotypic, glia-independent neuronal migration. *Neuron*, *18*(5), 779–791.

Willnow, T. E., Hilpert, J., Armstrong, S. A., Rohlmann, A., Hammer, R. E., Burns, D. K., & Herz, J. (1996). Defective forebrain development in mice lacking gp330/megalin. *Proceedings of the National Academy of Sciences of the United States of America*, *93*(16), 8460–8464. https://doi.org/10.1073/pnas.93.16.8460

Willnow, Thomas E., Christ, A., & Hammes, A. (2012). Endocytic receptor-mediated control of morphogen signaling. *Development*, *139*(23), 4311–4319. https://doi.org/10.1242/dev.084467

Willnow, Thomas E., Hammes, A., & Eaton, S. (2007). Lipoproteins and their receptors in embryonic development: More than cholesterol clearance. *Development*, *134*(18), 3239–3249. https://doi.org/10.1242/dev.004408

Winkler, T., Mahoney, E. J., Sinner, D., Wylie, C. C., & Dahia, C. L. (2014). Wnt Signaling Activates Shh Signaling in Early Postnatal Intervertebral Discs, and Re-Activates Shh Signaling in Old Discs in the Mouse. *PLOS ONE*, *9*(6), e98444. https://doi.org/10.1371/journal.pone.0098444

Worthington, W. C., & Cathcart, R. S. (1963). Ependymal cilia: Distribution and activity in the adult human brain. *Science (New York, N.Y.)*, *139*(3551), 221–222.

Wu, C.-C., Hou, S., Orr, B. A., Kuo, B. R., Youn, Y. H., Ong, T., … Han, Y.-G. (2017). MTORC1-Mediated Inhibition of 4EBP1 Is Essential for Hedgehog Signaling-Driven Translation and Medulloblastoma. *Developmental Cell*, *43*(6), 673-688.e5. https://doi.org/10.1016/j.devcel.2017.10.011

Xia, Y. R., Bachinsky, D. R., Smith, J. A., McCluskey, R. T., Warden, C. H., & Lusis, A. J. (1993a). Mapping of the glycoprotein 330 (Gp330) gene to mouse chromosome 2. *Genomics*, *17*(3), 780–781. https://doi.org/10.1006/geno.1993.1408

Xia, Y. R., Bachinsky, D. R., Smith, J. A., McCluskey, R. T., Warden, C. H., & Lusis, A. J. (1993b). Mapping of the glycoprotein 330 (Gp330) gene to mouse chromosome 2. *Genomics*, *17*(3), 780–781. https://doi.org/10.1006/geno.1993.1408

Xiong, B., Li, A., Lou, Y., Chen, S., Long, B., Peng, J., … Gong, H. (2017). Precise Cerebral Vascular Atlas in Stereotaxic Coordinates of Whole Mouse Brain. *Frontiers in Neuroanatomy*, *11*. https://doi.org/10.3389/fnana.2017.00128

Yamamoto, T., Davis, C. G., Brown, M. S., Schneider, W. J., Casey, M. L., Goldstein, J. L., & Russell, D. W. (1984). The human LDL receptor: A cysteine-rich protein with multiple Alu sequences in its mRNA. *Cell*, *39*(1), 27–38.

Yang, W., Garrett, L., Feng, D., Elliott, G., Liu, X., Wang, N., … Gao, B. (2017). Wnt-induced Vangl2 phosphorylation is dose-dependently required for planar cell polarity in mammalian development. *Cell Research*, *27*. https://doi.org/10.1038/cr.2017.127

Yao, S., Lum, L., & Beachy, P. (2006). The ihog cell-surface proteins bind Hedgehog and mediate pathway activation. *Cell*, *125*(2), 343–357. https://doi.org/10.1016/j.cell.2006.02.040

Zacchi, P., Stenmark, H., Parton, R., Orioli, D., Lim, F., Giner, A., … Murphy, C. (1998). Rab17 Regulates Membrane Trafficking through Apical Recycling Endosomes in Polarized Epithelial Cells. *The Journal of Cell Biology*, *140*, 1039–1053.

Zarbalis, K., May, S. R., Shen, Y., Ekker, M., Rubenstein, J. L. R., & Peterson, A. S. (2004). A focused and efficient genetic screening strategy in the mouse: Identification of mutations that disrupt cortical development. *PLoS Biology*, *2*(8), E219. https://doi.org/10.1371/journal.pbio.0020219

Zhang, W., Hong, M., Bae, G., Kang, J.-S., & Krauss, R. S. (2011). Boc modifies the holoprosencephaly spectrum of Cdo mutant mice. *Disease Models & Mechanisms*, *4*(3), 368–380. https://doi.org/10.1242/dmm.005744

Zhang, W., Kang, J.-S., Cole, F., Yi, M.-J., & Krauss, R. S. (2006). Cdo functions at multiple points in the Sonic Hedgehog pathway, and Cdo-deficient mice accurately model human holoprosencephaly. *Developmental Cell*, *10*(5), 657–665. https://doi.org/10.1016/j.devcel.2006.04.005

Zhang, X. M., Ramalho-Santos, M., & McMahon, A. P. (2001). Smoothened mutants reveal redundant roles for Shh and Ihh signaling including regulation of L/R asymmetry by the mouse node. *Cell*, *105*(6), 781–792.

Zhao, H., Chen, Q., Fang, C., Huang, Q., Zhou, J., Yan, X., & Zhu, X. (2019). Parental centrioles are dispensable for deuterosome formation and function during basal body amplification. *EMBO Reports*, e46735. https://doi.org/10.15252/embr.201846735

Zhao, S., Chen, Q., Hung, F.-C., & Overbeek, P. A. (2002). BMP signaling is required for development of the ciliary body. *Development (Cambridge, England)*, *129*(19), 4435–4442.

Zheng, G., Bachinsky, D. R., Stamenkovic, I., Strickland, D. K., Brown, D., Andres, G., & McCluskey, R. T. (1994). Organ distribution in rats of two members of the low-density lipoprotein receptor gene family, gp330 and LRP/alpha 2MR, and the receptor-associated protein (RAP). *The Journal of Histochemistry and Cytochemistry: Official Journal of the Histochemistry Society*, *42*(4), 531–542. https://doi.org/10.1177/42.4.7510321

Zheng, L.-Q., Chi, S.-M., & Li, C.-X. (2017). Rab23's genetic structure, function and related diseases: A review. *Bioscience Reports*, *37*(2). https://doi.org/10.1042/BSR20160410

Zoncu, R., Efeyan, A., & Sabatini, D. M. (2011). mTOR: From growth signal integration to cancer, diabetes and ageing. *Nature Reviews. Molecular Cell Biology*, *12*(1), 21–35. https://doi.org/10.1038/nrm3025

7 Appendices

7.1 Publications

Zywitza V, Misios A, **Bunatyan L**, Willnow TE, Rajewsky N.

Single-Cell Transcriptomics Characterizes Cell Types in the Subventricular Zone and Uncovers Molecular Defects Impairing Adult Neurogenesis. *Cell Rep. 2018 Nov 27*

7.2 Acknowledgement

I would like to express my sincere gratitude and appreciation to my supervisor Professor Dr. Thomas Willnow for the opportunity to work on such an exciting project in a truly encouraging scientific environment. You have been a tremendous mentor with all your constructive critique and intellectual support. I was constantly inspired by your genuine dedication and enthusiasm to conduct research. I want to extend my deepest gratitude to Dr. Annabel Christ, for her unwavering guidance during the entire process of my Ph.D. studies. You have given me a hand to deal with the practicalities of working in the lab, constantly encouraged my new ideas providing valuable suggestions to implement them.

I am very grateful to Professor Dr. Petra Knaus for her willingness to be the external supervisor and second reviewer during my doctorate procedure at FU. Your feedback helped me a lot to think about new approaches towards the realization of my research goals.

Special thanks I want to express to Nikolaus Rajewsky and Camille Boutin for an astonishing opportunity of collaborative work.

I'm very grateful to Kristin Kampf, Maria Kahlow, Maria Kamprath, Christine Kruse for great technical support. Many thanks go to all nice colleagues that I've got the chance to work within this group. Thank you Verona Kuhle for being so proactive and helpful to solve any problems inside and outside of the lab.

Finally, special thanks to my family, old and new friends, whose immense support and love I feel each moment. Thanks for just being…

7.3 Selbstständigkeitserklärung

Hiermit erkläre ich, dass ich die vorliegende Arbeit mit dem Titel " The role of LRP2 in sonic hedgehog dependent adult neurogenesis" selbstständig und ohne Hilfe Dritter angefertigt habe. Sämtliche Hilfsmittel, Hilfen sowie Literaturquellen sind als solche kenntlich gemacht. Außerdem erkläre ich hiermit, dass ich mich nicht anderweitig um einen entsprechenden Doktorgrad beworben habe. Die Promotionsordnung des Fachbereichs Biologie, Chemie und Pharmazie der Freien Universität Berlin habe ich gelesen und akzeptiert.

Berlin, Aug 2019

Lena Bunatyan

7.4 Curriculum vitae

For reasons of data protection, the curriculum vitae is not published in the electronic version.

For reasons of data protection, the curriculum vitae is not published in the electronic version.